

The University of Maine

DigitalCommons@UMaine

Electronic Theses and Dissertations

Fogler Library

Spring 5-5-2023

Rab27a as a Regulator of Thoracic Aorta Reactivity and Exosome Signaling

Ashley Soucy

University of Maine, Ashley.n.soucy@maine.edu

Follow this and additional works at: <https://digitalcommons.library.umaine.edu/etd>



Part of the [Laboratory and Basic Science Research Commons](#)

Recommended Citation

Soucy, Ashley, "Rab27a as a Regulator of Thoracic Aorta Reactivity and Exosome Signaling" (2023).
Electronic Theses and Dissertations. 3769.

<https://digitalcommons.library.umaine.edu/etd/3769>

This Open-Access Thesis is brought to you for free and open access by DigitalCommons@UMaine. It has been accepted for inclusion in Electronic Theses and Dissertations by an authorized administrator of DigitalCommons@UMaine. For more information, please contact um.library.technical.services@maine.edu.

**RAB27A AS A REGULATOR OF THORACIC AORTA REACTIVITY AND EXOSOME
SIGNALING**

By

Ashley N. Soucy

B.S. Biochemistry, The University of Maine, 2018

A DISSERTATION

Submitted in Partial Fulfillment of the

Requirements for the Degree of

Doctor of Philosophy

(in Biomedical Science)

The Graduate School of Biomedical Science and Engineering

The University of Maine

May 2023

Advisory Committee:

Lucy Liaw, Faculty Scientist III, MaineHealth Institute for Research, Advisor

Aaron Brown, Faculty Scientist I, MaineHealth Institute for Research, Chair

Calvin Vary, Faculty Scientist III, MaineHealth Institute for Research

Michaela Reagan, Faculty Scientist II, MaineHealth Institute for Research

Benjamin King, Associate Professor of Bioinformatics, The University of Maine

RAB27A AS A REGULATOR OF THORACIC AORTA REACTIVITY AND EXOSOME SIGNALING

By: Ashley N. Soucy
Dissertation Advisor: Dr. Lucy Liaw

An Abstract for the Dissertation Presented in
Partial Fulfillment of the Requirements for the
Degree of Doctor of Philosophy
(in Biomedical Science)
May 2023

Cardiovascular disease (CVD) is a leading cause of mortality globally. Metabolic diseases, such as obesity, are major risk factors for CVD development. Obesity changes adipose tissue physiology, thereby contributing to the establishment and progression of CVD. The perivascular adipose tissue (PVAT) is a unique depot that surrounds the vasculature. During obesity, PVAT secretes factors that induce vascular inflammation and contraction. Recent work has indicated a role for adipose-derived exosomes in regulating disease pathology. However, very little is known about the importance of PVAT-derived exosomes in modulating vascular health. Therefore, to study the importance of communication within the vascular microenvironment, *Rab27a* was selected for mutagenesis to induce the global loss of functional protein product within the mouse. RAB27A is a known regulator of exosome secretion due to its role in trafficking endosomal compartments to the plasma membrane. We hypothesize that RAB27A regulates paracrine signaling within the vascular microenvironment via exosome secretion.

Molecular, morphological, proteomic, and physiological approaches were used to determine whether the global loss of *Rab27a* altered the vascular microenvironment physiology. The data discussed herein provide evidence that a global loss of *Rab27a* uniquely impacts thoracic aorta contractile and dilative abilities for both male and female mice in an age-dependent manner. These observed changes in vessel contractility were supported through

proteomic analysis and occur in the absence of gross morphological changes in the aorta and multiple adipose depots. The absence of morphological changes in the face of physiological adaptations suggest that global *Rab27a* loss causes a dysregulation of intercellular communication. Evidence of altered cellular communication is presented with proteomic studies suggesting that global loss of *Rab27a* alters exosome protein cargo. Furthermore, global loss of *Rab27a* during a high fat diet (HFD) exacerbates the physiological impact on male thoracic aorta by increasing contractile responses. Again, these observed changes in aorta physiology occur in the absence of altered morphology in both the PVAT and aorta. This work therefore provides a foundational study implicating the importance of *Rab27a* in the maintenance of vascular reactivity in connection to metabolic health.

DEDICATION

This thesis is dedicated to my family who has supported me and my love for learning throughout my life. To my mother, Kathy Soucy, and father, James Soucy, for giving me the opportunities that have shaped me into the resilient and hardworking individual I am today. To my sister, Madeline Soucy, for always being supportive and thoughtful. To my grandmother, Doris Michaud, for the time spent throughout my early education helping me to complete my homework after school. To my fiancé, Jonah Paris, for his endless encouragement, support, and faith in me throughout this program. And finally, to our beagle, Aurora, for her companionship through many, many hours of writing.

This thesis is also dedicated in loving memory to my family who are not here to share this day with me.

Veronique Soucy, Robert Soucy, and Alfred Michaud.

ACKNOWLEDGMENTS

I would like to first acknowledge Dr. Lucy Liaw for her role as my mentor and advocate throughout my years as a GSBSE graduate student. Dr. Liaw consistently worked to create a safe and constructive learning environment for her mentees and lab members. I sincerely thank Dr. Liaw for her efforts to provide me with the best learning opportunities throughout this program and for providing me with this environment to grow in.

Many Liaw lab members, both past and present, have contributed to this work by applying their unique talents and skills. Among others, I am especially grateful for the following individuals: Benjamin Tero for the establishment of the lipid quantification method utilized throughout these studies and for the initial immunoblot and immunofluorescence experiments; Christian Potts for his work in developing our proteomic analyses and for assisting in immunofluorescence studies; and Jacob Seeker for the many hours spent completing lipid accumulation quantifications. I also recognize the contributions of Anne Harrington for her patience and dedication in teaching me mouse handling and wire myography techniques; Abigail Kaija for spending many hours alongside me to complete wire myography experiments; and Larisa Ryzhova for her dedication to improving our methodology.

I thank my Committee Members for their time, guidance, and support throughout my graduate training. I thank Drs. Calvin Vary and Benjamin King for their insights on approaches to proteomic data analysis; Dr. Aaron Brown for his suggestions regarding exosome isolation and analysis; and Dr. Michaela Reagan for her assistance with applying statistical analysis.

I would also like to thank the MaineHealth Institute for Research (MHIR) Mouse Genome Modification Core (Dr. Larisa Ryzhova, Anne Harrington, and Abigail Kaija) for the development of and assistance in characterizing the *Rab27a* mouse strains. I am grateful to the MHIR

Proteomics and Lipidomics Core (Drs. Calvin Vary and Carlos Gartner) for the acquisition of our proteomic data, and to the MHIR Histopathology Core (Dr. Volkhard Lindner and Armie Mangoba) for tissue processing and histology. I am also grateful to the MHIR Microscopy Instrumentation Core (Dr. Igor Prudovsky) for training in confocal microscopy imaging.

Finally, I would like to recognize several individuals within administration who have been supportive of me over the past five years: Jennifer Chiarell (GSBSE), Zhen Zang (GSBSE) Elisabeth Bergst (MHIR), Christine Ellis (MHIR), and Dr. Clarissa Henry (MHIR).

SOURCES OF FUNDING

This work was supported by NIH grants R01HL141149 (Liaw PI), and the 1T32GM132006 (Henry and Liaw PIs, in support of A. Soucy). Core facilities utilized in this project were supported by P20GM121301 (Liaw PI) and U54GM115516 (Rosen PI).

TABLE OF CONTENTS

DEDICATION	i
ACKNOWLEDGEMENTS.....	ii
SOURCES OF FUNDING	iv
LIST OF TABLES	xviii
LIST OF FIGURES	xix
1. CHAPTER 1: INTRODUCTION.....	1
1.1. Defining Cardiovascular Disease.....	1
1.2. The Components of the Cardiovascular System.....	1
1.3. Vascular Physiology During Cardiovascular Disease	2
1.4. The Global Prevalence of Cardiovascular Disease is Increasing	4
1.4.1. Hypertension is a Risk Factor for Cardiovascular Disease.....	5
1.4.1.1. Hypertension Leads to Atherosclerosis Development	5
1.4.1.2. Hypertension Induces Changes in Vascular Morphology	5
1.4.2. Sex is a Risk Factor for Cardiovascular Disease.....	7
1.4.2.1. Proposed Protective Effects of Estrogen Against Cardiovascular Disease.....	7
1.4.3. Age is a Risk Factor for Cardiovascular Disease	8
1.5. Metabolic Disease is a Factor for Cardiovascular Disease.....	8
1.5.1. Obesity is a Global Concern for All Ages of Life.....	9
1.6. Defining the Types of Adipose Depot Expansion.....	10
1.6.1. Hypertrophy: The Initial Form of Adipose Tissue Expansion.....	11
1.6.2. Hyperplasia: An Induced Form of Adipose Tissue Expansion.....	12

1.6.3. Differences in Hypertrophic and Hyperplastic Responses Between Adipose Depots	12
1.6.4. A Need for Effective Therapies for Patients with Obesity	13
1.7. Considering the Physiological Differences Between Adipose Depots and Their Role in Human Health	13
1.7.1. The Heterogeneous Composition of Adipose Tissue.....	14
1.7.2. Classical Brown Adipocytes: A Thermogenic Physiology	16
1.7.2.1. Classical Brown Adipocytes Exhibit a Distinct Phenotype	16
1.7.2.2. Approaches for the Activation of Brown Adipocytes	16
1.7.2.3. Potential Therapeutic Implications for BAT Activation	17
1.7.3. Classical White Adipocytes: A Lipid Storage Physiology	17
1.7.3.1. Classical White Adipocytes Exhibit a Distinct Phenotype	18
1.7.3.2. Potential Therapeutic Implications for WAT Activation	18
1.7.4. Beige Adipocytes: A Metabolically Dynamic Physiology.....	18
1.7.4.1. Beige Adipocytes: A Thermogenic Phenotype from Non-Thermogenic Lineages	19
1.7.4.2. Potential Therapeutic Implications for Beige Adipocytes	19
1.8. Perivascular Adipose Tissue: A Distinct Depot at the Interface Between Metabolic and Vascular Health	20
1.8.1. PVAT Adipocytes: A Unique Lineage.....	20
1.8.2. PVAT Secreted Factors That Induce Vascular Constriction	21
1.8.3. PVAT Secreted Factors That Induce Vascular Dilation	21
1.9. Extracellular Vesicles as Signaling Factors	22
1.9.1. Exosomes as Regulators of Vascular Health.....	23
1.9.2. The Effects of Obesity on Exosome Secretion.....	23
1.9.3. The Effects of Obesity on Exosome Cargo	23

1.9.4. A Potential Role for PVAT-Derived Exosomes in Regulating Aorta Vasoreactivity	24
1.10. Exosome Biogenesis and Release: A Rab Family Mediated Process	24
1.10.1. Endosome Formation is Mediated by Rab5.....	25
1.10.2. ESCRT-Dependent Multivesicular Body Development and Cargo Sorting	26
1.10.3. Multivesicular Body Trafficking is Mediated by Multiple Rab Proteins.....	26
1.10.4. Exosome Secretion via Multivesicular Body Fusion with the Plasma Membrane Is Mediated by SNARE Proteins	27
1.11. Selection of <i>Rab27a</i> to Study Exosome Dysregulation in the Vascular Microenvironment	28
1.11.1. <i>RAB27A</i> and <i>Rab27a</i> have Conserved Transcript Sequences.....	29
1.11.2. Human and Mouse <i>RAB27A</i> have Highly Conserved Amino Acid Sequences	30
1.11.3. Comparing the Tissue Expression Profiles of <i>RAB27A</i> and <i>Rab27a</i>	30
1.12. Characterization of Previously Established <i>Rab27a</i> Null Mouse Strains	31
1.13. Project Goal: Determine Whether Loss of <i>Rab27a</i> Alters Vascular Physiology via the Dysregulation of Exosome Secretion	32
2. CHAPTER 2: METHODS	33

2.1. <i>In Vivo</i> Methods	33
2.1.1. Commercially Available Strains.....	33
2.1.2. Single-Guide RNA Design for CRISPR-Cas9	
Targeting of <i>Rab27a</i> Introns 3 and 4	33
2.1.3. Validation of Single-Guide RNA for CRISPR-Cas9	
Targeting of <i>Rab27a</i> Introns 3 and 4	34
2.1.4. Establishment of the Novel <i>Rab27a</i> Global	
and Conditional Null Strains.....	36
2.1.5. <i>Rab27a</i> Global Null Genotyping.....	37
2.1.6. Confirmation of loxP Site Insertion.....	37
2.1.7. <i>Rab27a</i> Conditional Null Genotyping	38
2.1.8. Maintenance of <i>Rab27a</i> Global and Conditional	
Null Strains.....	39
2.1.9. 60% High Fat Diet Feeding	39
2.1.10. Body Weight Recording	42
2.1.11. Body Composition Analysis of Mice From	
the 60% High Fat Diet Study	42
2.1.12. Tissue Collection	42
2.2. Primary Human Cell Culture	42
2.3. Wire Myography	43
2.3.1. Chow Diet Experiments.....	43
2.3.2. 60% High Fat Diet Experiments	44
2.3.3. Statistical Analysis	44
2.4. Immunoblot	45
2.4.1. Protein Isolation and SDS-PAGE.....	44
2.4.2. Quantification	46

2.5. Immunofluorescence	47
2.5.1. Staining	47
2.5.2. Quantification	48
2.6. Mass Spectrometry	49
2.6.1. Data Acquisition: Tissues	49
2.6.2. Exosome Sample Preparation	50
2.6.3. Data Acquisition: Exosomes	51
2.6.4. Data Analysis	53
2.7. STRING Analysis of Tissue Samples.....	53
2.8. Histological Staining.....	54
2.8.1. Hematoxylin and Eosin	54
2.8.2. Mason's Trichrome.....	55
2.8.3. Verhoeff.....	56
2.9. Gross Morphological Analyses.....	56
2.9.1. Lipid Area Quantification	56
2.9.2. Thoracic Aorta Area Quantification	57
2.10. Exosome Isolation	57
2.10.1. Lipid Precipitation	57
2.10.2. Ultrafiltration and Size Exclusion Chromatography	58
2.11. Exosome Analysis	59
2.11.1. qNano Gold, iZon.....	59
2.11.2. Dual Laser ZetaView, Particle Metrix.....	60
3. CHAPTER 3: GLOBAL LOSS OF RAB27A SIGNIFICANTLY ALTERS THORACIC AORTA REACTIVITY	63
3.1. Overview	63

3.2. Evaluating <i>RAB27A</i> Association with Human Metabolic and Vascular Phenotypes.....	63
3.2.1. Rare <i>RAB27A</i> Variants Associate with Metabolic Phenotypes.....	64
3.2.2. Body Mass Index is Significantly Associated with Two <i>RAB27A</i> Variants	65
3.3. <i>RAB27A</i> is Expressed Within the Human and Mouse Vascular Microenvironment.....	66
3.3.1. <i>RAB27A</i> is Expressed Within Human PVAT, VSMC, and Vascular Endothelial Cells	66
3.3.2. <i>RAB27A</i> Is Expressed Within Mouse PVAT, VSMC, and Vascular Endothelial Cells	67
3.4. Establishment of Novel <i>Rab27a</i> Global and Conditional Null Strains.....	68
3.4.1. Establishment of the <i>Rab27a</i> Global Null Strain	69
3.4.2. Deletion of Exon 4 Results in Loss of <i>RAB27A</i> Expression.....	70
3.4.3. Establishment of the <i>Rab27a</i> Conditional Null Strain	72
3.5. Characterization of the <i>Rab27a</i> Null Body Mass and Vascular Microenvironment Morphology.....	73
3.5.1. Global <i>Rab27a</i> Expression is Not Associated with Changes in Body Weight	73
3.5.2. Global <i>Rab27a</i> Expression is Not Associated with Changes in Lipid Accumulation Within Male Mice	73
3.5.3. Global <i>Rab27a</i> Expression is Not Associated with Changes in Lipid Accumulation Within Female Mice	75

3.5.4. <i>Global Rab27a</i> Expression Does Not Affect the Thoracic Aorta Area of Male Mice	76
3.5.5. <i>Global Rab27a</i> Expression is Not Associated with Changes in the Thoracic Aorta Area of Female Mice	77
3.6. Global Loss of <i>Rab27a</i> Alters the Proteomic Signature of the Vascular Microenvironment and Other Adipose Tissues	78
3.6.1. <i>Rab27a</i> Null PVAT and Aortae Show Unique Patterns of Altered Protein Expression	78
3.6.2. Male <i>Rab27a</i> Null PVAT and Thoracic Aortae are Enriched for Metabolic and Cardiovascular System Phenotypes	79
3.6.3. Cardiac and Aortic Phenotypes Populate the Parent Cardiovascular System Enrichment Category	81
3.6.4. Consideration of the Enriched Metabolic and Adipose Phenotypes in <i>Rab27a</i> Null PVAT and Aorta.....	84
3.6.5. Proteins Contributing to the Enrichment of Cardiovascular Phenotypes Exhibit Three Expression Patterns with Aging	85
3.6.5.1. <i>Rab27a</i> Null PVAT and Aortae Show Normal Elastin and Collagen Morphology	87
3.6.5.2. Decreased Expression of ACTA2 and MYH6 are Confirmed via Immunofluorescence Microscopy	88
3.6.6. <i>Rab27a</i> Null iWAT and BAT Have Protein Profiles Different from PVAT and Aorta Signatures	90

3.6.7. The Cardiovascular System and Metabolism are Not the Top Enriched Phenotypes for <i>Rab27a</i> Null BAT and iWAT	91
3.6.8. <i>Rab27a</i> Null BAT and iWAT Show Reduced Association with Aortic and Cardiac Phenotypes.....	92
3.6.9. <i>Rab27a</i> Null BAT and iWAT Have a Reduced Number of Significantly Altered Proteins Associated with Cardiovascular System Phenotypes	93
3.7. Wire Myograph Studies Revealed Genotype, Age, and Sex Dependent Physiological Responses to the Global Loss of <i>Rab27a</i>	95
3.7.1. <i>Rab27a</i> Null Male Mice Exhibit Increased Vascular Contractility at 8 Weeks of Age	97
3.7.2. Global loss of <i>Rab27a</i> Uniquely Affects Experimental Group Associations with Vessel Sensitivity in Male Mice.....	98
3.7.3. <i>Rab27a</i> Null Female Aortae Exhibit Increased Vascular Contractility and Dilation at 20 Weeks of Age	99
3.7.4. Global loss of <i>Rab27a</i> Uniquely Affects Experimental Group Associations with Vessel Sensitivity in Female Mice	100
3.8. RAB27A is Differentially Expressed in Male and Female PVAT and iWAT	101
3.9. The Characterization of Plasma-Derived Exosomes from <i>Rab27a</i> Null Mice.....	103
3.9.1. The Global Loss of <i>Rab27a</i> Did Not Affect Circulating Exosome Size or Number	103

3.9.2. The Global Loss of <i>Rab27a</i> Affected Exosome	
Protein Cargo Profiles	104
3.10. Chapter Discussion	105
3.10.1. Conclusions	106
3.10.2. Study Limitations	107
3.10.2.1. Sole Use of the Novel Global <i>Rab27a</i> Null Strain	108
3.10.2.2. Accounting for Sex as a Biological Variable	108
3.10.3. Future Directions	109
3.10.3.1. Addressing the Importance of Cell-Specific loss of <i>Rab27a</i>	109
3.10.3.2. Identifying the Mechanism for How	
<i>Rab27a</i> Alters Vascular Physiology.....	109
3.10.3.3. Elucidating the Mechanism Underlying	
the Sex Dependent Trends in Vascular Physiology.....	110
4. CHAPTER 4: GLOBAL LOSS OF RAB27A INCREASES	
THORACIC AORTA CONTRACTION IN MICE FED A HIGH FAT DIET	111
4.1. Overview	111
4.2. Characterizing the Effects of Global <i>Rab27a</i> Loss	
on Body Composition During a 60% High Fat Diet	112
4.2.1. Global <i>Rab27a</i> Loss Does Not Affect the	
Weight Gain of Male Mice Fed a 60% High Fat Diet.....	112
4.2.2. The Global Loss of <i>Rab27a</i> Expression Does	
Not Alter Fat Body Mass in Male Mice Fed a 60% High Fat Diet.....	113
4.3. Characterizing the Effects of Global <i>Rab27a</i> Loss	
on Adipose Tissue and Thoracic Aorta Morphology	
After a 60% High Fat Diet	114

4.3.1. Global <i>Rab27a</i> Loss Does Not Affect PVAT	
Lipid Accumulation in Male Mice Fed a 60% High Fat Diet	115
4.3.2. The Global <i>Rab27a</i> Loss Does Not Alter	
Thoracic Aorta Gross Morphology of Male	
Mice Fed a 60% High Fat Diet	116
4.4. The Global Loss of <i>Rab27a</i> Affected Male Thoracic	
Aorta Vasoreactivity After a 60% High Fat Diet	117
4.4.1. The Global Loss of <i>Rab27a</i> Increased Thoracic	
Aortic Vasocontractility in Male Mice Fed a 60% High Fat Diet	117
4.4.2. The Global Loss of <i>Rab27a</i> Does Not Alter	
Vessel Sensitivity in Mice Fed a 60% High Fat Diet	119
4.5. Chapter Discussion	120
4.5.1. Conclusions.....	120
4.5.2. Limitations	122
4.5.2.1. C57BL/6J Background Variability with Weight Gain	123
4.5.2.2. Sole Use of the Global <i>Rab27a</i> Null Strain	123
4.5.2.3. The Impact of Insulin Sensitivity on Vascular Reactivity	123
4.5.3. Future Directions.....	124
4.5.3.1. Increasing Statistical Power by Expanding Sample Size	125
4.5.3.2. Extending the Diet Study Duration to Determine the	
Long-Term Effects of <i>Rab27a</i> Loss on Male Mice	
Fed a 60% High Fat Diet.....	125
4.5.3.3. Evaluating the Importance of Sex as a	
Biological Variable.....	126

4.5.3.4. Utilize Proteomic Analysis to Identify Possible Mechanisms Driving Altered Aortic Physiology in <i>Rab27a</i> Null Mice Fed a 60% High Fat Diet.....	126
4.5.3.5. Characterizing the Effects of Global <i>Rab27a</i> Loss After a 60% High Fat Diet on Circulating Exosome Populations	127
5. CHAPTER 5: GLOBAL DISCUSSION.....	128
5.1. Overview	128
5.1.1. Global Loss of <i>Rab27a</i> Alters Thoracic Aorta Reactivity Uniquely in Male and Female Mice	128
5.1.2. Global Loss of <i>Rab27a</i> Increased the Thoracic Aorta Contractile Response of Male Mice After a 60% High Fat Diet.....	130
5.2. Important Considerations for Future Studies	131
5.2.1. Accounting for the Differences in the Effects of <i>Rab27a</i> Loss Between Human Primary Cell and Murine <i>In Vivo</i> Studies	131
5.2.1.1. Differences Between Human and Mouse Adipose Depots	132
5.2.1.2. Differences Between Human and Mouse PVAT	132
5.2.1.3. Differences of Cellular Responses Between <i>In Vivo</i> and <i>In Vitro</i> Methods	133
5.2.2. An Absence of <i>Rab27a</i> -Induced Changes in Exosome Size and Concentration.....	134
5.2.2.1. Different Extracellular Vesicle Isolation Approaches.....	134
5.2.2.2. Different Approaches to Normalization of Extracellular Vesicle Concentrations.....	135
5.3. Potential Compensatory Mechanisms for Global <i>Rab27a</i> Loss.....	135

5.3.1. RAB27B Regulates Endosome Speed and Docking to Plasma Membrane	136
5.3.2. RAB35 Regulates Protein Recycling to the Plasma Membrane via Endosome Trafficking.....	137
5.3.3. RAB11A Regulates Exosome Secretion via Endosomal Recycling.....	137
5.4. A Need for Conditional <i>Rab27a</i> Loss Within the Vascular Microenvironment.....	138
5.4.1. Targeting <i>Rab27a</i> Loss Within PVAT APCs	138
5.4.1.1. Establishing the <i>Rab27a^{fl/fl};tdTomato;Myf5^{Cre}</i> Mouse Strain	139
5.4.1.2. Use of the <i>Rab27a^{fl/fl};tdTomato;Myf5^{Cre}</i> May Limit the Activation of Compensatory Mechanisms	140
5.4.2. Targeting <i>Rab27a</i> Loss in Vascular Smooth Muscle Cells	141
5.4.2.1. Establishment of the <i>Rab27a^{fl/fl};tdTomato;SMMHC^{CreERT2}</i> Strain	141
5.4.2.2. Study Limitations Due to the <i>SMMHC^{CreERT2}</i> Strain.....	142
5.4.2.3. Potential for Compensatory Mechanism within the <i>Rab27a^{fl/fl};tdTomato;SMMHC^{CreERT2}</i>	143
5.4.3. Targeting <i>Rab27a</i> Loss in the Vascular Endothelial Cells Using a <i>Rab27a^{fl/fl};-Cdh5^{Cre}</i> Mouse Strain	143
5.4.3.1. Potential Limitation of the <i>Rab27a^{fl/fl};-Cdh5^{Cre}</i> Strain.....	143
5.5. A Growing Need for Comparative Studies Examining Sex as a Biological Variable.....	144
5.6. Establishing the Human Connection: Translational Focus for Future Studies.....	144
REFERENCES	146

BIOGRAPHY OF THE AUTHOR..... 168

LIST OF TABLES

Table 2.1 Mouse strains from commercial sources	33
Table 2.2 sgRNA sequences and predicted efficiencies for targeting of <i>Rab27a</i> introns 3 and 4	34
Table 2.3 Novel genetically modified mouse strains	36
Table 2.4 Primer sequences for novel <i>Rab27a</i> global and conditional null strains	39
Table 2.5 Nutritional values for the 60% high fat diet, sucrose control diet and breeder diet	41
Table 2.6 Antibody descriptions	48
Table 2.7 Proteomic data availability	53

LIST OF FIGURES

Figure 1.1 Depiction of the veins, arteries, and aorta of the cardiovascular system	2
Figure 1.2 Depiction of aorta vessel structure	4
Figure 1.3 Components of the atherosclerotic plaque.....	6
Figure 1.4 Obesity results in the expansion of adipose depots throughout the body	9
Figure 1.5 Comparison of hypertrophic and hyperplastic expansion within adipose tissue	11
Figure 1.6 Anatomical locations of beige, brown, and white adipose and adipocytes within the human	14
Figure 1.7 Comparison of differentiation processes for white, beige, and brown adipocytes	15
Figure 1.8 Rab proteins as mediators of exosome biogenesis	25
Figure 1.9 SNARE proteins drive membrane fusion by overcoming repulsive forces exerted by opposing membranes.....	28
Figure 1.10 <i>RAB27A</i> and <i>Rab27a</i> have conserved transcript sequences	29
Figure 1.11 Amino acid sequence alignment and similarity for human and mouse <i>RAB27A</i>	30
Figure 2.1 <i>In vitro</i> confirmation of sgRNA targeting efficacy	35
Figure 2.2 Resulting <i>Rab27a</i> alleles from CRISPR-Cas9 mutagenesis	36
Figure 2.3 Genotyping strategy for the novel <i>Rab27a</i> global and conditional null strains.....	38

Figure 2.4 Study design for evaluating the effects of global <i>Rab27a</i> loss during a 60% high fat diet	40
Figure 2.5 Ultrafiltration and size exclusion chromatography-based exosome isolation workflow	59
Figure 3.1 Establishing associations between <i>RAB27A</i> and metabolic phenotypes	65
Figure 3.2 Establishing associations between <i>RAB27A</i> SNPS and metabolic phenotypes	66
Figure 3.3 <i>RAB27A</i> is expressed in the human and mouse microvascular environment	68
Figure 3.4 Confirmation of <i>Rab27a</i> null genotype	70
Figure 3.5 Confirmation of <i>RAB27A</i> loss in <i>Rab27a</i> null tissues.....	71
Figure 3.6 <i>Rab27a^{fl/fl}:Sox-2 Cre</i> mice exhibit ashen phenotype	72
Figure 3.7 Global loss of <i>Rab27a</i> does not affect mouse body weight	74
Figure 3.8 Comparison of lipid accumulation between male <i>Rab27a</i> null and WT adipose depots.....	75
Figure 3.9 Comparison of lipid accumulation between female <i>Rab27a</i> null and WT adipose depots.....	76
Figure 3.10 Global loss of <i>Rab27a</i> does not affect male thoracic aorta morphology.....	77
Figure 3.11 Global loss of <i>Rab27a</i> does not affect female thoracic aorta morphology.....	78
Figure 3.12 PVAT and aortae from <i>Rab27a</i> null mice have altered proteomic profiles compared to WT controls.....	79

Figure 3.13 PVAT and aortae from <i>Rab27a</i> null mice	
have altered protein signatures associated with cardiac,	
metabolic, and adipose phenotypes.....	81
Figure 3.14 PVAT and aortic proteins that are significantly	
altered by global <i>Rab27a</i> loss are enriched for	
cardiac- and aorta-associated phenotypes	83
Figure 3.15 Comparisons of changes in fold change	
directionality of proteins associated with the cardiovascular	
system phenotype in PVAT and aortic tissue.....	86
Figure 3.16 Verhoef and trichrome staining remain comparable	
between <i>Rab27a</i> null and WT male tissues	88
Figure 3.17 <i>Rab27a</i> null males exhibit a reduced	
expression for select contractile proteins ACTA2 and MYH6.....	89
Figure 3.18 <i>Rab27a</i> null BAT and iWAT exhibit proteomic	
profiles that are unique from PVAT and aortic tissues	90
Figure 3.19 BAT and iWAT from <i>Rab27a</i> null mice	
have a different phenotype enrichment from the	
PVAT and aortae.....	91
Figure 3.20 Proteins significantly impacted by global	
<i>Rab27a</i> loss are enriched for cardiac associated phenotypes.....	93
Figure 3.21 Comparisons of changes in fold change directionality	
of proteins associated with the cardiovascular system	
phenotype in BAT and iWAT	95
Figure 3.22 Wire myography is used to examine changes in	
contractile and dilative responses of the thoracic aorta	96

Figure 3.23 <i>Rab27a</i> null male mice exhibit genotype and age dependent vascular reactivity phenotypes	98
Figure 3.24 Male thoracic aorta sensitivity and viability remains consistent with aging and global loss of <i>Rab27a</i> between experimental groups	99
Figure 3.25 <i>Rab27a</i> null female mice exhibit genotype and age dependent vascular physiological responses	100
Figure 3.26 Female thoracic aorta sensitivity and viability were unchanged between experimental groups.....	101
Figure 3.27 Female mice exhibited significantly higher RAB27A expression in PVAT and iWAT	102
Figure 3.28 Exosomes isolated from male <i>Rab27a</i> null plasma have genotype and age specific changes in proteomic cargo	104
Figure 3.29 Exosomes isolated from male <i>Rab27a</i> null plasma have genotype and age specific changes in proteomic cargo	105
Figure 3.30 A summary of Chapter 3 conclusions.....	107
Figure 4.1 <i>Rab27a</i> null males gain weight like WT controls when fed a 60% HFD.....	114
Figure 4.2 Male <i>Rab27a</i> null adipose tissues exhibit depot-specific differences in lipid accumulation after a HFD	116
Figure 4.3 <i>Rab27a</i> null mice on HFD show no change in aorta morphology	117

Figure 4.4 Aortae of <i>Rab27a</i> null male mice exhibit increased contractility compared to aortae of WT controls when fed a HFD	118
Figure 4.5 Aortae of <i>Rab27a</i> null male mice viability remained unaltered compared to the aortae of WT mice after a HFD.....	119
Figure 4.6 Summary of Chapter 4 conclusions	122
Figure 5.1 Rab proteins are structurally similar	136
Figure 5.2 Establishment of the <i>Rab27a^{fl/fl};tdTomato;Myf5^{Cre}</i> strain.....	140
Figure 5.3 Establishment of the <i>Rab27a^{fl/fl};tdTomato;SMMHC Cre-ERT2</i>	142

CHAPTER 1: INTRODUCTION

1.1. Defining Cardiovascular Disease

According to the World Health Organization, cardiovascular disease (CVD) is defined as the dysregulation of cardiac and vascular function⁴⁶. CVD is one of the leading causes of noncommunicable mortality globally and is increasing in prevalence⁴⁷. According to the data collected by the National Health and Nutrition Examination Survey from 2015-2018, almost 50% of the surveyed adults (20 years of age or older) experienced chronic heart disease, heart failure, stroke, and hypertension⁴⁸. Interestingly, the prevalence of CVD, when excluding hypertension, is 9.3% within the sample population⁴⁸. Suggesting that hypertension is a major contributor to the overall prevalence of CVD in adults. Additionally, high blood pressure and arterial diseases accounted for 11.7% and 2.8% of all CVD deaths in the United States in 2019, respectively⁴⁸. Many CVDs are the result of environmental, socioeconomic, and lifestyle factors^{49,50}. While different anatomical regions are affected depending on the type of CVD, all forms are the result of insufficient or loss of blood flow throughout the biological system⁴⁶. Since biological organisms require consistent nutrient and oxygen flow, it is crucial to understand the mechanisms that cause CVD pathology.

1.2. The Components of the Cardiovascular System

The human cardiovascular system has evolved to distribute nutrients and oxygen in addition to removing biological waste². Such a feat is possible through the constant and highly regulated flow of blood via the muscular contractions of the heart. A four chambered organ, the heart contracts and relaxes to create a pressure differential to direct blood flow in a single direction (**Figure 1.1**)². Deoxygenated blood enters the right side of the heart and flows into the lungs via the pulmonary arteries². Oxygenated blood then returns to the heart via the pulmonary veins and is then distributed to the rest of the body by exiting through the aorta (**Figure 1.1**)². The blood flows through the aorta and is distributed through veins and capillaries, where

nutrients and oxygen diffuse into surrounding tissues^{2,51}. While there is currently a ~12% prevalence of aortic calcification within elderly populations, this prevalence is predicted to dramatically increase over the next few decades⁴⁸. Furthermore, there is a reported global prevalence of 5.56% for peripheral artery disease between 2011 and 2019⁴⁸. These statistics therefore provide valuable insight of vascular disease contributions to the occurrence of CVD.

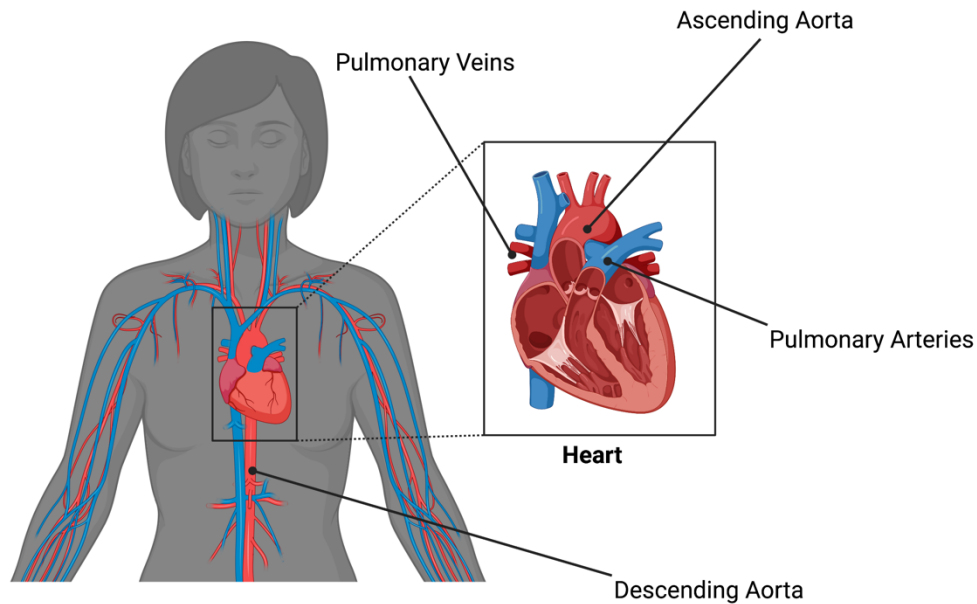


Figure 1.1. Depiction of the veins, arteries, and aorta of the cardiovascular system. Blood flow is directed through the heart in a single direction from the right to left side²⁻⁴. Blood flows through the pulmonary arteries and becomes oxygenated. Blood then flows through the left side of the heart and exits through the ascending aorta^{2,3}. The ascending aorta arches out from the heart, with the highest section of the curve termed the aortic arch, and the region below the arch to the diaphragm termed the thoracic aorta^{2,20}. *Created with BioRender.com.*

1.3. Vascular Physiology During Cardiovascular Disease

While the heart is the mechanical force creating the pressure necessary to oxygenate blood, the aorta and vasculature are responsible for blood distribution throughout system⁵¹.

Under healthy conditions, the aorta and other arterioles are responsible for the maintenance of blood circulation by modifying blood pressure and flow rate post ejection from the heart². The

aorta and arterioles are composed largely of the tunica intima, media, and externa (adventitia) (Figure 1.2)². During CVD, the physiology of these layers is altered, and the distinct phenotype of increased blood pressure arises⁵¹. Increased blood pressure, specifically within the aorta, is the result of vascular stiffening, inflammation, and atherosclerotic plaque formation⁵².

For example, it has been shown that the vascular smooth muscle cells (VSMC) that comprise the tunica media, identified via the expression of myosin heavy chain 11 (*MYH11*), reduce plaque stability when Kruppel-like factor 4 (*Klf4*) is also expressed⁵³. The expression of *Klf4* is predicted to identify a population of dedifferentiation VSMCs, which promotes vascular disease pathophysiology^{44,53}. Additionally, VSMCs contribute to the formation of the extracellular matrix (ECM) through the secretion of collagens and elastin. During plaque formation, it has been shown that VSMC increase ECM production and reduce the expression of contractile markers such as smooth muscle actin (*ACTA2*)⁴⁴. It has been well established that changes in ECM due to altered production and presence of specific collagens (*CO1A2* and *CO3A1*) are associated with aortic aneurysms. Further augmenting the importance of VSMC and ECM physiology in vascular health⁵⁴.

Multiple signaling pathways are involved with inducing changes in cellular phenotypes and therefore promote CVD pathophysiology^{55,56}. The activation and dysregulation of these signaling pathways can be induced by multiple types of risk factors^{57,58}. Due to the abundance of risk factors and the rise in global CVD prevalence, there is a need for the development of novel therapeutic targets to treat patients^{47,58}.

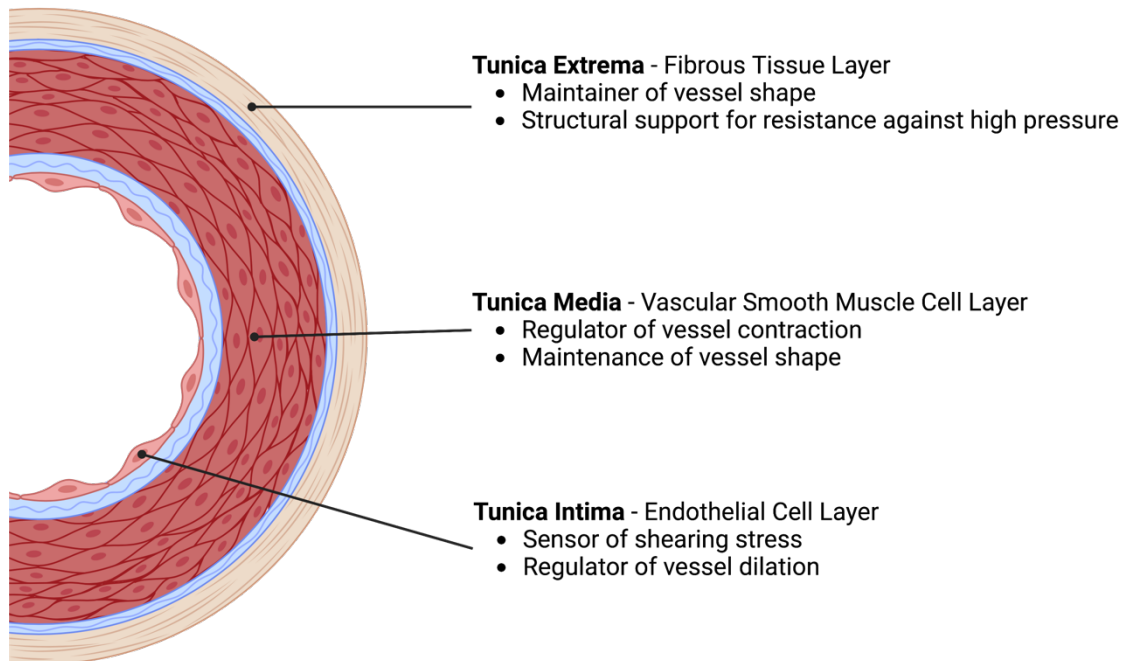


Figure 1.2. Depiction of aorta vessel structure. The physical structure of vessels confers their physiological role within the system. For example, the aorta is composed of three major regions with unique cell populations. Tunica extrema: Mainly composed of fibrous tissue with an extracellular matrix high in collagen, which helps to provide structural support to the other layers during periods of high blood pressure^{4,23}. Tunica media: Consists of vascular smooth muscle cells and is the active component in exerting vascular constriction²³. Tunica intima: Mainly comprised of vascular endothelial cells and largely regulates dilative responses due to changes in blood pressure^{23,39}. *Created with BioRender.com.*

1.4. The Global Prevalence of Cardiovascular Disease is Increasing

Historically, CVD was most prevalent within the populations of developed nations because of increased nutrient availability⁴⁷. Recently, there has been a shift of CVD prevalence globally with the wider distribution of nutrient rich foods and increased sedentary lifestyles⁴⁷. Additional factors that have been identified that increase the probability of CVD onset include an individual's local environment (urban compared to rural), alcohol consumption, and income^{47,57}. Importantly, these factors also impact the probability of an individual developing obesity and other metabolic diseases⁴⁷. However, it is also important to note that while the occurrence of CVD mortalities within the United States has decreased in recent years, CVD remains a leading

cause of mortality⁴⁸. According to data from 2019 (unpublished, NHLBI), the mortality rate for CVD-associated events was 214.6 per 100,000 individuals⁴⁸. While lifestyle is a major factor in the likelihood for CVD, non-environmental factors also affect an individual's predisposition for CVD⁴⁸. Non-environmental factors include hypertension, sex, age, and obesity.

1.4.1. Hypertension is a Risk Factor for Cardiovascular Disease

Hypertension is a sustained increase in blood pressure in the absence of an external stimulant⁵⁹. Risk factors for the development of hypertension include age, diet, and sedentary lifestyle⁶⁰⁻⁶². The incidence of hypertension is increasing within more developed nations in correlation to increased rates of metabolic disease⁵⁸.

Hypertension is sustained by increased vasoconstriction and reduced vasodilation in major vessels, such as the aorta⁵⁹. With increased constriction, higher blood pressure also leads to increased shearing force on the endothelial cells of the tunica intima⁵¹. Prolonged exposure to increased shearing force compromises the integrity of the vessel wall, leading to atherosclerotic plaque establishment⁶³.

1.4.1.1. Hypertension Leads to Atherosclerosis Development

Atherosclerotic plaques are established due to the increased recruitment of immune cells that stimulate changes in endothelial and vascular smooth muscle cell (VSMC) physiology³⁴. Immune cell recruitment occurs because of the increased expression of adhesion factors by endothelial cells due to chronic exposure to increased shearing force³⁴. The increased presence of immune cells also induces maturation of foam cells, resulting in plaque formation and expansion⁶⁴. Furthermore, T cells have also been reported within the atherosclerotic plaques⁴³. While classical VSMCs contribute to the formation of a fibrous cap that stabilizes the plaque, phenotype switching of VSMCs are also believed to promote the expansion of atherosclerotic plaques⁴⁴. For example, studies have shown that VSMCs can

undergo dedifferentiation to become macrophage-like, foam cells, or fibromyocytes³⁹. Each of these cell types promote the expansion of the atherosclerotic plaque through dissention into the luminal space and stabilization of the fibrous cap³⁹. Expansion of atherosclerotic plaques causes vessel narrowing, which further increases the shearing force, and thereby increases the potential for cardiovascular-associated events (**Figure 1.3**)⁵¹.

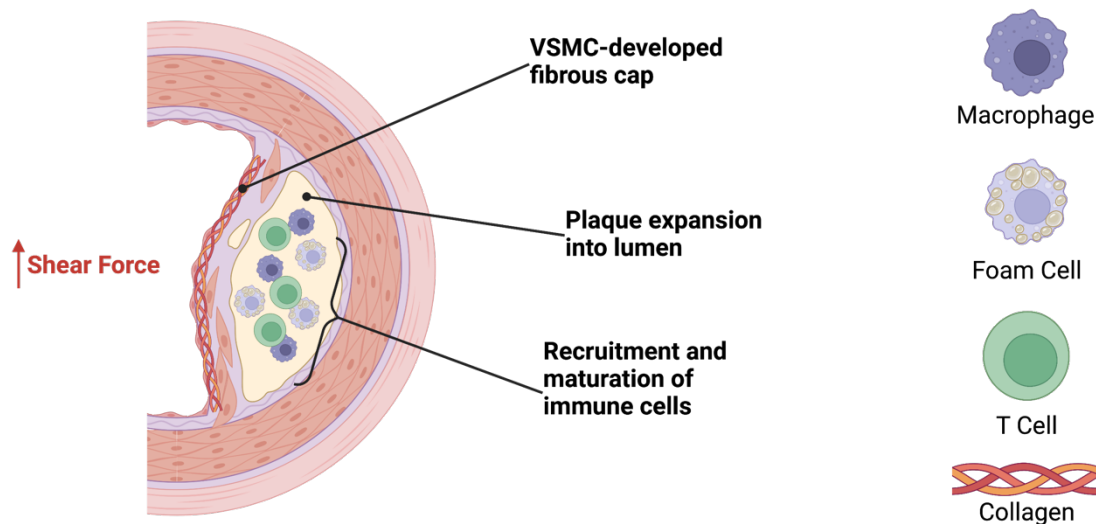


Figure 1.3. Components of the atherosclerotic plaque. Establishment and expansion of atherosclerotic plaques involves the recruitment of macrophage and monocytes to the endothelium layer on the luminal side of the vessel³⁴. Upon invasion of the vessel wall, monocytes mature into foam cells, resulting in dissention of the vessel wall into the luminal space^{19,39}. T cell recruitment and activity further add to the observed inflammatory phenotype⁴³. To stabilize the vessel wall expansion, VSMCs contribute to the production of extracellular matrix components including collagens⁴⁴. *Created with BioRender.com.*

1.4.1.2. Hypertension Induces Changes in Vascular Morphology

In addition to plaque development, hypertension has also been shown to modify vessel thickness⁶⁵. Quantification of changes in aortic VSMC mass showed that in male rat models with spontaneous hypertension, the tunica media mass was significantly increased compared to controls⁶⁶. Additionally, changes in the extracellular matrix of the vasculature have also been

observed in response to hypertension. Specifically, histological staining shows morphological changes in elastin and increased production of collagen⁶⁷. Interestingly, the thickening of the aortic wall due to hypertension appears to be unique to this vessel⁶⁸.

1.4.2. Sex is a Risk Factor for Cardiovascular Disease

Cardiovascular disease remains a primary cause of mortality for both males and females⁶². However, there are sex specific differences in the prevalence and form of CVDs^{62,69}. For example, one report provided data showing that while male patients exhibited higher rates of coronary artery disease, females tended to have a higher prevalence for ischemic heart disease⁷⁰. Another study comparing the prevalence of heart failure between males and post-menopausal females showed that the female cohort had a higher incidence of hypertension⁶⁹⁻⁷¹. Post-menopausal females also associated with larger statistical impacts for classic CVD risk factors than males⁷⁰. Meanwhile, pre-menopausal females exhibited statistically reduced risk of CVD compared to males of the same age⁶². Current studies have focused on defining sex-specific risk factors that may also help to identify females who are at a higher risk for CVD development. These potential factors include pregnancy-associated hypertension, autoimmune disease, and cancer therapies⁷⁰.

1.4.2.1. Proposed Protective Effects of Estrogen Against Cardiovascular Disease

Due to the difference in risk factor impact between pre- and post-menopausal females, sex specific hormones are thought to be important regulators of vascular health^{70,72}. In premenopausal females, the gonadal tissues are the major producers of circulating estrogen (estradiol, E2)⁷². Multiple studies have shown that estrogen signaling increases vascular endothelial growth factor (VEGF) and endothelial nitric oxide synthase (eNOS) production⁷². Importantly, both VEGF and eNOS are associated with the promotion of vascular health^{73,74}. It is predicted that the dramatic loss of circulating estrogen post-menopause, results in the loss of

these beneficial cardiovascular factors, leading to the dramatic shift in risk within female populations.

However, it is critical to note that other cell types including adipose, endothelial cells, and VSMC also produce low levels of estrogen even in males and postmenopausal females⁷⁵. While these cell types may be able to produce estrogen for local cellular communication and maintenance of physiological function, estrogen levels are not high enough to maintain systemic effects^{62,75}. Clinical studies have attempted to supplement post-menopausal females with estrogen; however, results suggested a worse prognosis for long-term cardiovascular health⁶². Therefore, while hormone replacement therapies are appealing, much more work is needed to better understand the importance of sex hormones in vascular physiology.

1.4.3. Age Is a Risk Factor for Cardiovascular Disease

For the proper management of blood pressure, the vasculature must be able to adapt via modification of contractile and dilative responses^{23,51}. Many studies have shown that increased vascular stiffness and constriction occur with aging, thereby reducing vascular responsiveness⁷⁶. Increased vascular stiffness, which occurs prior to hypertension, is largely the result of vessel wall thickening and expansion of the ECM⁷⁶. Aging is also associated with changes in sex hormone production and establishment of diabetes and obesity, which are also risk factors for CVD^{62,77}. Because many of these risk factors are impacted by each other, it is critical to consider the age, sex, and metabolic health within scientific studies.

1.5. Metabolic Disease is a Risk Factor for Cardiovascular Disease

Metabolic diseases, such as obesity, have long been a leading risk factor for CVD establishment^{48,78}. While obesity is defined as the expansion of adipose depots in response to imbalanced nutrient consumption, not all adipose depots expand equally (**Figure 1.4**)⁷⁹. Often disease pathology is dependent on which depot experiences preferential expansion¹³. As a

result, the level of risk for CVD development is also thought to be adipose depot specific. For example, the expansion of adipose tissue surrounding the abdominal organs (visceral) and heart (epicardial) is associated with increased risk of cardiovascular disease¹³. Meanwhile, the adipose depot surrounding the vasculature (perivascular) has been shown to have either beneficial or deleterious effects on vascular health depending on its metabolic state^{7,8}. Interestingly, expansion of adipose depots located under the dermis (subcutaneous) is thought to be advantageous to maintaining metabolic health in the face of obesity¹³.

Example of Depots Expanded by Obesity

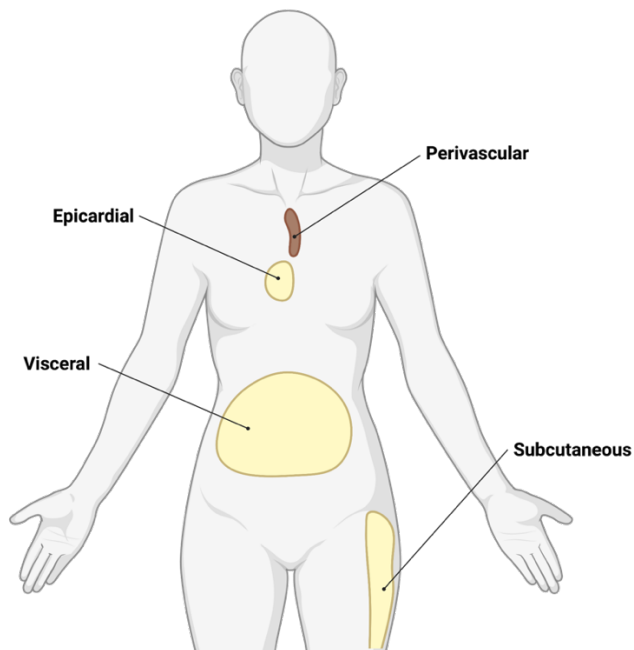


Figure 1.4. Obesity results in the expansion of adipose depots throughout the body. Depiction of the anatomical location of select adipose depots affected during obesity. Perivascular - surrounds the vasculature throughout the body^{7,8}. Epicardial - encompasses the heart¹³⁻¹⁵. Visceral - surrounds abdominal organs¹³. Subcutaneous - located under the dermis layer¹³. Created with BioRender.com. Adapted from Huang, E. (2022). Adipose Tissue Depots. <https://app.biorender.com/biorender-templates/figures/all/t-62050c4ceb716f00a565d765-adipose-tissue-depots>

1.5.1. Obesity is a Global Concern for All Ages of Life

Since the late 1900's, there has been a global increase in the prevalence of obesity in both males and females^{80,81}. More recently, there has also been an increased occurrence of childhood obesity in multiple countries. These rates are highly concerning as childhood obesity impacts an adolescent's physical, mental, and social health^{57,80,82}. Often these impacts are carried into adulthood and contribute to an increased risk for cardiovascular and metabolic disease⁸².

According to epidemiological studies, the dramatic increase of obesity globally can be attributed to complex interactions between an individual and their physical and social environments⁷⁹. Often, these factors influence the amount and type of nutrients consumed and the expenditure of stored energy via physical activity⁷⁹. As previously mentioned, obesity is a well-established risk factor for the development of CVD and many other diseases^{78,83}. Therefore, it will be critical to identify the underlying mechanisms driving these diseases in order to develop effective therapies for patients and at-risk individuals.

1.6. Defining the Types of Adipose Depot Expansion

To accommodate excess energy, adipocytes employ two different expansion methods (**Figure 1.5**). Hypertrophy is the increase of an individual cell's size, resulting in increased cytoplasmic storage of lipids⁵. Hyperplasia is the increase of total number of mature adipocytes within an adipose tissue, thereby limiting individual adipocyte size while expanding tissue volume⁵. The current paradigm holds that the efficiency of an adipose tissue to initiate hyperplastic expansion determines its metabolic impact²⁴. For this reason, there is growing interest in understanding how and when these different mechanisms are employed across various adipose depots. While there are multiple processes that occur in concert during adipose tissue expansion, the primary focus will be on adipocyte physiology²⁴.

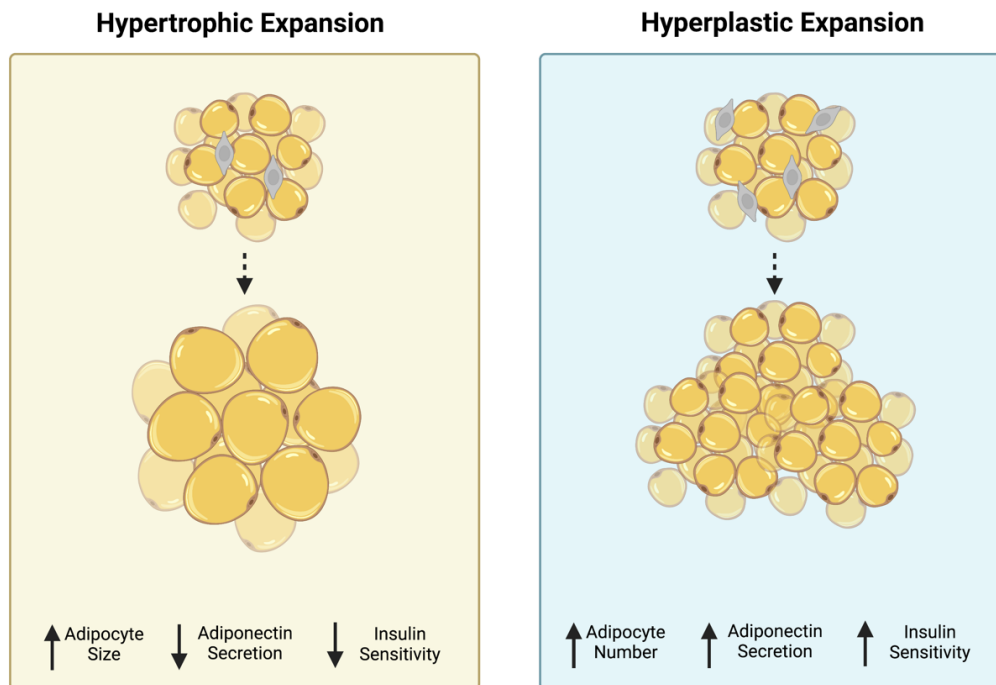


Figure 1.5. Comparison of hypertrophic and hyperplastic expansion within adipose tissue. Adipose tissue adapts to positive energy imbalances by increasing lipid storage capacity⁵. Two mechanisms of expansion are applied: hypertrophic and hyperplastic expansion⁵. Adipocytes are depicted as yellow cells. Adipocyte progenitor cells are depicted as grey cells interspersed among the adipocytes^{24,25}. Major characteristics of each phenotype are denoted in the bottom of each pane²⁴. *Created with BioRender.com.*

1.6.1. Hypertrophy: The Initial Method of Adipose Tissue Expansion

Hypertrophy is thought to be the first adaptive response to accommodate excess energy within the system⁵. As with all cell and tissue types, their function is dependent on the replacement rate of old cells with newer cells. For this reason, existing mature adipocytes are the first responders that are well equipped to sequester circulating glucose and free fatty acids (FFA) as cytoplasmic lipid droplets⁸⁴. This is accomplished via expanding adipocyte lipid droplet and total size (**Figure 1.5**)³. However, each adipocyte has a threshold for storage capacity, that when reached, is associated with decreased metabolic health⁸⁴. As an adaptation mechanism, expansion of adipose tissues is thought to also rely on adipogenesis, the differentiation of mature adipocytes from preadipocyte progenitor cells, resulting in hyperplastic expansion^{5,85}.

1.6.2. Hyperplasia: An Induced Method of Adipose Tissue Expansion

Among its cellular residents, adipose tissue hosts adipocyte progenitor cells to replenish mature adipocyte populations²⁴. During times of balanced energy in-take and expenditure, adipocyte replenishment is a theoretically balanced phenomenon⁵. However, in times of metabolic excess, these progenitor populations can assist with the sequestering of excess FFA by differentiating into mature adipocytes⁵. This form of adipose tissue expansion is termed hyperplastic growth (**Figure 1.5**). The adipocytes resulting from hyperplastic growth are smaller compared to the hypertrophic adipocytes as they store reduced quantities of lipid at an individual level⁸⁴. Specifically, hyperplastic expansion is associated with a stable secretion of adiponectin⁸⁴. Adiponectin is an adipokine responsible for anti-inflammatory responses, and maintenance of insulin sensitivity⁸⁶. For these reasons, hyperplastic expansion of adipose tissue is thought to be metabolically beneficial.

1.6.3. Differences in Hypertrophic and Hyperplastic Responses Between Adipose Depots

Each adipose depot contains characteristics that are unique to their anatomical location²⁴. This also holds true regarding their capacity for hypertrophic and hyperplastic expansion. Studies have shown that expansion of subcutaneous white adipose tissue (WAT) positively correlates with increased levels of adiponectin and reduced adipocyte size (**Figure 1.4**)⁸⁴. Meanwhile, visceral WAT is negatively associated with adiponectin levels and reduced adipocyte size (**Figure 1.4**)^{24,87}. A potential explanation for these phenomena is due to the difference in the number of resident progenitor cells between the two depots (**Figure 1.5**)²⁴. For example, visceral WAT is thought to contain limited population of adipocyte progenitor cells²⁴. Other studies have also provided evidence for unique differentiation potential and presence of progenitor populations between these depots⁸⁷. These studies therefore provide further evidence that therapies targeting the differentiation and metabolic activity of specific depots may be metabolically beneficial for patients suffering from obesity and at risk of CVD development.

1.6.4. A Need for Effective Therapies for Patients with Obesity

Initial approaches to treat obesity upheld the dogma that to reduce weight an individual simply had to reduce food intake and/or increase energy expenditure^{79,88}. Such approaches have been termed “lifestyle” changes and remain critical in combating obesity. However, in recent years, additional studies have shown that an individual’s ability to maintain weight loss for extended periods of time is complicated by multiple biological factors⁸⁸. Work has shown that genetic variations occur between individuals in the expression of neuroendocrine factors that promote nutrient consumption⁸⁸. For this reason, prolonged adherence to what are often dramatic lifestyle changes are ineffective and require medical interventions. Additional evidence shows that even in patients who receive medical interventions, the occurrence of weight regain remains high⁴. One theory for this phenomenon is that the body senses the dramatic loss of energy stores and increases neuroendocrine signaling to combat the perceived starvation threat⁸⁹.

Due to the challenges of maintaining long-term weight loss, it is important to better define how communication from endocrine organs, such as adipose tissues, changes in the face of obesity. Furthermore, for the identification and investigation of novel therapeutic targets, it will be critical to also examine the underlying mechanisms of adipose signaling with the vasculature. Development of such therapies would provide supportive treatments for patients with obesity who are at a high risk of cardiovascular events.

1.7. Considering the Physiological Differences Between Adipose Depots and Their Role in Human Health

Currently, there are three major classifications of adipose tissues that include white, brown, and beige (**Figure 1.6**). *Section 1.5* mainly described the effects of obesity on the visceral and subcutaneous WAT depot expansion. These depots are characterized as such because they exhibit a white colored phenotype due to the high levels of lipid stored within each

adipocyte¹⁷. Meanwhile, adipose within the neck region is characterized as brown adipose tissue (BAT) (**Figure 1.6**)^{3,14}. Again, these depots are characterized according to phenotype color caused by increased mitochondrial number and reduced amounts of stored lipid⁹⁰. PVAT is characterized as a beige depot due to its propensity of residential adipocytes to undergo phenotypic switching between WAT-like and BAT-like characteristics^{15,16}. Phenotype switching within beige tissue is largely associated with the metabolic state of the system^{17,18}.

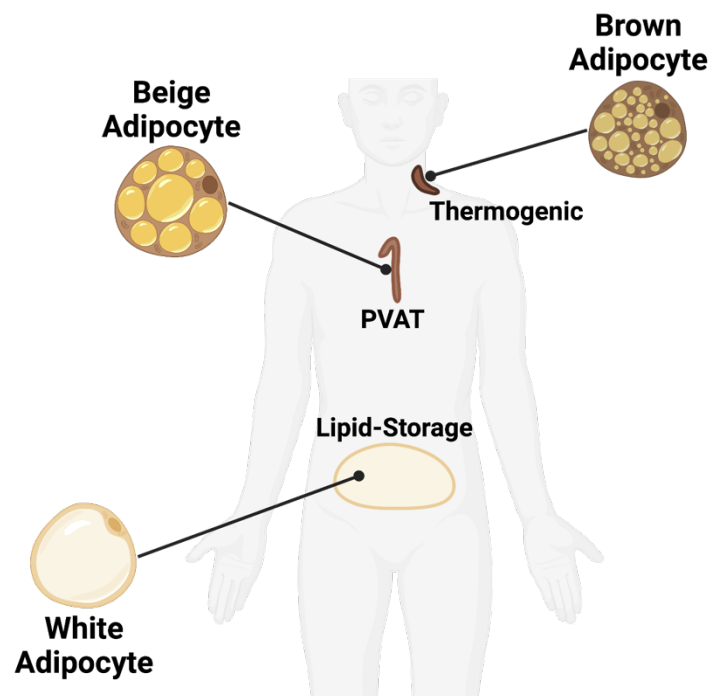


Figure 1.6. Anatomical locations of beige, brown, and white adipose tissue and adipocytes within the human. Schematic of anatomical locations of the perivascular adipose tissue (PVAT, beige), lipid-storage (white) adipose tissue, and thermogenic (brown) adipose tissue along with the primary adipocyte population within each depot^{3,4,14-18}. Created with Biorender.com. Adapted from Huang, E. (2022). *Adipose Tissue Depots*. <https://app.biorender.com/biorender-templates/figures/all/t-62050c4ceb716f00a565d765-adipose-tissue-depots>

1.7.1. The Heterogeneous Composition of Adipose Tissue

All adipose tissues are highly dynamic tissues comprised of a diverse population of cell types. Examples of the various cell types include adipocytes, fibroblasts, and endothelial cells³. Recent single cell RNA-sequencing studies of adipose tissue have provided evidence that these

cells arise from the differentiation of mesenchymal progenitor cells (**Figure 1.7**)¹. Interestingly, additional evidence has been found that suggests that the lineage of classical brown adipocytes and white and beige adipocytes diverge upon mesenchymal stem cell commitment¹⁹. Further separation by subsequent differentiation processes gives rise to the unique physiological capacities of these adipocytes^{19,91}. For this reason, it is critical to account for the unique physiology of these adipocytes when considering their impact on metabolic and vascular health.

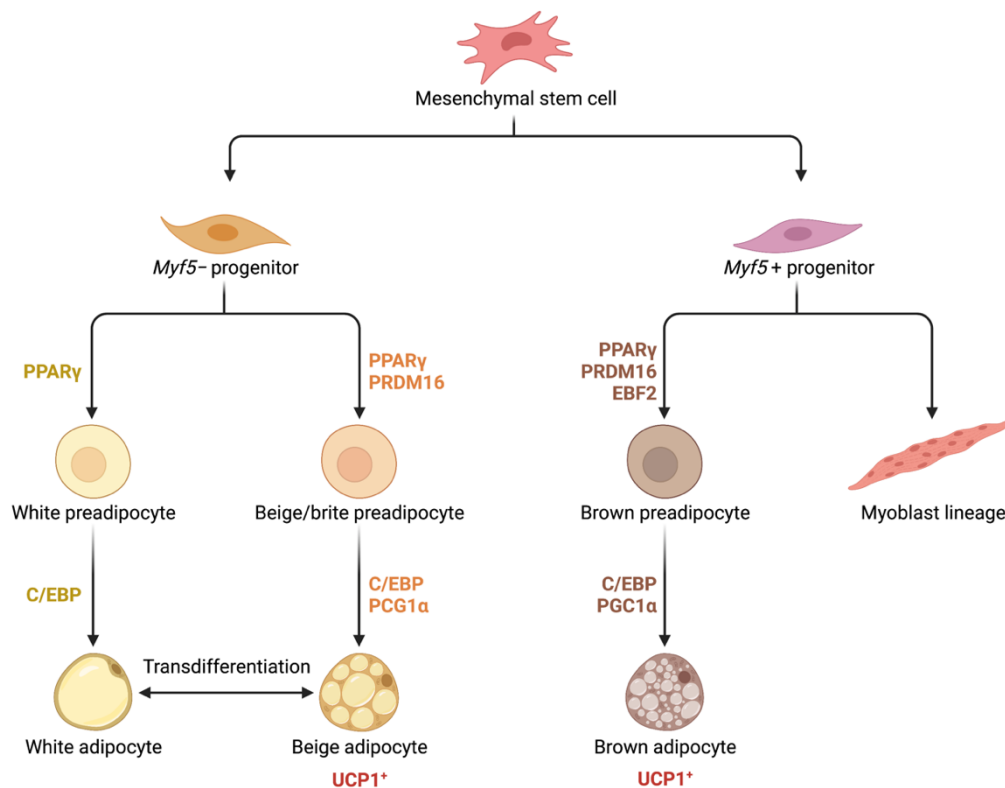


Figure 1.7. Comparison of differentiation processes for white, beige, and brown adipocytes. All adipocytes are derived from a mesenchymal stem cell lineage¹. The unique adipocyte physiologies and phenotypes arise from the divergence between Myf5⁺ cells, and downstream activation of PRDM16 and EBF2 to preferentially drive thermogenic gene expression¹⁹⁻²². Subsequent activation of PGC1α results in the brown adipocyte commitment to mature brown adipocytes¹⁹. PPARγ and C/EBP expression are required for commitment for these adipocytes^{41,42}. *Created with BioRender.com. Adapted from Huang, E. (2022). Adipocyte Lineage.*
https://app.biorender.com/profile/eunice_huang/templates/620659243208cc00a62c9bff

1.7.2. Classical Brown Adipocytes: A Thermogenic Physiology

Classical brown adipocytes are defined as thermogenic adipocytes derived from a myogenic factor 5 positive (*Myf5*⁺) mesenchymal stem cell lineage^{19,20}. While mesenchymal cells destined to become adipocytes require the activation of peroxisome proliferator-activated receptor gamma (PPAR γ) and CCAAT/Enhancer Binding Protein (C/EBP), two transcriptional regulators are unique to the differentiation process of brown adipocytes (**Figure 1.7**)^{19,41,42}. The first transcriptional regulator to be identified was PRD1-BF1-RIZ1 homologous domain containing 16 (PRDM16), a DNA binding transcriptional regulator that induces *Ucp1* and other characteristic brown adipocyte genes via direct interactions with PPAR γ ²¹. The second factor is known as early B cell factor 2 (EBF2), and binds to PPAR γ , influencing the transcription factor to preferentially bind to thermogenic genes²².

1.7.2.1. Classical Brown Adipocytes Exhibit a Distinct Phenotype

Mature brown adipocytes exhibit a unique phenotype characterized by the presence of cytoplasmic multilocular lipid droplets and a high mitochondrial count (**Figure 1.6**)³. The increased presence of mitochondria, and high expression of the mitochondrial uncoupling protein 1 (UCP1⁺), lends these cells their metabolic function as thermogenic adipocytes⁹². In producing heat via non-shivering thermogenesis, a result of futile ATP production, brown adipocytes expend the lipid stored within the multilocular droplets³.

1.7.2.2. Approaches for the Activation of Brown Adipocytes

Thermogenic activity of BAT via the stimulation of brown adipocyte differentiation and expenditure of energy stores can be induced via cold stimulation or treatment with chemical agonists^{92,93}. Exposure of animals to cold temperatures results in the activation of the β -adrenergic receptors, a class of G-protein coupled receptors, via norepinephrine⁹⁴. This activation of the β -adrenergic receptor is associated with an increased expression of

peroxisome proliferator-activated receptor gamma coactivator 1 α (PGC1 α), a co-activator of PPAR γ , leading to the preferential transcription of *Ucp1*⁹². Current research is interested in understanding how brown adipocyte populations could be stimulated to expand and increase metabolic activity.

1.7.2.3. Potential Therapeutic Implications for BAT Activation

While the biological mass of BAT, and therefore brown adipocytes, is strikingly less compared to WAT mass, studies have shown that there is an inverse association between BAT and BMI¹⁴. Furthermore, research has suggested that cold and chemical treatment are effective at inducing brown adipocyte differentiation both in BAT and WAT^{94,95}. For this reason, there has been gaining interest in stimulating brown adipocyte differentiation and activity as a therapy for patients suffering from obesity. However, much work is still needed to test the efficacy of thermogenic stimulation in humans as many studies have been completed using mouse models⁹⁶. This is an important factor to consider as there are differences between human and murine BAT depots.

1.7.3. Classical White Adipocytes: A Lipid Storage Physiology

As mentioned in *Section 1.6.2.*, classical brown and white adipocyte arise from differing progenitor populations also originate from a mesenchymal stem cell lineage (**Figure 1.6**)¹⁹. While previously described as being derived from a *Myf5*⁻ lineage, white adipocyte progenitor cells specifically arise from a CD24⁺ lineage that is distinct from endothelial and hematopoietic cell populations⁸⁵. Furthermore, unlike the differentiation of brown adipocytes, classical white adipocytes depend solely on PPAR γ and C/EBP expression to drive differentiation¹⁹. Therefore, differentiated white adipocytes are identified by the absence of thermogenic gene expression, like *Ucp1*.

1.7.3.1. Classical White Adipocytes Exhibit a Distinct Phenotype

Just as the regulation of gene expression differs between classical white and brown adipocytes, so do their phenotypes. Differentiated, classical white adipocytes organize stored lipids in a unilocular formation (**Figure 1.5**)¹⁷. Additionally, these adipocytes contain noticeably fewer mitochondria compared to brown adipocytes⁹⁷. It is thought that the reduced mitochondrial number is reflective of the lipid storage rather than expenditure nature of white adipocytes. Upon differentiation, classical white adipocytes physically increase their size dramatically due to their purpose of storing large amounts of lipid⁸⁷.

1.7.3.2. Potential Therapeutic Implications for WAT Activation

While classical white adipocytes populate multiple WAT depots throughout the body, there are distinct metabolic differences between these depots (**Figure 1.4**)^{3,24}. Statistical analysis has shown associations between the expansion of lower anatomical subcutaneous WAT and preserved metabolic health⁹⁸. Yet, expansion of visceral WAT exhibits detrimental effects to an individual's metabolic health (**Figure 1.4**)⁹⁹. The major differences between these depots are thought to be the expansion mechanism and tissue-specific secreted factors²⁴.

From these studies, evidence suggests that targeted expansion of healthy WAT could help maintain metabolic health in patients suffering from obesity⁹⁰. Future studies will need to focus on elucidating the mechanisms dictating a depot's preference for hypertrophic or hyperplastic expansion. Identification of such mechanisms could present novel therapeutic targets to drive metabolically healthy expansion of mature white adipocytes within WAT depots.

1.7.4. Beige Adipocytes: A Metabolically Dynamic Physiology

In attempts to understand the lineage and metabolic capacities of adipose tissues, a unique type of adipocyte was identified due to its thermogenic activation upon β 3-adrenergic receptor stimulation¹⁰⁰. These inducible brown adipocytes were found in various white and

brown adipose tissues²⁰. Lineage tracing of the inducible beige adipocytes within WAT suggested that, unlike classical brown adipocytes, they were derived from *Myf5*⁻ progenitors. However, these experiments identified the platelet derived growth factor receptor α (PDGFR α) as a lineage specific marker for these beige progenitor cells. Furthermore, induction of these beige adipocytes remains dependent on PRDM16 and PGC1 α to preferentially express thermogenic genes via PPAR γ transcriptional activity (**Figure 1.6**)¹⁰⁰.

1.7.4.1. Beige Adipocytes: A Thermogenic Phenotype from Non-Thermogenic Lineages

Upon β 3-adrenergic receptor stimulation, the morphology of the PDGFR α ⁺ progenitor population begins to transform into a more classical brown adipocyte morphology^{100,101}. It is important to note that in one study, data suggested that the PDGFR α ⁺ progenitors required active stimulation to commit to a thermogenic phenotype¹⁰⁰. These data further augment that beige cells arising from a PDGFR α ⁺ lineage are unique and therefore have a potentially unique role in metabolic health.

1.7.4.2. Potential Therapeutic Implications for Beige Adipocytes

As mentioned in *Section 1.6.3.2.*, gaining the ability to direct WAT toward a metabolically healthy phenotype during obesity could have significant implication in the treatment of patients with obesity, especially for those at risk of CVD. Identification of beige cells within various WAT provides an additional approach to improving the metabolic capacity of the depots. For example, being able to induce the expansion of mature beige cells within WAT could help increase thermogenic activity and energy expenditure⁹⁰. However, it is also important to consider that just as each WAT is unique, so is their capacity to expand their beige populations^{20,100}. For this reason, it is necessary to continue studying the mechanistic differences between depots to identify which ones have the best potential in modifying metabolic health.

1.8. Perivascular Adipose Tissue: A Distinct Depot at the Interface Between Metabolic and Vascular Health

As discussed in *Section 1.5*, obesity is a leading risk factor for the development and progression of cardiovascular disease⁷⁸. Adipose tissue is an endocrine organ that secretes factors that are capable of eliciting changes in vessel physiology⁸⁷. Obesity negatively impacts vascular physiology by modifying the signaling factors being released from the adipose tissue²⁴. While there are numerous adipose depots throughout the human body, one depot has been identified as a major regulator of thoracic aorta health. Named after its anatomical location, perivascular adipose tissue (PVAT) is similar to other depots in its heterogenous composition¹⁰². Yet, PVAT is unique due to the highly dynamic nature of its resident adipocyte population in response to the system's metabolic state¹⁸. It is through this dynamic nature and proximity to the vasculature that PVAT is a strong influencer of vascular health¹⁰².

1.8.1. PVAT Adipocytes: A Unique Lineage

Like the beige adipocytes discussed within *Section 1.7.4.*, the resident PVAT adipocytes exhibit a thermogenic morphology of multiple lipid droplets and increased presence of mitochondria when observed around the thoracic aorta¹⁰². Interestingly, the phenotype of these adipocytes is variable, with mature adipocytes appearing more closely related with WAT adipocytes. Recent studies attempting to determine the lineage of these highly dynamic adipocytes suggest that they arise from a unique progenitor cell line following mesenchymal commitment. These progenitors are identified as *Pdgfra*⁺, *Sac1*⁺, and *Pparγ*⁻ deriving from a fibroblast lineage in both mice and humans^{103,104}. Furthermore, PRDM16 is required for these cells to exhibit thermogenic physiology, mimicking classical brown and beige adipocytes¹⁶. These studies provide evidence that PVAT adipocytes have a highly dynamic physiology, which is likely how these cells secrete such a diverse population of signaling factors capable of regulating vascular physiology¹⁰².

1.8.2. PVAT Secreted Factors that Induce Vascular Constriction

Due to the proximity of PVAT to the thoracic aorta, it has been shown that this depot is well positioned to influence vascular contractility¹⁰⁵. Multiple studies have provided support for the actions of multiple secreted factors from PVAT that induce vascular constriction. Some of the PVAT secreted factors that have been best characterized include angiotensin II and norepinephrine^{106,107}. Angiotensin II induces smooth muscle contraction via activation of myosin due to increased calcium release into the cytoplasm, resulting in the stimulation of the angiotensin I receptor^{102,106}. Similarly, norepinephrine induces smooth muscle contraction via activation of the β 1-adrenergic receptor, also resulting in calcium release into the cytoplasm leading to the contractile activity of myosin fibers^{107,108}.

1.8.3. PVAT Secreted Factors that Induce Vascular Dilation

Just as PVAT-derived factors have been associated with vasocontractile effects, there is a body of work suggesting that under non-inflammatory conditions, secreted factors promote vasodilative effects on the vasculature. Of the factors studied, one of particular interest is adiponectin. As previously mentioned in *Section 1.6.*, adiponectin is beneficial to metabolic health and is associated with metabolically healthy hyperplastic expansion of adipose tissue⁸⁶. Interestingly, there is supporting evidence that secreted adiponectin binds to serotonin receptors thereby inhibiting serotonin-mediated contraction of vascular smooth muscle cells¹⁰⁹. This reduction in serotonin receptor activation reduces the release of intracellular Ca^{2+} stores, which hinders myosin smooth muscle cells contraction¹¹⁰.

Another mechanism by which PVAT regulates vasodilation is by stimulating nitric oxide (NO) release from endothelial cells. This process involves the secretion of angiotensin 1-7 from PVAT and inducing a paracrine effect via activation of the Mes G-protein coupled receptor in vascular endothelial cells^{111,112}. The released NO diffuses across the VSMC membrane and decreases the concentration of free cytoplasmic Ca^{2+} via activity of the

sarcoplasmic(endoplasmic reticulum Ca^{2+} ATPase (SERCA)¹¹³. This sequestering of Ca^{2+} results in myosin relaxation, thereby inducing vasodilation¹¹⁰.

Importantly, both adiponectin and angiotensin (1-7) are impacted by changes in metabolic health. Obesity has long been associated with decreased levels of circulating adiponectin which contributes to the dysregulation of adipose tissue⁸⁶. Meanwhile, a more recent study has identified an inverse correlation between obesity and circulating angiotensin (1-7)¹¹⁴. These studies augment the importance of PVAT-derived factors on vascular health and indicate that metabolic health impacts the factors being secreted and their physiological effects. Therefore, continued investigation into PVAT-secreted factors and their role in vascular health is important for the identification of potential novel therapeutic interventions for patients at risk for developing CVD.

1.9. Extracellular Vesicles as Signaling Factors

In recent years, there has been growing interest regarding the role of extracellular vesicles (EV) in human health. EV are assigned to a specific class according to their size origin of biogenesis¹¹⁵. Apoptotic vesicles range from 50nm-5 μm in diameter and have been reported to contain intact organelles¹¹⁵. Microvesicles are defined as vesicles from 100nm-1 μm in diameter and are formed by direct budding from the plasma membrane¹¹⁵. As a result, these vesicles contain cargo that is reflective of the plasma membrane composition. Meanwhile, exosomes are nanosized vesicles that range from 30-150nm in diameter and are formed within endosomal compartments called multivesicular bodies (MVBs, **Figure 1.8**)^{11,115}. Exosomes contain cargo from the plasma membrane and cytoplasmic bio-active molecules that are predicted to be actively selected for incorporation¹¹. Recent studies have shown that the cargo are bio-active components capable of eliciting signaling responses within recipient cells¹¹⁶⁻¹¹⁸. For this reason, studies are focused on understanding how changes in exosome cargo can be impacted by or impact disease pathology^{6,116}.

1.9.1. Exosomes as Regulators of Vascular Health

Extracellular vesicles and exosomes have gained attention for their role in disease pathology due to the diversity of their bio-active cargo. Earlier studies provided evidence that exosomes secreted from endothelial, smooth muscle, and macrophage cells within the vasculature had the potential to either mitigate or propagate atherosclerotic plaque development^{119,120}. Many of these studies indicated micro-RNA (miRNAs) as the mechanism by which exosomes impacted CVD development¹²⁰. However, it is important for future studies to also consider the role of the other bio-active cargo, such as proteins, that are present within these exosome populations¹¹.

1.9.2. The Effects of Obesity on Exosome Secretion

Due to the physiological changes observed throughout the body during obesity, it was predicted that the extracellular vesicle populations would also be impacted. Early studies examining the number of circulating exosomes in human plasma showed that obesity was positively correlated with exosome number¹¹⁷. Additional analyses also showed that exosome concentration was positively associated with fat tissue mass^{117,121}. However, due to the classification of the EVs in these studies, it is unclear as to the impact of obesity specifically on the exosome population. Further, number of particles has often been reported in terms of number/volume without normalizing for differences in body weight between subjects with and without obesity^{121,122}. For this reason, it is unclear whether these changes in number were due to increase cell numbers or increased rates of EV production and secretion.

1.9.3. The Effects of Obesity on Exosome Cargo

Exosome cargo is thought to be reflective of the state of the parent cell; if the conditions within the cell change, so does the exosome cargo. Cellular conditions during obesity have been shown to impact not only the physiology of multiple cell types, but also exosome

composition¹¹⁷. One study utilizing *in vitro* techniques, showed that induced hypertrophy altered exosome miRNA cargo, that in turn altered the expression of genes associated with insulin resistance in cardiac cells¹²³. Interestingly, another study suggested that long term obesity in mice induces exosome release from WAT adipocytes that contain oxidatively stressed mitochondria. This study suggests that delivery of these exosomes to cardiac cells helps to protect from metabolic damage¹¹⁶. While these studies therefore imply that exosome cargo is impacted by metabolic changes, further work is required to expand our understanding of metabolic impacts on protein cargo.

1.9.4. A Potential Role for PVAT-Derived Exosomes in Regulating Aorta Vasoreactivity

Until recently, there was a lack of study focusing on the effects of PVAT-derived exosomes on vascular health. So far, one study has provided evidence that PVAT exosomes from C57BL/6J mice limited the activation of foam cells, which are major contributors to atherosclerotic plaque development¹²⁴. As PVAT is also known to regulate vasocontractile responses, it is probable that PVAT-derived exosomes exhibit diverse effects on other cell types within the vascular microenvironment. It will be critical for future studies to not only define the effects of PVAT-EVs, but to also determine the underlying mechanism driving changes in exosome cargo.

1.10. Exosome Biogenesis and Release: A Rab Family Mediated Process

To identify potential mechanisms driving altered cargo packaging into exosomes, it is critical to first understand exosome biogenesis and release. Exosomes are formed and secreted via the following steps: endosome formation, multivesicular body development, cargo sorting and packaging, multivesicular body trafficking, and exosome release via membrane fusion^{6,11,125}. Each of these steps are believed to be regulated by a family of small GTPase proteins belonging to the Rab family (**Figure 1.8**)¹⁰.

Rab proteins are expressed by eukaryotic organisms, and more than 50 of these proteins have been identified¹⁰. Rab proteins are largely associated with intracellular trafficking of vesicle compartments⁶. While these proteins share high sequence similarity, each Rab protein performs a unique role¹⁰. Multiple Rab family members have been identified as contributors in the biogenesis and secretion of exosomes^{6,10,11}. Therefore, these Rab proteins may prove to be effective targets in regulating exosome mediated signaling.

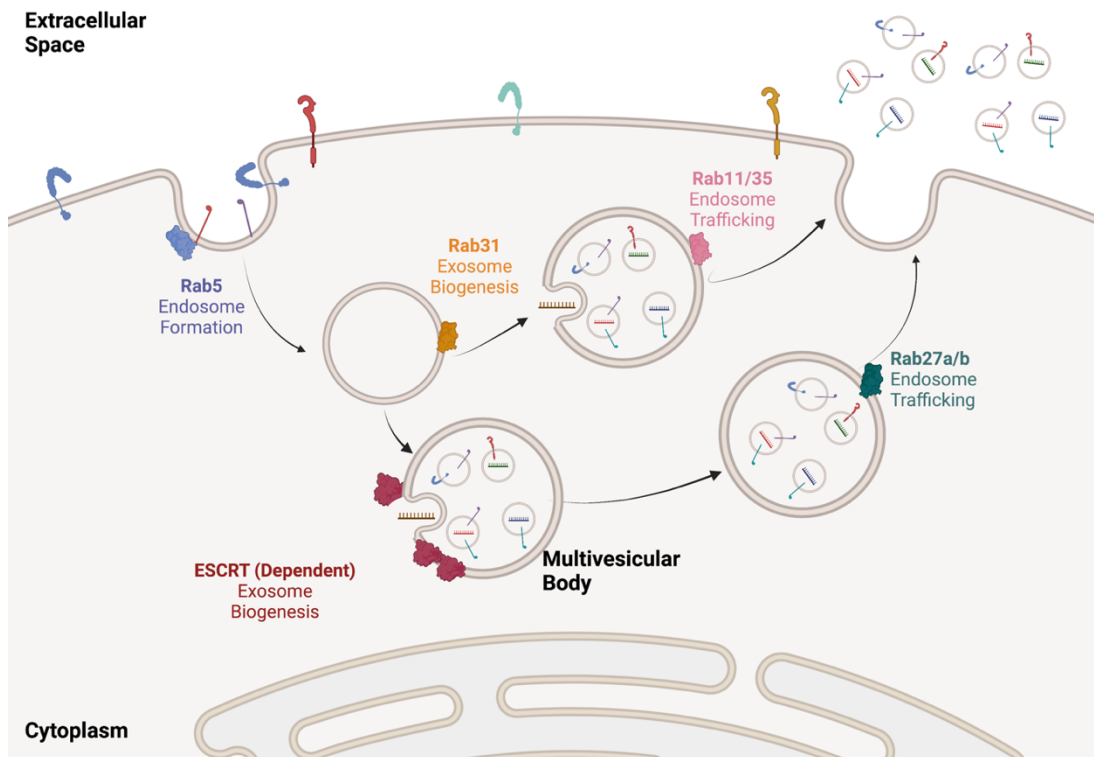


Figure 1.8. Rab proteins as mediators of exosome biogenesis. Depiction of the Rab proteins known to regulate various parts of exosome biogenesis. The primary role for Rab5, Rab31, Rab27a/b, Rab11, and Rab35 are noted below their respective IDs^{6,9-12}. Created with BioRender.com.

1.10.1. Endosome Formation is Mediated by Rab5

The first step in exosome formation is dependent on the formation of endosomal compartments. Endosomes were first identified as the foundation of exosome biogenesis via tracking of transferrin receptors from the plasma membrane to extracellular vesicles. A foundational study utilized WT and mutant forms of *Rab5* to show the protein's importance in

endosome formation (**Figure 1.8**)¹²⁶. These conclusions have been upheld through support of later studies and suggest that Rab5 mediates early endosome fusion with smaller cytoplasmic vesicles, contributing to the formation and function of the endosome¹²⁷.

1.10.2. ESCRT-Dependent Multivesicular Body Development and Cargo Sorting

The second step of exosome biogenesis is the transition of the early endosomal compartment into a multivesicular body (MVB)¹¹. These endosomal compartments are termed MVB as they undergo endocytic events, creating vesicles from their own membranes. These smaller vesicles are termed intraluminal vesicles (ILV), and are reclassified as exosomes upon secretion from the cell¹²⁵.

Alongside ILV formation, active processes dictate the incorporation and packaging of bio-active molecules including proteins, lipids, and nucleic acids. It is thought that the primary sorting of cargo is determined via endosomal sorting complex required for transport (ESCRT)-dependent mechanisms (**Figure 1.8**)¹²⁵. This mechanism functions by incorporating ubiquitinated proteins into the forming ILVs⁶. This is a multi-step process involving the recruitment of sequential ESCRT 0-III complexes and interactions with vacuolar protein sorting-associated proteins (VPS)¹¹. The sorting processes of the ESCRT complexes also mediate the budding of the ILVs into the cytoplasmic space of the MVBs¹¹.

1.10.3. Multivesicular Body Trafficking is Mediated by Multiple Rab Proteins

The act of ILV secretion redesignates the nanovesicles as exosomes. For secretion to occur, the MVB must be trafficked from the cytoplasm to the plasma membrane⁶. Multiple Rab proteins have been identified as mediators of this process including RAB27A, RAB27B, RAB11 and RAB35 (**Figure 1.8**)¹⁰. While these proteins support MVB relocation, each plays a unique role and therefore are all important for exosome secretion.

In the seminal paper by Ostrowski et al., the group showed that RAB27A was uniquely

responsible for regulating the size of the MVBs along with their efficiency of associating with the membrane⁹. Meanwhile, RAB27B altered plasma membrane association by limiting MVB trafficking from the perinuclear region. Interestingly, this study provided evidence that RAB27A knockdown had no effects on standard exosome protein markers⁹. Since then, RAB27A and RAB27B have been confirmed regulators of exosome secretion from other cell types¹²⁸⁻¹³⁰. Expression data from the NCBI Gene database further show that RAB27A is widely expressed in human tissues including fat, heart, and stomach^{131,132}.

Additionally, while RAB11 and RAB35 have also been identified as regulators of exosome secretion, the underlying mechanisms remain under investigation¹⁰. Both are associated with the recycling of endosomal compartments to the plasma membrane as cellular mechanisms for disposal¹²⁵. In one publication, both Rabs are depicted as regulating ILV release from an ESCRT-independent pathway¹⁰. Interestingly, in a recently published paper, RAB31 was identified as regulating ILV formation in the absence of ESCRT complex activity¹². Therefore, it is possible that RAB11 and RAB35 are regulators for the secretion of a unique exosome subpopulation.

1.10.4. SNARE Proteins Mediate Exosome Secretion

Membrane fusion is an essential function within cells and is largely regulated by soluble N-ethylmaleimide-sensitive factor attachment protein receptors (SNARE)⁶. SNAREs are helical proteins that produce heterocomplexes and are tethered to their respective membranes via transmembrane spanning domains⁴⁰. SNARE complexes from opposing membranes intertwine, inducing conformational changes, and bring the two membranes together (**Figure 1.9**)⁴⁰. These receptors therefore work in concert to overcome the charge repulsion of two membranes and mediate their fusion⁴⁰. For this reason, SNARE complexes are extremely important for mediating ILV release into the extracellular space.

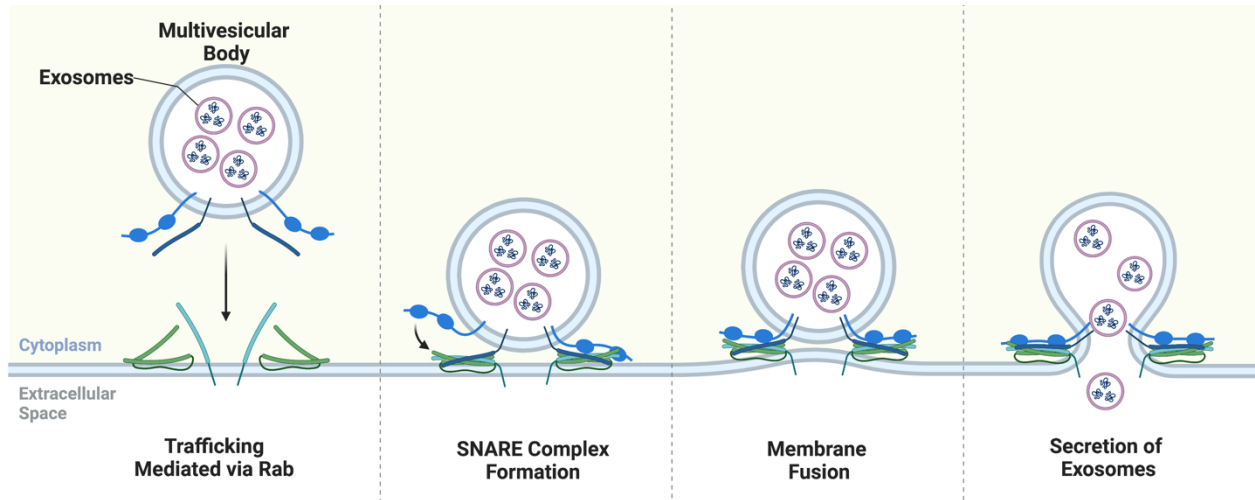


Figure 1.9. SNARE proteins drive membrane fusion by overcoming repulsive forces exerted by opposing membranes. This schematic outlines the general process for membrane fusion between multivesicular bodies and the plasma membrane⁶. SNARE proteins facilitate this process by binding with other SNARE proteins on opposing membranes and forming coiled complexes⁴⁰. This interaction draws the two membranes together and induces fusion⁴⁰. Created with BioRender.com. Adapted from “Ca²⁺-triggered Vesicle Fusion and Exocytosis of Neurotransmitters.” (2020). <https://app.biorender.com/biorender-templates/figures/all/t-5fcfe6cd9065d900a614f857-ca2-triggered-vesicle-fusion-and-exocytosis-of-neurotransmit>.

1.11. Selection of *Rab27a* to Study Exosome Dysregulation in the Vascular Microenvironment

In alignment with the overarching focus of the Liaw laboratory, we set out to define whether the dysregulation of exosome signaling impacts vascular microenvironment physiology. Defining the importance of exosome signaling has the potential to improve our understanding of the importance of these vesicles in vascular health. To disrupt exosome secretion within an *in vivo* model, we selected *Rab27a* as a target for endonuclease mutagenesis within the C57BL/6J mouse strain.

Rab27a was selected for mutagenesis for multiple reasons. Due to its well characterized role in regulating MVB translocation to the plasma membrane, *Rab27a* was a reasonable target for disrupting the secretion of exosomes. *Rab27a* has long been the only Rab protein associated with a human disease known as type II Griscelli syndrome, marked by a hypopigmentation and immune system phenotypes¹³³⁻¹³⁵. Type II Griscelli syndrome is a rare

disease that is not currently associated with cardiovascular phenotypes^{133,134}. The Liaw lab also published a manuscript providing evidence that RAB27A knockdown in human PVAT APCs resulted in reduced adipocyte differentiation and lipid accumulation¹³⁶. Finally, Rab27a is present not only in humans and mice, but also in all organisms belonging to the metazoan kingdom³⁵. This highly conserved expression of Rab27a suggests this gene has an important and conserved function between the two species.

1.11.1. RAB27A and Rab27a have Conserved Transcript Sequences

Although orthologs of Rab27a have been identified in humans and mice, we sought to understand the level of conservation between the two species. The BLAST alignment was completed using mRNA transcript sequences of RAB27A (RefSeq NM_183235) and Rab27a (RefSeq NM_001301230) that were obtained using the UCSC Genome Browser (**Figure 1.10A**)^{38,45}. Results from this alignment showed that there was an 88% sequence similarity between the two gene transcripts (**Figure 1.10B**).

A Transcript Sequence Alignment RAB27A vs Rab27a

Query	217	AGGTGAAC	ACTGAGT	CTCCTT	CAATAT	GTCTGAT	GGAGATT	TATGATT	ACCTCAT	CAAGTTT	276	
Subject	306GGC	..A.....	..C.....	..G.....C.....C.....C.....C.....C.....	365	
Query	277	TTAGCTT	GGGAGACT	CTGGT	GTAGG	AAGAC	CAGTGT	ACTTT	ACCA	TATAC	AGATGGT	336
Subject	366	..G..CG.....G.....C.....C.....C.....G.....C.....T.....	425	
Query	337	AAATT	TAAC	TCCAA	TTAT	CAACA	AGTGGG	CATT	GTTC	CAGG	AAAAAGAGTGGTG	396
Subject	426	..G..CC.....C.....C.....C.....G.....G.....G.....G.....	485	
Query	397	TACAG	AGCCAGT	GGCCGG	ATGG	AGCC	CACTGG	CAGAG	CCAG	AATCC	ACCTGCAGTTA	456
Subject	486A.....A.....TGTG.....C.....C.....C.....C.....C.....C.....	545	
Query	457	TGGG	CACAG	CAGGG	CAGG	AGGTTT	CGTAG	CTTA	ACG	ACG	CGTTCTTC	516
Subject	546G..G.....G.....G.....G.....G.....C..T..A.....G.....G.....C.....	605	
Query	517	ATGGG	TTTTCT	CTACT	TTTT	GTG	ATCTG	ACAA	TGAG	CAAGTTT	CTCA	576
Subject	606C..G..T..G..C..C.....C.....C.....C.....C.....C.....C.....C.....C.....	665	
Query	577	TGG	AAGC	AGCT	AC	AGAT	GCAT	ATTG	TGAA	ACC	CAGAT	636
Subject	666C..G..C.....C.....C.....C.....C.....C.....C.....C.....C.....	725	
Query	637	AACA	AGAGT	GATCT	GGAG	CAC	GAGAG	TAGT	GAA	GAGG	GAAGCC	696
Subject	726	..T.....C.....A.....G.....C.....G.....G.....G.....CGG..A...T..C	785	
Query	697	GAGA	AATAT	GGAA	TCCC	CTACT	TTGAA	ACTAG	TGC	CAATGG	CAAA	756
Subject	786G..C.....T.....C.....C.....C.....C.....C.....C.....C.....	845	
Query	757	GCA	ATTG	AGAT	GCTT	CTGG	ACCT	GATA	ATGA	AGCG	ATGTTG	816
Subject	846	..G.....C.....C.....C.....G.....G.....G.....G.....G.....	905	
Query	817	TGG	ATCT	GAA	GAGT	GGT	GCAT	CAAT	GGT	CA	TGCCT	876
Subject	906G..G.....A.....G.....C.....C.....A.....G.....C.....C.....	965	
Query	877	GAAA	AGG	AGAA	GGG	CATG	TGG	CTG	TG	AGAG	TCAG	915
Subject	966	..G.....G.....TTG.....C.....C.....C.....C.....C.....C.....	1004	

B % Sequence Similarity

Human (RAB27A) = 100%
Mouse (Rab27a) = 88%

Figure 1.10. RAB27A and Rab27a have conserved transcript sequences. A) The RAB27A mRNA transcript (variant 3, Query) is derived from the human genome version Dec. 2013 (GRCh38/hg38)³⁵. The Rab27a mRNA transcript (variant 1, Subject) is derived from the mouse genome version Jun. 2020 (GRCm39/mm39)³⁵. Dots indicate conserved nucleotides between the sequences. Presence of a letter in the Subject sequence indicates a divergence in nucleotide alignment⁴⁵. B) Summary of sequence similarity compared to the human transcript sequence.

1.11.2. Human and Mouse RAB27A have Highly Conserved Amino Acid Sequences

Both the human RAB27A (UniProt ID: P51159) and mouse RAB27A (UniProt ID: Q9ERI2) have reported peptide lengths of 221 amino acids³³. Alignment results of the RAB27A peptide sequences from the two species show that there is a 95.93% similarity (**Figure 1.11A**)³³. Furthermore, the identified binding sites are also conserved between the two sequences (**Figure 1.11B**). This similarity suggests that the function and activity of these proteins are conserved, despite *RAB27A* being located on chromosome 15 and *Rab27a* being located on chromosome 9^{137,138}.

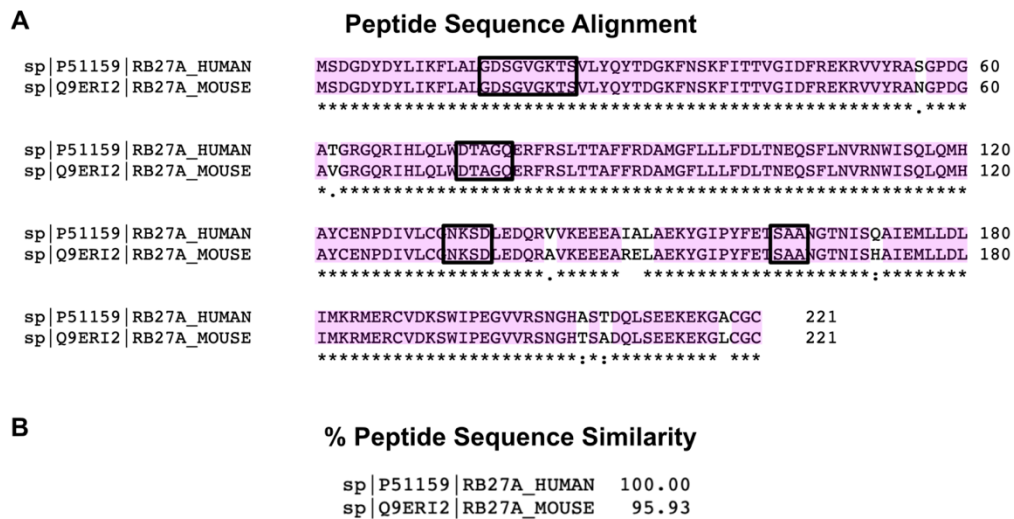


Figure 1.11. Amino acid sequence alignment and similarity for human and mouse RAB27A. A) Results of a peptide sequence alignment of human and mouse RAB27A utilizing Align via UniProt³³. (*) indicates a fully conserved amino acid. Similarity is further highlighted by highlighted region. (:) indicates variable amino acid with high conserved properties. (.), indicates variable amino acid with low conserved properties. Black outlines show conservation of protein binding sites. B) Alignment showed that the mouse amino acid sequence shares 95.93% similarity with the human sequence.

1.11.3. Comparing the Tissue Expression Profiles of *RAB27A* and *Rab27a*

In addition to the conserved gene and protein sequence of *Rab27a* between humans and mice, expression data between adipose and cardiovascular tissues is publicly available. The Jackson Laboratory's Gene Expression Database (GXD) provides a very inclusive review of *Rab27a* expression within mouse tissues and confirms expression within the cardiovascular

system and adipose among many others¹³⁹. Utilizing the Human Protein Atlas, we found evidence of *RAB27A* expression within adipose and the cardiovascular system¹⁴⁰. Therefore, we hypothesized that loss of *Rab27a* would elicit conserved physiological effects within the vascular microenvironment between humans and mice.

1.12. Characterization of Previously Established *Rab27a* Null Mouse Strains

Furthermore, prior mouse models containing mutations within *Rab27a* suggested that this gene can be reliably targeted. The first known mouse strain to carry a *Rab27a* mutation was identified at The Jackson Laboratory in 1979¹³⁸. Arising from a spontaneous mutation on a C3H/HeSN background, these mice exhibited a gray (*ashen*) coat color and were named the *ashen* strain (*Rab27a^{ashen}*). Using this strain, the research group was able to trace the mutation to chromosome 9¹³⁸. Later studies went on to show that unlike other *ashen* colored mice, this strain was due to a point mutation in *Rab27a* and results in reduced vesicle trafficking¹⁴¹. While we have been provided access to data concerning glucose sensitivity in the *Rab27a^{ashen}* mice, these mice are not readily available from The Jackson Laboratory (*Soucy et al., 2023 under revision*).

Since this original strain was identified, others have been established through genetic modification techniques. For example, one strain was created on a C57BL/6 background using TALEN endonuclease targeting to mutate *Rab27a* exon 2¹⁴². A later study also utilized a *Rab27a* null strain that was purchased from Cyagen Biosciences Company¹⁴³. However, due to a lack of characterization and genetic drift information between strains we deemed it necessary to establish novel *Rab27a* murine models on a true C57BL/6J background with specific targeting to exon 4.

1.13. Project Goal: Determine Whether Loss of *Rab27a* Alters Vascular Physiology via the Dysregulation of Exosome Secretion

Based on this existing body of work, we hypothesized that *Rab27a* regulates vascular health through its role as a mediator of exosome signaling. To test our hypothesis, we have established a novel global *Rab27a* null strain on a C57BL/6J background. Within the succeeding chapters, we provide evidence that the global loss of *Rab27a* affects thoracic aorta contractile and dilative responses uniquely according to diet, age, sex, and genotype. With these studies, we provide foundational evidence to the importance of *Rab27a* in the regulation of thoracic aorta health.

CHAPTER 2: EXPERIMENTAL METHODS

2.1. *In Vivo* Methods

All methods described under *Section 2.1* pertain to *in vivo* experiments utilized within this study. Each method was approved by the Institutional Animal Care and Use Committee.

2.1.1. Commercially Available Strains

Multiple commercially available mouse strains were utilized throughout this work for strain development, breeding, backcrossing, positive control for Cre-directed genetic recombination, and to diversify genetic backgrounds. The specific uses of each strain listed in **Table 2.1** will be described in detail within the *Results*.

Table 2.1. Mouse strains from commercial sources.

Species	Source	Description	Sex	Stock #
Mouse	Jackson Laboratory	C57BL/6J	M/F	#00064
Mouse	Jackson Laboratory	B6.Cg- <i>Edil3</i> ^{Tg(Sox2-cre)1Amc} /J	M	#008454
Mouse	Taconic	Swiss Webster	F	SW-F

2.1.2. Single-Guide RNA Design for CRISPR-Cas9 Targeting of *Rab27a* Introns 3 and 4

Genomic sequence of *Rab27a* intron 3 and intron 4 regions, roughly 1,000 nucleotides flanking exon 4, were used to identify sequences to direct CRISPR-Cas9 activity using CRISPOR¹⁴⁴. The program identified multiple options for protospacer adjacent motifs (PAM) sites and leading seed sequences. Sequences were selected by prioritizing sequences with the strongest Mreno-Mateos Efficiency Score that had potential for use as restriction digest sites. As a result, sequence 5'gRNA-Rab27a#2-93(+) was selected to target intron 3 and 3'gRNA-Rab27a#1-83(+) was selected to target intron 4 (**Table 2.2**).

Table 2.2. sgRNA sequences and predicted efficiencies for targeting of Rab27a introns 3 and 4.

Guide RNA sequence PAM, 5'→3'	MIT Specificity Score	Out-of-Frame Score	Moreno-Mateos Efficiency Score	Off-Target (Total #)	Off-Target (Exons, #)	Off-Target (Chr:9, #)	Off-Target Distribution	RE Site
5'gRNA-Rab27a#1-96(+) TCTCATGTATAGT AAGGCGG TGG	96	51	59	35	1	2	0-0-0-1-34 0-0-0-0-0	N/A
5'gRNA-Rab27a#2-93(+) ATGCCTGCTTTTA CGGTACA GGG	93	54	62	74	2	7	0-0-1-9-64 0-0-0-0-0	PAM site can be mutated into PciI
3'gRNA-Rab27a#1-83(+) GCCTGGTGAAC ATCTGGTC GGG	83	75	69	109	13	10 (E+crh:9-3)	0-0-1-9-99 0-0-1-2-2	PAM site can be mutated into Sall
3'gRNA-Rab27a#2-87(-) CCGGAACCCACA CAACTATT AGG	87	63	55	100	5	5	0-0-2-7-91 0-0-0-2-2	PAM site can be mutated into AvrII
3'gRNA-Rab27a#3-90(-) CCGGAACCCACA CAACTATT AGG	90	69	43	72	8	2 (E+crh:9-1)	0-0-0-4-68 0-0-0-0-1	N/A

2.1.3. Validation of Single-Guide RNA for CRISPR-Cas9 Targeting of Rab27a Introns 3 and 4

Efficacy of CRISPR-Cas9 targeting using these primers was tested *in vitro* prior to microinjection. This was completed by incubating 3μL of 10x Cas9 buffer (New England Biolabs), 1μL of a Cas9 enzyme (1μM stock, New England Biolabs), 20ng of the desired sgRNA, and RNA-free H₂O (volume required to bring reaction volume to 30μL once target DNA is added). The mixture is allowed to incubate at room temperature for 10 minutes. After which, 150-180ng of the pure wildtype Rab27a nucleotide sequences was added and incubated at 37°C for 60 minutes. Finally, the Cas9 enzyme was inactivated by incubation at 70°C for 10 minutes.

Products were separated utilizing a 2% agarose gel to determine whether the target DNA was sufficiently cut by the endonuclease. Gels were made using 6g of Agarose I (VWR, #0710, CAS 9012-36-6) dissolved into 300mL of 1x Tris-acetate-EDTA buffer (TAE 2M Tris-

base, 1M glacial acetic acid, 0.05M EDTA). Gels were then stained with SYBR™ Green Safe DNA Gel Stain (Invitrogen, Cat# S33102) and molded. To determine size, a 1Kb Plus DNA Ladder (3.5µL, Invitrogen, Cat# 10787026) was loaded into the first lane of the gel. For each sample, 10µl was loaded into subsequent lanes. Electric currents were passed through the gels submerged in 1x TAE. Gels were then imaged utilizing Fujifilm imager (LAS-4000). Imaging of the gel showed that roughly 50% of the target DNA was cut by both sgRNA (**Figure 2.1**). According to the standards set by the MaineHealth Institute for Research Mouse Genome Modification Core, this targeting efficiency was acceptable to utilize for microinjection.

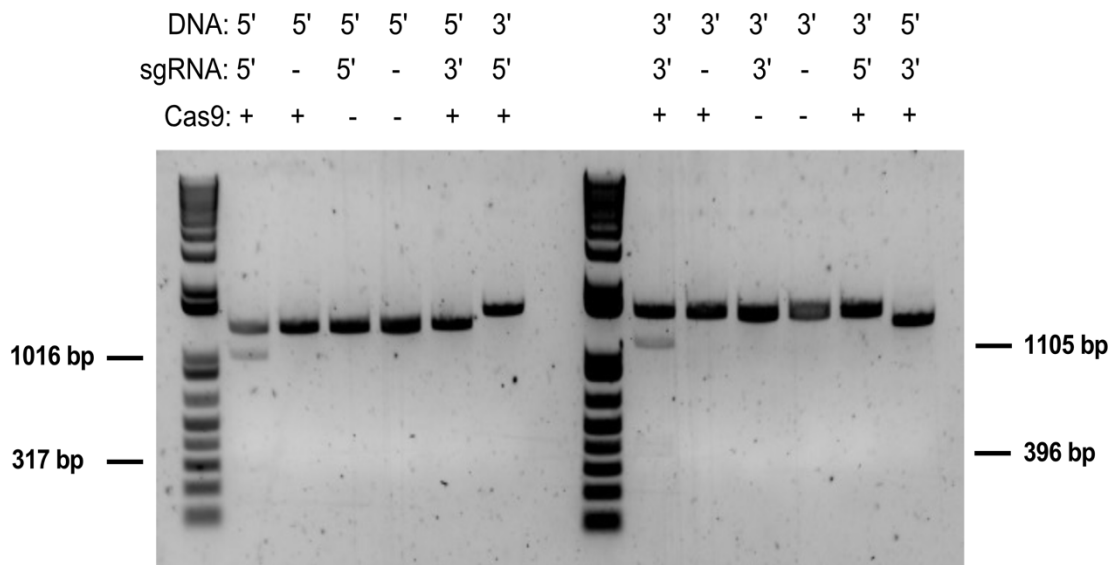


Figure 2.1. *In vitro* confirmation of sgRNA targeting efficacy. Target DNA (150-180 ng) of 1501 base pairs (bp) in length was incubated with the 5' and 3' sgRNA (30 ng) and Cas9 (1µM) at 37°C for 1 hr. The entire enzymatic reaction was run on a 1.5% TAE-agarose gel to determine whether cleavage occurred. Expected bands for cleaved 5'DNA are 1016 and 317 bp while cleaved 3'DNA would exhibit bands at 1105 and 396 bp. Although faint, both the 317 pb and 396 bp bands are present. With targeting efficacy ~50% or greater these guides were acceptable for microinjection.

2.1.4. Establishment of the Novel *Rab27a* Global and Conditional Null Strains

C57BL/6J embryos collected from the breeding of purchased C57BL/6J male and female mice (The Jackson Laboratory) were utilized for strain establishment (**Table 2.1**). *Rab27a* null mice were the result of nonhomologous end joining post genomic modification via CRISPR-Cas9 targeting of introns flanking exon 4 of *Rab27a* (**Figure 2.2**). Meanwhile, *Rab27a^{fl/fl}* mice were the result of homologous loxP site insertions flanking exon 4 of *Rab27a* through CRISPR-Cas9 targeting (**Figure 2.2**). All mutant alleles were segregated by backcrossing to wildtype (WT) C57BL/6J mice for 3 generations and verified by direct genomic sequencing (**Table 2.3**).

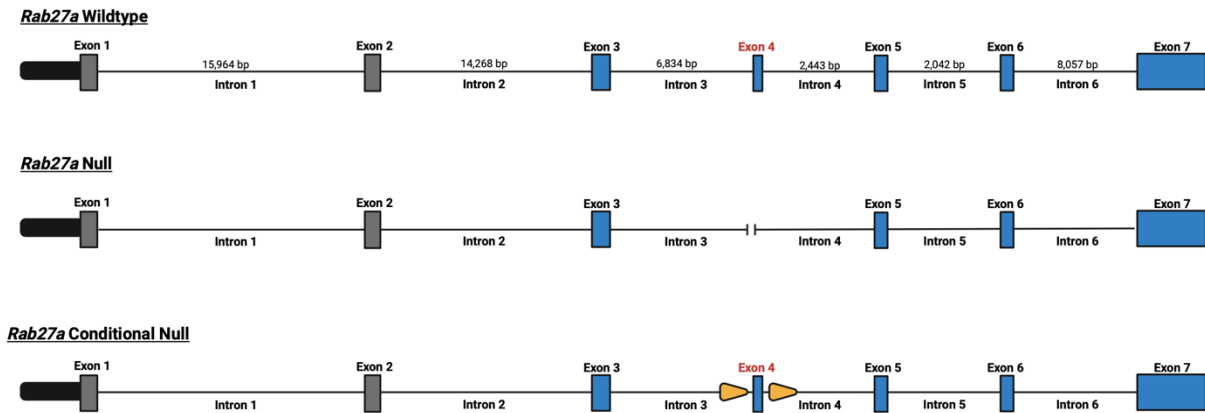


Figure 2.2. Resulting *Rab27a* alleles from CRISPR-Cas9 mutagenesis. The endogenous *Rab27a* WT gene with mapped exons of the longest transcript (top), *Rab27a* global null allele (middle) with the deletion of exon 4, and *Rab27a^{fl/fl}* allele (bottom) are presented. Gray boxes = non-coding exons, blue boxes = coding exons, orange triangles = loxP sites. Gene structure is from the GRCm38/mm10 mouse genome alignment³⁸. Created with BioRender.com.

Table 2.3. Novel genetically modified mouse strains.

Species	Strain Name	Source	Background	Strain ID
Mouse	<i>Rab27a</i> global null	Liaw laboratory	C57BL/6J	<i>C57BL/6J-Rab27a^{em10L/w}</i>
Mouse	<i>Rab27a</i> conditional null	Liaw laboratory	C57BL/6J	<i>C57BL/6J-Rab27a^{em24L/w}</i>

2.1.5. *Rab27a* Global Null Genotyping

Murine genomic DNA was isolated from tissue samples using an in-house alkaline lysis reagent (25mM NaOH, 0.2mM disodium EDTA, pH 12.0), boiled in a heat block for 30 minutes, and then neutralized with equal volume of 40mM Tris-HCl reagent (pH 5). Isolated DNA was used for genotyping via polymerase chain reaction (PCR) targeting exon 4 of *Rab27a*. The PCR reaction consisted of Apex Taq RED Master Mix, 2x, 1.5mM MgCl₂ (Cat #42-138B), nuclease free water, primers from IDT (**Table 2.4**), Forward primer (global null) and Reverse primer (global null), and template genomic DNA. The cycling conditions included a denaturing time of 30 seconds at 94°C, an annealing time of 20 seconds at 60°C, and an extension time of 30 seconds at 72°C for 34 cycles utilizing primers listed in **Table 2.4**. PCR products were separated, and sizes were determined as previously described (*Section 2.1.3*). A WT product was expected to be 850 bp (**Figure 2.3A**). A *Rab27a* null product was expected to be 165 bp (**Figure 2.3B**).

2.1.6. Confirmation of loxP Site Insertion

Murine genomic DNA was isolated from tissue samples as described in *Section 2.1.2*. The cycling conditions included a denaturing time of 20 seconds at 94°C, an annealing time of 10 seconds at 55°C, and an extension time of 120 seconds at 68°C for 35 cycles utilizing primers listed in **Table 2.4**. The resulting PCR amplicon from a *Rab27a^{fl/fl}* mouse is 2185 bp. To confirm the insertion of functional loxP sites, the amplicon was then digested using restriction enzyme PciI (New England Biolabs) according to manufacturer recommendations. PCR products were separated, and sizes were determined as previously described (*Section 2.1.3*). If functional loxP sites were successfully inserted two products of 1693 bp and 492 bp would result (**Figure 2.3C**).

2.1.7. *Rab27a* Conditional Null Genotyping

Murine genomic DNA was isolated from tissue samples as described in *Section 2.1.2*. The PCR reaction consisted of Apex Taq RED Master Mix, 2x, 1.5mM MgCl₂ (Cat #42-138B), nuclease free water, primers from IDT, and template DNA. The cycling conditions for the floxed allele included a denaturing time of 30 seconds at 94°C, an annealing time of 15 seconds at 60°C, and an extension time of 30 seconds at 72°C for 34 cycles utilizing primers listed in **Table 2.4**. Conditional *Rab27a* null mice would produce an amplicon 334 bp in length (**Figure 2.3D**). The cycling conditions for the presence of Cre sequence for all strains include a denaturing time of 10 seconds at 94°C, an annealing time of 20seconds at 60°C, and an extension time of 20 seconds for 68°C using primes listed in **Table 2.4**. Presence of Cre would produce an amplicon 299 bp long.

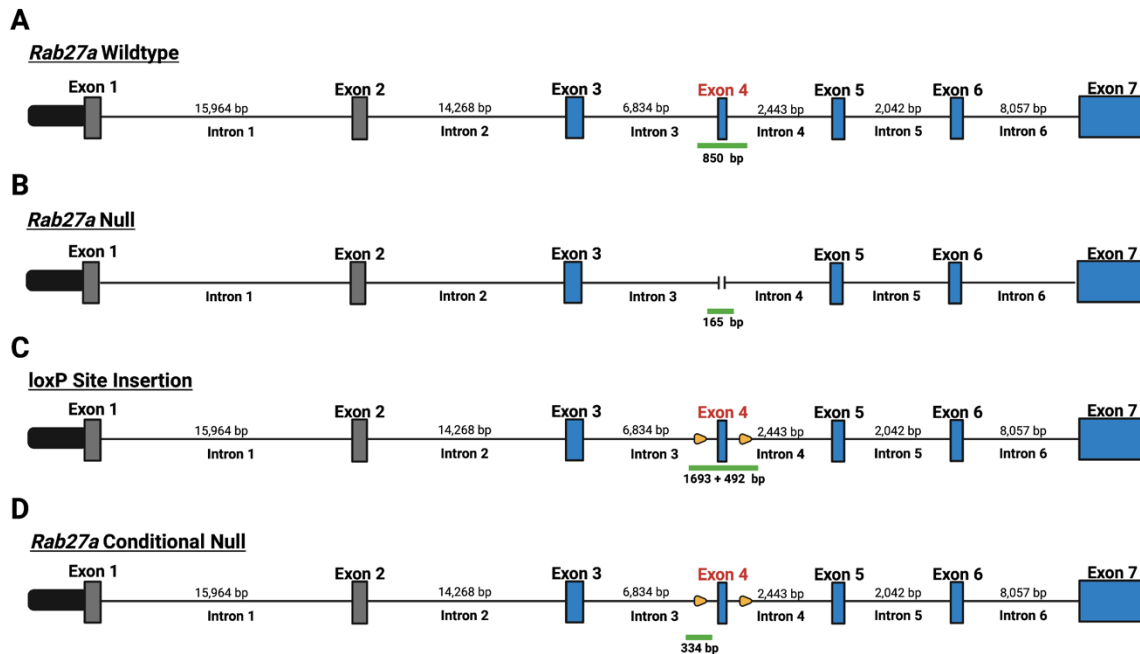


Figure 2.3. Genotyping strategy for the novel *Rab27a* global and conditional null strains. Schematic showing PCR products as green bars for A) WT, B) *Rab27a* null, C) loxP site confirmation, and D) *Rab27a* conditional null alleles. Product sizes are noted below their respective bars. Gene structure is from the GRCm38/mm10 mouse genome alignment³⁸. Created with BioRender.com.

Table 2.4. Primer sequences for novel *Rab27a* global and conditional null strains.

Description	Sequence
Forward primer (global null)	5'- GTAGCTAACTGAAAGCAGCCTTG -3'
Reverse primer (global null)	5'- AGTGACCTTTCTATCTTCTGTCTC -3'
Left arm forward loxP primer	5' - GACAGGAGTGCCCATGTATAAAG - 3'
Right arm reverse loxP primer	5' - TTCCCTCCAGGTAATATGGG - 3'
Forward primer (conditional floxed allele)	5'- GAAATTCTGAGACCAGCGGGC -3'
Reverse primer (conditional floxed allele)	5'- AGTGAACCTTTCTATCTTCTGTCTC -3'
Forward primer (Cre)	5'- TTCCCGCAGAACCTGAAGATG -3'
Reverse primer (Cre)	5'- CCCCAGAAATGCCAGATTACG -3'

2.1.8. Maintenance of *Rab27a* Global and Conditional Null Strains

Heterozygous *Rab27a* null males and females were bred to produce genetically mixed litters. Breeder mice were fed a breeder diet (Teklad, #2919) and provided water *ad libitum*. From those litters, *Rab27a* null males were mated with *Rab27a* null females to produce *Rab27a* null litters. WT littermates were bred together to produce WT offspring. Mice were group housed in an Association for Assessment and Accreditation of Laboratory Animal Care (AAALAC)-accredited mouse barrier facility and fed a chow diet (Teklad, #2918) and water *ad libitum* with a 12:12 light-dark cycle.

2.1.9. 60% High Fat Diet Feeding

Rab27a null and WT male mice at 7 weeks of age were moved from group to single housing. All mice were provided chow diet (Teklad, #2918) and water *ad libitum* and supplemented with a habitat structure. Random selection was applied to determine which subjects received a 60% high fat diet (HFD) (Research Diets, #D12492) or sucrose-matched control diet (SCD) (Research Diets, #D12450J) for 12 weeks. See **Table 2.6** for additional nutrition information for these diets. Animals were permitted food and drink *ad libitum* for the duration of the experiment. Food and cages were replaced and cleaned weekly by animal

technicians. Mice were weighed weekly, and body composition was determined at weeks 1, 6, and 12 of the diet. Post 12 weeks, mice were utilized for tissue collections and wire myograph studies (**Figure 2.4**).

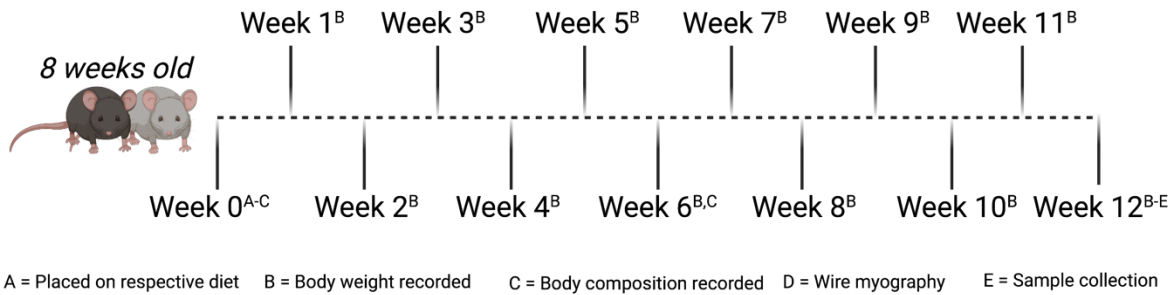


Figure 2.4. Study design for evaluating the effects of global *Rab27a* loss during a 60% high fat diet. Male WT and *Rab27a* null mice were separated into independent housing at 7 weeks old (not shown). At 8 weeks of age, mice were randomly selected to receive either a 60% HFD or SCD for 12 weeks (Week 0-12). Experimental procedures completed at each time point are denoted by superscript numbering: A=placed on respective diet, B=body weight recorded, C=body composition recorded, D=wire myography, E=sample collection. Group sample sizes were WT, HFD (n=4), WT, SCD (n=6), *Rab27a* null, HFD (n=6), and *Rab27a* null, SCD (n=8). Created with BioRender.com.

Table 2.5. Nutritional values for 60% HFD, SCD, chow, and breeder diets.

		Diet			
Class Description	Ingredient	D12492 (60% HFD)	D12450J (SCD)	Teklad #2918 (Chow Diet)	Teklad #2919 (Breeder Diet)
Protein	Casein, Lactic, 30 Mesh	200 g	200 g		
Protein	Cystine, L	3.00 g	3.00 g		
Carbohydrate	Starch (Corn)		506.2 g		
Carbohydrate	Lodex, 10	125 g	125 g		
Carbohydrate	Sucrose (fine granulated)	72.8 g	72.8 g		
Carbohydrate	Unkown	-	-	Est. 2-5%	Est. 2-5%
Fiber	Solka Floc (FCC200)	50.0 g	50.0 g		
Fat	Soybean oil (USP)	25.0 g	25.0 g		
Fat	Lard	245 g	20.0 g		
Mineral	-	50.0 g	50.0 g		
Vitamin	Choline bitartrate	2.00 g	2.00 g		
Vitamin	-	1.00 g	1.00 g		
Total		773.85 g	1055.05 g		

Caloric Information				
Protein	20% Kcal	20% Kcal		
Fat	60% Kcal	10% Kcal	26.2% Kcal	9% Kcal
Carbohydrate	20% Kcal	70% Kcal		
Energy density	5.21 Kcal/g	3.82 Kcal/g		

2.1.10. Body Weight Recording

Mouse body weights were recorded at predetermined timepoints according to individual study design. Myography mice were weighed using a ScoutPro scale and diet mice were weighed using an OHAUS CS series scale.

2.1.11. Body Composition Analysis of Mice From the 60% High Fat Diet Study

Post weighing, mice were individually placed into assay containers and analyzed for fat, free body fluid, and lean body mass (Minispec LF50, Bruker). These results were used in combination with the total body weight to determine % fat and % lean body composition for each mouse. Before each run, a daily machine check and calibration was completed to ensure accuracy of measurements.

2.1.12. Tissue Collection

Mice utilized for tissue collection were anesthetized with isoflurane (Patterson Vet, Cat #07-893-1389) and euthanized via cervical dislocation. Tissues were collected for either freezing at -80°C or fixation with 10% formalin overnight 4°C. Fixed samples were then processed for paraffin embedding, sectioning, and routine histology or immunostaining. Aorta and PVAT samples were collected from the remaining tissue after myograph mounting. The top half of the segment (PVAT and aorta intact) was fixed. For the lower half of the segment, the PVAT and aorta were frozen separately. For iWAT and BAT, one lobe of each was selected for either fixing or freezing. The lymph nodes were removed from male iWAT tissues during collection. Surrounding WAT was cleared from the BAT lobes prior to processing.

2.2. Primary Human Cell Culture

All human PVAT samples were collected under the MaineHealth Institute for Research. Cells were maintained in 6cm cell culture dishes. Human primary vascular smooth muscle cells

(ATCC, Cat# PCS-100-012) were maintained in complete SmGM2 media (Lonza, Cat# cc-3182). Human primary endothelial cells (Lonza, Cat# c-2535) were maintained in complete EGM2 media (Lonza, Cat# cc-3162). Media was changed every 3 days. All cell lines were passaged upon reaching confluency via lifting with 0.25% Trypsin-EDTA (Gibco, Cat# 25200-056). Cell lines were cultured in a humidified incubator with 5% CO₂ and 37°C.

2.3. Wire Myography

2.3.1. Chow Diet Experiments

Murine thoracic aortae were excised at 2mm in length, below the ascending aortic arch, and mounted into the wire myograph organ bath (Danish Myography Technologies A420 and 620M, Denmark). Aortae were bathed in physiological saline solution (PSS, 0.13M NaCl, 4.7mM KCl, 1.18mM KH₂PO₄, 1.17mM MgSO₄·7H₂O, 5.5mM glucose, 0.026mM EDTA, and 1.6mM CaCl₂) at 37°C and oxygenated (95% O₂ + 5% CO₂). PSS was replaced and equilibration under basal conditions with a 5 millinewton (mN) force was completed for 20 minutes¹⁴⁵. Aorta were subsequently treated with increasing concentrations of phenylephrine from 2nM-10µM (Sigma-Aldrich, Cat# P6126) and the maximum contractile force (mN) for each dose was recorded to determine contractile reactivity. Vessels were washed 4 times with fresh PSS buffer and allowed to reach basal force. If basal force was not achieved 20 minutes post wash, additional washes were performed. Vascular relaxation was measured by pre-contracting vessels to 50-80% of peak contraction (EC₅₀) with phenylephrine and then treating with increasing doses of acetylcholine from 2nM-10µM (Sigma-Aldrich, A2661). The minimum contractile force (mN) was recorded for each dose. Again, vessels were brought back to basal force by rinsing as described above. Lastly, vessel integrity was tested by dosing aortae with 100mM potassium chloride (KCl) and maximum contractile force (mN) was recorded at 8 minutes post addition.

2.3.2. 60% High Fat Diet Experiments

Upon completion of 12-week 60% HFD feeding, 2mm segments of the thoracic aortae were excised from below the ascending arch. Segments were mounted into the wire myograph organ bath (Danish Myography Technologies 620M, Denmark) in PSS at 37°C and oxygenated. PSS was replaced and equilibration under basal conditions with a 5mN force was completed for 20 minutes. Segments were then normalized to a force equivalent to blood physiological shearing force (13.3 kPa) to account for difference between aortae luminal area and tensile strength¹⁴⁶. Post normalization, chambers were electronically zeroed. All vessels were treated with a single 100mM dose of KCl as an initiating stimulant. Maximum contractile force (mN) was recorded at 8 minutes post addition. The aortae were then treated with phenylephrine (Phe) and acetylcholine (ACh) as describe above. Vessel integrity was also measured again by a final dose of 100mM KCl with maximum contractile force (mN) measured 8 minutes post addition.

2.3.3. Statistical Analysis

Data were exported from the LabChart 8 Pro DataPad into excel. All curves were normalized to starting forces of 0 mN based on the recorded force at the time of the initiating KCl or Phe dose. Contractile responses are normalized to the baseline corrected peak KCl force and reported as % Maximum Contraction (Relative KCl)¹⁴⁶. Dilative responses are normalized to the 50-80% maximal Phe contractile force are reported as % Pre-Contraction. *Viability Analysis:* Background corrected KCl forces were plotted within an XY sheet according to age and genotype and analyzed for outliers via a ROUT (Q=1%) test. Any detected outlier was removed from all downstream analyses. Data was then transferred to a Grouped sheet according to experimental designation and significance was evaluated via ordinary two-way ANOVA with a Tukey's multiple comparisons test. *Phe and ACh Contractile Response:* Dose responses for each mouse were transposed into XY sheets within GraphPad Prism (Version 9) as replicate columns according to experimental group. The Phe dose concentrations were plotted in Log10

scale. Outlier doses for each mouse was identified utilizing a non-linear regression, log(agonist) vs. response - Variable slope (four parameters) test (Q=1%). For each data set, if seven or more doses were detected as outliers, the mouse was removed from the final analysis. If less than seven doses were detected as outliers, all points are included for future analysis. These points are viewed as biological variations in agonist response. Significance between group responses was determined between two groups at a time, with the variable slope test mentioned above with an Extra sum-of-squares F Test. *EC₅₀ Analysis*: Individual curves were analyzed via Variable slope (four parameters) test (Q=1%) to calculate an EC₅₀ dose for each mouse. These doses were then transposed into a Grouped sheet according to genotype and age to evaluate significance via ordinary two-way ANOVA with a Tuckey's multiple comparisons test. For all analyses, significance is defined as a P<0.05.

2.4. Immunoblot

2.4.1. Protein Isolation and SDS-PAGE

Total protein was isolated from frozen tissues with mechanical grinding in the presence of radioimmunoprecipitation assay (RIPA, 50mM Tris HCl, 5mM EDTA diNa, 150 mM NaCl, 1% IGEPAL CA-630, 0.1% SDS, 1mM EGTA, 0.5% Na Deoxycholate) buffer supplemented with protease inhibitor (CST, #5872). Post grinding, samples were sonicated (Branson Sonifier 250, Branson Ultrasonics) for 10 pulses with 30% power and 25% duty cycle. Samples were incubated on ice for 20 minutes. Sample concentrations were determined by bicinchronic acid (BCA) protein assay with optical density quantified by absorbance with 760 nm wavelength (Epoch) in triplicate. The averaged sample absorbances were normalized to a standard bovine serum albumin (BSA, Calbiochem, Cat #9048-46-8) curve that achieved a $r^2 \geq 0.98$. BCA standard concentrations included 2-fold serial dilutions spanning 0.156-10 mg/mL. Once concentration was calculated, Laemmli buffer (0.4M SDS, 1mM bromophenol blue, 47% v/v glycerol, 12% v/v Tris (0.5M, pH6.8), 21% v/v H₂O) was added and boiled at 95°C for 5 minutes.

Samples were loaded into 12% SDS-PAGE gel (BioRad, Cat #1610175) with equivalent amounts of protein per lane. Specific amounts are noted in the respective figure legends. Loading volumes were normalized using RIPA buffer. Pre-stained protein ladder (7 μ L, Promethues, Cat #83-660) was loaded into lane one for protein size identification. Gels were run with a 90 millivolts (mV) current for 10 minutes to ensure efficient entry into the stacking gel. The electric current was then increased to 120mV for 20 minutes to allow for sufficient separation of proteins. Transfer materials and ethanol (Sigma-Alrich, Cat #DSP-NJ-158) activated PVDF membranes (BioRad, Cat #1704275) were equilibrated in transfer buffer (BioRad, Cat #10026938) for 10 minutes. Proteins were transferred to the membrane utilizing a BioRad Trans-Blot Turbo system using the BioRad 2x mini gel protocol, adjusted to run with a constant amperage (1.5 mA) for 30 minutes. Total protein transferred was evaluated with Ponceau S staining and imaged using a digital camera. Blots were rinsed with PBS supplemented with a few drops of sodium hydroxide (0.1M) to remove the stain, then blocked with 5% milk in PBS-T (PBS with 0.01% Tween-20) at room temperature (RT). Membranes were incubated with the selected primary antibody in 5% milk in PBS-T, rocking for designated times at 4°C. Membranes were washed and incubated with IgG-HRP secondary in 5% milk in PBS-T at RT for 1 hour. Blots were imaged utilizing Immobilon Forte Western HRP Substrate (Millipore, WBLUF0500) and the Azure C600. Antibody information is in **Table 2.7**.

2.4.2. Quantification

Membrane and Ponceau S images were opened in FIJI, converted to 8-bit images, and inverted. Rectangular regions of interest (ROIs) of equivalent areas were placed to encompass sample lanes in the Ponceau S image and the pixel density (Raw Integrated Density) value was recorded for each lane. The same process was used for the membrane images around the band of interest. Equivalent ROIs just above the bands were quantified for pixel density to determine the background intensity for each lane. Band intensity was corrected for background noise and

normalized to total protein transfer via Ponceau S stain. Bands were normalized to the average intensity for the male group. Significance was determined via Welch's t-test.

2.5. Immunofluorescence

2.5.1. Staining

Paraffin embedded tissues were sectioned at 5µm, dried at RT overnight. The following morning slides were heated (Globe Scientific Inc., Cat #1358W) for 45 minutes at 60°C. Samples were incubated in AmeriClear (CardinalHealth, Cat #C4200-1) for 15 minutes at RT three times and subsequently treated with dehydrating alcohol (VWR, Cat #10158-870) twice at 100%, 95%, 90%, and 75% (v/v) for 2 minutes. Antigen retrieval was completed using sodium citrate (0.1M) for 25 minutes utilizing a steamer. After cooling on wet ice, slides were blocked for overnight in blocking solution (PBS with 1% bovine serum albumin (BSA) (Calbiochem, Cat #9048-46-8), 5% goat serum (Jackson ImmunoResearch, Cat #005-000-121), and 0.5% Tween-20 (Sigma-Aldrich, Cat #P1379-1L)) at RT. Slides were washed three times for 15 minutes, shaking at RT with 1x tris-buffered saline (TBS, 50mM Tris-Cl, pH 7.6, and 150mM NaCl). Samples were incubated at 4°C overnight with primary antibody or appropriate IgG control at matching final concentrations in PBS + 2% BSA. Post incubation, slides were washed three times for 15 minutes shaking at RT in TBS-T (TBS with 0.1% Tween-20). Samples were subsequently incubated at RT for 1 hour with appropriate Alexa-Fluor conjugated secondary antibodies in PBS + 2% BSA. Sections were washed and treated with TrueVIEW Autofluorescence Quenching Kit (Vector Laboratories, SP-8400). Slides were washed and liquid mounted with DAPI mounting media (Vector Laboratories, H-2000). Sections were imaged with a Leica TCS SP8 laser scanning confocal microscope with a 63x/1.40 NA oil objective and the Leica SX software suit. Representative images were captured utilizing a single z-plane. Probe color balance was normalized across all images to respective IgG controls utilizing FIJI. DAPI color balance was adjusted to relative intensity across images.

2.5.2. Quantification

All images were opened using FIJI with each fluorescent channel displayed separately. Total DAPI were quantified for each field of view utilizing the CellCounter plugin. Pixel intensity was quantified according to Raw Integrated Intensity values. For aorta images, masks were applied to ensure PVAT within those fields of view were not contributing to raw quantifications. IgG and primary staining intensities were normalized to total number of DAPI counted for each image. Then, the DAPI/background normalized IgG stain intensity was subtracted from the matching DAPI normalized stain intensities. All values were then normalized to the 8-week-old WT sample value for each stain respectively.

Table 2.6. Antibody descriptions. IB = Immunoblot, IF = immunofluorescence

Target antigen	Source	Catalog #	Concentration (IB)	Concentration (IF)	Lot
RAB27A	Cell Signaling	69295	0.07 µg/mL	0.39 µg/mL	1
PLIN1	Cell Signaling	9349	0.15 µg/mL	N/A	5
ACTA2	Cell Signaling	19245	0.1 µg/mL	0.014 µg/mL	3
PECAM1	Cell Signaling	3528	0.5 µg/mL	N/A	4
MYH6	ThermoFisher	22281-1-AP	N/A	1.6 µg/nL	00101202
Rabbit IgG	Cell Signaling	3900	N/A	matched	50
HRP anti-rabbit	Cell Signaling	7074	0.066 µg/mL	N/A	28
HRP-anti-mouse	Cell Signaling	7076	0.15 µg/mL	N/A	32
Alexa-Fluor 488 anti-rabbit	Invitrogen	A11008	N/A	2 µg/mL	2256822

2.6. Mass Spectrometry

All samples submitted for mass spectrometry were prepared for data acquisition and analysis by the MaineHealth Institute for Research Proteomic and Lipidomic Core Facility. The protocols for data acquisition and analysis were provided by the Core in accordance with their operational procedures.

2.6.1. Data Acquisition: Tissues

A minimum of 20mg of iWAT and BAT was utilized from three mice from each experimental group based on age and genotype. Due to limited tissue, PVAT and thoracic aorta samples were pooled according to experimental group for a minimum 8mg tissue from the same mice that the iWAT and BAT samples were isolated from. Tissue samples were suspended in 400 μ L 8M urea/ 50mM Tris-HCl (pH 8) with phosphatase and protease inhibitors (Roche), then sonicated (Branson Sonifier 250, Branson Ultrasonics) three times for 30% power, 25% duty cycle, for 10 second pulses, and rested on ice as described^{15,147}. Lysates were reduced for 30 minutes with 8mM dithiothreitol (DTT) and alkylated for 30 minutes with 20mM iodoacetamide at RT. The 8M urea solution was diluted with 50mM Tris-HCl (pH 8), bringing the solution below 1.5M urea. Samples were digested overnight with 20 μ g sequencing grade trypsin (Promega, MS grade). Approximately 30 μ g of each sample was freed of salts and buffers via C18 spin columns (ThermoFisher, 89870) and evaporated on a centrifugal evaporator. Tryptic peptides were re-suspended in 5% formic acid in 3% acetonitrile in LC-MS grade water. Tryptic digests were run on a high resolution Sciex Triple time-of-flight (ToF) 5600 mass spectrometer connected to a Dionex Ultimate (RSLC_3000) chromatography system. Each sample was loaded onto an analytical reverse-phase C18 nanocolumn packed with Reprosil Pur C18, 1.9 μ m and resolved by an increasing acetonitrile gradient over 100 minutes at a flow rate of 220nL/minute. The mass spectrometer was operated using data dependent analysis (DDA) to create a spectral ion library. A Sequential Window Acquisition of all Theoretical spectra

(SWATH) was implemented for relative quantitation, as previously described^{15,148}. All data acquired in DDA mode used a high-resolution MS scan prior to MS/MS analysis using collision induced dissociation. For SWATH acquisition, a ToF MS scan with an accumulation time of 96 milliseconds was followed by 100 variable-width scan windows from 350 to 1500 m/z. Accumulation time was 89.9 milliseconds, cycle time 9.1 seconds. Identical chromatography parameters were used for SWATH and DDA analysis.

2.6.2. Exosome Sample Preparation

Exosome suspensions were diluted 10-fold with ice-cold RIPA buffer (Millipore Sigma) and the solutions subject to probe-tip sonication (Branson Ultrasonifier 250), at 25% duty cycle and 30% output power for 10 bursts. Debris in each sample was then pelleted at 4°C and maximal velocity on a tabletop centrifuge for 10 minutes. Supernatants were separated and pellets, if present, discarded. Protein content was not measured due to the expected low amounts expected from exosome samples. Each supernatant was precipitated with a 10-fold excess volume of ice-cold ethanol overnight and overlays discarded. Samples were then resuspended in 8.0 M urea (MP Biomedicals) and 5 mM tris-(2-carboxyethyl) phosphine (TCEP, Strem Chemicals) in 50-100 mM ammonium bicarbonate (ABC, MP Biomedicals). After incubation for 20 minutes at 55°C, samples were allowed to cool to room temperature and brought to 10 mM iodoacetamide (G-Biosciences, St. Louis, MO) from a 0.5 M stock solution prepared in water. After incubation in the dark at room temperature for 20 minutes, reactions were quenched with the addition of 1µL β-mercaptoethanol (BME, Sigma-Aldrich). Samples were diluted with 50 mM ABC containing 1.0 mM CaCl₂ to bring urea concentrations below 1.5 M. To each was added a 2.5 µg trypsin (Sequencing grade, modified, Promega Co, Madison, WI). Digestion was carried out overnight at 37°C.

Digested proteins were evaporated on a centrifugal evaporator (Savant, Thermo Fisher

Scientific) and each sample freed from salts and buffers by solid-phase extraction on C18 resin using cartridges prepared in-house. Briefly, for each sample a C18 StageTip was prepared as originally reported¹⁴⁹. To each tip, 4 mg octadecyl-derivatized silica (SiliaSphere PC, C18 monomeric, 25 µm particles, 90 Å pore size, SiliCycle Inc., Québec City, Canada) was added and suspended in LC-MS-grade isopropanol (Honeywell, Morris Plains, NJ). Each cartridge was then equilibrated, and samples purified on them according to the StageTip protocol referenced above. From each cartridge, the eluted purified peptides were transferred into autosampler vials to be used on the LC-MS instrumentation and solvent removed by vacuum centrifugation. Each sample was then resuspended in a volume of Sample Load Solvent to yield an approximate concentration of 1 µg/µL peptides. Sample Load Solvent was 5% formic acid (Optima grade, Thermo Fisher Scientific) and 4% acetonitrile (both water and acetonitrile were LC-MS-grade, Honeywell).

2.6.3. Data Acquisition: Exosomes

All sample separations performed in tandem with mass spectrometric analysis were performed on an Eksigent NanoLC 425 nano-UPLC System (Sciex, Framingham, MA) in direct-injection mode with a 3 µL sample loop. Fractionation was performed on a reverse-phase nano HPLC column prepared in-house (ReproSil-Pur C18-AQ, 5 µm particles, 120 Å pore size, Dr. Maisch, Ammerbuch, Germany, 50 µM ID × 20 cm length) held at 45°C and a flow rate of 300 nL/min. Solvents were blended from LC-MS-grade water and acetonitrile (both from Honeywell). Mobile phase A was a 2% acetonitrile solution, while mobile phase B was 100% acetonitrile. Both contained 0.1% formic acid (Optima grade, Thermo Fisher Scientific)

For each analysis, approximately 1 µg of peptides was applied to the column equilibrated at 4% B and loading continued for 12 minutes. The sample loop was then taken out of the flow path and the column washed for 30 seconds at starting conditions. A gradient to 39%

B was executed at constant flow rate over 90 minutes followed by a 3-minute gradient to 90% B. The column was washed for 5 minutes under these conditions before being returned to starting conditions over 2 minutes and re-equilibrated for 10 minutes.

Mass spectrometric analysis was performed in positive mode on a TripleTOF 5600 quadrupole time-of-flight (QTOF) mass spectrometer (Sciex, Framingham, MA) running Analyst software TF 1.8.1. The LC column eluate was directed to the mass spectrometer source through a silica capillary emitter (SilicaTip, 20 μm ID, 10 μm tip ID, New Objective, Littleton, MA) maintained at 2400-2600 V. Nitrogen nebulizer gas was held at 4-6 psi with the curtain gas at 21-25 psi. The source was kept at 150°C.

Data acquisition performed by information-dependent analysis (IDA) was executed under the following conditions: a parent ion scan was acquired over a range of 400-1200 mass units using a 250 msec accumulation time. This was followed by MS/MS scans of the 50 most-intense ions detected in the parent scan, over ranges from 100-1250 mass units. Criteria of a 2+-5+ charge state and of having intensities greater than a 350 counts-per-second (cps) threshold were also required for a candidate ion to be selected for MS/MS. Accumulation times for the MS/MS scans were 20 msec. Rolling collision energies were used according to the equation recommended by the manufacturer. Collision energy spread was not used. After an ion was detected and fragmented, its mass was excluded from subsequent analysis for 15 seconds. Data from 4-6 samples run by IDA was combined and proteins identified to form a single proteome library used for SWATH results analysis (details below).

SWATH analysis was also performed on the 5600 instruments. First, a single parent-ion scan was acquired over a range of 400-1200 mass units using a 250 msec accumulation time. For the remaining experiments, SWATH MS/MS windows of variable widths were generated using a variable window calculator tool available online through Sciex (<https://sciex.com/products/software>). The target number of windows was set to 100 and a minimum window width of 4 Da. Rolling collision energies were used, as well as fragmentation

conditions optimized for ions of a 2+ charge state. SWATH detection parameters were set to a mass range of $m/z = 100-1250$ with accumulation times of 25 msec in the high-sensitivity mode. Each sample was run in triplicate to obtain proper statistical parameters.

2.6.4. Data Analysis

To create a peptide ion library, DDA data were searched against the reviewed mouse UniProt database (37,201 proteins) using ProteinPilot software (Version 5.0.2, Sciex) with the Paragon algorithm. Peptides used for protein identification met a minimum confidence threshold of greater than 99%. Spectral alignment and targeted extraction of SWATH data were performed with the SWATH Processing Micro App in PeakView (Version 2.2.0, Sciex) using the reference DDA ion library. The data was imported into MarkerView (Version 1.2.1, Sciex), where data were most likely ratio normalized. Experimental groups were compared by principle component analysis, and compared for significance using the Fisher's modification of Student's t-test¹⁵⁰.

Table. 2.7. Proteomic data availability.

Description	Source / Repository	Persistent ID / URL
<i>Rab27a</i> null vs WT (two ages) proteomic data	PRoteomics IDentifications Database (PRIDE)	Pending
Exosome Isolations from <i>Rab27a null</i> vs WT (two ages) proteomic data	PRoteomics IDentifications Database (PRIDE)	Pending

2.7. STRING Analysis of Tissue Samples

Comparisons of experimental group SWATH results were completed utilizing the publicly available STRING bioinformatics analysis program^{151,152}. SWATH protein comparisons lists were filtered for fold changes of at least 20% with a significance of $P \leq 0.05$. Protein comparisons meeting these criteria were submitted for STRING analysis under the following parameters: full

STRING network, meaning of network edges – evidence, minimum required interaction score – 0.900, and hiding all disconnected nodes. Results for the Mammalian Phenotype Ontology (Monarch) databases were filtered for a strength of 1 and a false discovery rate (FDR) with $P \leq 0.05$. The remaining enrichment terms and directionality of targets within those terms were visualized utilizing R and the ggplot2 and ComplexHeatmap packages.

2.8. Histological Staining

All samples submitted for histological staining were paraffin embedded and prepared by the MaineHealth Institute for Research Histopathology Core Facility. The protocols for listed under this section were provided by the Core in accordance with their operational procedures.

2.8.1. Hematoxylin and Eosin

Paraffin blocks containing PVAT/Aorta, BAT, and iWAT tissues were sectioned and stained by the MHIR Histopathology Core facility as follows¹⁵³.

Deparaffinization-Rehydration: Sections were cut at 5 μ m thickness and incubated at RT in Clear-Rite3 (Eprelia, Cat #6915) for 10 minutes, 3 times. Slides were transferred to incubate at RT in 100% ethyl alcohol for 2 minutes, 2 times. Slides were then incubated in 95% ethyl alcohol for 1 minute. Slides were rinsed with water for 5 minutes. At each change, every slide was dipped in the solution 10-20 times. Between changes, slides were dripped dry. *Staining:* Slides were incubated at RT in Hematoxylin (Richard Alan, Cat #7231) for 5 minutes. Post incubation, slides were rinsed clear with water then placed in 5% acetic acid for 1 minute. Post washing with water, slides were incubated for 2 minutes in Bluing Agent (Richard Alan, Cat #7301). Following a wash, slides were transferred to ethanol for 1 minute. Slides were incubated in Eosin Y (Richard Alan, Cat #711) for 2 minutes. Slides were then rinsed in 95% ethanol for 30 seconds, two times. *Dehydrating:* Slides were incubated 3 times in 100% ethanol and followed by 3 incubations in clear agent, 1 time for 3 minutes and the rest 2 minutes.

Coverslip Mounting: Slides were mounted with a coverslip using Permount Mounting Medium (Fisher Chemical, Cat #SP15-100) and allowed to dry for 48 hours. Resulting color stains are nuclei = blue, cytoplasm/structures = pink, and erythrocytes, collages, muscle cytoplasm = shades of pink.

2.8.2. Mason's Trichrome

Paraffin blocks containing PVAT/aorta tissue samples were sectioned and stained by the MaineHealth Institute for Research Histopathology Core as follows¹⁵³.

Deparaffinization-Rehydration: Sections were cut at 5 μ m thickness and incubated at RT in Clear-Rite3 (Eprexia, Cat #6915) for 10 minutes, 3 times. Slides were incubated at RT in 100% ethyl alcohol for 2 minutes, 2 times. Slides were then incubated in 95% ethyl alcohol for 1 minute and then rinsed with water for 5 minutes. At each change, every slide was dipped in the solution 10-20 times. Between changes, slides were allowed to drip dry. *Staining:* Slides were placed in an uncovered coplin jar filled with 40 mL of Bouin's fixative (NewcomerSupply, Cat #1020A) for 30 seconds. Slides were then incubated in heated solution for 20 minutes on the bench. Slides were washed until water ran clear. Sections were then incubated for 10 minutes in Weigert's Hematoxylin. Post incubation, slides were washed for 10 minutes under running water. Slides were transferred for Biebrich's Scarlet-Acid Fuchsin solution for 10 minutes and subsequently washed with running water. Following washes, slides were incubated for 10 minutes in phosphotungstic/phosphomolybdic acid solution. Post incubation slides were transferred directly to incubate for 10 minutes in Aniline Blue (2.5% Aniline Blue in glacial acetic acid) solution. Slides were dunked twice in water followed by a 3-5 minute incubation in 1% acetic acid solution. Following a 1 minute wash in water, slides were incubated in 95% ethanol for 1 minute. *Dehydrating:* Slides were incubated 3 times in 100% ethanol and followed by 3 incubations in clear agent, 1 time for 3 minutes and the rest 2 minutes. *Coverslip Mounting:* Slides were mounted with a coverslip using a Permount Mounting Medium (Fisher Chemical,

Cat #SP15-100) and allowed to dry for 48 hours. Resulting color stains are collagen = blue, nuclei = black, muscle tissue = red.

2.8.3. Verhoef

Paraffin blocks containing PVAT/aorta tissue samples were sectioned and stained by our Histopathology Core facility as follows¹⁵³.

Deparaffinization-Rehydration: Sections were cut at 5 μ m thickness and incubated at RT in Clear-Rite3 (Epredia, Cat #6915) for 10 minutes, 3 times. Slides were transferred to incubate at RT in 100% ethyl alcohol for 2 minutes, 2 times. Slides were then incubated in 95% ethyl alcohol for 1 minute. Slides were rinsed with water for 5 minutes. At each change, every slide was dipped in the solution 10-20 times. Between changes, slides were allowed to drip dry.

Staining: Following a rinse with water, slides were incubated in Verhoeff's elastic stain for 1 hour. Slides were rinsed well with water 2 times before undergoing stain differentiation (removal of non-specific staining) with 2% ferric chloride. Slides were again rinsed with water for 2 minutes followed by a counter stain of Van Gieson with a 3-5 minute incubation. Stain differentiation was completed using 95% ethyl alcohol. *Dehydrating:* Slides were incubated 3 times in 100% ethanol and followed by 3 incubations in clear agent, 1 time for 3 minutes and the rest 2 minutes. *Coverslip Mounting:* Slides were mounted with a coverslip using Permount Mounting Medium (Fisher Chemical, Cat #SP15-100) and allowed to dry for 48 hours. Resulting color stains are elastin = black, nuclei = blue/black, collagen/mucus = red, other tissues = yellow.

2.9. Gross Morphological Analyses

2.9.1. Lipid Area Quantification

All images were captured using a Zeiss Axioskop 40 microscope with a Canon EOS 90D attachment. PVAT and BAT sections were imaged with an air Plan-NEOFL 40x/0.7 Ph2

objective. iWAT sections were imaged with an air Plan-NEOFL 20x/0.5 Ph2 objective. Changes in lipid area proportions in fixed PVAT and BAT were determined as previously described¹⁵⁴. Subcutaneous iWAT was quantified similarly, however due to low contrast in tissue borders, tissue area was selected through tracing with a Wacom sketching tablet (Wacom, Intuos⁴) and utilized to create a mask. Damaged areas of tissue were removed from the images or replaced with next closest region that was intact. The mask was then used as described in the original protocol. For all lipid area quantifications, 10 fields of view were analyzed per mouse and averaged together.

2.9.2. Thoracic Aorta Area Quantification

Thoracic aorta sections stained with H&E were imaged on a Zeiss Axioskop 40 microscope with a Canon EOS 90D attachment using an air Plan-NEOFL 20x/0.5 Ph2 objective in segments and stitched together utilizing Photoshop (Adobe Inc., 2022). Global scale based on pixel ratios was set according to a scalebar imaged at equivalent magnification with the same objective. Total area was determined by outlining the external wall of the vessel, luminal area was determined by outlining the internal vessel wall, and medial area was determined by subtracting the luminal area from the total area. Tracing was completed utilizing FIJI and a Wacom sketching pad (Wacom, Intuos⁴).

2.10. Exosome Isolation

2.10.1. Lipid Precipitation

Frozen plasma samples were thawed on wet ice and filtered using a 0.22 μ m spin column (Costar SpinX, Cat #CLS8169) at 10,000 xg for 10 minutes at 4°C (Eppendorf, 5804R) to remove cellular debris. The resulting filtrate was moved to a sterile 1.5mL Eppendorf tube and incubated with 1 μ L of thrombin (Qiagen, miCURY Exosome Kit, Cat #76603) for every 100 μ L of sample for 5 minutes at RT. Sample was again centrifuged at 10,000 xg for 5 minutes at 4°C

(Eppendorf, 5804R). Supernatant was transferred to a new tube and mixed with precipitation buffer (Qiagen, miCURY Exosome Kit, Cat #76603) at a 1:0.4 v/v ratio. The solution was vortexed for 5 seconds according to manufacturer recommendations. All samples were then incubated for 1 hour at 4°C without perturbations. Post incubation, samples were centrifuged at 1,500 xg for 30 minutes at 20°C (Eppendorf, 5804R). Resulting pellets were resuspended in sterile PBS and either analyzed immediately or stored at -20°C.

2.10.2. Ultrafiltration and Size Exclusion Chromatography

Once removed from storage at -80°C, plasma samples were thawed on wet ice and then filtered to remove cellular debris using a 0.22µm spin column (Costar SpinX, Cat #CLS8169) at 10,000 xg for 10 minutes at 4°C (Eppendorf, 5804R). For plasma samples, the effluent volume (~100µL) was then diluted into 5mL of sterile filtered 1x PBS. This dilution was filtered through a primed 100 kDa concentrator column by centrifuging at 4,000x g for 12 minutes at RT (Avanti J-15, Beckman Coulter). The concentrated sample (volume<0.5mL) was brought to 0.5mL utilizing sterile PBS and loaded onto a prepared gravitational size exclusion column (iZon, ICO-35) that had been rinsed with a minimum of 8.5mL of sterile PBS per manufacturer instructions. This resulting 0.5mL fraction was collected and labeled as *0-0.5 mL Sample Volume*. A 1mL volume of sterile PBS was added and the resulting fraction was collected and labeled *0-1mL Buffer Volume*. Another 1mL volume of sterile PBS was added and the resulting fraction was labeled *1-2mL Buffer Volume*. Next, 0.5mL of sterile PBS was added, and the collected fraction was labeled *2-2.5mL Buffer Volume*. Once collected, 4 more 0.5mL fractions will be collected sequentially using sterile PBS to obtain the following sample fractions - *0-0.5mL Concentrated Particle Volume (CPV)*, *0.5-1mL CPV*, *1-1.5mL CPV*, *1.5-2mL CPV*, and *2-2.5mL CPV*. Fractions *2-2.5mL Buffer Volume* through *1.5-2mL CPV* were then pooled and concentrated using another primed 100kDa concentrating column spun as described above (**Figure 2.5**). The final concentrate was brought to a 50µL volume and stored at -80°C overnight or until day of

analysis. The remaining fractions were also frozen for use as negative controls or quality control checks if needed. Columns were then washed with 8.5mL of 0.5M NaOH (Sigma-Aldrich) in PBS, followed by 17mL of sterile filtered PBS prior to isolating the next sample. If being stored, the column was washed and stored in 0.05% sodium azide (Sigma-Aldrich, Cat #58032-25G) in PBS. Preparation, cleaning, and storage of the columns was in accordance with manufacturer instructions.

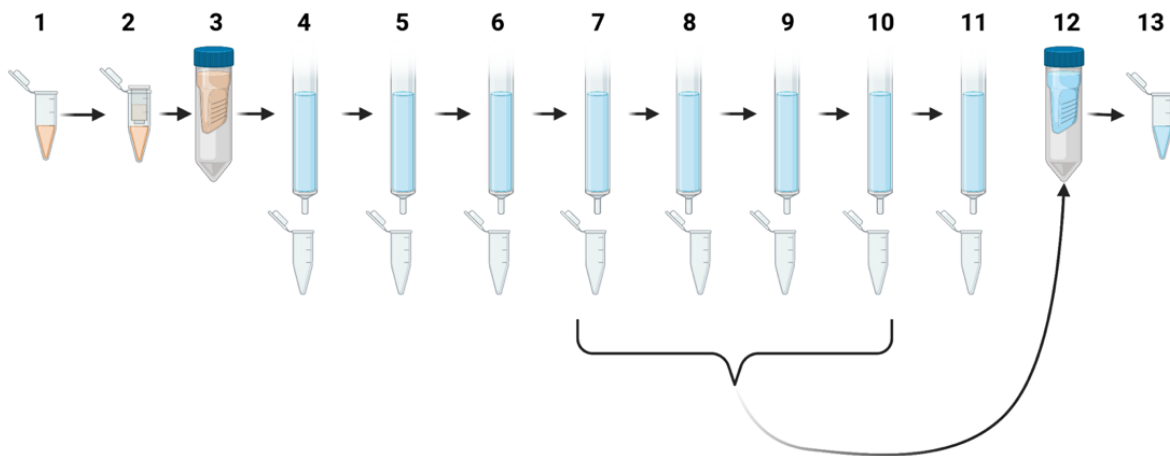


Figure 2.5. Ultrafiltration and size exclusion chromatography-based exosome isolation workflow. 1) Frozen plasma samples were thawed on ice. 2) Samples were filtered through a 0.22µm filter. Then plasma samples were diluted to 5mL and then 3) concentrated using a spin column. 4) The concentrated volume was brought to 0.5mL and loaded onto the prepared size exclusion column. The resulting fraction was collected and labeled 0-0.5mL Sample Buffer. 5) 1mL of PBS was added to the column, collected, and labeled as 0-1mL Buffer Volume. 6) Another 1mL of PBS was added, collected, and labeled as 1-2mL Buffer Volume. Five 0.5mL volumes of PBS were sequentially added and collected as 7) 2-2.5mL Buffer Volume, 8) 0-0.5mL CPV, 9) 0.5-1mL CPV, 10) 1-1.5mL CPV, 11) and 1.5-2mL CPV. 12) Fractions from steps 7-10 are pooled, concentrated to ~50µL and 13) stored at -80°C until analysis. Created with BioRender.com.

2.11. Exosome Analysis

2.11.1. qNano Gold, iZon

System Operation: After the machine was turned on and the iZon software suite was opened, 80µl of sterile diH₂O was added to the bottom fluid cell. The electrode was degassed at RT for 5 minutes. Water was removed using an absorbent wipe and the NP100 pore (iZon) was

attached to the prongs on the bottom fluid cells. Prong distance (stretch) was calibrated using calipers and stretched to 46mm. The upper fluid cell and cap was then assembled. To prime the pore, 80µl of the iZon wetting solution (iZon, TRPS Reagent Kit, #RK3) was loaded into the lower fluid cell and 45µL was dispensed into the upper fluid cell. The pressure nozzle was connected, and maximum vacuum was applied for 4 minutes while clicking the cap 4 times. Maximum pressure was applied for 4 minutes, again while clicking the cap 4 times. Pressure was removed, followed by emptying of the upper fluid cell. After removing the upper fluid cell, the lower fluid cell was washed with 0.22µm filtered PBS. Fresh 80µL of PBS was then loaded and the upper fluid cell reassembled. A maximum vacuum as applied, while clicking the shield 3 times, and allowed to sit for 4 minutes. The vacuum was removed and 35µL of PBS was added to the upper fluid cell and increase the machine voltage was increased to 0.24mV. If the pore was primed correctly, the resulting amperage would fall between 30-60nA. If no change in amperage was observed, the wetting procedure was repeated. Once primed, the voltage until an amperage of 120nA was achieved. A maximum pressure and vacuum were sequentially applied for 4 minutes each. Then the pressure nozzle and PBS was removed and reposed with 45µL of 100 nm calibration particles (iZon, CPC100) at a 1:1000 dilution in PBS. The stretch of the pore and voltage were adjusted to ensure the particles registered at an amplitude of 0.25mA and a flow rate of 200-2,000 particles/minute. Once the machine was calibrated to the particles, analysis of samples was accomplished by loading 45µL volumes of diluted samples in PBS. A minimum of 500 particles per sample was required for proper analysis.

2.11.2. Dual Laser ZetaView, Particle Metrix

System Operation: Analysis of exosome size and concentration was completed using a ZetaView system (Particle Metrix) equipped with a dual laser (480nm and 580nm) system. The system was controlled via the ZetaView Analysis software. Prior to turning on the system, fresh milliQ water was placed within the bottle attached to Pump 1 for the machine to limit bacterial

growth and presence of contaminating particles. Machine initialization was through a program automatic process consisting of 1) flushing the fluid cell with the fresh milliQ water, 2) inspection of cell quality with a minimum rating of “good” being required before progressing. 3) Synthetic polystyrene beads with a 100nm diameter (Applied Microspheres, Cat #75009-03) were diluted at 1:250,000 into 3mL of milliQ water. A 2mL volume of the dilution was loaded into the cell via 1mL sterile syringes. The machine then performed camera 4) auto-alignment and 5) auto-focus using these particles. If desired, 6) auto-symmetry was also checked in preparation for Zeta potential analysis. If Zeta potential was not being analyzed, this step was bypassed. As a control, a fresh region of the sample beads (depressing the syringe a few hundred microliters) was analyzed for a size and concentration control. Once quantified, the system was rinsed with 10mL of fresh, sterile filtered PBS. Isolated samples were diluted 1:100-1000 in the sterile filtered PBS in 3mL final volumes. Samples were loaded as described above and analyzed under the following system settings - Sensitivity=80, Shutter speed=100, Temperature=25°C, Video Recording Speed=Medium. The dilution factor was modified accordingly to ensure that a minimum of ~25 particles were quantified for each of the 11 fields of view. For each analysis, 5 different files were saved: a video recording of each 11 fields of view, a pdf. analysis report, an Excel (Microsoft Office) sheet containing raw data for size and concentration/field of view, an Excel (Microsoft Office) sheet containing raw data for histogram creation, and the raw analysis file formatted for the ZetaView software.

Statistical Analysis: The median diameter (X50) for each sample was recorded according to experimental group in a Grouped sheet format in GraphPad Prism (Version 9) when analyzing across genotype and age according to sex. The median of each experimental group was plotted with the interquartile range. Media was used for analysis to avoid potential skewing due to data that did not adhere to a Gaussian distribution. Significance was determined via an ordinary two-way ANOVA comparison with a Tukey’s multiple comparison test.

Significance was defined as $P \leq 0.05$.

The calculated original concentration (particles/mL) of each isolated sample was normalized to the body weight of the subject it was taken from. Normalization to individual body weight normalized the variability in mass, and therefore amount of tissue capable of producing exosomes at time of plasma collection. Normalized concentrations were then reported in a Grouped sheet format within Prism software when analyzing between genotype and age according to sex. The mean concentration and SEM are displayed, and significance was evaluated using an ordinary two-way ANOVA with a Tukey's multiple comparisons test. Significance was defined as $P \leq 0.05$.

CHAPTER 3:

GLOBAL LOSS OF RAB27A SIGNIFICANTLY ALTERS THORACIC AORTA REACTIVITY

3.1. Overview

RAB27A has been identified as a target of interest due to its role in regulating communication across cells and tissues^{10,155}. An endosomal trafficking protein, RAB27A mediates the trafficking of endosomal compartments to the plasma membrane for the secretion of signaling factors, such as exosomes⁹. Loss of functional RAB27A in humans causes type II Griscelli syndrome, which is classically associated with hypopigmentation and dysregulated immune responses^{133,134}. Furthermore, changes in RAB27A impact the progression of multiple human diseases^{129,156}.

Recently, we showed that RAB27A is expressed in preadipocytes derived from human PVAT, and that suppression of RAB27A expression decreased adipocyte differentiation and lipid storage¹³⁶. Although RAB27A is important in endothelial cell secretion, it has not been well studied in its regulation of vascular physiology¹²⁸. For these reasons, we hypothesized that RAB27A expression is necessary for maintaining vascular homeostasis through the regulation of exosome signaling.

The data presented within Chapter 3 are from a manuscript that was submitted to the American Heart Association journal of Arteriosclerosis, Thrombosis, and Vascular Biology. The manuscript is currently under revision in preparation for resubmission (Soucy et al., 2023, under revision).

3.2. Evaluating RAB27A Association with Human Metabolic and Vascular Phenotypes

Despite the role of RAB27A in multiple human diseases, little has been done to examine whether an association exists between its expression and metabolic and vascular health^{135,156}. For this reason, we set out to determine whether there is evidence for such connections using publicly available human genome wide association studies (GWAS). By using a publicly

available database of human GWAS data, we were able to evaluate whether *RAB27A* variants were statistically associated within a global sample population. This is important due to the global impact of both CVD and obesity.

3.2.1. Rare *RAB27A* Variants Associate with Metabolic Phenotypes

To complete this analysis, the Common Metabolic Disease (CMD) Knowledge Portal was queried for phenotypes associated with common and rare *RAB27A* variants. The CMD Knowledge Portal is a database formulated through federal, private, and academic collaborators and is overseen by the National Institutes of Health (NIH)¹⁵⁷. The database compiles publicly available human GWAS studies to streamline a researcher's process for identifying associations between human metabolic phenotypes and gene variants. These studies have been conducted from multiple countries and include human subjects across a wide demographic population.

Using these data sets, no significant association between common *RAB27A* gene variants and human cardiovascular or metabolic phenotypes. However, body mass index (BMI) was among one of the phenotypes with the lowest significance values (**Figure 3.1A**). Conversely, rare *RAB27A* variants were significantly correlated with increased BMI and glucose sensitivity²⁸ (**Figure 3.1B**). These data suggested that specific *RAB27A* variants may have an impact on human metabolic phenotypes.

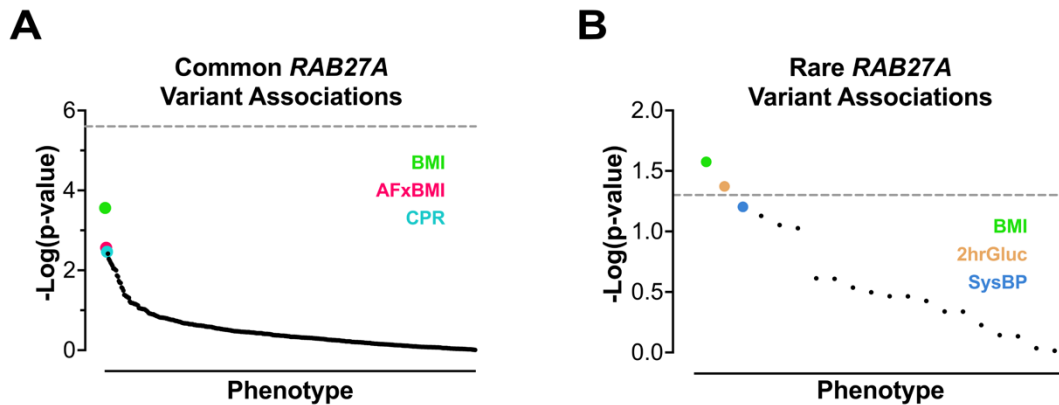


Figure 3.1. Establishing associations between *RAB27A* and metabolic phenotypes. A) The top phenotypes associated with common *RAB27A* gene variants in humans²⁸. BMI = body mass index ($p=0.0003$), AFxBMI = atrial fibrillation-SNP BMI interaction ($p=0.003$), and CRP = plasma C-reactive protein ($p=0.003$). B) The two phenotypes significantly associated with rare *RAB27A* gene variants. BMI ($p=0.027$) and 2-hour glucose levels ($p=0.04$).

3.2.2. Body Mass Index is Significantly Associated with Two *RAB27A* Variants

To understand whether specific *RAB27A* variants are uniquely associated with these two phenotypes, we utilized the CMD knowledge portal to examine the single nucleotide polymorphism (SNP) position of all the known variants²⁹. Only two naturally occurring variants were significantly associated with BMI and were located within intron 1 of *RAB27A* (**Figure 3.2A**). Meanwhile, no variants were significantly associated with two-hour (2hr) circulating glucose levels. However, the variants with the greatest association also aligned within *RAB27A* introns (**Figure 3.2B**). There were also fewer total variants that showed any association with two-hour circulating glucose levels. Therefore, while these data suggest that rare *RAB27A* variants are associated with BMI and glucose tolerance, no single variant appears to be significantly associated with glucose sensitivity.

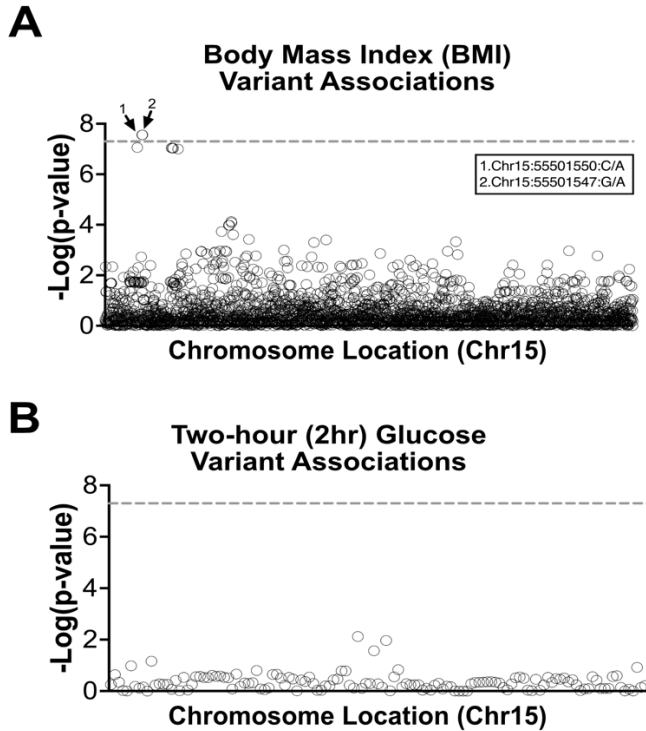


Figure 3.2. Establishing associations between *RAB27A* SNPs and metabolic phenotypes. A) Distribution of single nucleotide polymorphisms comprising the *RAB27A* variants associated with body mass index²⁹. Significantly associated variants are numbered and chromosomal position and the altered nucleotide is noted in the figure key. B) Distribution of single nucleotide polymorphisms comprising the *RAB27A* variants associated with two-hour glucose levels²⁹. Y-intercepts denote significance threshold set by the Common Metabolic Disease Knowledge Portal²⁹. Significance threshold for individual variant associations is $P \leq 5E-8$.

3.3. *RAB27A* is Expressed Within the Human and Mouse Vascular Microenvironment

Next, we aimed to establish that *RAB27A* is expressed with the human and mouse PVAT and aorta to support that this protein has a functional role within this microenvironment. Validation of *RAB27A* expression was critical for our work, as expression had largely been confirmed in the context of RNA expression in WAT and cardiac smooth muscle tissue (Section 1.). Previously, we identified a functional role for *RAB27A* in primary adipocyte progenitor cells isolated from human PVAT¹³⁶. While its mRNA is expressed in human white adipose tissue and cardiac tissue, *RAB27A* has not been well studied within the human or mouse vascular microenvironment¹⁴⁰.

3.3.1. *RAB27A* is Expressed Within Human PVAT, VSMC, and Vascular Endothelial Cells

To build a more comprehensive understanding of the various tissues and cell populations that express *RAB27A* within the human vascular microenvironment, we assessed

RAB27A expression from two human PVAT samples, and two major vascular cell types - smooth muscle cells (VSMC) and endothelial cells (**Figure 3.3A**)¹⁰². PVAT samples were isolated from patients undergoing cardiovascular-related surgery. Due to the availability of primary vascular endothelial and smooth muscle cells, commercially available cell lines were utilized.

The first human PVAT sample (lane 1) did not exhibit expression for perilipin-1 (PLIN1) but did express smooth muscle actin a (ACTA2)^{26,27}. A band for platelet endothelial cell adhesion molecule 1 (PECAM1) was determined to be nonspecific because it was not the appropriate molecular weight of PECAM1²⁵. It is possible that the PVAT tissue was highly vascularized or was isolated with a small portion of aorta that was undetectable during tissue processing, which would explain the difference in marker expressions. Differences in RAB27A band intensities are also present when comparing between the sample types, with the highest expression occurring in the endothelial cells. These results suggest that the different cell types within the vascular microenvironment might respond differently to the loss of RAB27A.

3.3.2. RAB27A Is Expressed Within Mouse PVAT, VSMC, and Vascular Endothelial Cells

Confirmation of RAB27A expression within the mouse vascular microenvironment was obtained using immunofluorescence approaches (**Figure 3.3B**). Similar to the human RAB27A results, the mouse endothelial cells also exhibited the greatest intensity of RAB27A compared to the PVAT and vascular smooth muscle cells. These data suggest that relative RAB27A expression patterns may be comparable between both species. However, more work is needed to directly compare RAB27A expression between humans and mice. Because RAB27A is present in the major cell types comprising the vascular microenvironment, and potentially impacts human adipose-related disease phenotypes, we sought to define its importance in vascular physiology through targeted mutation.

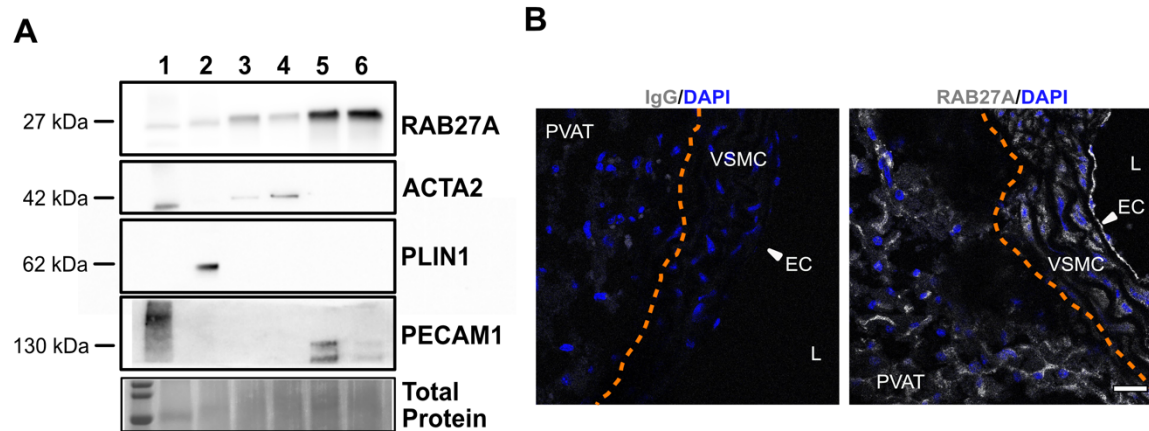


Figure 3.3. RAB27A is expressed in the human and mouse microvascular environment. A) RAB27A expression in human PVAT isolated from two human donors (lanes 1-2), human VSMC (lane 3, passage 2 and lane 4, passage 7), and human endothelial cells (lane 5, passage 4 and lane 6, passage 8). A total of 30 μ g of protein were loaded for each sample. Perilipin 1 (PLIN1) – adipose tissue marker, smooth muscle actin alpha (ACTA2) – VSMC marker, and platelet endothelial cell adhesion molecule (PECAM1) – endothelial cell marker^{26,27}. A non-specific band was detected in the first human PVAT sample, and the upper band in the endothelial cell samples are PECAM1 specific. Two membranes were imaged as only two antibodies could be probed for on a single blot due to expected band sizes. Therefore, RAB27A and PLIN1 were imaged on membrane 1, and ACTA2 and PECAM1 were imaged on membrane 2. A representative region of membrane 2 is provided to show total protein transfer per lane. All membrane sections were imaged on the Azur 600 under normal sensitivity. Exposure length was informed by the automatic detection for the intensities of each probe and are as follows; RAB27A=25 seconds, ACTA2=5 minutes, PLIN1=5 minutes, and PECAM1=5 minutes. B) Representative immunofluorescence images of RAB27a expression in WT mouse PVAT and aorta. DAPI staining was captured using UV laser a power=8%, excitation=405nm, absorbance=430-470nm. Alexa Fluor-488 staining was captured using the laser at power =8%, excitation=488nm, absorbance=500-550nm. Scale bar=20 μ m and is equivalent across images. PVAT=perivascular adipose tissue, VSMC=vascular smooth muscle cell, EC=endothelial cell, L=lumen. Orange dotted line denotes the boundary between the PVAT and aorta.

3.4. Establishment of Novel *Rab27a* Global and Conditional Null Strains

The *ash/ash* strain was the first recorded murine model to have a *Rab27a* null mutation from a spontaneous mutation in a colony of C3H/HeSN mice at The Jackson Laboratory^{138,141}. While other strains have since been established, we present a novel strain that uniquely targets exon 4 of *Rab27a* on a true C57BL/6J background^{142,143}. Utilizing CRISPR-Cas9 technology, we created novel *Rab27a* global and conditional null strains via deletion of exon 4, which is the first

conserved exon among all known *Rab27a* transcripts. *In vitro* validation of the designed sgRNA was performed to identify selectivity in targeting the flanking regions *Rab27a* exon 4 sequence prior to microinjection (**Figure 2.1**).

3.4.1. Establishment of the *Rab27a* Global Null Strain

Single-cell C57BL/6J embryos were injected with a CRISPR-Cas9 complex targeting exon 4 of *Rab27a* for the insertion of a template strand containing *loxP* sequences flanking the endogenous WT *Rab27a* exon 4. Zygotes were transferred to oviducts of pseudo-pregnant Swiss Webster surrogate mothers and carried to term. A mosaic pup was used as a founder and backcrossed to C57BL/6J mice to establish the *Rab27a* global null strain (**Figure 3.4A**). These backcrosses yielded a pup containing a homozygous deletion of exon 4 via non-homologous end-joining, leading to the ashen coat color phenotype (*C57BL/6J-Rab27a^{em10Llw}*, *Rab27a* null), as confirmed through genotyping and sequencing (**Figure 3.4B and C**)¹³⁵.

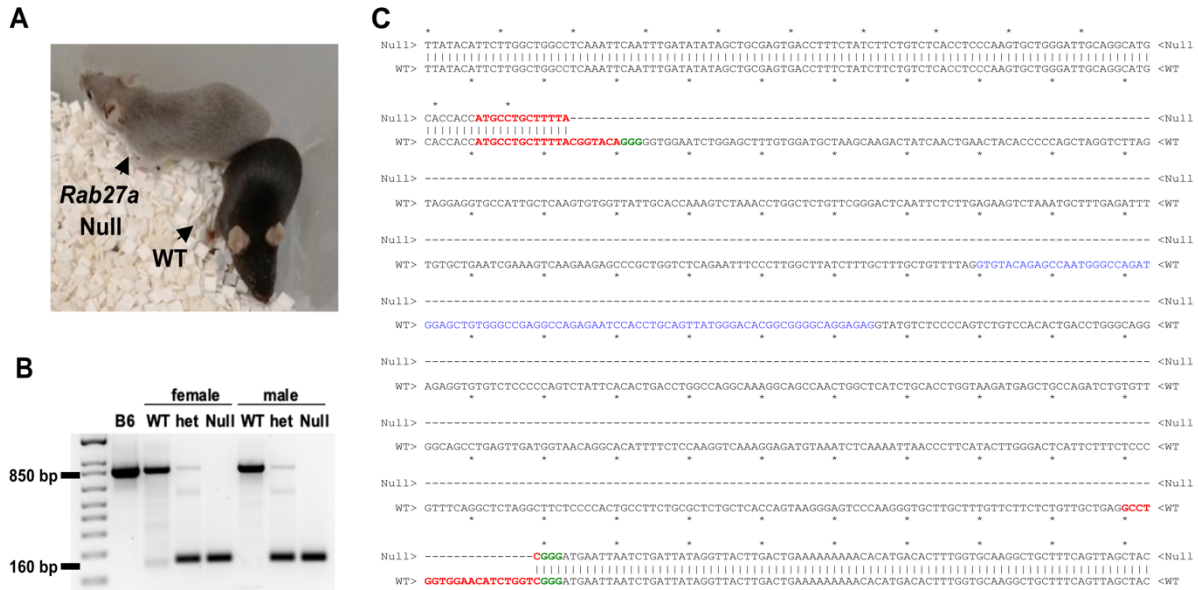


Figure 3.4. Confirmation of *Rab27a* null genotype. A) *Rab27a* null mouse with ashen coat color and a WT littermate. B) Representative genotyping of *Rab27a* null and WT mice compared to a C57BL/6J control. C) Genomic DNA sequencing was completed to confirm deletion of the *Rab27a* exon 4 in the suspected *Rab27a* null mice. Alignments were completed using A plasmid Editor (A.P.E.)³⁷. The deletion was 695 bp in total. Red text indicates single guide target sequence, green text denotes PAM sites, and blue text indicates exon 4 sequence.

3.4.2. Deletion of Exon 4 Results in Loss of RAB27A Expression

Deletion of *Rab27a* exon 4 was predicted to cause a frameshift mutation, resulting in premature termination of transcription. While we provided proof of successful deletion of *Rab27a* exon 4, it was also critical to provide evidence for the loss of RAB27A expression across multiple tissue types. Initial confirmation of RAB27A was completed using immunoblot approaches with PVAT, iWAT, BAT, and gWAT collected from *Rab27a* null and WT controls (Figure 3.5A and B). Lung and spleen tissues were also included as positive controls because they were predicted to express RAB27A (Figure 3.5C)¹⁴⁰. Results showed an absence of RAB27A expression in the *Rab27a* null samples. The heterozygous *Rab27a* null mice showed a decrease in RAB27A expression for all tissues with the exception of iWAT (Figure 3.5A). We then confirmed the loss of RAB27A within the vascular microenvironment using

immunofluorescence approaches. Imaging revealed that *Rab27a* null mice exhibit a near complete loss of RAB27A expression within the PVAT and aorta, including the VSMC and endothelial cells (**Figure 3.5D**).

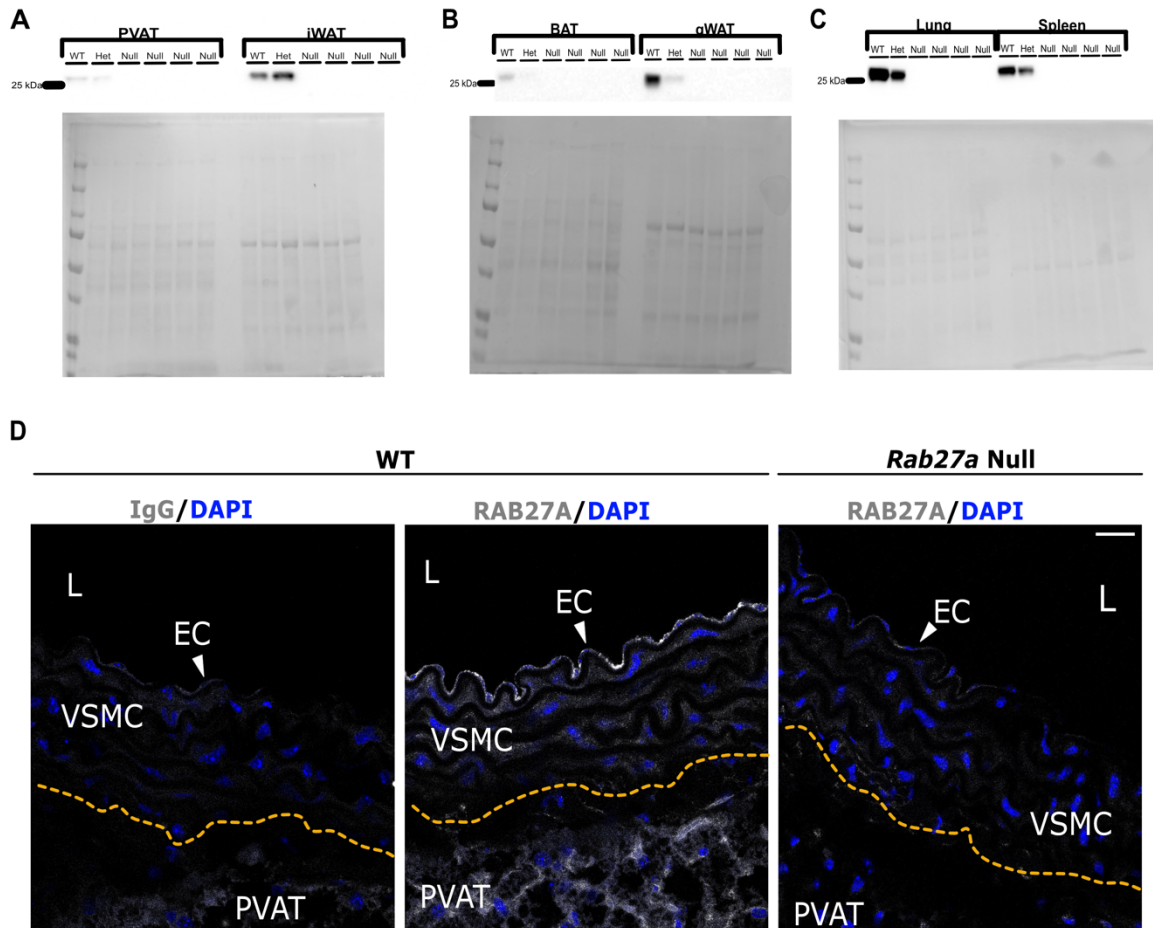


Figure 3.5. Confirmation of RAB27A loss in *Rab27a* null tissues. Immunoblot results for RAB27A expression in A) PVAT and iWAT; B) BAT and gWAT; C) lung and spleen tissues from *Rab27a* (WT) (n=1), *Rab27a*^{+/-} (Het) (n=1), and *Rab27a* null (n=4) mice. A total of 45µg was loaded per lane. Blots were incubated with IgG-HRP anti-rabbit at 1:8,000 dilution. *Rab27a* null mice showed loss of a RAB27A band compared to WT and Het mice. D) Representative images of RAB27A expression in PVAT and aortic VSMC and endothelial cells from WT or *Rab27a* null male mice (n=1/group). DAPI staining was captured using UV laser a power=8%, excitation=405nm, and absorbance=430-450nm. Alexa Fluor-488 staining was captured using a laser power=8%, excitation=488nm, absorbance=500-550nm. Scale bar=20µm and is equivalent across all images. Orange dotted line denotes PVAT and aorta tissue boundaries.

3.4.3. Establishment of the *Rab27a* Conditional Null Strain

A second founder, containing intact *loxP* sites, was also backcrossed to the C57BL/6J strain to establish the conditional *Rab27a* null strain (C57BL/6J-*Rab27a*^{em24Lw}, *Rab27a*^{fl/fl}) (Figure 3.6A). These *Rab27a*^{fl/fl} mice were crossed with Sox2-Cre (B6.Cg-*Edi3*^{Tg(Sox2-cre)}1Amc/J, The Jackson Laboratory) mice on a C57BL/6J background (Table 2.1) for global deletion of the conditional allele. Resulting *Rab27a*^{fl/fl};Sox2-Cre pups exhibited the expected ashen coat color phenotype with the homozygous null genotype (Figure 3.6B and C). To characterize the effects of homologous *Rab27a* mutation on the vascular microenvironment, the *Rab27a* global null strain was further characterized in this study.

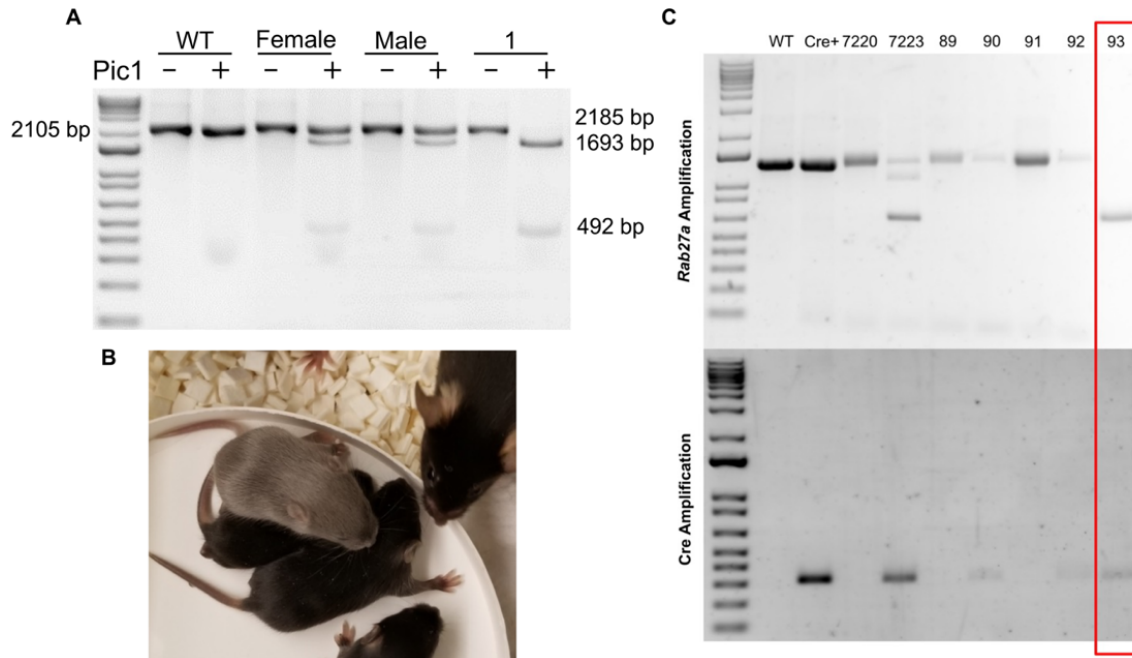


Figure 3.6. *Rab27a*^{fl/fl};Sox-2 Cre mice exhibit an ashen phenotype. A) Restriction digest of PCR products from the *Rab27a*^{fl/fl} strain showing presence of *loxP* sites. Samples were incubated in the digestion buffer with or without PciI. Wildtype = WT, Female = female parent, Male = male parent, 1 = Offspring of the female and male. B) Image of the *Rab27a*^{fl/fl};Sox2-Cre mouse. Due to the constitutive, global expression of Sox2, these mice exhibit an ashen phenotype. C) Genotyping of the litter sown in (B), where pup 93 is the genotyping results for the *Rab27a*^{fl/fl};Sox-2 Cre pup.

3.5. Characterization of the *Rab27a* Null Body Mass and Vascular Microenvironment Morphology

The microvascular environment is a highly dynamic region and is influenced by metabolic changes within the body^{55,158}. PVAT responds to metabolic changes via phenotype switching, that results in morphological changes such as altered lipid accumulation within the tissue^{5,90}. Furthermore, the vasculature modifies medial and luminal areas to aid the stabilization of blood circulation due to changes in metabolic health, vascular injury, and aging^{159,160}. An additional study also showed that the metabolic phenotype of PVAT impacts vessel recovery¹⁶. Because we predict *Rab27a* to be a regulator of the vascular microenvironment physiology, we hypothesized that its loss would lead to a reduction in lipid accumulation and cause changes in aorta vessel area.

3.5.1. Global *Rab27a* Expression is Not Associated with Changes in Body Weight

To characterize this novel *Rab27a* null strain, we evaluated the average body weight of male and female mice at 8 weeks and 20 weeks of age. Male and female *Rab27a* null mice have similar body weights as WT controls at both ages (**Figure 3.7A and B**). As a result, there is no statistically significant association between global *Rab27a* expression and body mass for *Rab27a* null males ($P=0.53$) and females ($P=0.85$). This is in contrast to the data from the CMD Knowledge portal, that associated rare *RAB27A* variants with increased BMI ($\beta=0.065$, $P=0.027$)²⁸. There was, however, a significant association between age and body weight for both *Rab27a* null and WT mice for males ($P<0.0001$) and females ($P<0.0001$). These data therefore suggest that the *Rab27a* null mice gain weight normally on a chow diet.

Often changes in adipose morphology, such as lipid accumulation, indicate altered adipose signaling and metabolic activity^{16,90,136}. Due to the lack of genotype-associated effects on mouse body weight after a chow diet, limited changes in adipose tissue morphology were also expected. However, recent studies suggest that adipose tissues respond heterogeneously

to changes in metabolic states. Therefore, it was possible that PVAT, a relatively small depot, exhibited changes in tissue morphology. For this reason, we sought to understand whether global loss of *Rab27a* impacts adipose tissue morphology by quantifying lipid accumulation in multiple adipose depots¹⁵⁴.

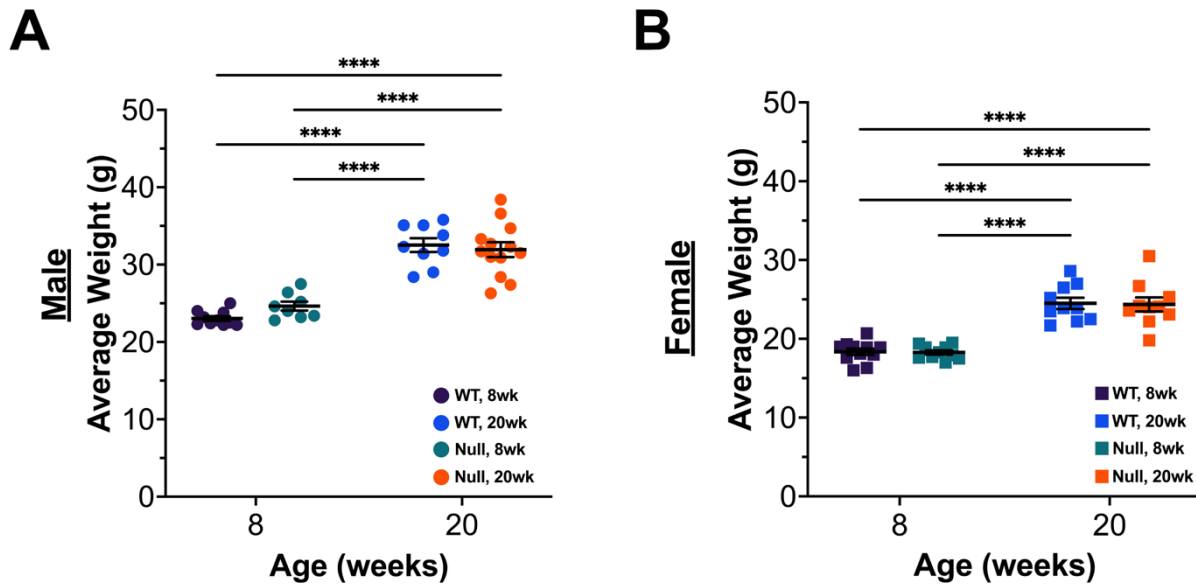


Figure 3.7. Global loss of *Rab27a* does not affect mouse body weight. A) Body weights of WT and *Rab27a* null male mice at 8 or 20 weeks of age ($n \geq 9$ /group). B) Body weights of WT or *Rab27a* null female mice at 8 or 20 weeks of age ($n=9-10$ /group). Bars represent the mean and SEM. A two-way ANOVA with a multiple comparisons test was used to determine significance. ****, $P < 0.0001$.

3.5.2. Global *Rab27a* Expression is Not Associated with Changes in Lipid Accumulation Within Male Mice

A subset of the male *Rab27a* null mice from *Section 3.5.1* were randomly selected for the quantification of lipid accumulation in multiple adipose types. Here, we report no significant changes in the proportion of lipid area in PVAT (**Figure 3.8A**), BAT (**Figure 3.8B**), or iWAT (**Figure 3.8C**) tissues from *Rab27a* null versus WT male mice at either 8 or 20 weeks of age. However, the proportion of lipid area in adipose tissue was significantly associated with age for

PVAT ($P=0.003$), BAT ($P=0.008$), and iWAT ($P=0.009$). It is also important to note that of the three depots examined, PVAT experienced the greatest change in age-associated lipid accumulation in males compared to females (**Figure 3.8A and Figure 3.9A**). These data recapitulate trends from other studies showing that PVAT has a highly dynamic phenotype¹⁰². These findings also corroborate studies in both humans and mice showing that there are sex-dependent differences in adipose tissue expansion and weigh gain^{161,162}.

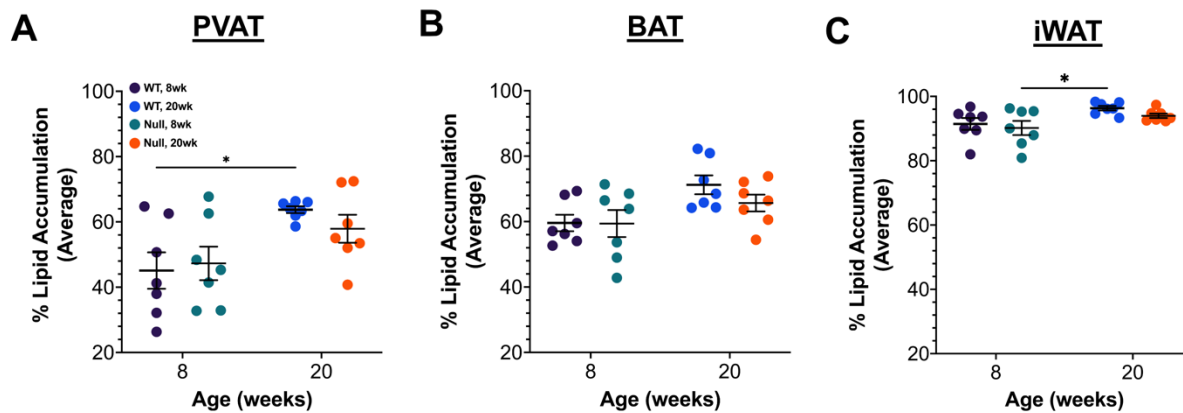


Figure 3.8. Comparison of lipid accumulation between male *Rab27a* null and WT adipose depots. A) Quantification of lipid area proportion within A) PVAT, B) BAT, and C) iWAT of male *Rab27a* null and WT mice at both ages ($n=7$ /group). Bars represent the mean and SEM. A two-way ANOVA with a multiple comparisons test was used to determine significance. *, $P<0.05$. Only significant comparisons are shown.

3.5.3. Global *Rab27a* Expression is Not Associated with Changes in Lipid Accumulation Within Female Mice

Differences in weight gain distributions between sexes have been well established^{161,162}. For this reason, despite an absence of altered lipid accumulation with *Rab27a* null male adipose tissues, we repeated the analysis using female adipose tissues. Here, as with the male data, we found no significant changes in the proportion of lipid area in PVAT (**Figure 3.9A**), BAT (**Figure 3.9B**), or iWAT (**Figure 3.9C**) from *Rab27a* null versus WT female mice at either 8 or 20 weeks of age. Furthermore, the proportion of lipid area in adipose tissue was not significantly associated with age for PVAT ($P=0.9$), BAT ($P=0.67$), and iWAT ($P=0.89$). These finding help to

further corroborate studies in both humans and mice showing that there are sex-dependent differences in adipose tissue expansion and weight gain^{161,162}.

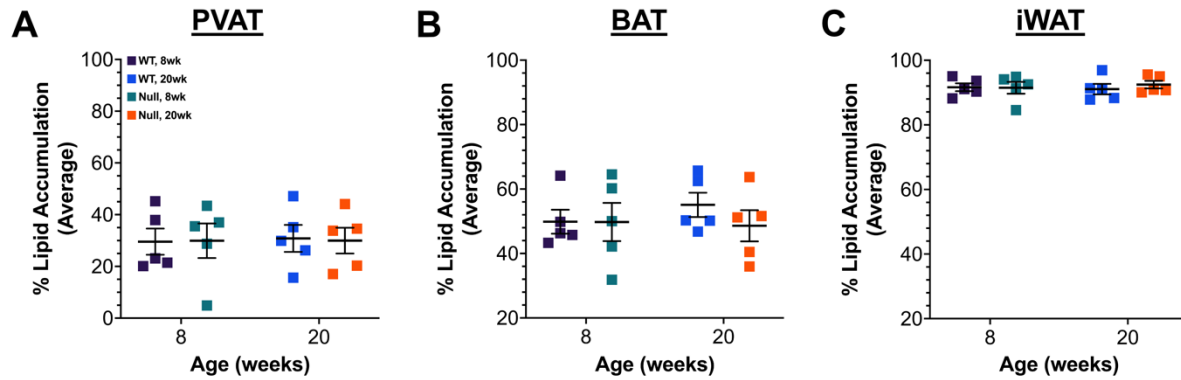


Figure 3.9. Comparison of lipid accumulation between female *Rab27a* null and WT adipose depots. Quantification of lipid area proportion within A) PVAT, B) BAT, and C) iWAT of female *Rab27a* null and WT mice at 8 and 20 weeks of age (n=5/group). Bars represent the mean and SEM. A two-way ANOVA with a multiple comparisons test was used to determine significance. Only significant comparisons are shown.

3.5.4. Global *Rab27a* Expression Does Not Affect the Thoracic Aorta Area of Male Mice

Having shown *RAB27A* to be expressed within mouse VSMCs and vascular endothelial cells, it was possible that global loss of *Rab27a* would alter thoracic aorta gross morphology. As changes in vessel morphology can indicate altered vascular physiology, histological sections of thoracic aortae were analyzed for changes in vessel area^{159,160}. Quantification showed that global loss of *Rab27a* did not affect the gross vascular morphology of male aortae in terms of aorta total (**Figure 3.10A**), medial (**Figure 3.10B**), or luminal (**Figure 3.10C**) area. However, while genotype was not associated with change in vessel area, aging was significantly associated with male aorta total (P=0.0035), medial (P=0.004), and luminal (P=0.01) area. These findings are consistent with a previous study that showed that aorta vessel area increased with age in C57BL/6 mice¹⁶⁰.

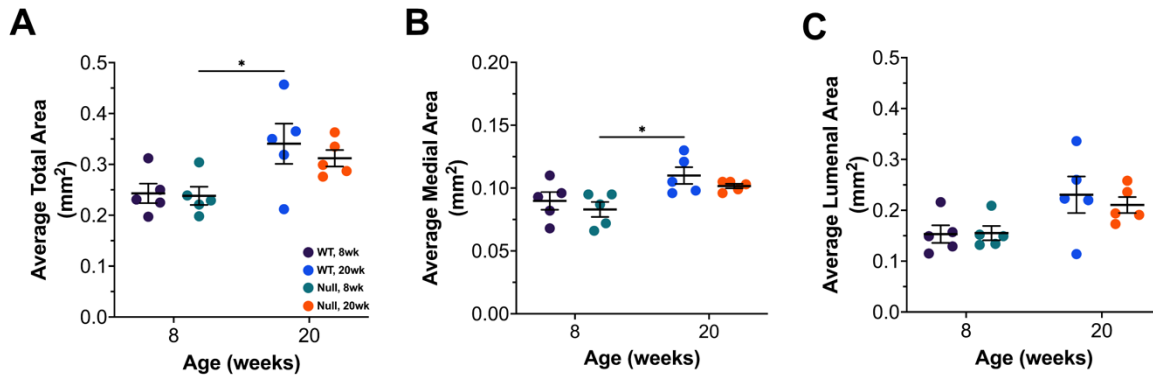


Figure 3.10. Global loss of *Rab27a* does not affect male thoracic aorta morphology. Thoracic aorta quantification of A) total, B) medial, and C) lumenal areas of male *Rab27a* null and WT mice ($n=5/\text{group}$). Bars represent the mean and SEM. Two-way ANOVA with a multiple comparisons test was used to determine significance. *, $P < 0.05$.

3.5.5. Global *Rab27a* Expression Is Not Associated with Changes in the Thoracic Aorta Area of Female Mice

To remain consistent with evaluating sex as a biological variable, thoracic aortae of female mice were also quantified for changes in vessel area. Consistent with the male results, female aortae showed no significant changes in total (**Figure 3.11A**), medial (**Figure 3.11B**), or lumenal (**Figure 3.11C**) areas compared to WT controls (**Figure 3.11**). Furthermore, age was not significantly associated with changes in aorta total ($P=0.22$), medial ($P=0.12$), or lumenal ($P=0.67$) area. This distinction is important as the previously mentioned study was limited to the analysis of male C57BL/6 mice¹⁶⁰. Therefore, these data further support that there are differences in male and female vascular microenvironment physiology.

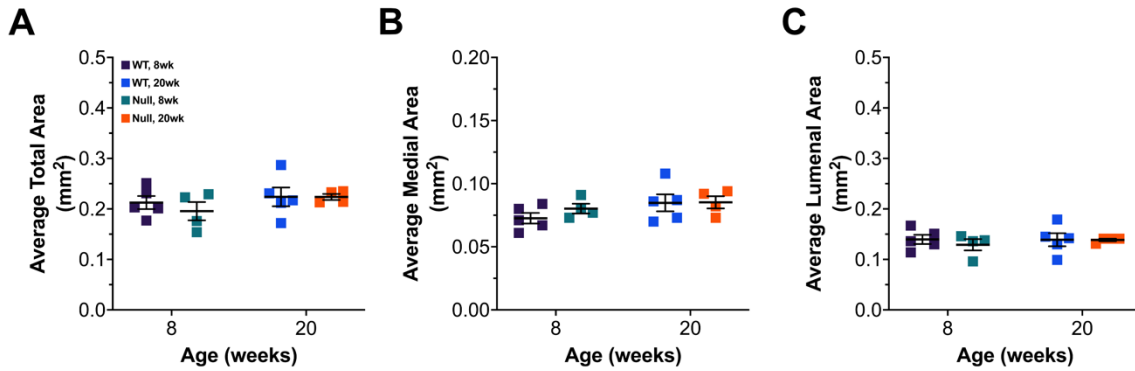


Figure 3.11. Global loss of *Rab27a* does not affect female thoracic aorta morphology. Quantification results of aortic measurements from female mice were A) total area, B) medial area, and C) luminal area ($n=5/\text{group}$). Bars represent the mean and SEM. A two-way ANOVA with a multiple comparisons test was used to determine significance. Only significant comparisons are shown.

3.6. Global Loss of *Rab27a* Alters the Proteomic Signature of the Vascular Microenvironment and Other Adipose Tissues

Due to the lack of *Rab27a* associated changes in body weight and PVAT and aorta morphology, we completed a mass spectrometry study to determine whether the proteomic signatures of *Rab27a* null mice differed from WT controls. For this exploratory study, only tissues from 8- and 20-week-old males were utilized. Modest differences in total number of altered proteins were predicted as *Rab27a* is not involved with transcriptional regulation.

3.6.1. Male *Rab27a* Null PVAT and Aortae Show Unique Patterns of Altered Protein Expression

PVAT and aortae proteomic data showed a relatively symmetrical distribution of upregulated and downregulated proteins at both ages when comparing the *Rab27a* null to WT samples. The total number of altered proteins increased with aging, nearly doubling, in the PVAT (**Figure 3.12A**). However, the total number of altered proteins identified within the aortic tissues remained more consistent across the experimental age groups (**Figure 3.12B**).

By using STRING, protein lists can be queried for enriched associations with biological functions, tissues, and pathways. For this study, enrichment analysis focused on understanding what phenotypes were associated with the significantly altered proteins within our proteomic dataset. Initial enrichment analysis provided lower hierarchical terms and were highly diverse.

To better understand the range of general phenotype associations, the lower hierarchical terms were binned according to upper hierarchical terms. To display enrichment results, the enriched phenotype terms were listed on the y-axis and the number of terms contributing to the parent category are on the x-axis (**Figure 3.13**). The width of each bar displays the relative proportion of the total number of lower hierarchical terms associated with the data set.

Enrichment analysis of the PVAT showed that at both ages, the cardiovascular system phenotype had the greatest number of terms associated and contained the greatest proportion of terms compared to other enriched phenotypes (**Figure 3.13A**). Metabolic and homeostasis phenotypes were also enriched for the *Rab27a* null PVAT compared to WT samples, however not to the same extent as cardiovascular system or other phenotypes. These results therefore suggest that the global loss of *Rab27a* results in the altered expression of proteins that impact the phenotype of the cardiovascular system.

Enrichment results for the aortic tissues from *Rab27a* null mice at 8 weeks of age were also significantly enriched for cardiovascular system phenotypes compared to WT controls (**Figure 3.13B**). Interestingly, for the aorta of *Rab27a* null mice at 20 weeks of age, homeostasis and metabolism had the greatest enrichment. Cardiovascular system phenotypes were the next highly enriched phenotype. These analyses suggest that global loss of *Rab27a* alters the proteomic signature in association with the cardiovascular system and possibly homeostasis and metabolism within the vascular microenvironment.

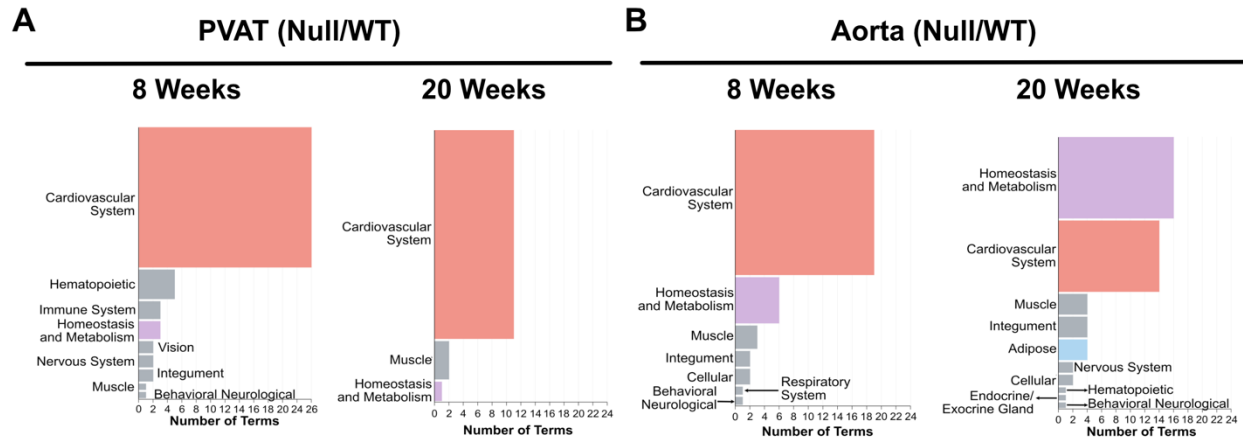


Figure 3.13. PVAT and aortae from *Rab27a* null mice have altered protein signatures associated with cardiac, metabolic, and adipose phenotypes. Phenotype enrichment analysis of significantly altered proteins from the PVAT and aortic tissue of male *Rab27a* null compared to WT control mice at both ages. Most targets were associated with the cardiovascular system, metabolism, and adipose. Bar length indicates the number of phenotypic terms associated with these parent category terms. Bar width indicates the proportion of total proteins associated with each parent term. Colors are coded as follows: cardiovascular system (red); homeostasis and metabolism (purple); adipose-specific (blue); other (gray).

3.6.3. Cardiac and Aortic Phenotypes Populate the Parent Cardiovascular System Enrichment Category

As the cardiovascular system is comprised of multiple anatomical features (*Section 1.1*) it was important to understand whether phenotypes associated with the aorta were enriched within our data set². For this analysis, the same set of protein targets were analyzed for phenotype enrichment according to lower hierarchical associations for phenotypes associated with the cardiovascular system, metabolism, and adipose (**Figure 3.14**). Phenotypes not included under these parent categories were identified as other.

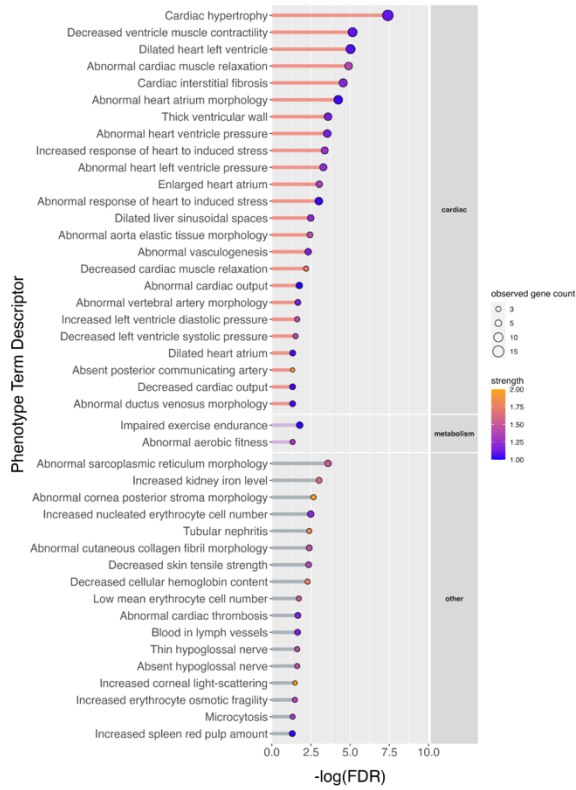
Results from this analysis were displayed using a lollipop chart to provide information regarding the significance of the enrichment, the number of proteins populating each category, and the strength of the associations (**Figure 3.14**). For this analysis, the phenotype terms are displayed on the y-axis. The significance of each phenotype is reported as the $-\log$ of the false

discovery rate ($-\log(\text{FDR})$) on the x-axis and is displayed by the lollipop stem length. The number of genes associated with each term is displayed by the size of the dot on the lollipop. Meanwhile, the color of the lollipop indicates the strength of that association. Strength reports the ratio of (the number of genes from our data set/the total number of genes that are associated with that term) to (the number of randomly selected genes compared/the total number of genes that are associated with that term)^{151,152}. Therefore, a high strength association indicates low probability of a random association is indicated by a yellow-colored dot^{151,152}. A moderate strength association indicates a moderate probability of a random association and is indicated by a purple-colored dot^{151,152}. It is important to also note that results were filtered for a strength >1 prior to analysis.

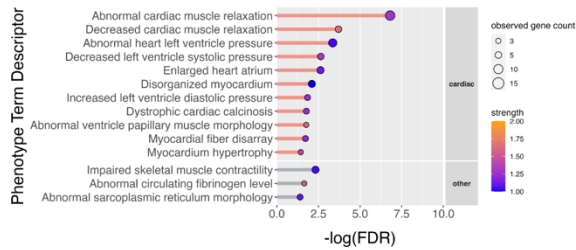
Of the most significantly enriched phenotypes associated with the PVAT from *Rab27a* null vs WT mice at 8 weeks of age, most were associated with cardiac structure and physiology. Some of these phenotypes included *cardiac hypertrophy*, *abnormal cardiac muscle relaxation*, and *cardiac interstitial fibrosis* (**Figure 3.14A**). Very similar phenotype associations were found when comparing the same tissues from mice of 20 weeks of age (**Figure 3.14B**). However, it is important to also note that there was a reduction in total number of associated phenotypes between these experimental group comparisons.

Meanwhile, when applying this analysis approach to the aortic tissues, enriched phenotypes were more closely associated with changes in aorta morphology and physiology. Some examples of these associated phenotypes include *decreased left ventricle systolic pressure*, *abnormal aorta wall morphology*, and *abnormal ascending aorta morphology* (**Figure 3.14C**). These phenotype enrichments were largely preserved in the comparison of aortic tissues from mice at 20 weeks of age (**Figure 3.14D**). With this analysis, there was further evidence that the changes in the proteomic signatures within the microvascular environment are associated not only with cardiovascular phenotypes, but specifically aorta phenotypes as well.

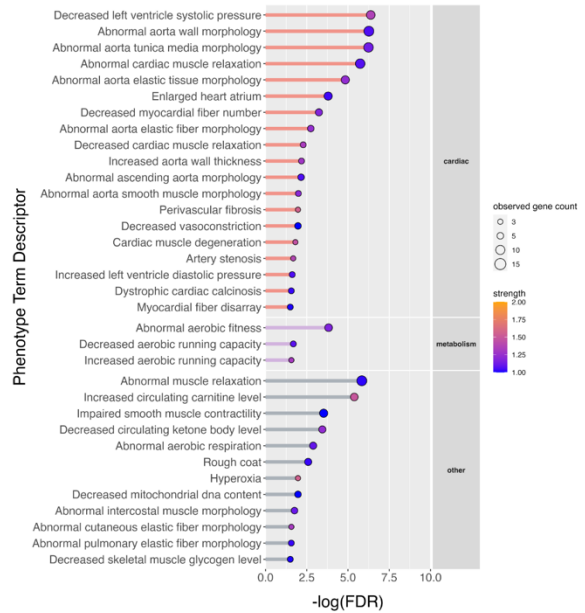
A PVAT-8 weeks, Null to WT
Mammalian Phenotype Ontology



B PVAT-20 weeks, Null to WT
Mammalian Phenotype Ontology



C AO-8 weeks, Null to WT
Mammalian Phenotype Ontology



D AO-20 weeks, Null to WT
Mammalian Phenotype Ontology

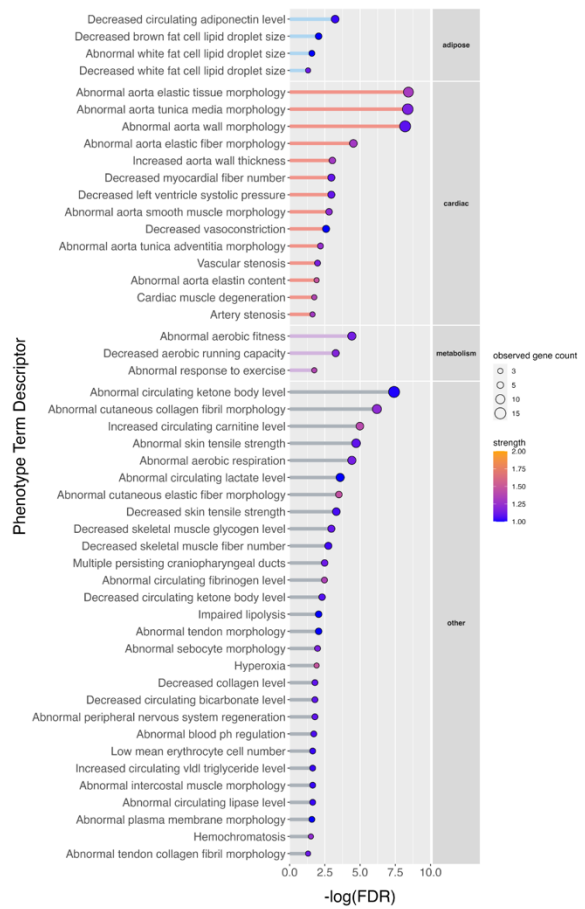


Figure 3.14. PVAT and aortic proteins that are significantly altered by global *Rab27a* loss are enriched for cardiac- and aorta-associated phenotypes. Protein targets meeting the threshold requirements were analyzed for phenotype enrichments for A,B)PVAT and C,D)aortic tissues from *Rab27a* null and WT mice at 8 and 20 weeks of age, respectively. Analyses showed that these proteins were associated largely with cardiac phenotypes in addition to metabolic and adipose phenotypes. For each graph, bar length indicates significance of enrichment by $-\log(\text{FDR})$ and bar color indicates the associated parent phenotype term: adipose (blue), cardiac (red), metabolism (purple), and other (gray). Dot size represents the number of targets associated with each term. Dot color represents the strength of the association.

3.6.4. Consideration of the Enriched Metabolic and Adipose Phenotypes in *Rab27a* Null PVAT and Aorta

The phenotype terms classified under the metabolic category are associated with physical and aerobic fitness (**Figure 3.14**). This is interesting as cardiac health is largely associated to an individual's physical health¹⁶⁸. While this is suggestive that the physical health of these animals may be impacted by global loss of *Rab27a*, we have not completed studies examining for differences in physical abilities. At this time, maintenance of the global *Rab27a* null colony has not revealed observable differences in these animals' physical health compared to WT controls.

Furthermore, unlike the other comparisons, the aortae of 20-week-old *Rab27a* null mice show an association with adipose phenotypes included decreased circulating adiponectin levels, and adipose lipid droplet size (**Figure 3.14D**). Despite this suggested association between *Rab27a* expression and lipid accumulation, we did not observe such changes when we quantified lipid accumulation in multiple types of adipose tissues (**Figure 3.9 and 3.8**). As we have not examined for levels of circulating adiponectin levels, we cannot confirm this association. It is interesting however, due to the importance of adiponectin's role in the maintenance of VSMC physiology (*Section 1.8.3*)¹⁰⁹.

3.6.5. Proteins Contributing to the Enrichment of Cardiovascular Phenotypes Exhibit Three Expression Patterns with Aging

The initial phenotype enrichment analyses were completed independently of the direction of expression for proteins meeting the thresholding criteria. Therefore, heatmaps were generated to determine how the expression of proteins contributing to the enrichment of cardiovascular phenotypes were different between the 8- and 20-week-old experimental groups. The proteins utilized for these plots were limited to those conserved across both age groups as the major focus was to understand how expression changes between *Rab27a* null and WT mice with age.

Heatmaps showed that the proteins that populated these cardiovascular-associated phenotypes largely fit into three expression categories when comparing PVAT and aorta *Rab27a* null to WT tissues: upregulated at both ages, upregulated at 8-weeks-old then downregulated at 20-weeks-old, and downregulated at both ages (**Figure 3.15**). Proteins that exhibited conserved upregulation in PVAT, when comparing *Rab27a* null to WT age groups, are known components of the extracellular matrix (CO1A1, CO1A2, CO3A1, and FINC) (**Figure 3.15A**)¹⁶⁹⁻¹⁷¹. Meanwhile, proteins that exhibited increased downregulation between ages are largely associated with contractile roles (MYH6, MLRA, and TNNTs)¹⁷²⁻¹⁷⁴. However, ACTA2, also a regulator of VMSC contraction, was overexpressed in the PVAT of 8-week-old *Rab27a* null mice and then downregulated at 20 weeks of age¹⁷⁵. Comparisons within the aorta also showed a consistent downregulation of contractile proteins (MYH6, ACTA2, and MYH11) (**Figure 3.15B**)^{27,172}. It was predicted that these changes were indicative a compensation of the extracellular matrix for reduced contractile ability in the aorta.

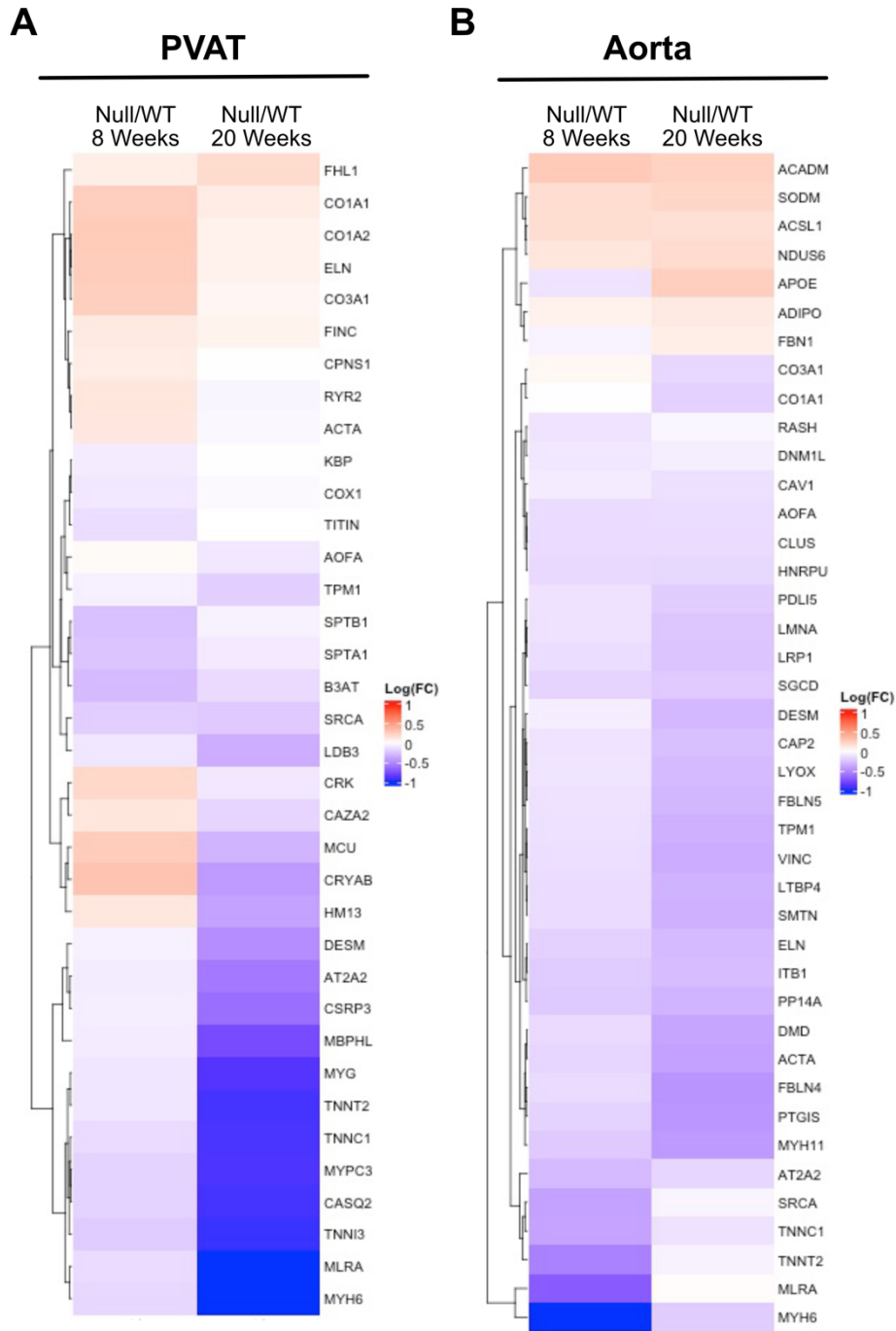


Figure 3.15. Comparisons of changes in fold change directionality of proteins associated with the cardiovascular system phenotype in PVAT and aortic tissue. Heatmaps displaying directional changes of proteins conserved between the 8 week and 20 week timepoints within A) PVAT and B) aortic tissues that populate the cardiovascular system phenotype (Figure 4.13). Directionality for changes in expression are reported as log(FC). Red indicates an upregulation of expression in *Rab27a* null tissues compared to WT controls. Blue indicates a downregulation of expression in *Rab27a* null tissues compared to WT controls.

3.6.5.1. *Rab27a* Null PVAT and Aortae Showed Normal Elastin and Collagen Morphology

Many of the phenotypes associated with the proteomic changes in the *Rab27a* null PVAT and aortic tissues were associated with altered aortic elastin morphology, abnormal stenosis, and aortic morphology (**Figure 3.15**). To further examine whether morphological changes occurred in the *Rab27a* null mice, aside from the analyses conducted in *Section 3.5*, paraffin embedded intact PVAT and aortic tissues were subjected to Verhoef and trichrome staining. *Rab27a* null elastin morphology did not visibly differ from WT controls at either time point either in elastin intensity or misalignment in the vascular smooth muscle cells (**Figure 3.16**). These results were also observed when examining the aortic wall with trichrome staining. Furthermore, no differences were qualitatively observed when examining the PVAT samples for collagen using the same trichrome staining. The absence of morphological changes in the PVAT and aortic tissues of *Rab27a* null mice, despite the evidence provided by proteomic analysis, suggests that different changes are occurring within the vascular microenvironment than what can be detected by gross morphological analysis techniques.

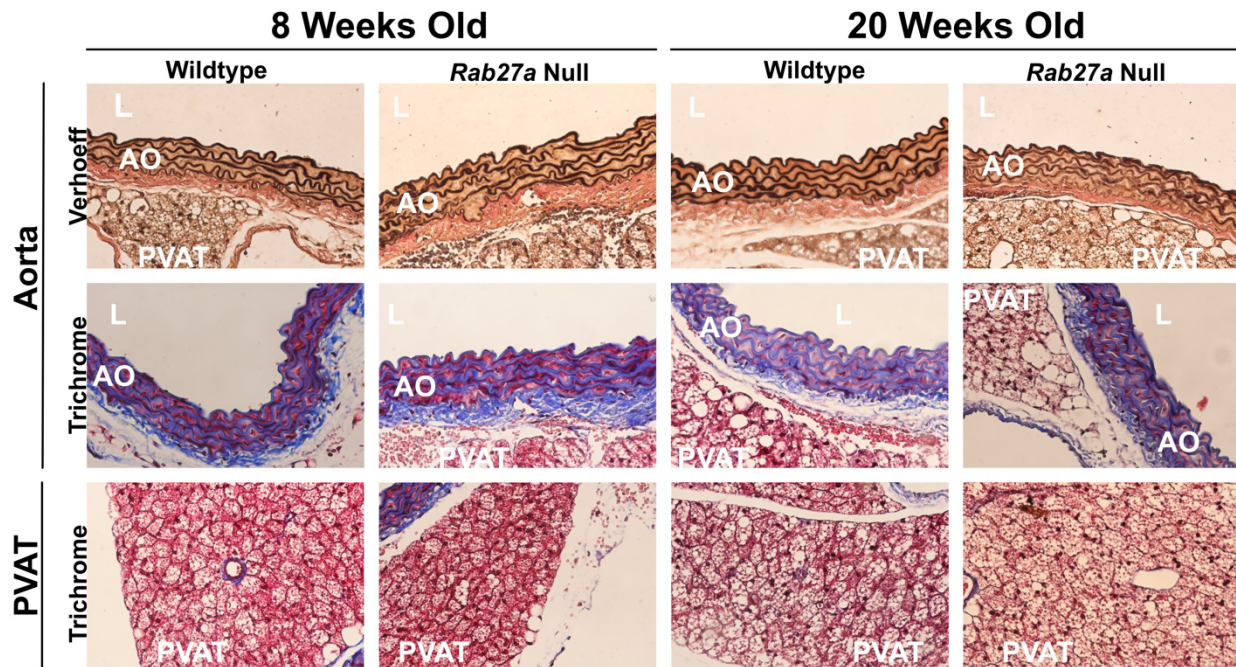


Figure 3.16. Verhoeff and trichrome staining remain comparable between *Rab27a* null and WT male tissues. Representative images of PVAT and aorta tissue cross sections. *Top)* Verhoeff staining for elastin within the aortic wall. *Middle)* Trichrome staining for collagen in the aorta wall. *Bottom)* Trichrome staining for collagen in PVAT. All images were captured using air Plan-NEOFL 40x/0.7 Ph2 objective on a Zeiss Axioskop 40 microscope with a Canon EOS 90D attachment.

3.6.5.2. Decreased Expression of ACTA2 and MYH6 are Confirmed via Immunofluorescence Microscopy

Due to the lack of morphological changes within the vascular microenvironment, despite the result from our mass spectrometry analysis, we sought to validate the changes in expression for select contractile proteins. Utilizing immunofluorescence approaches, we confirmed that expression of ACTA2, a contractile marker, was decreased in an 8-week-old (41% reduction) and 20-week-old (56% reduction) *Rab27a* null aorta compared with age-matched controls (n=1/group). Validation was also completed for MYH6 expression in the aortae of an 8-week-old (50% decrease) and a 20-week-old (16.6% increase) *Rab27a* null mouse compared to an age-matched WT control (n=1/group, **Figure 3.17A**). Validation for the

downregulation of MYH6 in PVAT was also confirmed in an 8-week-old (47% decrease) and 20-week-old (60% decrease) *Rab27a* null aortae compared to the WT control (n=1/group, **Figure 3.17B**). These data suggest that global loss of *Rab27a* uniquely alters the proteomic signature of the vascular microenvironment in a manner associated with cardiovascular and metabolically associated phenotypes.

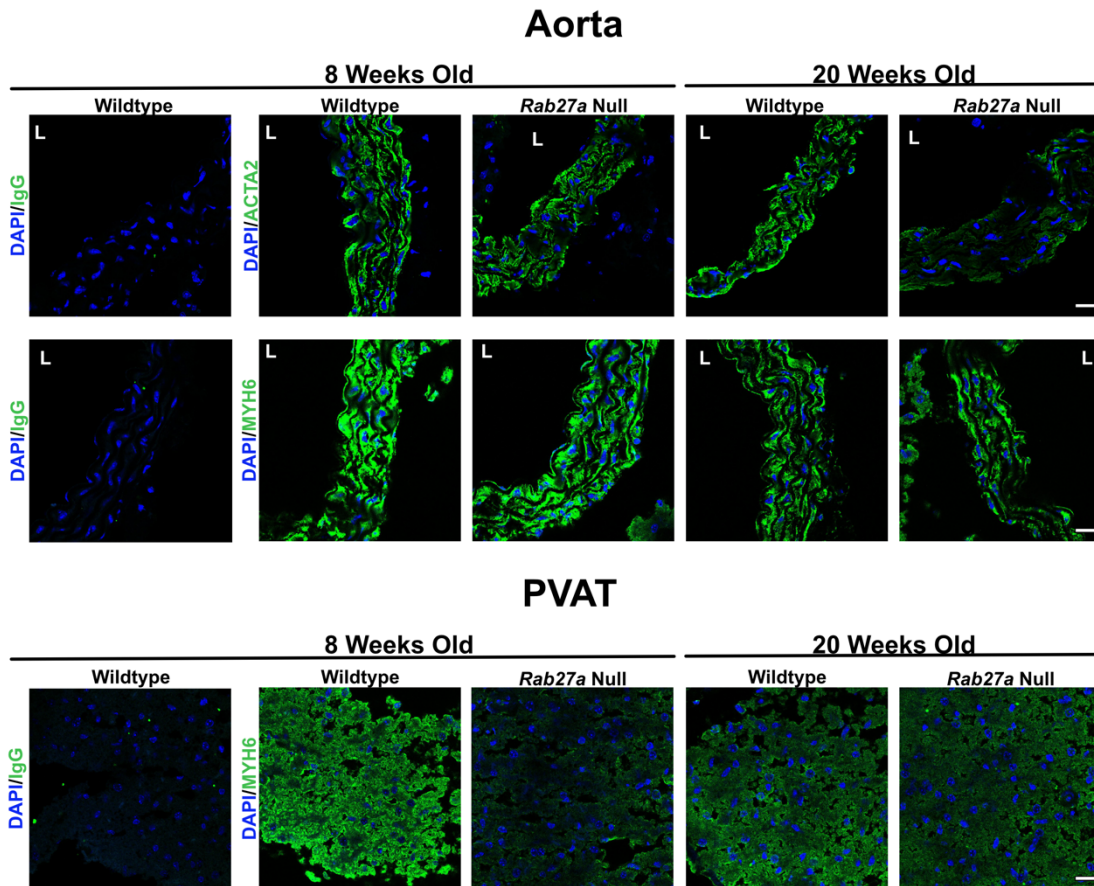


Figure 3.17. *Rab27a* null males exhibit a reduced expression of contractile proteins ACTA2 and MYH6. A) Representative images from immunofluorescence staining for ACTA2 and MYH6 in fixed aorta sections (n=1) for WT and *Rab27a* null mice at 8 and 20 weeks of age. B) Representative images from immunofluorescence staining to detect MYH6 in fixed PVAT sections (n=1). The first panel in each row is the matched primary IgG control for the 8-week-old WT mouse. Scalebar=20 μ m and is equivalent across all images. DAPI staining was captured using UV laser a power=7%, excitation=405nm, absorbance=430-450nm. The Alexa Fluor-488 secondary, for ACTA2 and MYH6 staining was captured using a laser power=7%, excitation=488nm, absorbance=509-534nm. Single z-plane images were captured using a Leica TCS SP8 laser scanning confocal microscope with a 63x/1.40 NA oil objective.

3.6.6. *Rab27a* Null iWAT and BAT Have Protein Profiles Different from PVAT and Aorta Signatures

We also completed a mass spectrometry analysis of BAT and iWAT to act as phenotype controls for PVAT. Also, this analysis provided additional insight to whether beige, thermogenic, and white adipose depots responded similarly to global *Rab27a* loss. Like PVAT, the BAT proteomic profile showed a slight increase in total number of altered proteins with age (**Figure 3.18A and 3.12A**). Many of these proteins were also associated with roles in contractility (MYH1, MYH4, and MYL1) and the extracellular matrix (CO1A1, CO1A2, and CO5A1) like what was observed with the PVAT data^{164,176,177}. Conversely, iWAT's proteomic profile remained relatively unaffected by age, and maintained a relatively narrow distribution in terms of fold change of expression (**Figure 3.18B**). Of the proteins that were on the periphery of the distributions, only a few were structural or contractile in function, suggesting that global loss of *Rab27a* uniquely impacts iWAT compared to BAT and PVAT under these metabolic conditions. It is possible that under an altered metabolic state, such as diet-induced weight gain, the proteomic signatures of iWAT and PVAT may become more similar.

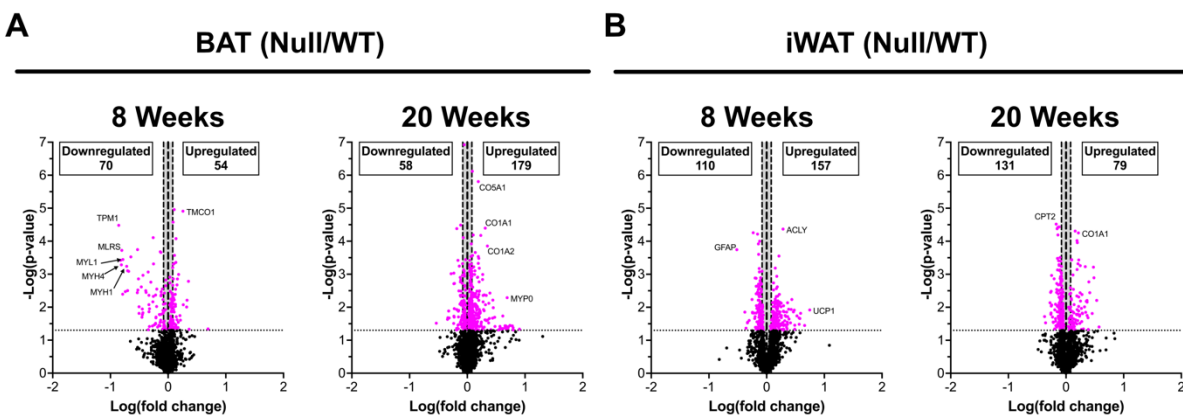


Figure 3.18. *Rab27a* null BAT and iWAT exhibit proteomic profiles that are unique from PVAT and aortic tissues. Proteomic profiles of *Rab27a* null vs WT male A) BAT and B) iWAT at 8- and 20-weeks-old, respectively. Distributions of each comparison are displayed by volcano plots. Significantly regulated proteins are plotted in magenta ($P \leq 0.05$). Only significant proteins with a fold change $\geq 20\%$ (magenta plots in the white quadrants) were utilized for phenotypic enrichment analysis.

3.6.7. The Cardiovascular System and Metabolism are Not the Top Enriched Phenotypes for *Rab27a* Null BAT and iWAT

Another observed difference between the BAT (**Figure 3.19A**) and iWAT (**Figure 3.19B**) signatures was that proteins meeting the thresholding criteria associated with non-cardiac muscle and integument phenotypes (**Figure 3.19**). These data also suggested that the iWAT from 20-week-old *Rab27a* null males were uniquely affected compared to the other adipose depots that were examined. Unlike the iWAT from 8-week-old *Rab27a* null males, the 20-week-old, *Rab27a* null iWAT showed the least enrichment for cardiovascular and metabolism phenotypes. However, these results are in line with the comparisons made in **Figure 3.18** regarding the differences in the BAT and iWAT proteomic profiles. Therefore, these data suggested that the effects of global *Rab27a* loss are unique to each depot and tissue type. To better characterize the effects of *Rab27a* loss on iWAT and BAT tissue, additional characterization studies will need to be completed.

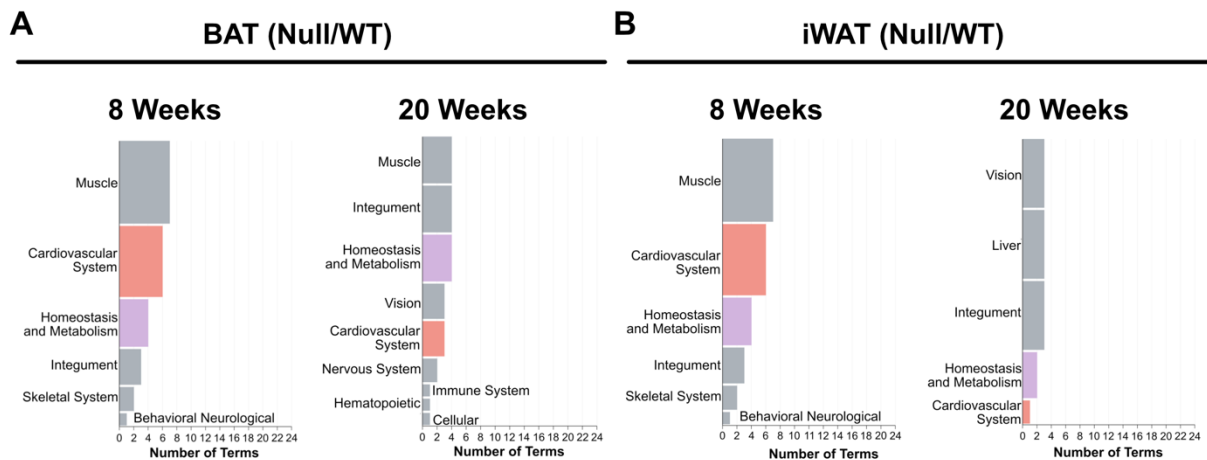


Figure 3.19. BAT and iWAT from *Rab27a* null mice have a different phenotype enrichment from the PVAT and aortae. Phenotype enrichment analysis of significantly altered proteins from the PVAT and aortic tissue of *Rab27a* null compared to WT male mice at both ages. Most still associated with the cardiovascular system, metabolism; however, to a lesser extent. Bar length indicates the number of phenotypic terms associated with these parent category terms. Bar width indicates the proportion of total proteins associated with each parent term. Colors are coded as follows: cardiovascular system (red); homeostasis and metabolism (purple); adipose-specific (blue); other (gray).

3.6.8. *Rab27a* Null BAT and iWAT Show Reduced Association with Aortic and Cardiac Phenotypes

As with the PVAT and aortic analyses, we sought to define the more specific phenotype terms contributing to the population of the parent categories (**Figure 3.19**). Of the limited associated cardiovascular system phenotypes, most still associated with altered aorta morphology for *Rab27a* null BAT and iWAT compared to WT controls (**Figure 3.20A, B, and D**). Meanwhile, the daughter terms populating the designated *other* phenotypes category are highly diverse. Some examples include *decreased skeletal muscle size*, *decreased skin tensile strength*, and *increased circulating carnitine levels*. Interestingly, the iWAT from *Rab27a* null mice at 8 weeks of age also show an enrichment of phenotypes associated with adipose (**Figure 3.20C**). These phenotypes include *impaired thermogenesis*, *decreased circulating adiponectin*, and *lipid droplet morphology*. While it is interesting that these phenotypes are enriched in iWAT and PVAT (**Figure 3.14**), it is unclear why BAT and PVAT are not showing enrichment for adipose phenotypes.

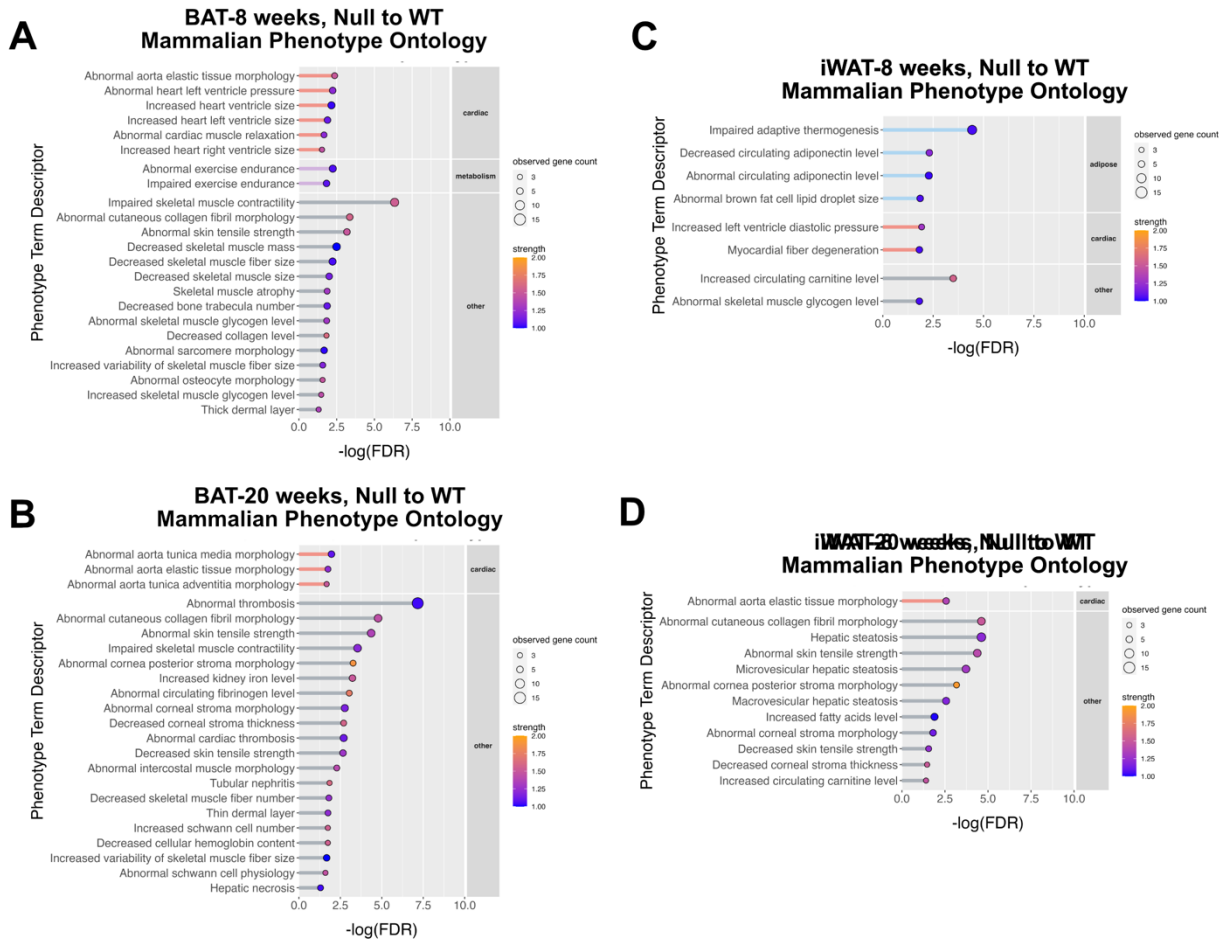


Figure 3.20. Proteins significantly impacted by global *Rab27a* loss are enriched for cardiac-associated phenotypes. Protein targets meeting the threshold requirements were analyzed for phenotype enrichments for A,B) BAT and C,D) iWAT from *Rab27a* null and WT mice at 8 and 20 weeks of age. Results show that these proteins are associated are less associated with cardiac phenotypes and metabolic phenotypes. For each graph, bar length indicates significance of enrichment by $-\log(\text{FDR})$ and bar color indicates the associated parent phenotype term: adipose (blue), cardiac (red), metabolism (purple), and other (gray). Dot size represents the number of targets associated with each term. Dot color represents the strength of the association.

3.6.9. *Rab27a* Null BAT and iWAT Have a Reduced Number of Significantly Altered Proteins Associated with Cardiovascular System Phenotypes

To further understand the differences in proteomic signatures of *Rab27a* null BAT and iWAT in relation to the PVAT and aortic signatures, heatmaps were generated for both

experimental age groups. Again, only the proteins contributing to the enrichment of the cardiovascular system phenotype were examined. All of the significantly altered proteins identified in the *Rab27a* null BAT are down regulated at 8 weeks of age, and then over expressed at 20 weeks of age in comparison to WT BAT controls (**Figure 3.21A**). This is unique from the other tissues, which show three major expression patterns described in *Section 3.6.1*. Meanwhile, three expression patterns were also observed within the *Rab27a* null iWAT data set (**Figure 3.21B**). One pattern that was consistent for all four tissue signatures was the increased overexpression of extracellular matrix proteins with aging. When considered together, these proteomic data suggest that global loss of *Rab27a* may be impacting the structure of extracellular matrixes in multiple tissues. However, further studies are necessary to confirm this possibility.

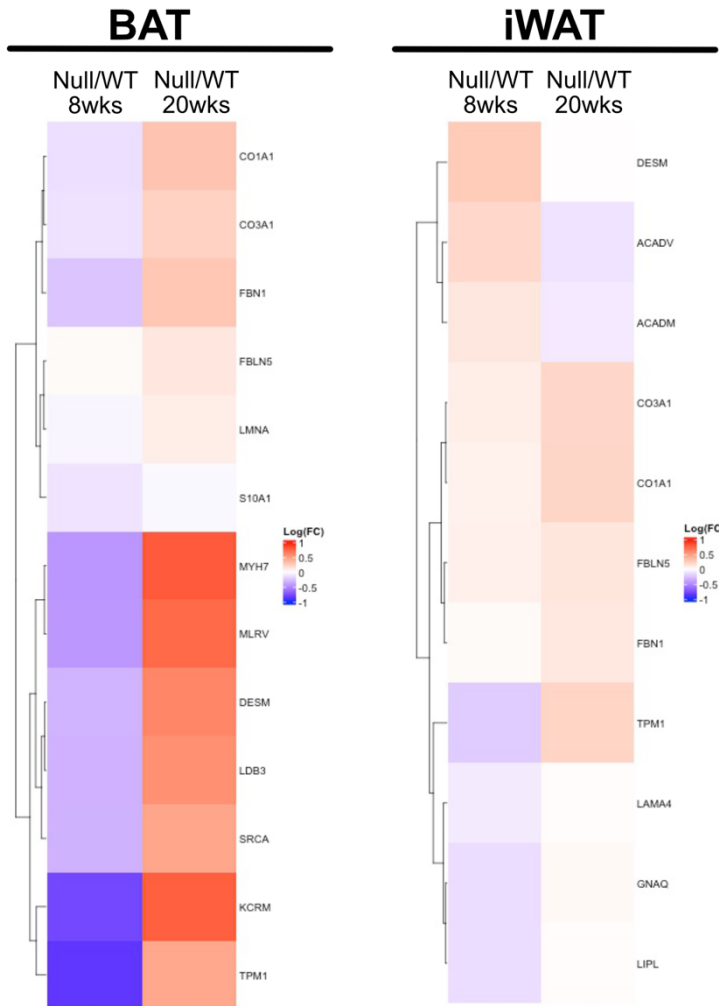


Figure 3.21. Comparisons in fold change directionality of proteins associated with the cardiovascular system phenotype in BAT and iWAT. Heatmap display directional changes of proteins conserved between the 8 week and 20 week timepoints within A) BAT and B) iWAT that populate the cardiovascular system phenotype (Figure 4.19). Directionality for changes in expression are reported as log(FC). Red indicates an upregulation of expression in *Rab27a* null tissues compared to WT controls. Blue indicates a downregulation of expression in *Rab27a* null tissues compared to WT controls.

3.7. Wire Myograph Studies Revealed Genotype, Age, and Sex Dependent Physiological Responses to the Global Loss of *Rab27a*

Myography is a well-established method utilized to study vascular and muscular reactivity *ex vivo* (Figure 3.22)^{145,146}. With this technique, excised cross sections of the thoracic aorta are mounted to two jaws by threading two wires through the luminal space. To account for luminal area variability, all aortae were sectioned to equivalent lengths, equilibrated to an equivalent starting force, and tested for viability and maximum contractile ability¹⁴⁵. The PVAT was left on the aorta because our goal was to evaluate the effects of global *Rab27a* loss on the vascular microenvironment.

One of the two jaws is connected to a force transducer that detects changes in force exerted on the wire. Changes in force are recorded in millinewtons (mN) of force. Quantification of contractile responses was completed by stimulating vessels utilizing phenylephrine, a known agonist of the α 1-adrenergic receptor¹⁷⁸. While the α 1-adrenergic receptor is known to be expressed within the aorta, its expression is lower compared to other members of the adrenergic receptor family¹⁷⁹. To quantify dilative responses, acetylcholine, an agonist of nicotinic acetylcholine receptors, was selected¹⁸⁰. Acetylcholine mediates smooth muscle relaxation through the nicotinic receptors that are expressed by the vascular endothelial cells¹⁸¹. While other chemical agonists have been shown to be effective inducers of C57BL/6J aortic contraction and dilation, both phenylephrine and acetylcholine are effective by our approaches¹⁸².

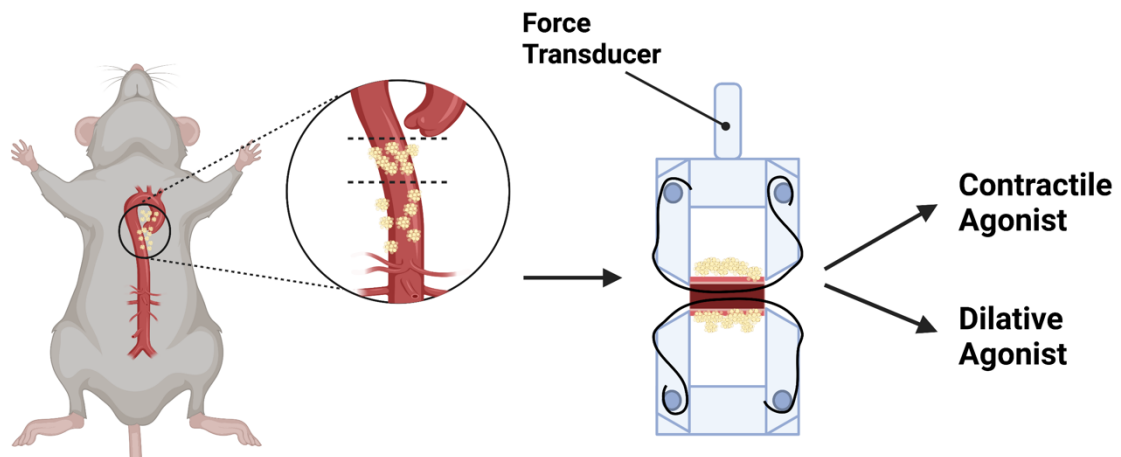


Figure 3.22. Wire myography is used to examine changes in contractile and dilative responses of the thoracic aorta. Segments of the thoracic aorta are mounted to a force transducer by two wires. Vessel contractile and dilative responses are induced using chemical agonists. *Created with BioRender.com.*

3.7.1. *Rab27a* Null Male Mice Exhibit Increased Vascular Contractility at 8 Weeks of Age

To evaluate whether the global loss of *Rab27a* impacts cardiovascular physiology, thoracic aortae were examined for changes in vasoreactivity. Using wire myography, we observed significantly increased vascular contractile and reduced vascular dilative responses when comparing the 8-week-old *Rab27a* null and WT male mice to their genotype-matched, 20-week-old counterparts (**Figure 3.23A and D**). This was expected, as vasoreactivity is an indicator for vascular stiffness with aging for human and murine vessels^{23,160}. Reactivity studies via wire myography revealed 8-week-old male, *Rab27a* null mice were significantly more contractile when stimulated with increasing doses of phenylephrine compared to age-matched WT controls (**Figure 3.23B**). This outcome was not observed in the 20-week-old *Rab27a* null mice when compared to age-matched WT controls (**Figure 3.23C**). Additionally, only 8-week-old *Rab27a* null male mice exhibited reduced vasodilation when treated with acetylcholine (**Figure 3.32E and F**). Since vascular health is dependent upon both contraction and relaxation, these data suggest that global loss of *Rab27a* induces an age associated vasoactive phenotype in young adult, male mice^{2,23}.

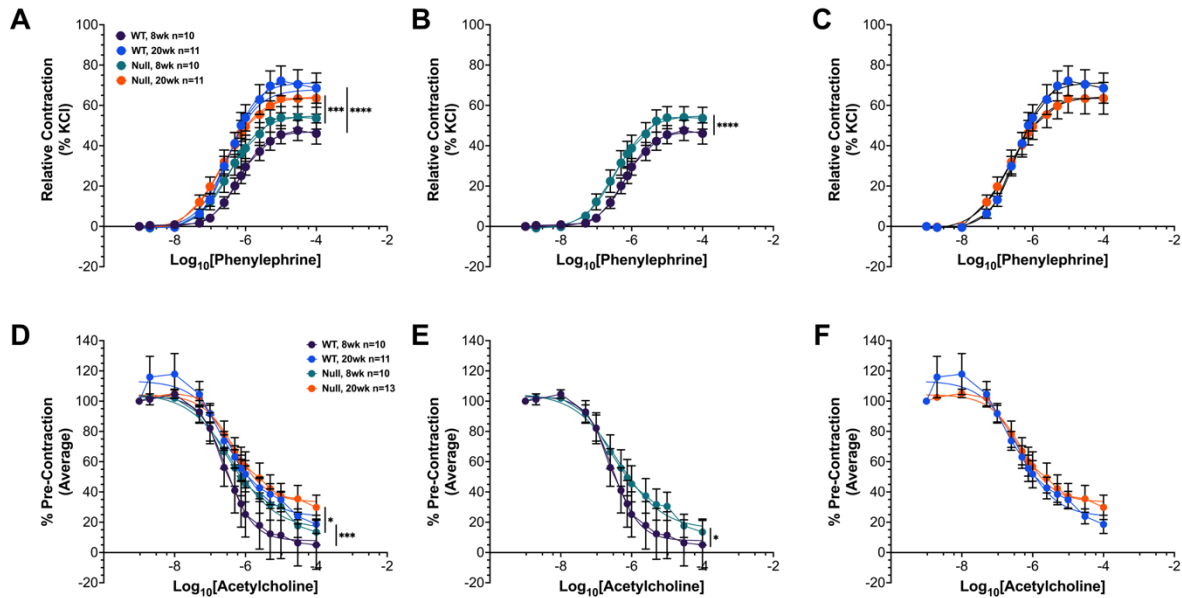


Figure 3.23. *Rab27a* null male mice exhibit genotype and age dependent vascular reactivity phenotypes. Thoracic aorta segments from male *Rab27a* null and WT mice at 8 or 20 weeks old were examined for changes in vasoconstriction and vasodilation. A) Comparison of vasoconstriction responses of genotype-matched male aortae between ages when treated with increasing doses of phenylephrine. B) Data for 8-week-old and C) 20-week-old male aortae examining for changes in contractile responses according to genotype were separated for comparison. D) Vasodilative responses for male aortae of both genotypes across ages are displayed. E) Data for 8-week-old and F) 20-week-old male aortae comparisons for vasodilation. Significance was determined via four-parameter non-linear regression test. *, P<0.05. ***, P<0.001. ****, P<0.0001.

3.7.2. Global loss of *Rab27a* Uniquely Affects Experimental Group Associations with Vessel Sensitivity in Male Mice

To account for vessel damage or deterioration that can result from the procedure, all vessels were subjected to a viability test post contractile and dilative testing (**Figure 3.24A**). No significant difference was found between experimental groups or in association with genotype or age. Vessel sensitivity (EC_{50}) to phenylephrine remained mostly unaltered, with the significant difference being observed when comparing the EC_{50} of the 8-week-old WT and 20-week-old *Rab27a* null aortae (**Figure 3.24B**). A significant association was found between vessel sensitivity with age (P=0.007) but not with genotype (P=0.128). Meanwhile, comparisons of

vessel sensitivity (EC_{50}) to acetylcholine showed that the 20-week-old *Rab27a* null aortae were significantly more sensitive to the agonist compared to the WT aortae of both groups (**Figure 3.24C**). This is most likely due to the wider distribution in EC_{50} responses compared to the other experimental groups. This distribution in data may be the cause for a significant association between vessel sensitivity and genotype ($P=0.029$) but not age ($P=0.1$).

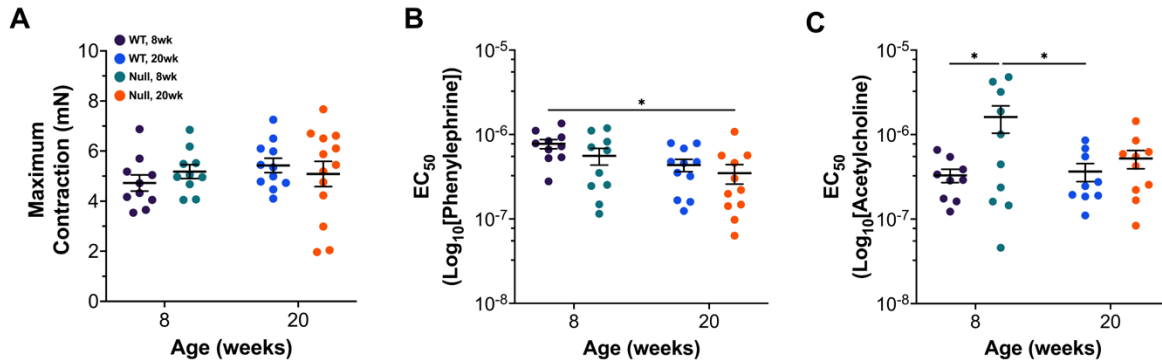


Figure 3.24. Male thoracic aorta sensitivity and viability remains consistent with aging and global loss of *Rab27a* between experimental groups. A) Vessel viability was tested with a 100 mM KCl dose for all male experimental groups. B) Sensitivity (EC_{50}) of male aortae to phenylephrine were calculated for all experimental groups. C) Acetylcholine sensitivity for male aortae across all groups was also calculated. Sensitivity was calculated to account for difference in contractile or dilative responses to each agonist. Each data point displays the calculated result for an individual mouse. Significance was evaluated via two-way ANOVA analyses with multiple comparisons tests. *, $P<0.05$.

3.7.3. *Rab27a* Null Female Aortae Exhibit Increased Vascular Contractility and Dilation at 20 Weeks of Age

Due to known differences in the prevalence of cardiovascular disease and other risk factors between human males and females, female mice of matching genotypes and age groups were also examined for changes in aortic vasoreactivity⁶². In contrast to the male cohorts, WT females showed reduced vasoconstriction in the older cohort compared to younger WT controls (**Figure 3.25A**). Meanwhile, *Rab27a* null females showed no significant change in vasoconstriction between ages (**Figure 3.25A**). Therefore, female *Rab27a* null mice appeared to resist the age-related changes in vasoreactivity that were observed in the WT controls. The 8-

week-old female *Rab27a* null and WT mice exhibited statistically similar contractile profiles (Figure 3.25B). However, the 20-week-old female *Rab27a* null mice retained contractility compared to the age-matched WT controls (Figure 3.25C). No significant difference in vasodilative capacity was observed with aging for either genotype in response to acetylcholine (Figure 3.25D). In contrast to males, 8-week-old *Rab27a* null females showed no change in vasodilation, while the 20-week-old *Rab27a* null females exhibited increased vasodilation (Figure 3.25E and F).

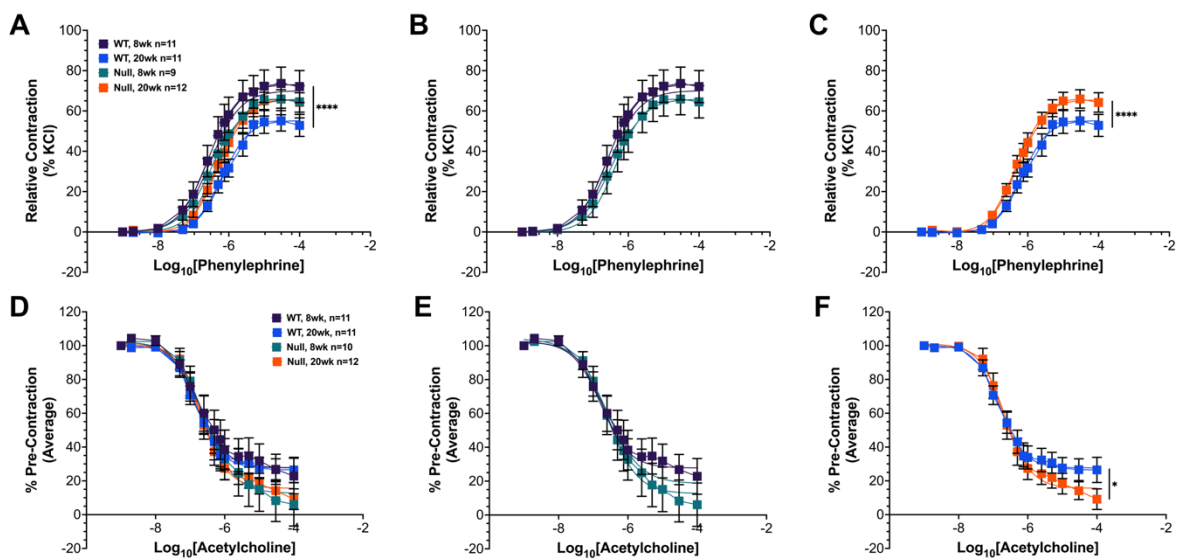


Figure 3.25. *Rab27a* null female mice exhibit genotype and age dependent vascular physiological responses. Thoracic aorta segments from female *Rab27a* null and WT mice at 8 or 20 weeks of age were examined for changes in vasoconstriction and vasodilation response. A) Comparison of vasoconstrictive responses of genotype-matched female aortae between ages when treated with increasing doses of phenylephrine. B) Data for 8-week-old and C) 20-week-old female aortae examining for changes in contractile responses according to genotype were separated for comparison. D) Vasodilative responses for female aortae of both genotypes across ages are displayed. E) Data for 8-week-old and F) 20-week-old female aortae comparisons for vasodilation. Significance was determined via four-parameter non-linear regression test. *, $P < 0.05$. ****, $P < 0.0001$.

3.7.4. Global loss of *Rab27a* Uniquely Affects Experimental Group Associations with Vessel Sensitivity in Female Mice

Like the male aortae, all female aortae were subjected to a viability test after completing

the contractile and dilative response curves (**Figure 3.25A**). No significant difference was found between experimental groups or in association with genotype or age. Vessel sensitivity (EC_{50}) to phenylephrine remained similar between groups and showed no significant association with genotype ($P=0.9$) or age ($P=0.057$) (**Figure 3.26B**). Comparisons of vessel sensitivity (EC_{50}) to acetylcholine showed a significance association occurring between the experimental groups with regards to age ($P=0.031$), but not genotype ($P=0.11$) (**Figure 3.26C**). However, because only the 20-week-old *Rab27a* null females showed a difference in vasodilative responses compared to WT controls at the same age, changes in aorta reactivity from *Rab27a* loss are not likely due to altered vessel sensitivity to acetylcholine.

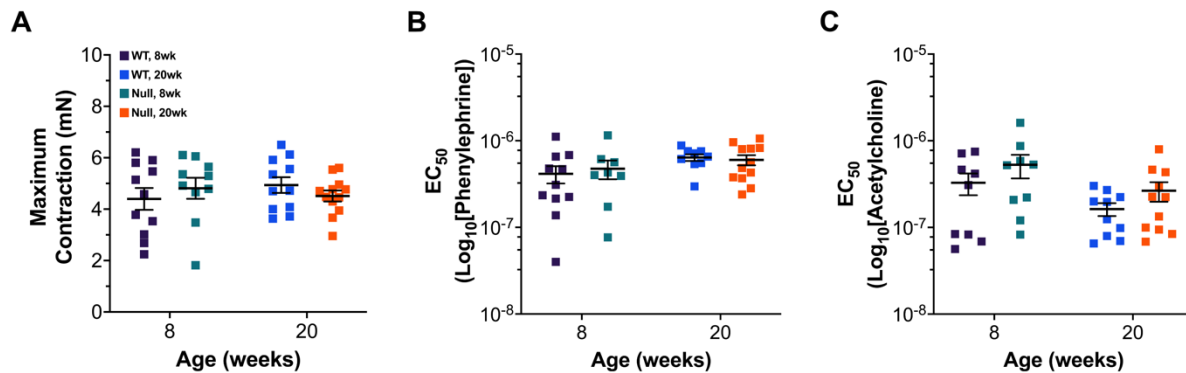


Figure 3.26. Female thoracic aorta sensitivity and viability were unchanged between experimental groups. A) Vessel viability was tested with a 100 mM KCl dose for all female experimental groups. B) Sensitivity (EC_{50}) of female aortae to phenylephrine were calculated for all experimental groups. C) Acetylcholine sensitivity for male aortae across all groups was also calculated. Sensitivity was calculated to account for difference in contractile or dilative responses to each agonist. Each data point displays the calculated result for an individual mouse. Significance was evaluated via two-way ANOVA analyses with multiple comparisons tests. Only significant comparisons are shown.

3.8. RAB27A is Differentially Expressed in Male and Female PVAT and iWAT

It is well established that there are sex-dependent differences in cardiovascular response to aging in humans and mice^{69,77,183}. However, to our knowledge, no studies have addressed sex-dependent differences in murine aortae due to the loss of *Rab27a*. Furthermore, it is unclear whether RAB27A was differentially expressed between the sexes. Here, we provide

evidence that RAB27A was differentially expressed between the PVAT and iWAT male and female mice at 20 weeks of age (**Figure 3.27A and C**). However, while trending, there was no significant difference in RAB27A within the aorta of male and female mice (**Figure 3.27B**). There is also no difference in RAB27A expression between the sexes within BAT (**Figure 3.27D**). While mechanism causing this tissue-specific difference in RAB27A expression is unclear, it does provide a possible explanation for the differences between the sexes in their response to a global loss of *Rab27a*.

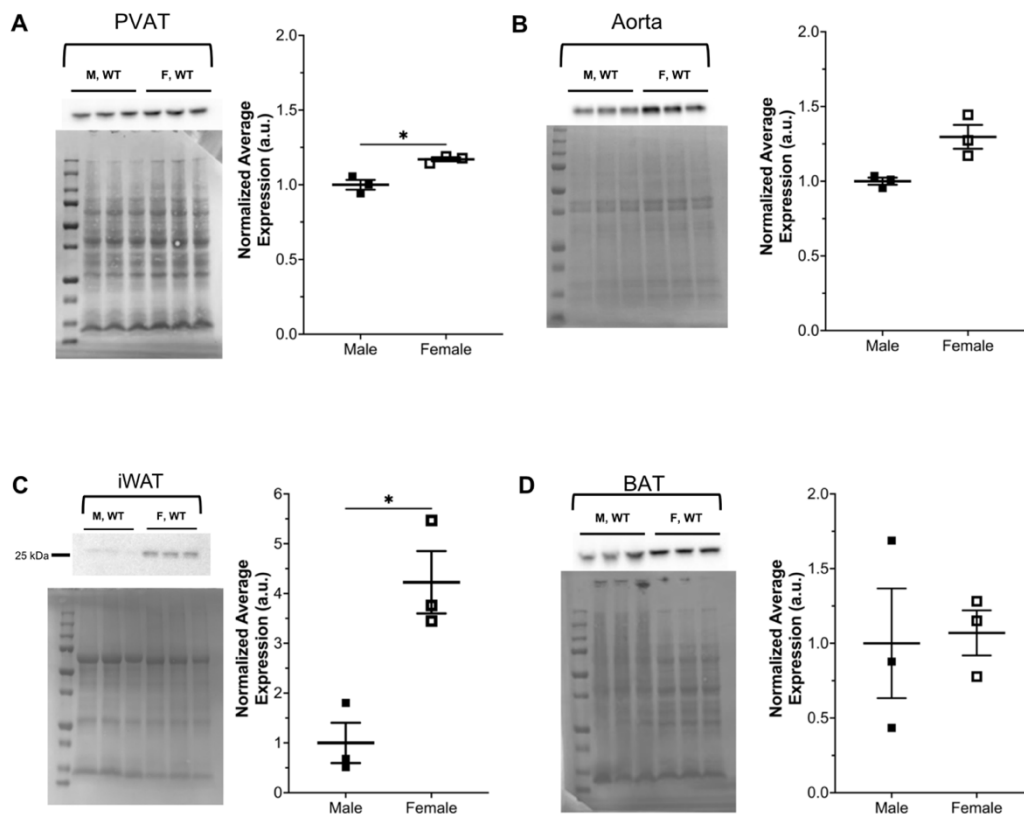


Figure 3.27. Female mice exhibited significantly higher RAB27A expression in PVAT and iWAT. Whole tissue lysates for A) PVAT, B) aorta, C) iWAT, and D) BAT were utilized for immunoblot analysis for RAB27A expression between WT male and female mice at 20 weeks of age. PVAT (n=3) and thoracic aorta (n=3) were pooled prior to isolation and examined as technical replicates due to limited tissue mass. Quantifications were based off the technical replicates. For iWAT and BAT, tissues were not pooled and instead were loaded into individual lanes for biological replicates three times to account for technical variability. Representative blots are shown. All raw values were normalized to the male controls. Statistical significance was tested via Welch's t-test. *, P<0.05.

3.9. The Characterization of Plasma Derived Exosomes from *Rab27a* Null Mice

Methodological approaches to studying nano-sized vesicles have been developing rapidly in the past few years. Currently there are multiple approaches for sample collection, purification, and analysis. While ultracentrifugation is the preferential method for isolation, the method is characterized as producing isolates with high purity but low yield¹⁸⁴. Our initial attempts to isolate exosomes using lipid precipitation techniques resulted in analysis difficulties when analyzed using tunable resistive pulse sensing (TRPS) (qNano Gold system, iZon). Due to the limited volumes of our samples, we adapted an isolation method utilizing ultrafiltration and subsequent size exclusion chromatography for exosome isolation. Sample purity was examined by confirming that detected particles met the classification standards according to diameter size. Furthermore, albumin, an indicator of sample contamination, was not the most prominent protein within these samples when they were evaluated via mass spectrometry.

3.9.1. The Global Loss of *Rab27a* Did Not Affect Circulating Exosome Size or Number

As a regulator of exosome secretion, we hypothesized that global loss of *Rab27a* would significantly reduce the concentration of circulating exosomes⁹. Analysis of our samples via nanoparticle tracking analysis (NTA) showed that the isolated exosomes were within the defined diameter range (**Figure 3.28A**). For this reason, the analyzed particles were classified as exosomes rather than extracellular vesicles¹¹. However, no significant changes in median exosome diameter or mean concentration were identified between any of the experimental groups (**Figure 3.28A and B**). No significant associations with age ($P=0.17$) or genotype ($P=0.83$) were found in relation to exosome size. Further, no significant associations with aging ($P=0.06$) or genotype ($P=0.16$) were found in relation to exosome concentration. Because of these findings, proteomic analysis was completed in order to determine whether there were changes in protein cargo due to *Rab27a* loss.

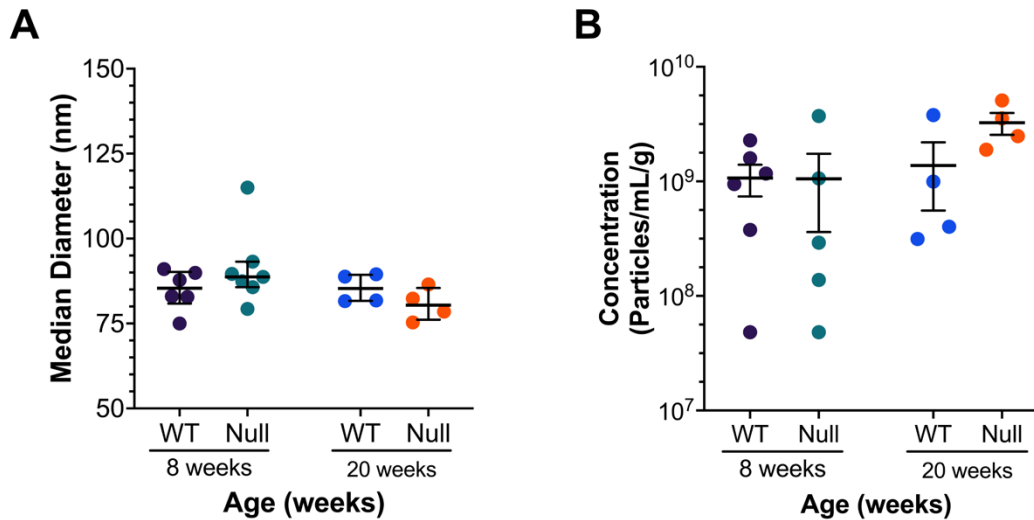


Figure 3.28. Exosomes isolated from male *Rab27a* null plasma have genotype and age specific changes in proteomic cargo. A) Comparison of exosome median diameters between male *Rab27a* null and WT plasma samples. Bars display the median diameter interquartile ranges. B) Comparison of particle concentration as normalized to individual body weight. Bars displays the average and SEM. Each plot displays the results of a single biological replicate. Significance was evaluated via two-way ANOVA analyses with multiple comparisons tests. Only significant comparisons are shown.

3.9.2. The Global Loss of *Rab27a* Affected Exosome Protein Cargo Profiles

A comparison of profile distributions of identified proteins was completed to characterize whether genotype or age affected exosome cargo. Of the four comparisons completed, *Rab27a* null versus WT (8 weeks of age) and WT (8 versus 20 weeks of age) showed the most symmetrical distribution with the fewest number of altered proteins (**Figure 3.29A and D**). Meanwhile, comparisons of *Rab27a* null and WT exosomes from mice at 20 weeks of age revealed that most of the altered proteins were upregulated in the *Rab27a* null exosomes compared to the WT group (**Figure 3.29D**). Additionally, comparison of exosomes from *Rab27a* null 8-week-old versus 20-week-old mice showed that most of the altered proteins were down regulated at a younger age (**Figure 3.29B**). Multiple proteins that were differentially regulated in our data have been previously identified in exosomes including thrombospondin-1 (TSP1), serotransferrin (TRFE), tenascin (TENA), and serum amyloid A-4 protein (SAA4)¹⁸⁵⁻¹⁸⁸. These data suggest that while aging alone may change the protein cargo of plasma derived exosomes,

loss of *Rab27a* also impacts cargo uniquely depending on age. Future studies will need to be completed in order to determine whether these changes in protein cargo are biologically significant.

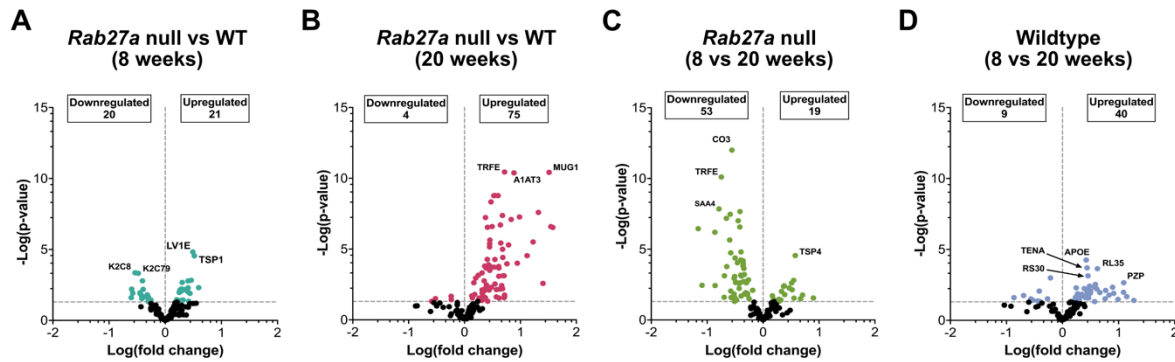


Figure 3.29. Exosomes isolated from male *Rab27a* null plasma have genotype and age specific changes in proteomic cargo. Volcano plots were used to display the difference in proteomic profiles between experimental groups. Comparison between exosome proteomic profiles of *Rab27a* null versus WT male mice at A) 8 weeks of age and B) 20 weeks of age (n=4/group). C) Comparison between exosome proteomic profiles of 8-week-old versus 20-week-old *Rab27a* null mice. D) Comparison between exosome proteomic profiles of 8-week-old and age and 20-week-old WT mice.

3.10. Chapter Discussion

An endosomal trafficking protein that regulates exosome secretion, RAB27A is classically associated with Griscelli syndrome and cancer progression^{10,129,134}. Recent studies have shown that exosomes are able to influence cardiovascular health^{120,121,189}. However, none of these studies evaluated the role of RAB27A as an underlying regulator for the dysregulation of exosome signaling within the cardiovascular microenvironment. Herein, we provide evidence for an association between metabolic activity and *RAB27A*. This association aligns with our previous study identifying a role for *RAB27A* in human PVAT preadipocyte differentiation¹³⁶. Due to the known impact of PVAT signaling on vascular health, our goal was to determine whether the loss of RAB27A also impacts vascular health^{102,105}.

3.10.1. Conclusions

With this study, we expanded our knowledge of RAB27A expression within the mouse and human PVAT and aortic wall using a novel global *Rab27a* null mouse strain (**Figure 3.30**). We show that the changes in protein signatures due to a global loss of *Rab27a* are associated with metabolic and cardiovascular phenotypes for PVAT and aortic tissues. These metabolic phenotype associations align with both the GWAS and altered glucose sensitivity that was observed within the original *Rab27a^{ashen}* strain. (Soucy et al., 2023 under revision). However, no morphological changes were detected in multiple *Rab27a* null adipose tissue for either sex at two different ages. While *Rab27a* null males showed increased lipid area with aging, *Rab27a* null females showed no association. These trends align with a previously published study showing distinct sex differences in C57BL/6J mouse susceptibility to diet-induced obesity¹⁶².

Functional vascular reactivity studies demonstrated that a global loss of *Rab27a* changed thoracic aorta contractile and dilative responses for both sexes. These physiological effects manifest independently of gross morphological changes, suggesting that modifications in cellular communication may be responsible. Additionally, while we noted differences in vasoreactivity between the males and females for both genotypes, the physiological relevance remains to be examined. We predict that these vascular physiology trends may be due to differences in basal RAB27A expression across tissues. These findings further highlight the importance of including both male and female mice in future cardiovascular disease studies.

Furthermore, we provide evidence that global loss of *Rab27a* impacted the protein cargo of plasma-derived exosomes. Proteomic analysis revealed that the greatest change in protein cargo was within the exosomes of 20-week-old male *Rab27a* null mice. However, these results conflict with the leading paradigm within the field that loss of RAB27A reduces exosome secretion¹⁵⁵. We predict that compensatory mechanisms are being activated in order to maintain this important mode of cellular communication. While exploratory, this work supports our hypothesis that *Rab27a* is important in the regulation of exosome signaling.

Global *Rab27a* loss impacts the vascular microenvironment

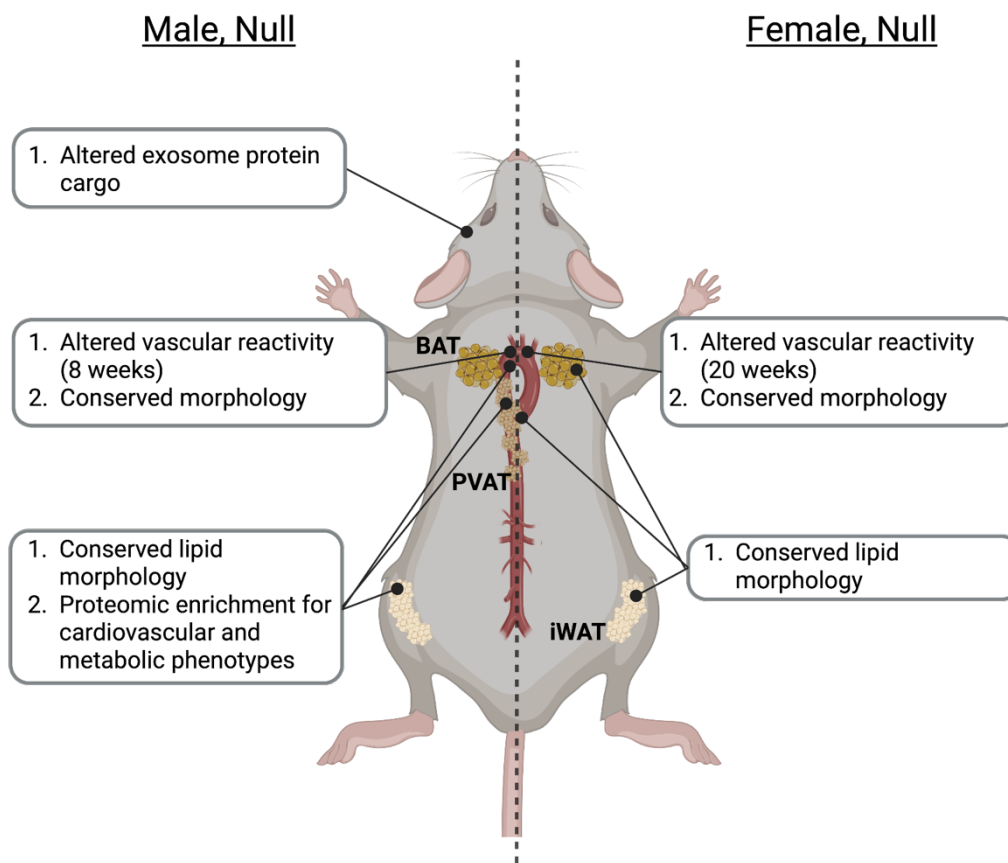


Figure 3.30. A summary of Chapter 3 conclusions. Graphical depiction of major study conclusions for both male and female *Rab27a* null mice in comparison to WT controls. Created with BioRender.com

3.10.2. Study Limitations

This study was designed with the intention of accounting for age, sex, and genotype as biological variables. However, there are experimental limitations that impact the conclusions that can be inferred. Future studies addressing the limitations discussed below will help the augment the findings discussed within this work.

3.10.2.1. Sole Use of the Novel Global *Rab27a* Null Strain

This study utilizes a global knockout model to study the effects of *Rab27a* loss on the vascular microenvironment. While this model allowed us to determine the significance of global *Rab27a* expression on vascular reactivity, it does not answer whether tissue specific expression within PVAT or the aorta impacts vascular tone. Therefore, it is possible that other organs, such as iWAT, may be contributing to these reported effects within the vascular microenvironment. It is also possible, that the global loss of *Rab27a* is eliciting a global compensatory mechanism that is leading to the dampening of physiological effects.

3.10.2.2. Accounting for Sex as a Biological Variable

In designing these experiments, we included female experimental groups that were examined in parallel with male experimental groups. However, female samples were not utilized for each analysis. Therefore, the proteomic results and conclusions are based only upon male samples. The male samples were initially selected for analysis and, due to the amount of information produced from these samples, we decided to focus on these data to produce an effective workflow for future analyses. Subsequently, only male tissues were used to confirm directionality changes found from proteomic analysis. Additionally, only plasma-derived exosomes from male samples were characterized and subjected to proteomic analysis.

This is a limitation within this study and will need to be addressed in future studies. With the current differences observed between the sexes, it is likely that the female proteomic signatures of tissues and exosomes would also exhibit unique proteomic signatures due to global *Rab27a* loss. These studies can be completed as the necessary samples were collected from the female experimental groups at the time of myograph experimentation.

3.10.3. Future Directions

With the increasing prevalence of CVD, and a lack of effective therapeutic targets for disease treatment, establishing a better understanding of how intercellular and tissue-tissue communication impacts disease progression is imperative⁵⁸. To accomplish this goal, future studies must answer whether the results presented are dependent on *Rab27a* loss in a specific organ or cell type; identifying the mechanism by which *Rab27a* loss alters vascular physiology; and defining the mechanism causing the sex-specific response in vasoreactivity.

3.10.3.1. Addressing the Importance of Cell-Specific loss of *Rab27a*

To determine whether a specific cellular population can recapitulate the above results, we plan to utilize the *Rab27a* conditional knockout strain to induce recombination in PVAT preadipocyte progenitor cells (APCs), vascular smooth muscle cells (VSMCs), and vascular endothelial cells (**Figure 3.6**). Recombination of *Rab27a* within PVAT APCs will be accomplished through breeding of the *Rab27a^{fl/fl}* to the C57BL/6J *Myf5*-Cre strain. Recombination of *Rab27a* within VSMCs will be also accomplished by breeding the *Rab27a^{fl/fl}* to the C57BL/6J *SMMHC*-CreERT2 strain. Lastly, vascular endothelial cells will be recombined through breeding of the *Rab27a^{fl/fl}* to the C57BL/6J *DLL1*-Cre strain. Analyses, like those applied in study discussed above, would be completed to evaluate whether vascular trends a recapitulated in the targeted knockout strains.

3.10.3.2. Identifying the Mechanism of How *Rab27a* Alters Vascular Physiology

Due to the proteomic changes that we reported above, it is possible that *Rab27a* null exosomes are responsible to changes in vascular tone. Therefore, *in vitro* experiments will be critical to study the molecular changes occurring within WT vascular smooth muscle cells when treated with exosomes from *Rab27a* null PVAT adipocytes and APCs. As controls, *Rab27a* null derived VSMC and vascular endothelial cells will also be cultured with and without exosomes

derived from WT, PVAT-APC to account for cell specific effects of *Rab27a* loss. Additionally, to show that the presence of functional RAB27A recapitulates the WT control trends, *Rab27a* null cells can be transfected with a plasmid containing the WT *Rab27a* gene, like what was done in a previous paper¹⁹⁰. Further, phenotype associations can be examined based on the varying expression of RAB27A post transfection. Based on previous studies, initial pathways that would be examined for changes include the eNOS, AMPK, and calcium signaling^{55,158,191}.

3.10.3.3. Elucidating the Mechanism Underlying the Sex Dependent Trends in Vascular Physiology

Due to the impact of estrogen signaling in adipose physiology, it will be important to study the effect of *Rab27a* loss on vascular reactivity in ovariectomized female mice compared to sham-ovariectomized females¹⁶¹. This study would include 8-week-old and 20-week-old timepoints to evaluate how loss of estrogen impacts vascular reactivity in *Rab27a* null females. As an aging control, female mice could also be kept until at least 12 months of age to study whether the natural loss of estrogen due to menopause elicits the same response as the younger ovariectomized female mice¹⁹². Due to the biological importance of estrogen signaling, we predict that there would be differences between the ovariectomized and menopausal female experimental groups.

CHAPTER 4:

A GLOBAL LOSS OF RAB27A INCREASES THORACIC AORTA CONTRACTILE RESPONSE IN MALE MICE FED A HIGH FAT DIET

4.1. Overview

Murine diet-induced obesity models have been widely utilized to study the effects of obesity on metabolic health and cardiovascular disease^{162,193}. Some of these studies provide evidence that the presence of PVAT during HFD reduces thoracic aorta vasodilative abilities^{158,191}. Thereby suggesting that communication between the PVAT and aorta are impacted by diet. However, no study had evaluated whether *Rab27a* expression impacts vascular reactivity during HFD. With our newly establish global *Rab27a* null strain, we began studying whether such an association exists. Furthermore, because this *Rab27a* null strain was developed on a C57BL/6J background, the trends observed from this study are comparable to prior vascular and diet studies completed using C57BL/6J mice.

Through our *Rab27a* null studies completed on a chow diet, we showed that the proteomic signatures of PVAT and aortic tissues were enriched for association with cardiovascular and metabolic phenotypes (*Section 3.6*). Despite the absence of altered in lipid accumulation within *Rab27a* null PVAT compared to WT controls, it was possible that adipose depots may not be able to respond normally when metabolically challenged with a HFD. This theory was also supported by our previous *in vitro* study linking RAB27A expression with PVAT adipocyte differentiation¹³⁶. Because PVAT-aorta communication is critical for maintaining vascular reactivity, we hypothesized that a global loss of *Rab27a* during a HFD would intensify vascular disease physiology.

4.2. Characterizing the Effects of Global *Rab27a* Loss on Body Composition During a 60% High Fat Diet

Having shown that *Rab27a* null mice gain weight comparably to WT controls on a chow diet (**Figure 3.7**), we decided to also track the weight gain of male *Rab27a* null mice when fed a HFD. This information was necessary to determine whether global *Rab27a* loss impacted mouse weight gain. For this reason, the body weights of *Rab27a* null were compared to WT controls fed the same diets and the *Rab27a* null mice that were fed a SCD. Percent body fat mass was also calculated to confirm that any weight gained during the diets was due to increased adipose expansion¹⁹⁴.

4.2.1. Global *Rab27a* Loss Does Not Affect the Weight Gain of Male Mice Fed a 60% High Fat Diet

Male mice were fed either a 60% HFD or SCD for 12-weeks as outlined in *Section 2.1.11*. Consistent with previous literature, WT males gained considerable weight over the 12-week period when fed the 60% HFD compared to a control diet (**Figure 4.1A**)¹⁹⁵. Statistical analysis confirmed that the body weights of WT mice fed either the HFD or SCD began to significantly differ beginning at week 3 ($P=0.01$) of feeding. Significant differences in weight between the *Rab27a* null mice fed a HFD or SCD was observed starting at week 2 ($P=0.02$) on the diets. With the dramatic changes in weight between the *Rab27a* null HFD and SCD groups there was a significant association between weight and diet ($P<0.0001$) and time ($P<0.001$). However, no significant difference was observed at any week when comparing the body weights of *Rab27a* null and WT mice when fed the same diet (**Figure 4.1A**). However, there was a significant association for body weight that was attributed the genotype for both the HFD ($P<0.0001$) and SCD ($P=0.005$) comparisons that were independent of any statistical interactions ($P=0.96$ for both diets).

4.2.2. The Global Loss of *Rab27a* Expression Does Not Alter Fat Body Mass in Male Mice Fed a 60% High Fat Diet

With the significant changes in weight in the mice fed a HFD compared to SCD we wanted to determine whether body composition was also changing similarly between the *Rab27a* null and WT controls. Body composition of mice from all four experimental groups was at weeks 0 and 12 of the study. As expected, all mice started the diet with comparable % fat body mass between all groups; WT, SCD (mean=12.7, SEM=0.63), WT, HFD (mean=13.1, SEM=0.54), *Rab27a* null, SCD (mean=11.3, SEM=0.65), and *Rab27a* null, HFD (mean=11.3, SEM=0.79) (**Figure 4.1B**). No significant association was found between % fat body mass and diet ($P=0.7764$) at this time point. However, there was a significant association between % fat body mass and genotype ($P=0.033$), suggesting that there may be differences in body composition at 8 weeks of age for *Rab27a* null mice compared to WT controls.

By week 12 of the study, the *Rab27a* null and WT mice fed a HFD had significantly increased % fat body masses compared genotype controls on the SCD (**Figure 4.1C**). Furthermore, there were no significant differences between the two genotypes when fed the same diet. As a result, there is a significant association of % fat body mass with diet ($P<0.001$), but not genotype ($P=0.73$). These data suggest that while body composition may differ between *Rab27a* null mice at a younger age when fed a chow diet, the *Rab27a* null adipose depots are capable of expansion during a HFD.

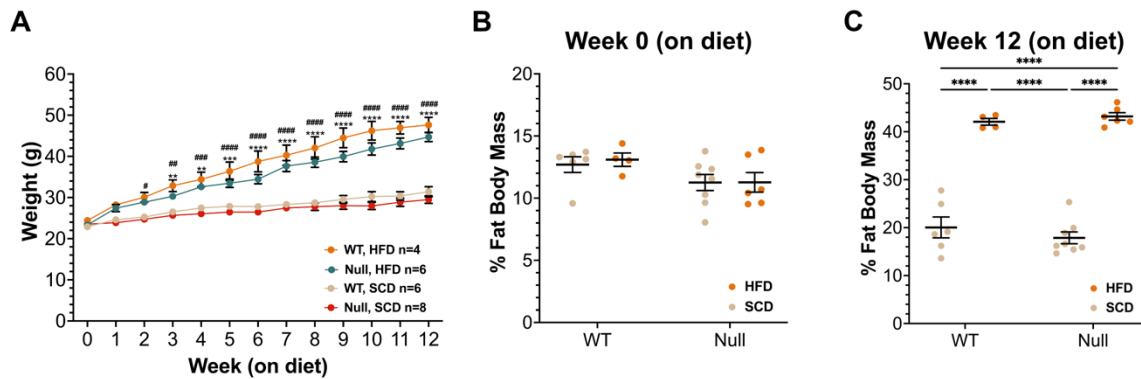


Figure 4.1. *Rab27a* null males gain weight like WT controls when fed a 60% HFD. A) Weight gain trends of *Rab27a* null and WT male mice fed either a HFD or SCD diet over 12 weeks. Sample size is displayed within the panel key. Stars denote WT HFD vs SCD statistical comparisons for each timepoint. *, P<0.05. **, P<0.01. ***, P<0.001. ****, P<0.0001 Pound symbols denote *Rab27a* null HFD vs SCD statistical comparisons for each timepoint. The number of symbols displayed matches the same notation scheme used for the WT diet comparisons. B) Comparison of % fat body mass between experimental groups at week 0 on the diet. C) Comparison of % fat body mass between experimental groups at week 12 on the diet. ****, P<0.001. For all panels, bars display the means and SEM for the respective experimental group. Significance was determined via an ordinary 2-way ANOVA with a multiple comparisons test. Only significant comparisons are shown.

4.3. Characterizing the Effects of Global *Rab27a* Loss on Adipose Tissue and Thoracic Aorta Morphology After a 60% High Fat Diet

Of the adipose depots examined in this work, PVAT is the smallest and has a highly dynamic metabolic nature¹⁶. This depot's response to HFD is also unique as its metabolic activity becomes less thermogenic and begins to secrete factors that impact thoracic aorta tone^{158,196,197}. Due to the low total mass contribution of PVAT to the total % fat body mass, body composition analysis would not provide insight to physiological or morphological changes occurring within this tissue of *Rab27a* null mice fed a HFD. For this reason, we evaluated the % lipid accumulation in PVAT from the *Rab27a* null and WT mice that were fed either a HFD or SCD.

To further determine the effects of *Rab27a* loss on vascular morphology after a HFD, we also quantified the thoracic aortae for changes in vessel total, medial, and luminal area.

Despite lack of gross morphological changes in *Rab27a* null mice fed a chow diet, it was possible that the aortae might exhibit altered morphology due to diet-induced weight gain. Especially as obesity has been shown to cause hypertension and modifications in vessel structure^{56,159,198}.

4.3.1. Global *Rab27a* Loss Does Not Affect PVAT Lipid Accumulation in Male Mice Fed a 60% High Fat Diet

Average % lipid accumulation was quantified in the PVAT of *Rab27a* null and WT mice fed either a HFD or SCD. While no difference was observed when directly comparing experimental groups, there was a significant association with diet ($P=0.025$) (**Figure 4.2A**). As phenotype controls, BAT and iWAT were also quantified and exhibited unique trends in lipid accumulation from PVAT.

Analysis revealed that the BAT from male *Rab27a* null mice fed a HFD had significantly increased % lipid accumulation compared to the *Rab27a* null SCD controls (**Figure 4.2B**). The same comparison was not significant when comparing lipid accumulation in BAT from the WT mice across diets, however the trend remained similar. This was also supported through the statistical association between lipid accumulation and diet ($P=0.0004$). Like BAT, iWAT from *Rab27a* null male fed a HFD showed increased lipid accumulation compared to SCD controls (**Figure 4.2C**). Again, no significant difference was observed between diets for the WT tissues. However, diet was significantly associated with lipid accumulation ($P=0.0001$). These results are expected, given the increase in % fat body mass observed in both *Rab27a* null and WT male mice fed a HFD.

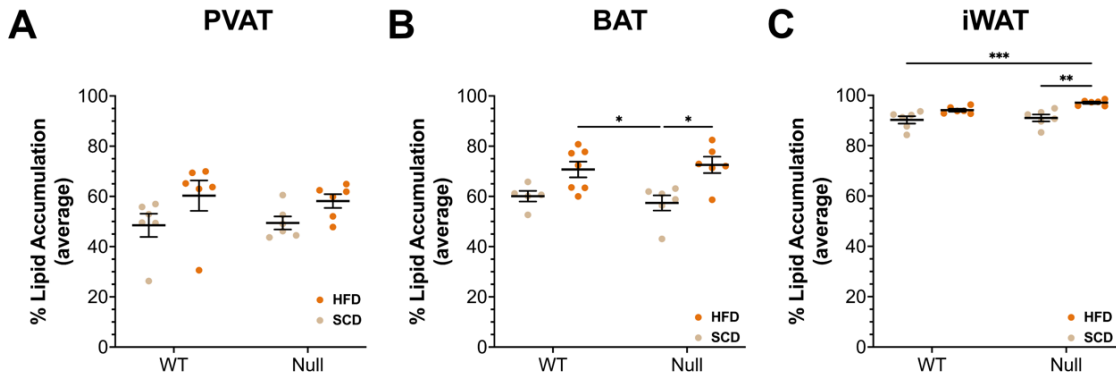


Figure 4.2. Male *Rab27a* null adipose tissues exhibit depot-specific differences in lipid accumulation after a HFD. Quantification of % lipid accumulation in A) PVAT, B) BAT, and C) iWAT from mice belonging to all experimental groups. Tissues were from mice at week 12 of the respective diet. Each data plot represents the average % lipid accumulation of one biological replicate, which is the average % lipid accumulation from 10 fields of view. Bars display the mean and SEM. Statistical significance was determined using an ordinary two-way ANOVA with a multiple comparison test. *, P<0.05. **, P<0.01. ***, P<0.001. Only significant comparisons are shown.

4.3.2. The Global *Rab27a* Loss Does Not Alter Thoracic Aorta Gross Morphology of Male Mice Fed a 60% High Fat Diet

Because there were diet associated effects for all three adipose tissues tested above, changes in gross thoracic morphology in association with diet and genotype were also examined. No significant changes in total vessel area were observed between any of the experimental groups and no statistical associations were found for either genotype (P=0.22) or diet (P=0.42) (**Figure 4.3A**). The same results were also observed when comparing medial or luminal areas between experimental groups. Again, no associations between area and genotype or age (**Figure 4.3B and C**). These data show that *Rab27a* expression does not impact aorta morphology in mice fed a 60% HFD.

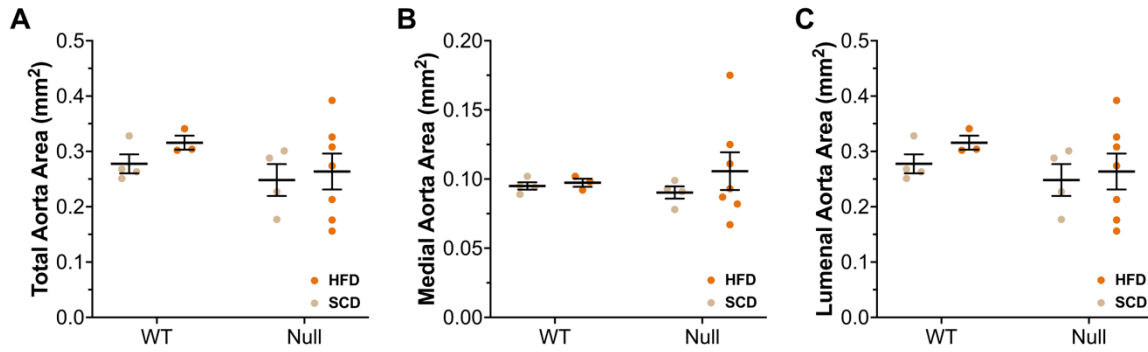


Figure 4.3. *Rab27a* null mice on HFD show no change in aorta morphology.

Quantification of thoracic aorta A) total, B) medial, and C) luminal areas from *Rab27a* null and WT male mice that were fed either a HFD or SCD. Tissues were from mice at week 12 of the respective diet. Each data plot represents the respective area of one biological replicate. Bars display the mean and SEM. Statistical significance was determined using an ordinary two-way ANOVA. Only significant comparisons are shown.

4.4. The Global Loss of *Rab27a* Affected Male Thoracic Aorta Vasoreactivity After a 60% High Fat Diet

It has been well established that HFD in humans and mice impact vascular physiology^{56,158,198}. In *Chapter 3* we provided evidence that the global loss of *Rab27a* altered thoracic aorta vasoreactivity in an age- and sex-dependent manner (**Figures 3.12 and 3.14**). Due to the importance of signaling within the vascular microenvironment for the development of CVD, we sought to evaluate whether global *Rab27a* loss during a HFD significantly contributes to increased vascular reactivity^{18,105,158}.

4.4.1. The Global Loss of *Rab27a* Increased Thoracic Aortic Vasocontractility in Male Mice Fed a 60% High Fat Diet

Wire myography was utilized to evaluate whether a global loss of *Rab27a* modified thoracic aorta physiology in male mice fed a HFD. Data from this study showed that the aortae of *Rab27a* null male mice fed a HFD exhibited increased vasocontractile responses compared to all the other experimental groups (**Figure 4.4A**). Meanwhile, the aortae of WT male mice fed

a HFD exhibited greater contractile responses compared to aortae of *Rab27a* null male mice fed a SCD (**Figure 4.4A**). However, no significant difference was found when comparing aortic contractile responses between WT male mice fed either a HFD or SCD. Importantly, no significant difference between the vasocontractile responses of the aortae from *Rab27a* null and WT male mice fed a SCD.

From this contractility study, it was predicted that the aortae of *Rab27a* null males fed a HFD would exhibit reduced dilative abilities compared to the other experimental groups. However, the aortae of WT male mice fed a SCD mice were significantly different compared to aortae of *Rab27a* null mice on either diet (**Figure 4.4B**). No significant difference between aortae responses of WT mice fed a HFD or SCD. These findings are likely due to the high variability in the response of aortae to acetylcholine stimulation (**Figure 4.4B**).

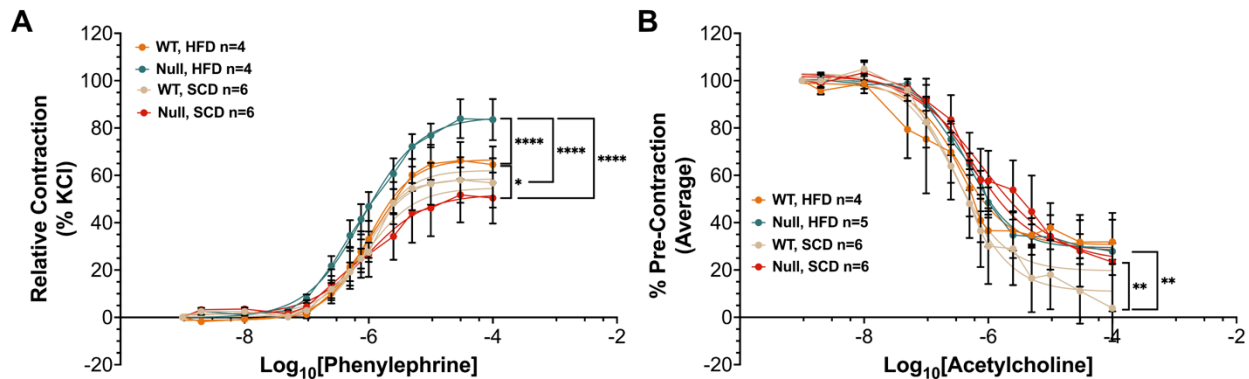


Figure 4.4. Aortae of *Rab27a* null male mice exhibit increased contractility compared to aortae of WT controls when fed a HFD. Thoracic aorta segments from male *Rab27a* null and WT mice at Week 12 of their respective diet and examined for changes in vasoconstriction and vasodilation. A) Comparison of vasoconstriction responses of aortae when treated with increasing doses of phenylephrine. B) Comparison of vasodilative responses of aortae when treated with increasing doses of acetylcholine. Significance was determined using a four-parameter non-linear regression test. *, P<0.05. **, P<0.01. ****, P<0.0001.

4.4.2. The Global Loss of *Rab27a* Does Not Alter Vessel Sensitivity in Mice Fed a 60% High Fat Diet

To confirm that contractile differences were not the result of altered vessel viability, we compared maximum contractile responses when treated with a single dose of KCl. Analysis showed that *Rab27a* loss during HFD had no effect on aortae viability (**Figure 4.5A**). There were also no associations between vessel viability and either genotype ($P=0.26$) or diet ($P=0.62$). Furthermore, vessel sensitivity to both chemical agonists was examined to evaluate whether changes vasoreactivity were due to an inability to respond to the agonists. No significant changes in the EC_{50} of phenylephrine was found between any groups and no associations with genotype ($P=0.45$) or diet ($P=0.38$). Sensitivity to acetylcholine showed similar results for intergroup comparisons along with no associations with genotype ($P=0.37$) or diet ($P=0.35$). These data there for suggest that global loss of *Rab27a* increases thoracic aorta contractility during a HFD, which is a phenotype associated with the development and progression of CVD¹⁹⁷.

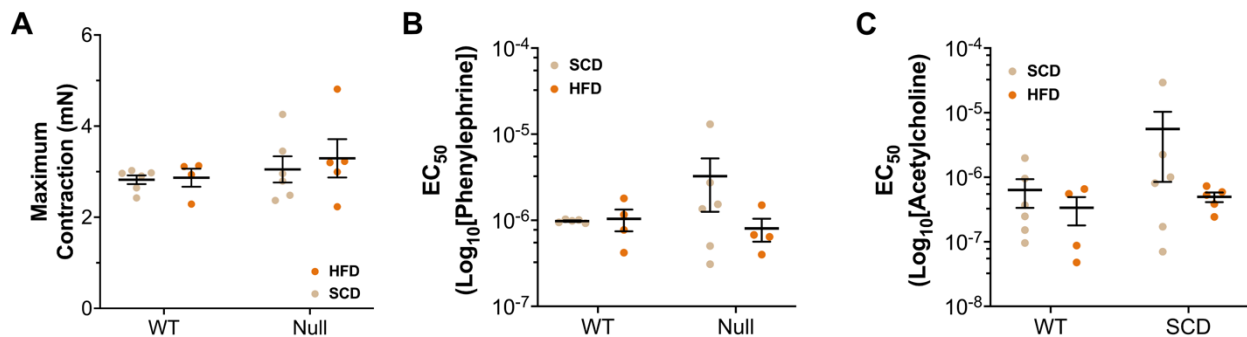


Figure 4.5. Aortae of *Rab27a* null male mice viability remained unaltered compared to the aortae of WT mice after a HFD. A) Vessel viability was tested with a 100 mM KCl dose for all experimental groups. B) Sensitivity (EC_{50}) of male aortae to phenylephrine were calculated for all experimental groups. C) Acetylcholine sensitivity for male aortae across all groups was also calculated. Sensitivity was calculated to account for difference in contractile or dilative responses to each agonist. Each data point displays the calculated result for an individual mouse. Significance was determined using an ordinary two-way ANOVA with a multiple comparisons test. Only significant comparisons are shown.

4.5. Chapter Discussion

With the increasing prevalence of obesity and high prevalence of CVD, it is imperative improve to our understanding of biological mechanisms connecting these medical conditions^{13,48,82}. Despite the on-going attempts to identify effective therapeutic targets to treat obesity, none have been successful in sustaining weight loss for extended periods of time within large patient populations⁷⁹. Furthering our knowledge of the obesity and cardiovascular disease interface has the potential of identifying novel therapeutic targets that could applied to prevent cardiovascular disease establishment in patients with obesity. In *Chapter 3*, we established that rare *RAB27A* variants are associated with BMI and glucose handling, and that global loss of *Rab27a* impacted vascular reactivity in an age and sex dependent manner (**Figures 3.1, 3.12, and 3.14**)²⁸. For this purpose, we studied whether *Rab27a* plays a role in regulating vascular physiology of the male mouse after a 60% HFD.

4.5.1. Conclusions

We have implemented a diet-induced weight gain study to evaluate the importance of *Rab27a* in regulating vascular activity during a HFD. With this work, we applied anthropometric, histological, and physiological response studies to lay the foundational work showing that *Rab27a* impacts vascular reactivity during times of metabolic challenge (**Figure 4.6**).

As with the chow diet study, changes in the weight gain of *Rab27a* null and WT mice that were fed either a HFD or SCD were quantified. As previously reported, the WT male mice that were fed a HFD gained weight significantly compared to the WT controls fed a SCD. No significant difference in weight between *Rab27a* null and WT mice that were fed the same diet was found at any time point. However, when comparing the variation between the *Rab27a* null and WT male mice fed a HFD, there was a genotype association ($P < 0.001$), suggesting that loss of *Rab27a* may be impacting the overall weight gain trends (**Figure 4.1**). When statistically comparing the body composition of the *Rab27a* null and WT mice, genotype was significantly

associated at week 0 of the diet. Further, no significant association was found in connection with genotype when analyzing for changes in % lipid accumulation within PVAT, BAT, or iWAT. These data therefore support that global *Rab27a* expression does not affect weight gain or the lipid storage capabilities of adipose depots of male mice after a HFD.

However, there is evidence that global loss of *Rab27a* impacts vascular reactivity. After 12 weeks on a HFD diet, *Rab27a* null aortae show increased contractility when stimulated with increasing doses of phenylephrine compared to all other experimental groups. However, while contractile of the WT diet groups were not significantly different, the WT, HFD and *Rab27a* null, SCD responses were. Additionally, these changes in contractile responses occurred in the absence of gross morphological changes.

These *Rab27a* null diet results are distinct from those of chow fed mice, as the 20-week-old aortae showed no changes in vasocontractility, which is the age of the mice upon completion of the diet. Furthermore, previous studies also showed that the PVAT of animals fed a HFD significantly limits aorta dilation^{191,199}. Another study also showed that obesity in mice inhibited the anticontractile effects of PVAT on the thoracic aorta⁵⁵. This study is therefore the first to show that global loss of *Rab27a* increases the thoracic aorta contractile response after a 60%, even when limited to a 12-week diet.

Global *Rab27a* loss increases aorta contractility during HFD

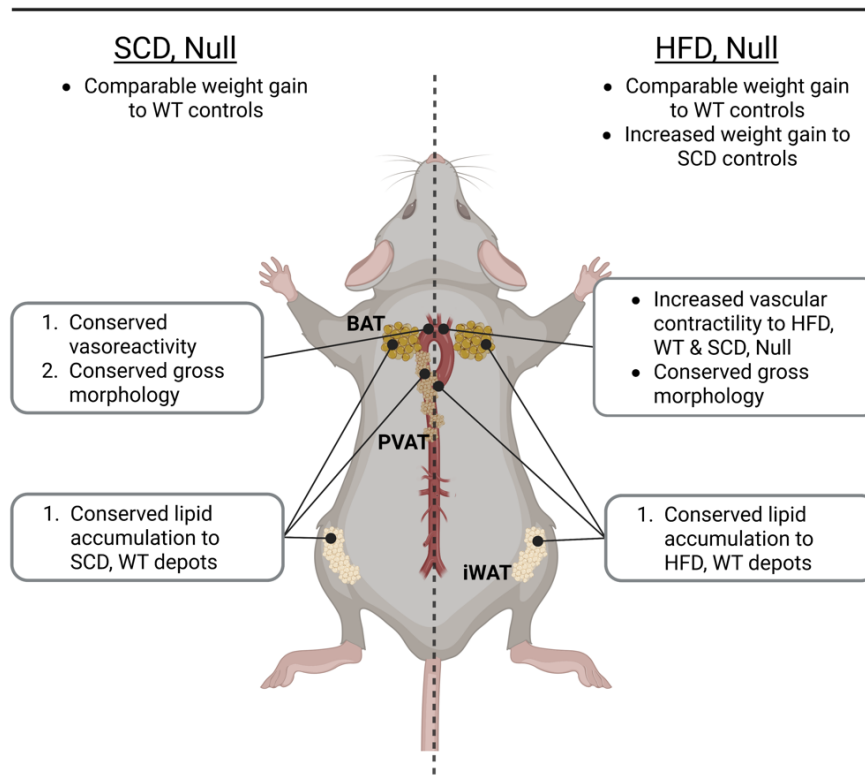


Figure 4.6 Summary of Chapter 4 conclusions. Graphical depiction of major study conclusions for male *Rab27a* null mice fed a HFD or SCD in comparison to WT controls. Created with BioRender.com

4.5.2. Limitations

While this study was intentionally designed to account for the effects of genotype and diet, there are experimental limitations that impacted the conclusions that we made. Future experiments are necessary to either expand up or provide additional information to augment the findings discussed in the above sections. Some of the major limitations and potential solutions are described as follows.

4.5.2.1. C57BL/6J Background Variability with Weight Gain

Throughout this study, we utilized the novel global *Rab27a* null strain that was created on a C57BL/6J background. This strain was intentionally selected as much of the HFD, and cardiovascular work completed by the Liaw laboratory, has also used the C57BL/6J background. Literature has also favored the used of the C57BL/6J strain for diet-induced obesity and metabolic disease studies due to their propensity for weight gain and for the males to develop insulin resistance^{193,194}. However, it is also important to consider that there are many other strains that have been shown to respond to diets uniquely²⁰⁰. For this reason, the conclusions reached within this paper must take the genetic background of the mice into account. Unfortunately, it is not reasonable to establish a global *Rab27a* null strain for all the strains utilized for metabolic and cardiovascular studies. Therefore, it will be important to expand the sample size for each group to account for weigh gain variability.

4.5.2.2. Sole Use of the Global *Rab27a* Null Strain

Also noted as a limitation for the study completed in *Chapter 3*, conclusions to the effects of *Rab27a* loss on vascular tone is limited to the context of global expression. Due to the wide expression of *Rab27a* throughout the body, no conclusion can currently be made on whether a specific cell type or tissue is primarily responsible for these phenomena. To address this current limitation, the *Rab27a* conditional null strain will be utilized for targeted recombination. Based upon results from this study, it will be important to target *Rab27a* loss within the major cell types within the vascular microenvironment (*refer to Section 3.10.3.1*).

4.5.2.3. The Impact of Insulin Sensitivity on Vascular Reactivity

Communication between the PVAT and aorta is dependent on the depot's metabolic phenotype and changes in communication impact vascular tone^{55,158}. It has been shown that when fed a HFD, C57BL/6J mice develop insulin and leptin resistance after 9 and 10

weeks^{162,193,201}. This information is important as insulin sensitivity is also associated with vessel physiology²⁰². Therefore, it is possible that changes in insulin sensitivity of the mice fed a HFD is impacting aortic reactivity.

Future work will need to complete insulin and glucose sensitivity tests to determine whether *Rab27a* null mice exhibit changes compared to WT and diet controls. While the diet-induced weight gain may be impacting insulin sensitivity in the *Rab27a* null mice, it may not be responsible for the significant difference in contractile responses between the aortae of *Rab27a* null and WT mice fed a HFD. Furthermore, no significant differences in dilative responses were observed between these groups, further suggesting the effect may be specific to contractile responses.

If male mice prove to exhibit changes in insulin sensitivity, then the female *Rab27a* null and WT mice might be used as insulin and glucose sensitive controls during HFD. This could be possible as the *Rab27a^{ashen}* females showed no significant changes in glucose sensitivity with aging (*Soucy et al., 2023 under revision*) and C57BL/6J retain glucose and insulin sensitivity longer when fed a HFD¹⁶². Furthermore, C57BL/6J females have are also known to not develop insulin resistance during a HFD¹⁹⁵. Therefore, it is expected that the *Rab27a* null females would exhibit similar trends.

4.5.3. Future Directions

The prevalence of metabolic disease and associated comorbidities are on the rise globally⁸². For this reason, it is critical to increase our understanding of how obesity impacts vascular health. While the current study provides evidence that *Rab27a* expression impacts thoracic aorta contractile abilities after a HFD, many more questions remain that could be addressed through future studies.

4.5.3.1. Increasing Statistical Power by Expanding Sample Size

Data and statistical analyses presented within this study consisted of four experimental groups with sample sizes ranging from 4-8 mice per group. Statistical analyses revealed that experimental groups of these sizes do show significant differences in body weight and composition, lipid accumulation, and vasoreactivity. However, expanding the sample size to n=10/group would be statistically stronger based upon our study completed in *Chapter 3* of this document. Having an increased sample size per group will also help to overcome the occurrence of thoracic aortae that are unresponsive to chemical agonists or determined to be statistical outliers.

4.5.3.2. Extending the Diet Study Duration to Determine the Long-Term Effects of *Rab27a* Loss on Male Mice Fed a 60% High Fat Diet

In the earlier study, we attempted to account for age as a biological variable by quantifying the vessel area of thoracic aorta from mice at 8 and 20 weeks of age and saw no significant differences. Here, we again show that at 20 weeks of age, diet also has no effect on vessel area. However, the lack morphological changes may be the result of examining young adult mice and concluding the diets at 12 weeks. Previous studies showed that changes in vessel morphology begin around 16-20 weeks of a HFD within the rat mesenteric arteries⁵⁶. Furthermore, because of the age-dependent effects on thoracic aorta reactivity observed during the chow diet, it is also possible that expanding the HFD diet duration would help us to better understand the effects of global *Rab27a* loss during HFD due to aging. Meanwhile changes in vessel physiology were not observed in C57BL/6J mice until week 18 on a HFD from other studies^{191,199}.

4.5.3.3. Evaluating the Importance of Sex as a Biological Variable

There is increasing evidence that sex is an important biological variable that must be considered when studying metabolic and cardiovascular^{62,69}. Studies have shown that while male and female mice of most strains gain weight when fed a HFD, females tend to accumulate weight at a slower rate¹⁶². Also, the distribution of fat mass, due to the expansion of different adipose depots, is unique between males and females^{161,162}. It is suggested that differences in body composition and depot expansion can be impacted by estrogen expression²⁰³.

Together with the evidence provided in *Chapter 3*, it is probable that there are sex dependent effects of global *Rab27a* loss during HFD. To improve the relevance of this study, *Rab27a* null and WT female mice need to also be examined in the same manner as their male counterparts. Should the results support these predictions, it would also be important to expand the study to examine the effects of global *Rab27a* loss during HFD on ovariectomized females^{72,161}. Such a study would help to determine whether the loss of estrogen during development results in male associated vascular reactivity trends¹⁹².

4.5.3.4. Utilize Proteomic Analysis to Identify Possible Mechanisms Driving Altered Aortic Physiology in *Rab27a* Null Mice Fed a 60% High Fat Diet

Obesity has been shown to impact the metabolic state of adipose tissues and adipocytes through multiple proteomic studies. Some data has also suggested that there are also proteomic signature differences between metabolically healthy and metabolically diseased patients with obesity. However, no study has examined how global loss of *Rab27a* during a HFD impacts the proteomic profile of the vascular microenvironment.

With this study, we provide evidence that *Rab27a* null males exhibit increase thoracic aorta contractility when fed a HFD. Utilizing frozen tissue samples from these mice, a proteomic analysis of multiple adipose depots and thoracic aortae is possible. We have already shown that global loss of *Rab27a* in chow fed mice alters the expression of proteins associated with

metabolic and cardiovascular phenotypes. Therefore, it is predicted that global *Rab27a* loss during a HFD would also affect the proteome of the vascular microenvironment. Completion of this study will provide insight will help to identify the signaling pathways that are regulated by *Rab27a* during HFD.

4.5.3.5. Characterizing the Effects of Global *Rab27a* Loss After a 60% High Fat Diet on Circulating Exosome Populations

Complementary to the proposed tissue proteomic study described above, examining the circulating exosome populations from these experimental groups is another important study. In Chapter 3, we provided evidence that global loss of *Rab27a* in male mice on a standard diet show moderate changes in protein cargo without changes in size or concentration (**Figure 3.27**). As obesity has already been shown to alter exosome cargo, we predict that loss of *Rab27a* during a HFD would result in additional changes to exosome cargo^{117,204}. This study would therefore have the potential to identify specific protein cargo associated with vascular contractile physiology. Identification of such a protein would be an enticing candidate as a therapeutic target for CVD.

CHAPTER 5: GLOBAL DISCUSSION

5.1. Overview

The primary goal of this work was to establish whether *Rab27a* is a mediator of thoracic aorta reactivity. *Rab27a* has a known role as a regulator of cellular communication via extracellular vesicle secretion⁹. Communication between the PVAT and aorta are a critical component of vascular health¹⁰². Further, an original study from our lab suggested that RAB27A expression impacts PVAT APC differentiation and lipid storage capabilities¹³⁶. Together, these works suggested that *Rab27a* may play a regulatory role in thoracic aorta physiology via PVAT-aorta signaling.

To best study the impact of *Rab27a* loss on vascular physiology, a novel global *Rab27a* null mouse strain on a C57BL/6J background was established through the Mouse Genome Modification Core at the MaineHealth Institute of Research. This strain allowed us to complete molecular, proteomic, morphological, and physiological experiments to evaluate whether global loss of *Rab27a* impacted the vascular microenvironment. Furthermore, with the growing prevalence of obesity, we were also able to apply this model to a pilot investigation into the impact of global *Rab27a* in mice with diet-induced weight gain⁷⁹.

5.1.1. Global Loss of *Rab27a* Alters Thoracic Aorta Reactivity Uniquely in Male and Female Mice

Within *Chapter 3*, we lay foundational work characterizing a vascular phenotype within male and female *Rab27a* null mice at 8 and 20 weeks of age. To our knowledge, connecting *Rab27a* expression to vascular reactivity is a novel contribution to this field. Previous studies on *Rab27a* knockout mice and humans diagnosed with type II Griscelli syndrome have not been reported to exhibit cardiovascular phenotypes^{134,141,205}. However, initial studies were focused on understanding the dysregulation of immune responses, which is a primary phenotype associated with Griscelli syndrome^{134,135}.

Using wire myography, we showed that *Rab27a* null males exhibit increased vasocontractile and reduced vasodilative responses at 8 weeks of age compared to age-matched WT controls. Because our data show increased contractility with aging between WT mice at 8- and 20-weeks-old, we conjecture that these data indicate an aging effect in the aorta of male mice at 8 weeks of age. However, this trend is not observed when comparing the data of the male *Rab27a* null and WT cohorts at 20 weeks of age. Interestingly, while no changes in vasoreactivity was observed in male mice at 20 weeks of age, the female *Rab27a* null mice did. At 20 weeks of age, female *Rab27a* null mice displayed increased vasoconstriction and vasodilation compared to age-matched WT controls. According to the female data, we postulate that the global loss of *Rab27a* in female mice may be protective against the effects of aging, as WT trends show decreased contractility and no effect on vasodilation when comparing WT females at 8 and 20 weeks of age. However, it is again critical to recognize that additional work is necessary to determine whether these changes in vasoreactivity are biologically significant to the health of these animals.

Supporting evidence of altered vascular physiology was obtained through mass spectrometry analysis of PVAT and aortic tissues from the male *Rab27a* null and WT mice at 8 and 20 weeks of age. Analysis of significantly altered proteins showed that the *Rab27a* null PVAT and aortic tissue were enriched for phenotypes associated with the cardiovascular system in addition to metabolic and homeostasis phenotypes. Immunofluorescence was used as a validation method with representative male tissues to confirm the directionality changes of ACTA2 and MYH6. The reduced expression of contractile and increased ECM markers suggests that the VSMC phenotypes may be impacted by loss of global *Rab27a* expression^{44,54}. Interestingly, no gross morphological changes were detected either in the PVAT or aortae, suggesting that more subtle changes are occurring within these tissues. Therefore, additional studies are required to test this prediction.

As a proposed mechanism inducing these changes within the vascular

microenvironment, we provide evidence that the population of exosomes circulating throughout *Rab27a* null male mice have altered protein cargo compared to their WT controls. These changes occur in the absence of altered vesicle diameter and concentration, suggesting that global loss of *Rab27a* is impacting exosome-mediated communication. However, additional mechanistic studies are necessary to understand whether these altered proteins are capable of inducing changes in aorta vascular reactivity.

These data support the need for continued study of how *Rab27a* impacts vascular physiology. Additionally, the association of rare *RAB27A* variants with human metabolic phenotypes, and the presence of *RAB27A* in the vascular microenvironment, provide evidence of a conserved importance between the two species²⁸. Therefore, it is possible that a better understanding of the role *Rab27a* in vascular health could help to identify a novel therapeutic target for cardiovascular disease patients.

5.1.2. Global Loss of *Rab27a* Increased the Thoracic Aorta Contractile Response of Male Mice After a 60% High Fat Diet

Having established a vascular phenotype with the global *Rab27a* null mice under baseline metabolic conditions, we aimed to determine whether these mice exhibited a unique phenotype when after being fed a 60% HFD for 12 weeks. Wire myograph data showed that global loss of *Rab27a* during a HFD significantly increased thoracic contractility without altering dilation abilities. Again, these changes occur without significant genotype-associated differences in vascular or adipose tissue morphology. The combined effect of global *Rab27a* loss and HFD in male elicited a very different vascular physiological response compared to the chow diet cohort where no significant in contractility was observed at 20 weeks of age. These data therefore suggest that diet and genotype need to be examined together to better understand the importance of *Rab27a* expression in vascular health. These results should therefore be considered when evaluating the effects of targeted *Rab27a* loss in future studies, as a metabolic

challenge may be required to fully characterize novel mouse strains.

It is possible that global loss of *Rab27a* during a HFD limits intercellular and inter-organ communication. A recent study showed that exosomes from adipose tissue can confer cardiac protective effects¹¹⁶. Other studies have also produced evidence that altered exosome cargo contribute to atherosclerotic plaque development^{121,189}. Although analysis of proteomic signatures and circulating extracellular vesicles have yet to be completed, these initial findings support that *Rab27a* is a modulator of vascular health during diet-induced weight gain.

5.2. Important Considerations for Future Studies

Due to the growing concern of reproducibility and conclusion disparities between studies, it is important to recognize and discuss such disparities within this work. Of particular importance are differences in the role of *Rab27a* in regulating lipid accumulation within adipose tissue and the dysregulation of exosome secretion^{9,136}. While there is no reason to question the reproducibility of these studies, identifying potential explanations for how these disparities arose could help with the design and interpretation of future studies.

5.2.1. Accounting for the Differences in the Effects of *Rab27a* Loss Between Human Primary Cell and Murine *In Vivo* Studies

The premise for the studies discussed above was based on findings that showed loss of *RAB27A* expression in human PVAT APCs reduced their differentiation and lipid storage capacity¹³⁶. We predicted that the global loss of *Rab27a* in mice would recapitulate these findings. However, no changes in in % lipid accumulation within the PVAT, BAT, and iWAT of *Rab27a* null vs WT mice was observed. Similarly, no significant difference was observed in % lipid accumulation between *Rab27a* null and WT mice when fed a HFD for 12 weeks. These studies therefore require consideration regarding the underlying factors which may be contributing to these inconsistencies.

5.2.1.1. Differences Between Human and Mouse Adipose Depots

C57BL/6J mice have been a favored murine strain for studying the effects of diet-induced obesity and metabolic disease comorbidities²⁰⁶. However, it is important to recognize that there are inter-species differences between human and mouse adipose depots. For example, while both species have subcutaneous and interorgan adipose depots, the anatomical locations are unique to each species²⁰⁷. Because of these differences in anatomical locations, recent studies have been working to identify which murine depots best match those found in humans^{207,208}. However, even when isolated from matching anatomical regions, differences in adipocyte lineage compositions are found between humans and mice⁹⁶. Furthermore, due to the invasive nature of acquiring human adipose depots, including PVAT, there is limited work in characterizing inter-species differences²⁰⁹. Therefore, there may be unique properties of human PVAT that lead to differences in the effects of *Rab27a* on adipocyte. Future studies in this field are required to increase the relevance of mouse-based research models for cardiovascular and metabolic diseases.

5.2.1.2. Differences Between Human and Mouse PVAT

The presence of PVAT surrounding the vasculature is highly conserved between humans and mice¹⁰². Prior studies have also indicated that human and mouse PVAT impact vascular contractile and dilative responses^{18,210}. Recent studies showed that rodent PVAT exhibits distinct metabolic phenotypes depending on its anatomical location^{8,211}. Due to the invasive procedures required to obtain human PVAT and vascular samples, most studies examining the vasoreactivity effects of PVAT have been completed in rodent models^{136,196,212,213}.

There are, however, studies showing that there are differences between the WAT of humans and mice. Of particular relevance to this work is that visceral WAT is thought to have higher browning potential in humans, while subcutaneous WAT has greater browning potential in mice⁹⁶. It is also important to note that while most adipose depots are conserved between the

two species, mice do have unique depots and pads compared to humans²⁰⁷. For this reason, there are likely species-dependent differences between the human and rodent that are currently unknown²⁰⁹.

5.2.1.3. Differences of Cellular Responses Between *In Vivo* and *In Vitro* Methods

The application of both *in vivo* and *in vitro* experimental approaches has been critical to allow for the study of biological phenomena and their underlying mechanisms. For example, the identification of genes that regulate adipocyte differentiation was accomplished using *in vitro* techniques^{91,214}. However, other studies have shown that utilizing *in vitro* analyses alone do not provide the full complexity of biological interactions that illicit cellular response that occur *in vivo*^{21,85}. Therefore, the limitations of both experimental approaches are proposed reasons for why no change in % lipid accumulation was observed in PVAT, BAT, or iWAT histological sections within this study.

As an endocrine tissue, PVAT is a dynamic depot composed of multiple cell types capable of communicating with each other^{215,216}. *In vitro* culture of human PVAT APCs eliminates the diversity of cellular communication found within the tissue²⁴. Loss of these dynamic signaling pathways potentially impacts their ability to adapt to the loss of RAB27A expression. Therefore, while the application of adipogenic media is widely used to induce adipocyte differentiation and *de novo* lipogenesis, without stimuli from other cell types they may not be able to differentiate as when in their native niche²¹².

Another important consideration is the duration of *Rab27a* loss within the experimental model. The original study that provided evidence for the importance of RAB27A in the differentiation and lipid accumulation of PVAT APCs utilized *in vitro* methods¹³⁶. Therefore, it is assumed that these PVAT APCs were derived from a human that expressed *RAB27A* throughout development. Meanwhile, *Rab27a* is absent during the development and life of the *Rab27a* null mice utilized in this study. As a regulator of intercellular signaling and immune

system response, there is potential for a compensatory mechanism within this novel *Rab27a* null strain^{9,135}.

5.2.2. An Absence of *Rab27a*-Induced Changes in Exosome Size and Concentration

The role of *RAB27A* in regulating exosome secretion is connected to an original research article utilizing HeLa cells⁹. Since then, additional experiments have been completed with knockdown of *Rab27a* in other human and murine studies providing further evidence^{129,143,156}. Another study also provided evidence that bone marrow endothelial cells from a different *Rab27a* null strain exhibited reduced exosome secretion *in vitro*²¹⁷. Conversely, the data we provided suggested that global loss of *Rab27a* does not impact the size or number of circulating exosomes. While these results do not align with previously published trends, the particles isolated and analyzed from the *Rab27a* null and WT mouse plasma samples adhere to the defined diameter range of 30-150 nm^{11,115}. Based on the size of these analyzed particles, we predict that these discrepancies may be the result of differences in experimental approaches and the use of *in vivo* versus *in vitro* models.

5.2.2.1. Different Extracellular Vesicle Isolation Approaches

Another possible explanation for differences in our results from previous studies are the applied isolation procedures. While ultracentrifugation has been set as the preferred method for the isolation of extracellular vesicles, this method results in high purity samples with low yields¹⁸⁴. Due to limited sample sizes, commercially available lipid precipitation kits are often used to improve yield at the cost of sacrificing purity depending on the sample type¹⁸⁴. This study utilized ultrafiltration and size exclusion chromatography to isolate exosomes from mouse plasma. Therefore, it is possible that these different isolation procedures contribute to the differences between exosome studies.

5.2.2.2. Different Approaches to Normalization of Extracellular Vesicle Concentrations

One potential difference between these previous studies and ours is the application of normalization methods. For example, in our study, exosome concentrations were normalized to the body weight of the mouse that the samples were collected from. As almost every cell type is capable of secreting extracellular vesicles, normalizing to body weight would help to account for differences in cellular mass capable of contributing to the circulating exosome and extracellular vesicle populations^{121,122}. Normalization methods for *in vitro* experiments, such as cell number and quantified tissue area, were applied in other studies^{122,143,218}. Because most *in vitro* studies isolate extracellular vesicles from conditioned media, cell number and growth rates are important factors that should be accounted for^{218,219}. Therefore, the difference in normalization methods between *in vivo* and *in vitro* approaches may also help to explain some of the disparities between studies.

5.3. Potential Compensatory Mechanisms for Global *Rab27a* Loss

Rab27a belongs to a larger family of proteins that are associated with endosomal formation and trafficking²²⁰. While most share conserved structures, Rab proteins exhibit a wide range of unique functions^{10,221}. The biological function of a Rab protein is determined by sequence variability in the Switch II binding domain: the binding site for effector proteins (**Figure 5.1**)^{31,32,36,220,222}. Due to their similar yet distinct roles, it is possible that Rab family members may be able to serve as compensatory mechanisms^{6,10,11}. We conjecture that a global loss of *Rab27a* within an animal model may elicit a compensatory mechanism due to the age-associated changes in both protein expression and thoracic aorta vasoreactivity observed within our study. Of the proteins constituting the Rab family, three possibilities stand out as potential compensatory mechanisms: RAB27B, RAB35, and RAB11A¹⁰. Defining whether these Rabs experience altered expression patterns during RAB27A loss would increase our understanding of the dynamic natures of these endosomal trafficking proteins.

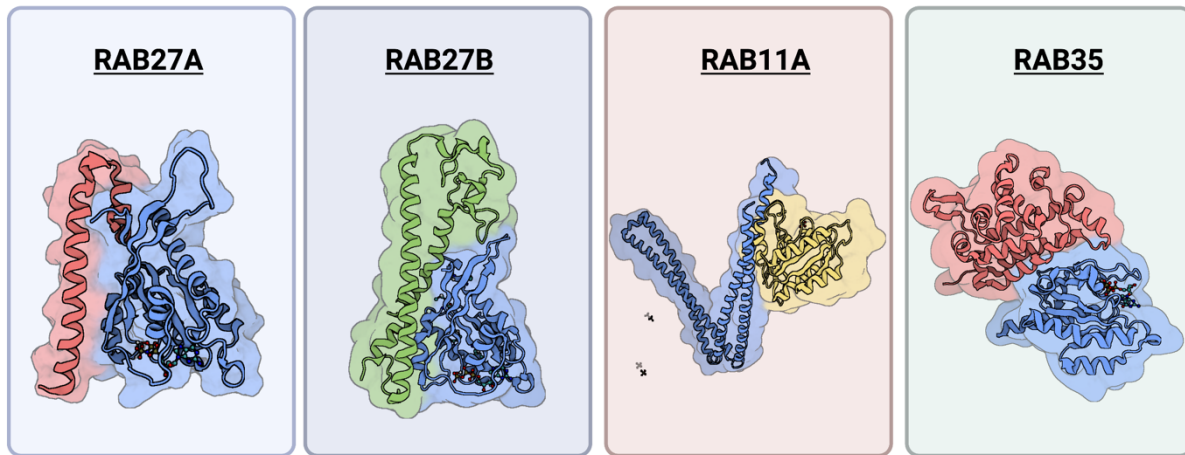


Figure 5.1. Rab proteins are structurally similar. Protein structures were obtained from the Protein Data Bank (wwpdb.org)³⁰. RAB27A structure (3BC1, blue) when bound to its effector Spi2a (red)³¹. RAB27B structure (2ZET, blue) when bound to its effector Slac2 (green)³². RAB11A structure (6IXV, yellow) when bound to its effector SH3BP5 (yellow)³². RAB35 structure (6IF2, blue) when bound to its effector protein RUSC2 (red)³⁶. Created with BioRender.com.

5.3.1. RAB27B Regulates Endosome Speed and Docking to Plasma Membrane

RAB27B has been shown to impact exosome secretion through limiting late endosome fusion with the plasma membrane⁹. According to the original study, that was completed in HeLa cells, there was a distinct perinuclear colocalization pattern of MVBs during RAB27B knockdown⁹. Interestingly, an additional study provided evidence that overexpression of RAB27B is connected to increased extracellular vesicle secretion and changes in protein cargo²²³. Another study also provided evidence that RAB27B is expressed in humans and mice, suggesting a conserved biological function between species²²⁰. RAB27B is also predicted to be the most like RAB27A based upon sequence similarity, further suggesting the two have similar biological roles^{220,221}. Due to sensitivity thresholds for mass spectrometry analysis, RAB27B and RAB27A were not quantifiable within our current proteomic study. Similarly, compilation of publicly available tissue expression data (accessed through the Common Metabolic Disease Portal) also suggests that RAB27B has relatively low expression in adipose tissue and the cardiovascular system^{157,224}. It is currently unknown whether our novel global *Rab27a* null mice

exhibit increased RAB27B expression to maintain extracellular vesicle-mediated communication. However, the effects of altered RAB27B expression on exosome secretion and protein cargo may help explain the unchanged concentration of circulating exosome populations and their altered cargo observed in this study^{9,223}.

5.3.2. RAB35 Regulates Protein Recycling to the Plasma Membrane via Endosome Trafficking

The primary role of RAB35 is regulating protein recycling to the plasma membrane via endosomal trafficking¹⁰. Other work also suggested a role for RAB35 in exosome secretion^{10,11}. In addition to being expressed in both mice and humans, expression has also been recorded within adipose and cardiovascular tissues based on data from the Common Metabolic Disease Knowledge Portal^{220,225}. Additionally, RAB35 is predicted to be the next closest related Rab to RAB27A of the three mentioned in *Section 5.3*²²¹. However, RAB35 does not show as strong associations with cardiovascular phenotypes when compared to RAB11A and RAB27A²²⁵. A study also exists that provides evidence of a role for RAB35 in glucose transporter 4 (GLUT4) transport within adipocytes²²⁶. Therefore, despite the lack of high expression within adipose and cardiovascular tissue, there is evidence that RAB35 has potential as a compensatory mechanism for global loss of *Rab27a*.

5.3.3. RAB11A Regulates Exosome Secretion via Endosomal Recycling

RAB11A has been established as a regulator of the endosomal recycling pathway, that is also associated with extracellular vesicle secretion¹⁰. A recent study has also provided evidence that RAB11A expression is critical for maintaining vascular endothelial barriers via VE-cadherin recycling²²⁷. Like both RAB27A and RAB27B, RAB11A is expressed within humans and mice²²⁰. Interestingly, unlike the RAB27 family members, homozygous knockout of RAB11A results in an embryonic lethal phenotype²²⁸. Additionally, *Rab11a* and *Rab27a* are located on the same chromosome within mice and humans^{135,138,229,230}. According to the Common

Metabolic Disease Knowledge Portal, human RAB11A is expressed within adipose tissue and the cardiovascular system²³¹. The *RAB11A* gene page from the Common Metabolic Disease Knowledge Portal also suggests that rare *RAB11A* variants are associated with increased odds for myocardial infarctions and decreased diastolic blood pressure²³¹. This is interesting because, of the three Rabs suggested as possible compensatory mechanisms, RAB11A is the least similar to RAB27A²²¹. Together, this information suggests that RAB11A may be a potential compensatory mechanism during global *Rab27a* loss.

5.4. A Need for Conditional *Rab27a* Loss Within the Vascular Microenvironment

To expand this current project, it will be necessary to utilize our novel *Rab27a^{fl/fl}* strain to induce recombination, and therefore loss, of *Rab27a* within specific cell types. Such work will help to identify the unique cell populations that can regulate thoracic aorta contractility and to better study the underlying mechanisms. Cell types that are of particular interest include PVAT APCs, VSMCs, and vascular endothelial cells^{105,217,232}. While each of these cell types are known contributors of vascular reactivity, the importance of *Rab27a* in these cells for the maintenance of vascular physiology is poorly understood^{105,183,232,233}.

5.4.1. Targeting *Rab27a* Loss Within PVAT APCs

While PVAT is composed of multiple cell types, studies provide evidence that PVAT adipocytes exhibit different phenotypes depending on their anatomical location¹⁰². Classified as beige adipocytes, PVAT adipocytes of the thoracic aortic region have been shown to arise from *Pdgfra*⁺ lineages¹⁰³. However, additional studies have also shown the PVAT adipocytes also express the myogenic 5 positive (*Myf5*⁺)^{210,234}. For this reason, inducing *Rab27a* loss in *Myf5*⁺ cells may allow us to study the importance of *Rab27a* expression within PVAT APCs in regulating thoracic aorta reactivity.

5.4.1.1. Establishing the *Rab27a^{fl/fl};tdTomato;Myf5^{Cre}* Mouse Strain

To establish this model, we selected to breed the B6.129S4-*Myf5^{tm3(cre)Sor/J}* strain (The Jackson Laboratory, #007893) with our novel *Rab27a^{fl/fl}* mice with the assistance of the Mouse Genome Modification Core within the MaineHealth Institute for Research^{235,236}. Although derived from 129 embryonic cells, the strain was backcrossed to a C57BL/6J background and therefore allowed us to match genetic backgrounds with our *Rab27a^{fl/fl}* strain²³⁶. The *Myf5^{Cre}* strain had been previously crossed with the ROSA26-tdTomato strain (B6.Cg-Gt(*ROSA*)26Sortm14(CAG-tdTomato)Hze/J, The Jackson Laboratory, #007914) to track Cre expression within tissues²³⁷. Genotyping of initial litters confirmed the presence of tri-genic offspring (**Figure 5.2**). Due to the rederivation process and necessary breeding scheme, characterization of these tissues is just beginning. With the genotyping confirmed, it will be important to begin confirming specific loss of RAB27A expression within PVAT, BAT, and skeletal muscle because all are known to express *Myf5*²³⁵.

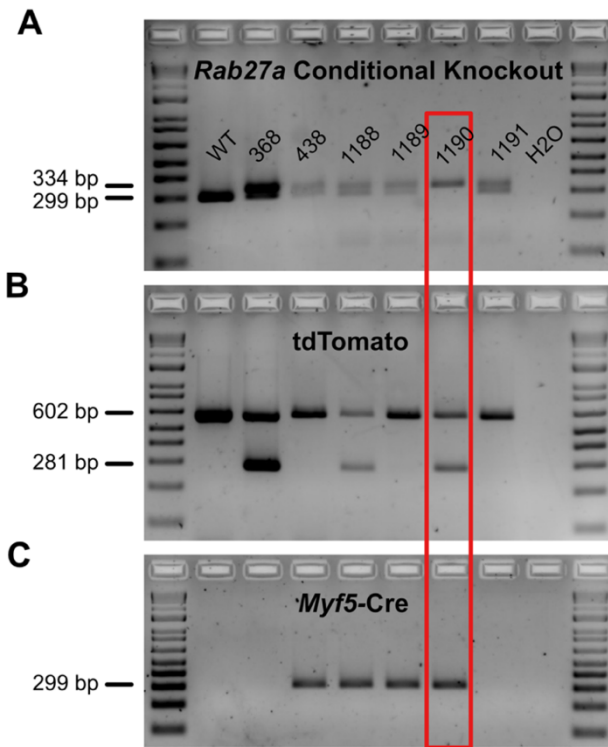


Figure 5.2. Establishment of the *Rab27a^{fl/fl}*;tdTomato;Myf5^{Cre} strain.

Gel images of a representative genotyping if the tri-genic *Rab27a^{fl/fl}*;tdTomato;Myf5^{Cre} mouse strain. A) *Rab27a* PCR products with WT exhibiting product length of 299 bp while presence of loxP sites increases product size to 334 bp. B) PCR products separated according to size for the presence of the tdTomato sequence. Presence of the tdTomato product results in a band size of 602 bp without recombination and 281 bp with recombination. C) PCR products separated for size determining the presence of the Cre sequence. Presence of Cre sequence should result in PCR product of 299 bp. Genomic DNA was isolated from IACUC approved tissues. *Genotyping was completed by Abby Kaija, Research Assistant (Liaw laboratory, MHIR).*

5.4.1.2. Use of the *Rab27a^{fl/fl}*;tdTomato;Myf5^{Cre} May Limit the Activation of Compensatory Mechanisms

With the *Rab27a* null strain, there is a potential that compensatory mechanisms are occurring²³⁸. This is a possible explanation for why male *Rab27a* null mice exhibit altered thoracic aorta contractility at 8 weeks of age, but not 20 weeks of age. The presence of a compensatory mechanism would also help to explain why a reduction in adipocyte differentiation and lipid storage capacity is observed with *in vitro* model and not *in vivo* models. Therefore, by limiting *Rab27a* loss to specific cellular lineages, there is the potential that we will limit the activation of global compensatory mechanisms. If this is true, then we would expect to observe consistent expression of close Rab family members and effector proteins. To our current knowledge, no specific compensation mechanism for *Rab27a* has been identified; however, it is critical to consider that such a mechanism exists.

5.4.2. Targeting *Rab27a* Loss in Vascular Smooth Muscle Cells

We have provided evidence that RAB27A is expressed within the VSMCs of the human and mouse thoracic aorta. Through proteomic immunofluorescence approaches, we provide evidence that global loss of *Rab27a* impacts the expression of multiple contractile proteins. Combined with the altered thoracic aorta reactivity observed using wire myography, it is plausible that loss of *Rab27a* within VSMCs is responsible for the altered vessel contractile and dilative responses.

5.4.2.1. Establishment of the *Rab27a^{fl/fl};tdTomato;SMMHC^{CreERT2}* Strain

To target recombination of *Rab27a* we bred our novel *Rab27a^{fl/fl}* strain with the B6.FVB-Tg(Myh11-icre/ERT2)1Soff/J (*SMMHC^{CreERT2}*, The Jackson Laboratory, #019079) under the guidance of our Mouse Genome Modification Core Facility²³⁹. The *SMMHC^{CreERT2}* strain was generously donated by Dr. Stephan Offermanns (Max-Planck Institute for Heart and Lung). This ERT2-inducible *SMMHC^{CreERT2}* strain has been utilized to induce recombination within smooth muscle tissues²³⁹. For this reason, recombination of *Rab27a* within our *Rab27a^{fl/fl}* strain should occur within VSMCs, which compose the aorta vessel wall, without disrupting expression in the other tissues of the vascular microenvironment²³⁹. To assist with confirming tissue-specific expression of the Cre upon tamoxifen injection, the Mouse Genome Modification Core interbred the *Rab27a^{fl/fl};SMMHC^{CreERT2}* mice with the ROSA26-*tdTomato* strain (B6.Cg-Gt(ROSA)26Sortm14(CAG-*tdTomato*)Hze/J, The Jackson Laboratory, # 007914) to create a tri-genic strain (**Figure 5.3**)²³⁷.

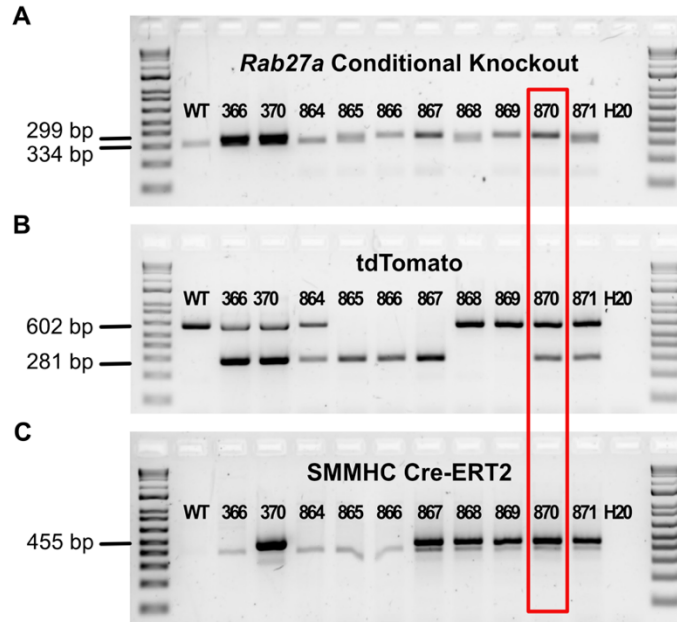


Figure 5.3. Establishment of the *Rab27a^{fl/fl}*; *tdTomato*; *SMMHC Cre-ERT2*. Gel images of a representative genotyping of the tri-genic *Rab27a^{fl/fl}*; *tdTomato*; *SMMHC Cre-ERT2* mouse strain. Genomic DNA was isolated from IACUC approved tissues. A) *Rab27a* PCR products with WT exhibiting product length of 299 bp while presence of loxP sites increases product size to 334 bp. B) PCR products separated according to size for the presence of the *tdTomato* sequence. Presence of the *tdTomato* product results in a band size of 602 bp without recombination and 281 bp with combination. C) PCR products separated for size determining the presence of the Cre-ERT2 sequence. Presence of Cre-ERT2 produces a product of 455 bp. WT = C57BL/6J control, 366 = female parent and 370 = male parent of matching (*Rab27a^{fl/fl}*; *tdTomato^{+/-}*; *SMMHC Cre-ERT2^{+/+}*) genotypes. Red box identifies offspring with desired matching genotype as parents. *Genotyping was completed by Abby Kaija, Research Assistant (Liaw laboratory, MHIR).*

5.4.2.2. Study Limitations Due to the *SMMHC^{CreERT2}* Strain

One limitation with this strain is that the *SMMHC^{CreERT2}* is Y-chromosome linked²³⁹. Therefore, only *Rab27a^{fl/fl}* male mice will be able to undergo recombination upon tamoxifen injection. This is a limitation for our future studies that utilize this tri-genic strain, as we have shown that male and female mice exhibit unique vascular phenotypes. It will be important to consider alternative approaches to direct *Rab27a* loss within the vascular smooth muscle cells of female mice in future studies.

5.4.2.3. Potential for Compensatory Mechanisms within the

Rab27a^{fl/fl};tdTomato;SMMHC^{CreERT2}

A major benefit to utilizing the inducible *SMMHC^{CreERT2}* is that the male mice will be able to develop with basal *Rab27a* expression²³⁹. Therefore, we hope to limit the activation of compensatory responses until recombination is induced. By taking this experimental approach, our goal is to determine whether trends of thoracic aorta morphology and reactivity are different than those of the global *Rab27a* null male mice. Furthermore, will also be able to test whether the age at which loss of *Rab27a* occurs also impacts vascular function by inducing Cre expression at earlier and later stages in life.

5.4.3. Targeting *Rab27a* Loss in the Vascular Endothelial Cells Using a *Rab27a^{fl/fl};-Cdh5^{Cre}* Mouse Strain

Cadherins are a class of proteins associated with cellular adherence and maintenance of cellular barriers. While there are multiple types of cadherins, Cadherin-5 is specific for vascular endothelial cells²⁴⁰. The Liaw lab currently has access to a Cadherin-5^{Cre} strain (*Cdh5^{Cre}*, B6.FVB-Tg(Cdh5-cre)7Mlia/J, The Jackson Laboratory #006317) and therefore could begin interbreeding these strains²⁵. These *Cdh5^{Cre}* mice are not reported to show phenotypic abnormalities for male or female mice²⁵.

5.4.3.1. Potential Limitation of the *Rab27a^{fl/fl};-Cdh5^{Cre}* Strain

As with the global *Rab27a* null strain, it will be important to recognize that loss of *Rab27a* will occur during embryonic development and will be sustained throughout the animals' lives. Therefore, we should again be mindful of potential compensatory mechanisms and how they may impact changes in morphological or reactivity studies. At the same time, by directing loss of *Rab27a* to the vascular endothelium, there should be a reduced risk of global activation of compensatory mechanisms. In designing experiments, it will be important to isolate and

examine primary endothelial cultures for differences in Rab family expression to examine for possible compensatory mechanisms^{10,11}.

5.5. A Growing Need for Comparative Studies Examining Sex as a Biological Variable

As the scientific inquiry regarding the importance of *Rab27a* in vascular health is developed, it will be essential to continue examining the impact of sex as a biological variable. In addition to the data that we have provided within the above studies, an abundance of evidence suggests that there are important differences in disease pathologies between males and females^{62,69,77,162}. Therefore, to fully characterize the mechanisms driving cardiovascular and metabolic disease, studies must identify the mechanistic differences between the sexes.

However, as discussed with the transgenic strains above, there are instances when tools for studying only one sex are available. When these limitations occur, it will be critical for the researchers to address them and adapt their conclusions accordingly. Also, it is important to recognize both sexes are not equally affected by all diseases, and therefore the study populations should be designed to represent those population as best as possible^{48,69}. However, due to the prevalence of cardiovascular and metabolic diseases, it remains imperative that both sexes are further studied⁴⁸.

5.6. Establishing the Human Connection: Translational Focus for Future Studies

The goal of this work was to determine whether *Rab27a* is a regulator of vascular physiology. To study the impact of *Rab27a* loss on adipose and vascular physiology *in vivo*, we established a novel *Rab27a* null strain on a C57BL/6J background. While we were able to provide evidence that global loss of *Rab27a* impacted vascular reactivity in male and female mice, much work is required to determine whether *Rab27a* expression impacts human vascular health.

Our hope for this work is that it can be used as a reference for future studies evaluating

the importance of *Rab27a* in human vascular health. We are excited about the potential opportunities to examine whether targeted knockdown of *Rab27a* in primary human VSMCs alters the expression of contractile proteins. Or perhaps, examining whether targeted knockdown of *Rab27a* in primary adipocytes also results in the dysregulation of exosome cargo that are associated with metabolic or cardiovascular phenotypes. In developing a translational focus for future studies, we will be better able to understand the role of the small GTPase proteins in the regulation of human disease²²⁰. Such knowledge has the potential to help identify novel therapeutic targets for those at risk of or suffering from cardiovascular disease.

REFERENCES

- 1 Zuk, P. A. *et al.* Multilineage cells from human adipose tissue: implications for cell-based therapies. *Tissue Eng* **7**, 211-228 (2001). <https://doi.org:10.1089/107632701300062859>
- 2 SEER Training Modules. *Introduction to the Cardiovascular System* <https://training.seer.cancer.gov/anatomy/cardiovascular/> (2023 Apr 10).
- 3 Cypess, A. M. Reassessing Human Adipose Tissue. *N Engl J Med* **386**, 768-779 (2022). <https://doi.org:10.1056/NEJMra2032804>
- 4 Sarwer, D. B., von Sydow Green, A., Vetter, M. L. & Wadden, T. A. Behavior therapy for obesity: where are we now? *Curr Opin Endocrinol Diabetes Obes* **16**, 347-352 (2009). <https://doi.org:10.1097/MED.0b013e32832f5a79>
- 5 Jo, J. *et al.* Hypertrophy and/or Hyperplasia: Dynamics of Adipose Tissue Growth. *PLoS Comput Biol* **5**, e1000324 (2009). <https://doi.org:10.1371/journal.pcbi.1000324>
- 6 Hessvik, N. P. & Llorente, A. Current knowledge on exosome biogenesis and release. *Cell Mol Life Sci* **75**, 193-208 (2018). <https://doi.org:10.1007/s00018-017-2595-9>
- 7 Fox, C. S. *et al.* Periaortic fat deposition is associated with peripheral arterial disease: the Framingham heart study. *Circ Cardiovasc Imaging* **3**, 515-519 (2010). <https://doi.org:10.1161/CIRCIMAGING.110.958884>
- 8 Police, S. B., Thatcher, S. E., Charnigo, R., Daugherty, A. & Cassis, L. A. Obesity promotes inflammation in periaortic adipose tissue and angiotensin II-induced abdominal aortic aneurysm formation. *Arterioscler Thromb Vasc Biol* **29**, 1458-1464 (2009). <https://doi.org:10.1161/ATVBAHA.109.192658>
- 9 Ostrowski, M. *et al.* Rab27a and Rab27b control different steps of the exosome secretion pathway. *Nat Cell Biol* **12**, 19-30; sup pp 11-13 (2010). <https://doi.org:10.1038/ncb2000>
- 10 Blanc, L. & Vidal, M. New insights into the function of Rab GTPases in the context of exosomal secretion. *Small GTPases* **9**, 95-106 (2018). <https://doi.org:10.1080/21541248.2016.1264352>
- 11 Kowal, J., Tkach, M. & Thery, C. Biogenesis and secretion of exosomes. *Curr Opin Cell Biol* **29**, 116-125 (2014). <https://doi.org:10.1016/j.ceb.2014.05.004>

- 12 Wei, D. *et al.* RAB31 marks and controls an ESCRT-independent exosome pathway. *Cell Res* **31**, 157-177 (2021). <https://doi.org/10.1038/s41422-020-00409-1>
- 13 Piche, M. E., Poirier, P., Lemieux, I. & Despres, J. P. Overview of Epidemiology and Contribution of Obesity and Body Fat Distribution to Cardiovascular Disease: An Update. *Prog Cardiovasc Dis* **61**, 103-113 (2018). <https://doi.org/10.1016/j.pcad.2018.06.004>
- 14 Cypess, A. M. *et al.* Identification and importance of brown adipose tissue in adult humans. *N Engl J Med* **360**, 1509-1517 (2009). <https://doi.org/10.1056/NEJMoa0810780>
- 15 Boucher, J. M. *et al.* Pathological Conversion of Mouse Perivascular Adipose Tissue by Notch Activation. *Arterioscler Thromb Vasc Biol* **40**, 2227-2243 (2020). <https://doi.org/10.1161/ATVBAHA.120.314731>
- 16 Adachi, Y. *et al.* Beiging of perivascular adipose tissue regulates its inflammation and vascular remodeling. *Nat Commun* **13**, 5117 (2022). <https://doi.org/10.1038/s41467-022-32658-6>
- 17 van Dam, A. D., Boon, M. R., Berbee, J. F. P., Rensen, P. C. N. & van Harmelen, V. Targeting white, brown and perivascular adipose tissue in atherosclerosis development. *Eur J Pharmacol* **816**, 82-92 (2017). <https://doi.org/10.1016/j.ejphar.2017.03.051>
- 18 Chatterjee, T. K. *et al.* Proinflammatory phenotype of perivascular adipocytes: influence of high-fat feeding. *Circ Res* **104**, 541-549 (2009). <https://doi.org/10.1161/CIRCRESAHA.108.182998>
- 19 Lynes, M. D. & Tseng, Y. H. The Thermogenic Circuit: Regulators of Thermogenic Competency and Differentiation. *Genes Dis* **2**, 164-172 (2015). <https://doi.org/10.1016/j.gendis.2015.03.001>
- 20 Sanchez-Gurmaches, J. & Guertin, D. A. Adipocytes arise from multiple lineages that are heterogeneously and dynamically distributed. *Nat Commun* **5**, 4099 (2014). <https://doi.org/10.1038/ncomms5099>
- 21 Seale, P. *et al.* PRDM16 controls a brown fat/skeletal muscle switch. *Nature* **454**, 961-967 (2008). <https://doi.org/10.1038/nature07182>
- 22 Rajakumari, S. *et al.* EBF2 determines and maintains brown adipocyte identity. *Cell Metab* **17**, 562-574 (2013). <https://doi.org/10.1016/j.cmet.2013.01.015>
- 23 Collins, J. A., Munoz, J. V., Patel, T. R., Loukas, M. & Tubbs, R. S. The anatomy of the

- aging aorta. *Clin Anat* **27**, 463-466 (2014). <https://doi.org:10.1002/ca.22384>
- 24 Lee, M. J., Wu, Y. & Fried, S. K. Adipose tissue heterogeneity: implication of depot differences in adipose tissue for obesity complications. *Mol Aspects Med* **34**, 1-11 (2013). <https://doi.org:10.1016/j.mam.2012.10.001>
- 25 Alva, J. A. *et al.* VE-Cadherin-Cre-recombinase transgenic mouse: a tool for lineage analysis and gene deletion in endothelial cells. *Dev Dyn* **235**, 759-767 (2006). <https://doi.org:10.1002/dvdy.20643>
- 26 Sun, Z. *et al.* Perilipin1 promotes unilocular lipid droplet formation through the activation of Fsp27 in adipocytes. *Nat Commun* **4**, 1594 (2013). <https://doi.org:10.1038/ncomms2581>
- 27 von Kleeck, R. *et al.* Decreased vascular smooth muscle contractility in Hutchinson-Gilford Progeria Syndrome linked to defective smooth muscle myosin heavy chain expression. *Sci Rep* **11**, 10625 (2021). <https://doi.org:10.1038/s41598-021-90119-4>
- 28 Common Metabolic Diseases Knowledge Portal (cmdkp.org). *RAB27A Gene page* (2023 Feb 1).
- 29 Common Metabolic Diseases Knowledge Portal (cmdkp.org). *Chr15:55,495,164-55,611,311 Region* <https://hugeamp.org/region.html?chr=15&end=55611311&phenotype=BMI&start=55495164> (2023 Mar 6).
- 30 ww, P. D. B. c. Protein Data Bank: the single global archive for 3D macromolecular structure data. *Nucleic Acids Res* **47**, D520-D528 (2019). <https://doi.org:10.1093/nar/gky949>
- 31 Chavas, L. M. *et al.* Elucidation of Rab27 recruitment by its effectors: structure of Rab27a bound to Exophilin4/Slp2-a. *Structure* **16**, 1468-1477 (2008). <https://doi.org:10.1016/j.str.2008.07.015>
- 32 Kukimoto-Niino, M. *et al.* Structural basis for the exclusive specificity of Slac2-a/melanophilin for the Rab27 GTPases. *Structure* **16**, 1478-1490 (2008). <https://doi.org:10.1016/j.str.2008.07.014>
- 33 UniProt, C. UniProt: the universal protein knowledgebase in 2021. *Nucleic Acids Res* **49**, D480-D489 (2021). <https://doi.org:10.1093/nar/gkaa1100>

- 34 Cybulsky, M. I. & Gimbrone, M. A., Jr. Endothelial expression of a mononuclear leukocyte adhesion molecule during atherogenesis. *Science* **251**, 788-791 (1991). <https://doi.org:10.1126/science.1990440>
- 35 Kuznetsov, D. *et al.* OrthoDB v11: annotation of orthologs in the widest sampling of organismal diversity. *Nucleic Acids Res* **51**, D445-D451 (2023). <https://doi.org:10.1093/nar/gkac998>
- 36 Lin, L. *et al.* Rab35/ACAP2 and Rab35/RUSC2 Complex Structures Reveal Molecular Basis for Effector Recognition by Rab35 GTPase. *Structure* **27**, 729-740 e723 (2019). <https://doi.org:10.1016/j.str.2019.02.008>
- 37 Davis, M. W. & Jorgensen, E. M. ApE, A Plasmid Editor: A Freely Available DNA Manipulation and Visualization Program. *Front Bioinform* **2**, 818619 (2022). <https://doi.org:10.3389/fbinf.2022.818619>
- 38 Kent, W. J. *et al.* The human genome browser at UCSC. *Genome Res* **12**, 996-1006 (2002). <https://doi.org:10.1101/gr.229102>
- 39 Miano, J. M., Fisher, E. A. & Majesky, M. W. Fate and State of Vascular Smooth Muscle Cells in Atherosclerosis. *Circulation* **143**, 2110-2116 (2021). <https://doi.org:10.1161/CIRCULATIONAHA.120.049922>
- 40 Han, J., Pluhackova, K. & Bockmann, R. A. The Multifaceted Role of SNARE Proteins in Membrane Fusion. *Front Physiol* **8**, 5 (2017). <https://doi.org:10.3389/fphys.2017.00005>
- 41 Wu, Z., Puigserver, P. & Spiegelman, B. M. Transcriptional activation of adipogenesis. *Curr Opin Cell Biol* **11**, 689-694 (1999). [https://doi.org:10.1016/s0955-0674\(99\)00037-x](https://doi.org:10.1016/s0955-0674(99)00037-x)
- 42 Tontonoz, P., Hu, E. & Spiegelman, B. M. Stimulation of adipogenesis in fibroblasts by PPAR gamma 2, a lipid-activated transcription factor. *Cell* **79**, 1147-1156 (1994). [https://doi.org:10.1016/0092-8674\(94\)90006-x](https://doi.org:10.1016/0092-8674(94)90006-x)
- 43 Jonasson, L., Holm, J., Skalli, O., Bondjers, G. & Hansson, G. K. Regional accumulations of T cells, macrophages, and smooth muscle cells in the human atherosclerotic plaque. *Arteriosclerosis* **6**, 131-138 (1986). <https://doi.org:10.1161/01.atv.6.2.131>
- 44 Bennett, M. R., Sinha, S. & Owens, G. K. Vascular Smooth Muscle Cells in Atherosclerosis. *Circ Res* **118**, 692-702 (2016). <https://doi.org:10.1161/CIRCRESAHA.115.306361>

- 45 Johnson, M. *et al.* NCBI BLAST: a better web interface. *Nucleic Acids Res* **36**, W5-9 (2008). <https://doi.org:10.1093/nar/gkn201>
- 46 Cardiovascular Diseases. *World Health Organization* **2023** (2021).
- 47 Laslett, L. J. *et al.* The worldwide environment of cardiovascular disease: prevalence, diagnosis, therapy, and policy issues: a report from the American College of Cardiology. *J Am Coll Cardiol* **60**, S1-49 (2012). <https://doi.org:10.1016/j.jacc.2012.11.002>
- 48 Tsao, C. W. *et al.* Heart Disease and Stroke Statistics-2022 Update: A Report From the American Heart Association. *Circulation* **145**, e153-e639 (2022). <https://doi.org:10.1161/CIR.0000000000001052>
- 49 Marelli, A. J. *et al.* Lifetime prevalence of congenital heart disease in the general population from 2000 to 2010. *Circulation* **130**, 749-756 (2014). <https://doi.org:10.1161/CIRCULATIONAHA.113.008396>
- 50 Vaduganathan, M., Mensah, G. A., Turco, J. V., Fuster, V. & Roth, G. A. The Global Burden of Cardiovascular Diseases and Risk: A Compass for Future Health. *J Am Coll Cardiol* **80**, 2361-2371 (2022). <https://doi.org:10.1016/j.jacc.2022.11.005>
- 51 Metcalfe, J., McAnulty, J. H. & Ueland, K. Cardiovascular physiology. *Clin Obstet Gynecol* **24**, 693-710 (1981). <https://doi.org:10.1097/00003081-198109000-00002>
- 52 Sethi, S., Rivera, O., Oliveros, R. & Chilton, R. Aortic stiffness: pathophysiology, clinical implications, and approach to treatment. *Integr Blood Press Control* **7**, 29-34 (2014). <https://doi.org:10.2147/IBPC.S59535>
- 53 Basatemur, G. L., Jorgensen, H. F., Clarke, M. C. H., Bennett, M. R. & Mallat, Z. Vascular smooth muscle cells in atherosclerosis. *Nat Rev Cardiol* **16**, 727-744 (2019). <https://doi.org:10.1038/s41569-019-0227-9>
- 54 Barallobre-Barreiro, J. *et al.* Extracellular Matrix in Vascular Disease, Part 2/4: JACC Focus Seminar. *J Am Coll Cardiol* **75**, 2189-2203 (2020). <https://doi.org:10.1016/j.jacc.2020.03.018>
- 55 Ketonen, J., Shi, J., Martonen, E. & Mervaala, E. Periadventitial adipose tissue promotes endothelial dysfunction via oxidative stress in diet-induced obese C57Bl/6 mice. *Circ J* **74**, 1479-1487 (2010). <https://doi.org:10.1253/circj.cj-09-0661>
- 56 Haddock, R. E. *et al.* Diet-induced obesity impairs endothelium-derived hyperpolarization

- via altered potassium channel signaling mechanisms. *PLoS One* **6**, e16423 (2011). <https://doi.org/10.1371/journal.pone.0016423>
- 57 Abdalla, S. M., Yu, S. & Galea, S. Trends in Cardiovascular Disease Prevalence by Income Level in the United States. *JAMA Netw Open* **3**, e2018150 (2020). <https://doi.org/10.1001/jamanetworkopen.2020.18150>
- 58 McAloon, C. J. *et al.* The changing face of cardiovascular disease 2000-2012: An analysis of the world health organisation global health estimates data. *Int J Cardiol* **224**, 256-264 (2016). <https://doi.org/10.1016/j.ijcard.2016.09.026>
- 59 Messerli, F. H., Williams, B. & Ritz, E. Essential hypertension. *Lancet* **370**, 591-603 (2007). [https://doi.org/10.1016/S0140-6736\(07\)61299-9](https://doi.org/10.1016/S0140-6736(07)61299-9)
- 60 Cutler, J. A., Follmann, D. & Allender, P. S. Randomized trials of sodium reduction: an overview. *Am J Clin Nutr* **65**, 643S-651S (1997). <https://doi.org/10.1093/ajcn/65.2.643S>
- 61 Whelton, S. P., Chin, A., Xin, X. & He, J. Effect of aerobic exercise on blood pressure: a meta-analysis of randomized, controlled trials. *Ann Intern Med* **136**, 493-503 (2002). <https://doi.org/10.7326/0003-4819-136-7-200204020-00006>
- 62 Rodgers, J. L. *et al.* Cardiovascular Risks Associated with Gender and Aging. *J Cardiovasc Dev Dis* **6** (2019). <https://doi.org/10.3390/jcdd6020019>
- 63 O'Rourke, M. Mechanical principles in arterial disease. *Hypertension* **26**, 2-9 (1995). <https://doi.org/10.1161/01.hyp.26.1.2>
- 64 Clinton, S. K. *et al.* Macrophage colony-stimulating factor gene expression in vascular cells and in experimental and human atherosclerosis. *Am J Pathol* **140**, 301-316 (1992).
- 65 Lee, R. M., Dickhout, J. G. & Sandow, S. L. Vascular structural and functional changes: their association with causality in hypertension: models, remodeling and relevance. *Hypertens Res* **40**, 311-323 (2017). <https://doi.org/10.1038/hr.2016.145>
- 66 Owens, G. K. & Schwartz, S. M. Alterations in vascular smooth muscle mass in the spontaneously hypertensive rat. Role of cellular hypertrophy, hyperploidy, and hyperplasia. *Circ Res* **51**, 280-289 (1982). <https://doi.org/10.1161/01.res.51.3.280>
- 67 Intengan, H. D. & Schiffrin, E. L. Structure and mechanical properties of resistance arteries in hypertension: role of adhesion molecules and extracellular matrix determinants. *Hypertension* **36**, 312-318 (2000). <https://doi.org/10.1161/01.hyp.36.3.312>

- 68 Gao, Y. J., Yang, L. F., Stead, S. & Lee, R. M. Flow-induced vascular remodeling in the mesenteric artery of spontaneously hypertensive rats. *Can J Physiol Pharmacol* **86**, 737-744 (2008). <https://doi.org/10.1139/Y08-079>
- 69 Beale, A. L., Meyer, P., Marwick, T. H., Lam, C. S. P. & Kaye, D. M. Sex Differences in Cardiovascular Pathophysiology: Why Women Are Overrepresented in Heart Failure With Preserved Ejection Fraction. *Circulation* **138**, 198-205 (2018). <https://doi.org/10.1161/CIRCULATIONAHA.118.034271>
- 70 Garcia, M., Mulvagh, S. L., Merz, C. N., Buring, J. E. & Manson, J. E. Cardiovascular Disease in Women: Clinical Perspectives. *Circ Res* **118**, 1273-1293 (2016). <https://doi.org/10.1161/CIRCRESAHA.116.307547>
- 71 Levy, D., Larson, M. G., Vasan, R. S., Kannel, W. B. & Ho, K. K. The progression from hypertension to congestive heart failure. *JAMA* **275**, 1557-1562 (1996).
- 72 Iorga, A. *et al.* The protective role of estrogen and estrogen receptors in cardiovascular disease and the controversial use of estrogen therapy. *Biol Sex Differ* **8**, 33 (2017). <https://doi.org/10.1186/s13293-017-0152-8>
- 73 Forstermann, U. & Munzel, T. Endothelial nitric oxide synthase in vascular disease: from marvel to menace. *Circulation* **113**, 1708-1714 (2006). <https://doi.org/10.1161/CIRCULATIONAHA.105.602532>
- 74 Zhao, T., Zhao, W., Chen, Y., Ahokas, R. A. & Sun, Y. Vascular endothelial growth factor (VEGF)-A: role on cardiac angiogenesis following myocardial infarction. *Microvasc Res* **80**, 188-194 (2010). <https://doi.org/10.1016/j.mvr.2010.03.014>
- 75 Simpson, E. R. Sources of estrogen and their importance. *J Steroid Biochem Mol Biol* **86**, 225-230 (2003). [https://doi.org/10.1016/s0960-0760\(03\)00360-1](https://doi.org/10.1016/s0960-0760(03)00360-1)
- 76 Lakatta, E. G. & Levy, D. Arterial and cardiac aging: major shareholders in cardiovascular disease enterprises: Part I: aging arteries: a "set up" for vascular disease. *Circulation* **107**, 139-146 (2003). <https://doi.org/10.1161/01.cir.0000048892.83521.58>
- 77 Merz, A. A. & Cheng, S. Sex differences in cardiovascular ageing. *Heart* **102**, 825-831 (2016). <https://doi.org/10.1136/heartjnl-2015-308769>
- 78 Powell-Wiley, T. M. *et al.* Obesity and Cardiovascular Disease: A Scientific Statement From the American Heart Association. *Circulation* **143**, e984-e1010 (2021). <https://doi.org/10.1161/CIR.0000000000000973>

- 79 Blüher, M. Obesity: global epidemiology and pathogenesis. *Nat Rev Endocrinol* **15**, 288-298 (2019). <https://doi.org/10.1038/s41574-019-0176-8>
- 80 Malik, V. S., Willet, W. C. & Hu, F. B. Nearly a decade on - trends, risk factors and policy implications in global obesity. *Nat Rev Endocrinol* **16**, 615-616 (2020). <https://doi.org/10.1038/s41574-020-00411-y>
- 81 Collaboration, N. C. D. R. F. Trends in adult body-mass index in 200 countries from 1975 to 2014: a pooled analysis of 1698 population-based measurement studies with 19.2 million participants. *Lancet* **387**, 1377-1396 (2016). [https://doi.org/10.1016/S0140-6736\(16\)30054-X](https://doi.org/10.1016/S0140-6736(16)30054-X)
- 82 Kones, R. & Rumana, U. Cardiometabolic diseases of civilization: history and maturation of an evolving global threat. An update and call to action. *Ann Med* **49**, 260-274 (2017). <https://doi.org/10.1080/07853890.2016.1271957>
- 83 Beyaz, S. *et al.* High-fat diet enhances stemness and tumorigenicity of intestinal progenitors. *Nature* **531**, 53-58 (2016). <https://doi.org/10.1038/nature17173>
- 84 Haczeyni, F., Bell-Anderson, K. S. & Farrell, G. C. Causes and mechanisms of adipocyte enlargement and adipose expansion. *Obes Rev* **19**, 406-420 (2018). <https://doi.org/10.1111/obr.12646>
- 85 Rodeheffer, M. S., Birsoy, K. & Friedman, J. M. Identification of white adipocyte progenitor cells in vivo. *Cell* **135**, 240-249 (2008). <https://doi.org/10.1016/j.cell.2008.09.036>
- 86 Nigro, E. *et al.* New insight into adiponectin role in obesity and obesity-related diseases. *Biomed Res Int* **2014**, 658913 (2014). <https://doi.org/10.1155/2014/658913>
- 87 Longo, M. *et al.* Adipose Tissue Dysfunction as Determinant of Obesity-Associated Metabolic Complications. *Int J Mol Sci* **20** (2019). <https://doi.org/10.3390/ijms20092358>
- 88 Sharma, A. M. & Padwal, R. Obesity is a sign - over-eating is a symptom: an aetiological framework for the assessment and management of obesity. *Obes Rev* **11**, 362-370 (2010). <https://doi.org/10.1111/j.1467-789X.2009.00689.x>
- 89 de Kloet, A. D. & Woods, S. C. Molecular neuroendocrine targets for obesity therapy. *Curr Opin Endocrinol Diabetes Obes* **17**, 441-445 (2010). <https://doi.org/10.1097/MED.0b013e32833c3013>

- 90 Bartelt, A. & Heeren, J. Adipose tissue browning and metabolic health. *Nat Rev Endocrinol* **10**, 24-36 (2014). <https://doi.org:10.1038/nrendo.2013.204>
- 91 Rosen, E. D. & MacDougald, O. A. Adipocyte differentiation from the inside out. *Nat Rev Mol Cell Biol* **7**, 885-896 (2006). <https://doi.org:10.1038/nrm2066>
- 92 Puigserver, P. *et al.* A cold-inducible coactivator of nuclear receptors linked to adaptive thermogenesis. *Cell* **92**, 829-839 (1998). [https://doi.org:10.1016/s0092-8674\(00\)81410-5](https://doi.org:10.1016/s0092-8674(00)81410-5)
- 93 Himms-Hagen, J. Role of thermogenesis in the regulation of energy balance in relation to obesity. *Can J Physiol Pharmacol* **67**, 394-401 (1989). <https://doi.org:10.1139/y89-063>
- 94 Peres Valgas da Silva, C., Hernandez-Saavedra, D., White, J. D. & Stanford, K. I. Cold and Exercise: Therapeutic Tools to Activate Brown Adipose Tissue and Combat Obesity. *Biology (Basel)* **8** (2019). <https://doi.org:10.3390/biology8010009>
- 95 Cero, C. *et al.* beta3-Adrenergic receptors regulate human brown/beige adipocyte lipolysis and thermogenesis. *JCI Insight* **6** (2021). <https://doi.org:10.1172/jci.insight.139160>
- 96 Zuriaga, M. A., Fuster, J. J., Gokce, N. & Walsh, K. Humans and Mice Display Opposing Patterns of "Browning" Gene Expression in Visceral and Subcutaneous White Adipose Tissue Depots. *Front Cardiovasc Med* **4**, 27 (2017). <https://doi.org:10.3389/fcvm.2017.00027>
- 97 Cedikova, M. *et al.* Mitochondria in White, Brown, and Beige Adipocytes. *Stem Cells Int* **2016**, 6067349 (2016). <https://doi.org:10.1155/2016/6067349>
- 98 Snijder, M. B. *et al.* Low subcutaneous thigh fat is a risk factor for unfavourable glucose and lipid levels, independently of high abdominal fat. The Health ABC Study. *Diabetologia* **48**, 301-308 (2005). <https://doi.org:10.1007/s00125-004-1637-7>
- 99 St-Pierre, J. *et al.* Relation of the "hypertriglyceridemic waist" phenotype to earlier manifestations of coronary artery disease in patients with glucose intolerance and type 2 diabetes mellitus. *Am J Cardiol* **99**, 369-373 (2007). <https://doi.org:10.1016/j.amjcard.2006.08.041>
- 100 Lee, Y. H., Petkova, A. P., Mottillo, E. P. & Granneman, J. G. In vivo identification of bipotential adipocyte progenitors recruited by beta3-adrenoceptor activation and high-fat feeding. *Cell Metab* **15**, 480-491 (2012). <https://doi.org:10.1016/j.cmet.2012.03.009>

- 101 Xue, B. *et al.* Genetic variability affects the development of brown adipocytes in white fat but not in interscapular brown fat. *J Lipid Res* **48**, 41-51 (2007). <https://doi.org/10.1194/jlr.M600287-JLR200>
- 102 Brown, N. K. *et al.* Perivascular adipose tissue in vascular function and disease: a review of current research and animal models. *Arterioscler Thromb Vasc Biol* **34**, 1621-1630 (2014). <https://doi.org/10.1161/ATVBAHA.114.303029>
- 103 Angueira, A. R. *et al.* Defining the lineage of thermogenic perivascular adipose tissue. *Nat Metab* **3**, 469-484 (2021). <https://doi.org/10.1038/s42255-021-00380-0>
- 104 Chang, L. *et al.* Loss of perivascular adipose tissue on peroxisome proliferator-activated receptor-gamma deletion in smooth muscle cells impairs intravascular thermoregulation and enhances atherosclerosis. *Circulation* **126**, 1067-1078 (2012). <https://doi.org/10.1161/CIRCULATIONAHA.112.104489>
- 105 Chang, L., Garcia-Barrio, M. T. & Chen, Y. E. Perivascular Adipose Tissue Regulates Vascular Function by Targeting Vascular Smooth Muscle Cells. *Arterioscler Thromb Vasc Biol* **40**, 1094-1109 (2020). <https://doi.org/10.1161/ATVBAHA.120.312464>
- 106 Wynne, B. M., Chiao, C. W. & Webb, R. C. Vascular Smooth Muscle Cell Signaling Mechanisms for Contraction to Angiotensin II and Endothelin-1. *J Am Soc Hypertens* **3**, 84-95 (2009). <https://doi.org/10.1016/j.jash.2008.09.002>
- 107 Kumar, R. K., Darios, E. S., Burnett, R., Thompson, J. M. & Watts, S. W. Fenfluramine-induced PVAT-dependent contraction depends on norepinephrine and not serotonin. *Pharmacol Res* **140**, 43-49 (2019). <https://doi.org/10.1016/j.phrs.2018.08.024>
- 108 Alhayek, S. & Preuss, C. V. in *StatPearls* (2023).
- 109 Fesus, G. *et al.* Adiponectin is a novel humoral vasodilator. *Cardiovasc Res* **75**, 719-727 (2007). <https://doi.org/10.1016/j.cardiores.2007.05.025>
- 110 Hafen, B. B. & Burns, B. in *StatPearls* (2023).
- 111 Gao, Y. J., Lu, C., Su, L. Y., Sharma, A. M. & Lee, R. M. Modulation of vascular function by perivascular adipose tissue: the role of endothelium and hydrogen peroxide. *Br J Pharmacol* **151**, 323-331 (2007). <https://doi.org/10.1038/sj.bjp.0707228>
- 112 Sampaio, W. O. *et al.* Angiotensin-(1-7) through receptor Mas mediates endothelial nitric oxide synthase activation via Akt-dependent pathways. *Hypertension* **49**, 185-192

- (2007). <https://doi.org:10.1161/01.HYP.0000251865.35728.2f>
- 113 Cohen, R. A. *et al.* Mechanism of nitric oxide-induced vasodilatation: refilling of intracellular stores by sarcoplasmic reticulum Ca²⁺ ATPase and inhibition of store-operated Ca²⁺ influx. *Circ Res* **84**, 210-219 (1999).
<https://doi.org:10.1161/01.res.84.2.210>
- 114 South, A. M. *et al.* Obesity is Associated with Higher Blood Pressure and Higher Levels of Angiotensin II but Lower Angiotensin-(1-7) in Adolescents Born Preterm. *J Pediatr* **205**, 55-60 e51 (2019). <https://doi.org:10.1016/j.jpeds.2018.09.058>
- 115 Doyle, L. M. & Wang, M. Z. Overview of Extracellular Vesicles, Their Origin, Composition, Purpose, and Methods for Exosome Isolation and Analysis. *Cells* **8** (2019).
<https://doi.org:10.3390/cells8070727>
- 116 Crewe, C. *et al.* Extracellular vesicle-based interorgan transport of mitochondria from energetically stressed adipocytes. *Cell Metab* **33**, 1853-1868 e1811 (2021).
<https://doi.org:10.1016/j.cmet.2021.08.002>
- 117 Kwan, H. Y., Chen, M., Xu, K. & Chen, B. The impact of obesity on adipocyte-derived extracellular vesicles. *Cell Mol Life Sci* **78**, 7275-7288 (2021).
<https://doi.org:10.1007/s00018-021-03973-w>
- 118 Abak, A., Abhari, A. & Rahimzadeh, S. Exosomes in cancer: small vesicular transporters for cancer progression and metastasis, biomarkers in cancer therapeutics. *PeerJ* **6**, e4763 (2018). <https://doi.org:10.7717/peerj.4763>
- 119 Hergenreider, E. *et al.* Atheroprotective communication between endothelial cells and smooth muscle cells through miRNAs. *Nat Cell Biol* **14**, 249-256 (2012).
<https://doi.org:10.1038/ncb2441>
- 120 Wang, Y. *et al.* Exosomes: An emerging factor in atherosclerosis. *Biomed Pharmacother* **115**, 108951 (2019). <https://doi.org:10.1016/j.biopha.2019.108951>
- 121 Pardo, F., Villalobos-Labra, R., Sobrevia, B., Toledo, F. & Sobrevia, L. Extracellular vesicles in obesity and diabetes mellitus. *Mol Aspects Med* **60**, 81-91 (2018).
<https://doi.org:10.1016/j.mam.2017.11.010>
- 122 Eguchi, A. *et al.* Circulating adipocyte-derived extracellular vesicles are novel markers of metabolic stress. *J Mol Med (Berl)* **94**, 1241-1253 (2016).
<https://doi.org:10.1007/s00109-016-1446-8>

- 123 Wen, Z. *et al.* Hypertrophic Adipocyte-Derived Exosomal miR-802-5p Contributes to Insulin Resistance in Cardiac Myocytes Through Targeting HSP60. *Obesity (Silver Spring)* **28**, 1932-1940 (2020). <https://doi.org:10.1002/oby.22932>
- 124 Liu, Y. *et al.* Perivascular Adipose-Derived Exosomes Reduce Foam Cell Formation by Regulating Expression of Cholesterol Transporters. *Front Cardiovasc Med* **8**, 697510 (2021). <https://doi.org:10.3389/fcvm.2021.697510>
- 125 Mathieu, M., Martin-Jaular, L., Lavieu, G. & Thery, C. Specificities of secretion and uptake of exosomes and other extracellular vesicles for cell-to-cell communication. *Nat Cell Biol* **21**, 9-17 (2019). <https://doi.org:10.1038/s41556-018-0250-9>
- 126 Bucci, C. *et al.* The small GTPase rab5 functions as a regulatory factor in the early endocytic pathway. *Cell* **70**, 715-728 (1992). [https://doi.org:10.1016/0092-8674\(92\)90306-w](https://doi.org:10.1016/0092-8674(92)90306-w)
- 127 Woodman, P. G. Biogenesis of the sorting endosome: the role of Rab5. *Traffic* **1**, 695-701 (2000). <https://doi.org:10.1034/j.1600-0854.2000.010902.x>
- 128 Nightingale, T. D., Pattni, K., Hume, A. N., Seabra, M. C. & Cutler, D. F. Rab27a and MyRIP regulate the amount and multimeric state of VWF released from endothelial cells. *Blood* **113**, 5010-5018 (2009). <https://doi.org:10.1182/blood-2008-09-181206>
- 129 van Solinge, T. S. *et al.* Versatile Role of Rab27a in Glioma: Effects on Release of Extracellular Vesicles, Cell Viability, and Tumor Progression. *Front Mol Biosci* **7**, 554649 (2020). <https://doi.org:10.3389/fmolb.2020.554649>
- 130 Zeng, M. *et al.* FOXO1-Mediated Downregulation of RAB27B Leads to Decreased Exosome Secretion in Diabetic Kidneys. *Diabetes* **70**, 1536-1548 (2021). <https://doi.org:10.2337/db20-1108>
- 131 Fagerberg, L. *et al.* Analysis of the human tissue-specific expression by genome-wide integration of transcriptomics and antibody-based proteomics. *Mol Cell Proteomics* **13**, 397-406 (2014). <https://doi.org:10.1074/mcp.M113.035600>
- 132 Sayers, E. W. *et al.* Database resources of the national center for biotechnology information. *Nucleic Acids Res* **50**, D20-D26 (2022). <https://doi.org:10.1093/nar/gkab1112>
- 133 Malhotra, A. K. *et al.* Griscelli syndrome. *J Am Acad Dermatol* **55**, 337-340 (2006). <https://doi.org:10.1016/j.jaad.2005.11.1056>

- 134 Masri, A. *et al.* Griscelli syndrome type 2: a rare and lethal disorder. *J Child Neurol* **23**, 964-967 (2008). <https://doi.org/10.1177/0883073808315409>
- 135 Menasche, G. *et al.* Mutations in RAB27A cause Griscelli syndrome associated with haemophagocytic syndrome. *Nat Genet* **25**, 173-176 (2000). <https://doi.org/10.1038/76024>
- 136 Boucher, J. M. *et al.* Rab27a Regulates Human Perivascular Adipose Progenitor Cell Differentiation. *Cardiovasc Drugs Ther* **32**, 519-530 (2018). <https://doi.org/10.1007/s10557-018-6813-y>
- 137 Tolmachova, T. *et al.* Cloning, mapping and characterization of the human RAB27A gene. *Gene* **239**, 109-116 (1999). [https://doi.org/10.1016/s0378-1119\(99\)00371-6](https://doi.org/10.1016/s0378-1119(99)00371-6)
- 138 Lane P. W., W. J. E. Ashen, a new color mutation on chromosome 9 of the mouse. *Journal of Heredity* **70**, 133-135 (1979). [https://doi.org:https://doi.org/10.1093/oxfordjournals.jhered.a109208](https://doi.org/https://doi.org/10.1093/oxfordjournals.jhered.a109208)
- 139 Baldarelli, R. M. *et al.* The mouse Gene Expression Database (GXD): 2021 update. *Nucleic Acids Res* **49**, D924-D931 (2021). <https://doi.org/10.1093/nar/gkaa914>
- 140 Karlsson, M. *et al.* A single-cell type transcriptomics map of human tissues. *Sci Adv* **7** (2021). <https://doi.org/10.1126/sciadv.abh2169>
- 141 Wilson, S. M. *et al.* A mutation in Rab27a causes the vesicle transport defects observed in ashen mice. *Proc Natl Acad Sci U S A* **97**, 7933-7938 (2000). <https://doi.org/10.1073/pnas.140212797>
- 142 Hu, M. *et al.* The harsh microenvironment in infarcted heart accelerates transplanted bone marrow mesenchymal stem cells injury: the role of injured cardiomyocytes-derived exosomes. *Cell Death Dis* **9**, 357 (2018). <https://doi.org/10.1038/s41419-018-0392-5>
- 143 Ma, X. *et al.* Rab27a-dependent exosomes protect against cerebral ischemic injury by reducing endothelial oxidative stress and apoptosis. *CNS Neurosci Ther* **28**, 1596-1612 (2022). <https://doi.org/10.1111/cns.13902>
- 144 Concordet, J. P. & Haeussler, M. CRISPOR: intuitive guide selection for CRISPR/Cas9 genome editing experiments and screens. *Nucleic Acids Res* **46**, W242-W245 (2018). <https://doi.org/10.1093/nar/gky354>
- 145 Wenceslau, C. F. *et al.* Guidelines for the measurement of vascular function and

- structure in isolated arteries and veins. *Am J Physiol Heart Circ Physiol* **321**, H77-H111 (2021). <https://doi.org:10.1152/ajpheart.01021.2020>
- 146 Konja, D. *et al.* Assessment of Vascular Tone Responsiveness using Isolated Mesenteric Arteries with a Focus on Modulation by Perivascular Adipose Tissues. *J Vis Exp* (2019). <https://doi.org:10.3791/59688>
- 147 Bond, K. H. *et al.* The Extracellular Matrix Environment of Clear Cell Renal Cell Carcinoma Determines Cancer Associated Fibroblast Growth. *Cancers (Basel)* **13** (2021). <https://doi.org:10.3390/cancers13235873>
- 148 Wu, J. X. *et al.* SWATH Mass Spectrometry Performance Using Extended Peptide MS/MS Assay Libraries. *Mol Cell Proteomics* **15**, 2501-2514 (2016). <https://doi.org:10.1074/mcp.M115.055558>
- 149 Rappsilber, J., Mann, M. & Ishihama, Y. Protocol for micro-purification, enrichment, pre-fractionation and storage of peptides for proteomics using StageTips. *Nat Protoc* **2**, 1896-1906 (2007). <https://doi.org:10.1038/nprot.2007.261>
- 150 Ivosev, G., Burton, L. & Bonner, R. Dimensionality reduction and visualization in principal component analysis. *Anal Chem* **80**, 4933-4944 (2008). <https://doi.org:10.1021/ac800110w>
- 151 Snel, B., Lehmann, G., Bork, P. & Huynen, M. A. STRING: a web-server to retrieve and display the repeatedly occurring neighbourhood of a gene. *Nucleic Acids Res* **28**, 3442-3444 (2000). <https://doi.org:10.1093/nar/28.18.3442>
- 152 Szklarczyk, D. *et al.* The STRING database in 2021: customizable protein-protein networks, and functional characterization of user-uploaded gene/measurement sets. *Nucleic Acids Res* **49**, D605-D612 (2021). <https://doi.org:10.1093/nar/gkaa1074>
- 153 Freida L. Carson, C. H. *Histotechnology: A Self-Instructional Text*. 3rd edn, (American Society for Clinical Pathology, 2009).
- 154 Tero, B. W., Fortier, B., Soucy, A. N., Paquette, G. & Liaw, L. Quantification of Lipid Area within Thermogenic Mouse Perivascular Adipose Tissue Using Standardized Image Analysis in FIJI. *J Vasc Res*, 1-7 (2021). <https://doi.org:10.1159/000517178>
- 155 Pylypenko, O., Hammich, H., Yu, I. M. & Houdusse, A. Rab GTPases and their interacting protein partners: Structural insights into Rab functional diversity. *Small GTPases* **9**, 22-48 (2018). <https://doi.org:10.1080/21541248.2017.1336191>

- 156 Guo, D. *et al.* RAB27A promotes melanoma cell invasion and metastasis via regulation of pro-invasive exosomes. *Int J Cancer* **144**, 3070-3085 (2019). <https://doi.org:10.1002/ijc.32064>
- 157 Accelerating Medicines Partnership - Common Metabolic Diseases. *National Institutes of Health* <https://www.nih.gov/research-training/accelerating-medicines-partnership-amp/common-metabolic-diseases> (July 28, 2021).
- 158 Almagro, T. A. M. *et al.* High Fat Diet Attenuates the Anticontractile Activity of Aortic PVAT via a Mechanism Involving AMPK and Reduced Adiponectin Secretion. *Front Physiol* **9**, 51 (2018). <https://doi.org:10.3389/fphys.2018.00051>
- 159 Schiffrin, E. L. Reactivity of small blood vessels in hypertension: relation with structural changes. State of the art lecture. *Hypertension* **19**, II1-9 (1992). https://doi.org:10.1161/01.hyp.19.2_suppl.ii1-a
- 160 De Moudt, S. *et al.* Progressive aortic stiffness in aging C57Bl/6 mice displays altered contractile behaviour and extracellular matrix changes. *Commun Biol* **5**, 605 (2022). <https://doi.org:10.1038/s42003-022-03563-x>
- 161 Chang, E., Varghese, M. & Singer, K. Gender and Sex Differences in Adipose Tissue. *Curr Diab Rep* **18**, 69 (2018). <https://doi.org:10.1007/s11892-018-1031-3>
- 162 Medrikova, D. *et al.* Sex differences during the course of diet-induced obesity in mice: adipose tissue expandability and glycemic control. *Int J Obes (Lond)* **36**, 262-272 (2012). <https://doi.org:10.1038/ijo.2011.87>
- 163 Posch, M. G. *et al.* Cardiac alpha-myosin (MYH6) is the predominant sarcomeric disease gene for familial atrial septal defects. *PLoS One* **6**, e28872 (2011). <https://doi.org:10.1371/journal.pone.0028872>
- 164 Frantz, C., Stewart, K. M. & Weaver, V. M. The extracellular matrix at a glance. *J Cell Sci* **123**, 4195-4200 (2010). <https://doi.org:10.1242/jcs.023820>
- 165 Norton, M. *et al.* ROMO1 is an essential redox-dependent regulator of mitochondrial dynamics. *Sci Signal* **7**, ra10 (2014). <https://doi.org:10.1126/scisignal.2004374>
- 166 Filadi, R., Pendin, D. & Pizzo, P. Mitofusin 2: from functions to disease. *Cell Death Dis* **9**, 330 (2018). <https://doi.org:10.1038/s41419-017-0023-6>
- 167 Subramanian, A. *et al.* Gene set enrichment analysis: a knowledge-based approach for

- interpreting genome-wide expression profiles. *Proc Natl Acad Sci U S A* **102**, 15545-15550 (2005). <https://doi.org:10.1073/pnas.0506580102>
- 168 Wilmore, J. H. Aerobic exercise and endurance: improving fitness for health benefits. *Phys Sportsmed* **31**, 45-51 (2003). <https://doi.org:10.3810/psm.2003.05.367>
- 169 Barallobre-Barreiro, J. *et al.* Extracellular matrix remodelling in response to venous hypertension: proteomics of human varicose veins. *Cardiovasc Res* **110**, 419-430 (2016). <https://doi.org:10.1093/cvr/cvw075>
- 170 Kuivaniemi, H. & Tromp, G. Type III collagen (COL3A1): Gene and protein structure, tissue distribution, and associated diseases. *Gene* **707**, 151-171 (2019). <https://doi.org:10.1016/j.gene.2019.05.003>
- 171 Pankov, R. & Yamada, K. M. Fibronectin at a glance. *J Cell Sci* **115**, 3861-3863 (2002). <https://doi.org:10.1242/jcs.00059>
- 172 Barrick, S. K. & Greenberg, M. J. Cardiac myosin contraction and mechanotransduction in health and disease. *J Biol Chem* **297**, 101297 (2021). <https://doi.org:10.1016/j.jbc.2021.101297>
- 173 Hailstones, D. *et al.* Differential regulation of the atrial isoforms of the myosin light chains during striated muscle development. *J Biol Chem* **267**, 23295-23300 (1992).
- 174 Mogensen, J. *et al.* Severe disease expression of cardiac troponin C and T mutations in patients with idiopathic dilated cardiomyopathy. *J Am Coll Cardiol* **44**, 2033-2040 (2004). <https://doi.org:10.1016/j.jacc.2004.08.027>
- 175 Guo, D. C. *et al.* Mutations in smooth muscle alpha-actin (ACTA2) cause coronary artery disease, stroke, and Moyamoya disease, along with thoracic aortic disease. *Am J Hum Genet* **84**, 617-627 (2009). <https://doi.org:10.1016/j.ajhg.2009.04.007>
- 176 Ahn, J. S. *et al.* Ectopic Overexpression of Porcine Myh1 Increased in Slow Muscle Fibers and Enhanced Endurance Exercise in Transgenic Mice. *Int J Mol Sci* **19** (2018). <https://doi.org:10.3390/ijms19102959>
- 177 Schiaffino, S., Rossi, A. C., Smerdu, V., Leinwand, L. A. & Reggiani, C. Developmental myosins: expression patterns and functional significance. *Skelet Muscle* **5**, 22 (2015). <https://doi.org:10.1186/s13395-015-0046-6>
- 178 Richards, E., Lopez, M. J. & Maani, C. V. in *StatPearls* (2022).

- 179 Perez, D. M. Current Developments on the Role of alpha(1)-Adrenergic Receptors in Cognition, Cardioprotection, and Metabolism. *Front Cell Dev Biol* **9**, 652152 (2021). <https://doi.org:10.3389/fcell.2021.652152>
- 180 Sam, C. & Bordoni, B. in *StatPearls* (2022).
- 181 del Campo, L. & Ferrer, M. Wire Myography to Study Vascular Tone and Vascular Structure of Isolated Mouse Arteries. *Methods Mol Biol* **1339**, 255-276 (2015). https://doi.org:10.1007/978-1-4939-2929-0_18
- 182 Russell, A. & Watts, S. Vascular reactivity of isolated thoracic aorta of the C57BL/6J mouse. *J Pharmacol Exp Ther* **294**, 598-604 (2000).
- 183 Barros, P. R., Costa, T. J., Akamine, E. H. & Tostes, R. C. Vascular Aging in Rodent Models: Contrasting Mechanisms Driving the Female and Male Vascular Senescence. *Front Aging* **2**, 727604 (2021). <https://doi.org:10.3389/fragi.2021.727604>
- 184 They, C. *et al.* Minimal information for studies of extracellular vesicles 2018 (MISEV2018): a position statement of the International Society for Extracellular Vesicles and update of the MISEV2014 guidelines. *J Extracell Vesicles* **7**, 1535750 (2018). <https://doi.org:10.1080/20013078.2018.1535750>
- 185 Bauer, E. M. *et al.* Thrombospondin-1 supports blood pressure by limiting eNOS activation and endothelial-dependent vasorelaxation. *Cardiovasc Res* **88**, 471-481 (2010). <https://doi.org:10.1093/cvr/cvq218>
- 186 Awdishu, L. *et al.* Urinary Exosomes Identify Inflammatory Pathways in Vancomycin Associated Acute Kidney Injury. *Int J Mol Sci* **22** (2021). <https://doi.org:10.3390/ijms22062784>
- 187 Albacete-Albacete, L., Sanchez-Alvarez, M. & Del Pozo, M. A. Extracellular Vesicles: An Emerging Mechanism Governing the Secretion and Biological Roles of Tenascin-C. *Front Immunol* **12**, 671485 (2021). <https://doi.org:10.3389/fimmu.2021.671485>
- 188 Gao, Y., Chen, Y., Wang, L., Li, C. & Ge, W. Serum-derived extracellular vesicles inhibit osteoclastogenesis in active-phase patients with SAPHO syndrome. *Ther Adv Musculoskelet Dis* **13**, 1759720X211006966 (2021). <https://doi.org:10.1177/1759720X211006966>
- 189 Blaser, M. C. & Aikawa, E. Roles and Regulation of Extracellular Vesicles in Cardiovascular Mineral Metabolism. *Front Cardiovasc Med* **5**, 187 (2018). <https://doi.org:10.3389/fcvm.2018.00187>

- 190 Yi, Z. *et al.* The Rab27a/granuphilin complex regulates the exocytosis of insulin-containing dense-core granules. *Mol Cell Biol* **22**, 1858-1867 (2002). <https://doi.org/10.1128/MCB.22.6.1858-1867.2002>
- 191 Xia, N. *et al.* Uncoupling of Endothelial Nitric Oxide Synthase in Perivascular Adipose Tissue of Diet-Induced Obese Mice. *Arterioscler Thromb Vasc Biol* **36**, 78-85 (2016). <https://doi.org/10.1161/ATVBAHA.115.306263>
- 192 Diaz Brinton, R. Minireview: translational animal models of human menopause: challenges and emerging opportunities. *Endocrinology* **153**, 3571-3578 (2012). <https://doi.org/10.1210/en.2012-1340>
- 193 Lin, S., Thomas, T. C., Storlien, L. H. & Huang, X. F. Development of high fat diet-induced obesity and leptin resistance in C57Bl/6J mice. *Int J Obes Relat Metab Disord* **24**, 639-646 (2000). <https://doi.org/10.1038/sj.ijo.0801209>
- 194 Yang, Y., Smith, D. L., Jr., Keating, K. D., Allison, D. B. & Nagy, T. R. Variations in body weight, food intake and body composition after long-term high-fat diet feeding in C57BL/6J mice. *Obesity (Silver Spring)* **22**, 2147-2155 (2014). <https://doi.org/10.1002/oby.20811>
- 195 Casimiro, I., Stull, N. D., Tersey, S. A. & Mirmira, R. G. Phenotypic sexual dimorphism in response to dietary fat manipulation in C57BL/6J mice. *J Diabetes Complications* **35**, 107795 (2021). <https://doi.org/10.1016/j.jdiacomp.2020.107795>
- 196 Aldiss, P. *et al.* Interscapular and Perivascular Brown Adipose Tissue Respond Differently to a Short-Term High-Fat Diet. *Nutrients* **11** (2019). <https://doi.org/10.3390/nu11051065>
- 197 Stanek, A., Brozyna-Tkaczyk, K. & Myslinski, W. The Role of Obesity-Induced Perivascular Adipose Tissue (PVAT) Dysfunction in Vascular Homeostasis. *Nutrients* **13** (2021). <https://doi.org/10.3390/nu13113843>
- 198 Stumpe, K. O. *et al.* Vascular wall thickness in hypertension: the Perindopril Regression of Vascular Thickening European Community Trial: PROTECT. *Am J Cardiol* **76**, 50E-54E (1995). [https://doi.org/10.1016/s0002-9149\(99\)80505-0](https://doi.org/10.1016/s0002-9149(99)80505-0)
- 199 Lang, P., Hasselwander, S., Li, H. & Xia, N. Effects of different diets used in diet-induced obesity models on insulin resistance and vascular dysfunction in C57BL/6 mice. *Sci Rep* **9**, 19556 (2019). <https://doi.org/10.1038/s41598-019-55987-x>
- 200 Montgomery, M. K. *et al.* Mouse strain-dependent variation in obesity and glucose

- homeostasis in response to high-fat feeding. *Diabetologia* **56**, 1129-1139 (2013).
<https://doi.org:10.1007/s00125-013-2846-8>
- 201 Avtanski, D., Pavlov, V. A., Tracey, K. J. & Poretsky, L. Characterization of inflammation and insulin resistance in high-fat diet-induced male C57BL/6J mouse model of obesity. *Animal Model Exp Med* **2**, 252-258 (2019). <https://doi.org:10.1002/ame2.12084>
- 202 Steinberg, H. O. & Baron, A. D. Vascular function, insulin resistance and fatty acids. *Diabetologia* **45**, 623-634 (2002). <https://doi.org:10.1007/s00125-002-0800-2>
- 203 Davis, K. E. *et al.* The sexually dimorphic role of adipose and adipocyte estrogen receptors in modulating adipose tissue expansion, inflammation, and fibrosis. *Mol Metab* **2**, 227-242 (2013). <https://doi.org:10.1016/j.molmet.2013.05.006>
- 204 Hartwig, S. *et al.* Exosomal proteins constitute an essential part of the human adipose tissue secretome. *Biochim Biophys Acta Proteins Proteom* **1867**, 140172 (2019).
<https://doi.org:10.1016/j.bbapap.2018.11.009>
- 205 Kasai, K. *et al.* Rab27a mediates the tight docking of insulin granules onto the plasma membrane during glucose stimulation. *J Clin Invest* **115**, 388-396 (2005).
<https://doi.org:10.1172/JCI22955>
- 206 Collins, S., Martin, T. L., Surwit, R. S. & Robidoux, J. Genetic vulnerability to diet-induced obesity in the C57BL/6J mouse: physiological and molecular characteristics. *Physiol Behav* **81**, 243-248 (2004). <https://doi.org:10.1016/j.physbeh.2004.02.006>
- 207 Chusyd, D. E., Wang, D., Huffman, D. M. & Nagy, T. R. Relationships between Rodent White Adipose Fat Pads and Human White Adipose Fat Depots. *Front Nutr* **3**, 10 (2016).
<https://doi.org:10.3389/fnut.2016.00010>
- 208 Zhang, F. *et al.* An Adipose Tissue Atlas: An Image-Guided Identification of Human-like BAT and Beige Depots in Rodents. *Cell Metab* **27**, 252-262 e253 (2018).
<https://doi.org:10.1016/j.cmet.2017.12.004>
- 209 Lempesis, I. G., Tsilingiris, D., Liu, J. & Dalamaga, M. Of mice and men: Considerations on adipose tissue physiology in animal models of obesity and human studies. *Metabol Open* **15**, 100208 (2022). <https://doi.org:10.1016/j.metop.2022.100208>
- 210 Hillock-Watling, C. & Gottlieb, A. I. The pathobiology of perivascular adipose tissue (PVAT), the fourth layer of the blood vessel wall. *Cardiovasc Pathol* **61**, 107459 (2022).
<https://doi.org:10.1016/j.carpath.2022.107459>

- 211 Galvez-Prieto, B. *et al.* Comparative expression analysis of the renin-angiotensin system components between white and brown perivascular adipose tissue. *J Endocrinol* **197**, 55-64 (2008). <https://doi.org:10.1677/JOE-07-0284>
- 212 Scott, S. S., Yang, X., Robich, M., Liaw, L. & Boucher, J. M. Differentiation Capacity of Human Aortic Perivascular Adipose Progenitor Cells. *J Vis Exp* (2019). <https://doi.org:10.3791/59337>
- 213 Lohn, M. *et al.* Periadventitial fat releases a vascular relaxing factor. *FASEB J* **16**, 1057-1063 (2002). <https://doi.org:10.1096/fj.02-0024com>
- 214 Dreyer, C. *et al.* Control of the peroxisomal beta-oxidation pathway by a novel family of nuclear hormone receptors. *Cell* **68**, 879-887 (1992). [https://doi.org:10.1016/0092-8674\(92\)90031-7](https://doi.org:10.1016/0092-8674(92)90031-7)
- 215 Corvera, S. Cellular Heterogeneity in Adipose Tissues. *Annu Rev Physiol* **83**, 257-278 (2021). <https://doi.org:10.1146/annurev-physiol-031620-095446>
- 216 Knights, A. J., Wu, J. & Tseng, Y. H. The Heating Microenvironment: Intercellular Cross Talk Within Thermogenic Adipose Tissue. *Diabetes* **69**, 1599-1604 (2020). <https://doi.org:10.2337/db20-0303>
- 217 Zhou, W. *et al.* Rab27a deletion impairs the therapeutic potential of endothelial progenitor cells for myocardial infarction. *Mol Cell Biochem* **476**, 797-807 (2021). <https://doi.org:10.1007/s11010-020-03945-x>
- 218 Connolly, K. D. *et al.* Characterisation of adipocyte-derived extracellular vesicles released pre- and post-adipogenesis. *J Extracell Vesicles* **4**, 29159 (2015). <https://doi.org:10.3402/jev.v4.29159>
- 219 Qiao, L. *et al.* microRNA-21-5p dysregulation in exosomes derived from heart failure patients impairs regenerative potential. *J Clin Invest* **129**, 2237-2250 (2019). <https://doi.org:10.1172/JCI123135>
- 220 Homma, Y., Hiragi, S. & Fukuda, M. Rab family of small GTPases: an updated view on their regulation and functions. *FEBS J* **288**, 36-55 (2021). <https://doi.org:10.1111/febs.15453>
- 221 Klopper, T. H., Kienle, N., Fasshauer, D. & Munro, S. Untangling the evolution of Rab G proteins: implications of a comprehensive genomic analysis. *BMC Biol* **10**, 71 (2012). <https://doi.org:10.1186/1741-7007-10-71>

- 222 Goto-Ito, S. *et al.* Structural basis of guanine nucleotide exchange for Rab11 by SH3BP5. *Life Sci Alliance* **2** (2019). <https://doi.org:10.26508/lsa.201900297>
- 223 Hendrix, A. *et al.* Effect of the secretory small GTPase Rab27B on breast cancer growth, invasion, and metastasis. *J Natl Cancer Inst* **102**, 866-880 (2010). <https://doi.org:10.1093/jnci/djq153>
- 224 *Common Metabolic Diseases Knowledge Portal (cmdkp.org)*. 2023 Mar 30).
- 225 *Common Metabolic Diseases Knowledge Portal (cmdkp.org)*. 2023 Mar 30).
- 226 Davey, J. R. *et al.* TBC1D13 is a RAB35 specific GAP that plays an important role in GLUT4 trafficking in adipocytes. *Traffic* **13**, 1429-1441 (2012). <https://doi.org:10.1111/j.1600-0854.2012.01397.x>
- 227 Yan, Z. *et al.* Rab11a Mediates Vascular Endothelial-Cadherin Recycling and Controls Endothelial Barrier Function. *Arterioscler Thromb Vasc Biol* **36**, 339-349 (2016). <https://doi.org:10.1161/ATVBAHA.115.306549>
- 228 Yu, S. *et al.* Global ablation of the mouse Rab11a gene impairs early embryogenesis and matrix metalloproteinase secretion. *J Biol Chem* **289**, 32030-32043 (2014). <https://doi.org:10.1074/jbc.M113.538223>
- 229 Ramalho, J. S. *et al.* Chromosomal mapping, gene structure and characterization of the human and murine RAB27B gene. *BMC Genet* **2**, 2 (2001). <https://doi.org:10.1186/1471-2156-2-2>
- 230 Gromov, P. S. *et al.* Human rab11a: transcription, chromosome mapping and effect on the expression levels of host GTP-binding proteins. *FEBS Lett* **429**, 359-364 (1998). [https://doi.org:10.1016/s0014-5793\(98\)00607-3](https://doi.org:10.1016/s0014-5793(98)00607-3)
- 231 *Common Metabolic Diseases Knowledge Portal (cmdkp.org)*. 2023 Mar 30).
- 232 Ferrante, S. C. *et al.* Adipocyte-derived exosomal miRNAs: a novel mechanism for obesity-related disease. *Pediatr Res* **77**, 447-454 (2015). <https://doi.org:10.1038/pr.2014.202>
- 233 Sorokin, V. *et al.* Role of Vascular Smooth Muscle Cell Plasticity and Interactions in Vessel Wall Inflammation. *Front Immunol* **11**, 599415 (2020). <https://doi.org:10.3389/fimmu.2020.599415>

- 234 Li, X., Ma, Z. & Zhu, Y. Z. Regional Heterogeneity of Perivascular Adipose Tissue: Morphology, Origin, and Secretome. *Front Pharmacol* **12**, 697720 (2021). <https://doi.org:10.3389/fphar.2021.697720>
- 235 Francetic, T. & Li, Q. Skeletal myogenesis and Myf5 activation. *Transcription* **2**, 109-114 (2011). <https://doi.org:10.4161/trns.2.3.15829>
- 236 Tallquist, M. D., Weismann, K. E., Hellstrom, M. & Soriano, P. Early myotome specification regulates PDGFA expression and axial skeleton development. *Development* **127**, 5059-5070 (2000). <https://doi.org:10.1242/dev.127.23.5059>
- 237 Madisen, L. *et al.* A robust and high-throughput Cre reporting and characterization system for the whole mouse brain. *Nat Neurosci* **13**, 133-140 (2010). <https://doi.org:10.1038/nn.2467>
- 238 El-Brolosy, M. A. & Stainier, D. Y. R. Genetic compensation: A phenomenon in search of mechanisms. *PLoS Genet* **13**, e1006780 (2017). <https://doi.org:10.1371/journal.pgen.1006780>
- 239 Wirth, A. *et al.* G12-G13-LARG-mediated signaling in vascular smooth muscle is required for salt-induced hypertension. *Nat Med* **14**, 64-68 (2008). <https://doi.org:10.1038/nm1666>
- 240 Breviario, F. *et al.* Functional properties of human vascular endothelial cadherin (7B4/cadherin-5), an endothelium-specific cadherin. *Arterioscler Thromb Vasc Biol* **15**, 1229-1239 (1995). <https://doi.org:10.1161/01.atv.15.8.1229>

BIOGRAPHY OF THE AUTHOR

Ashley Soucy is from a rural town in central New Hampshire. She earned a bachelor's degree in Biochemistry with a Minor in Microbiology from The University of Maine. During her time as an undergraduate, Ashley developed foundational research skills under the mentorship of Dr. Melissa Maginnis. This experience motivated her to pursue a doctoral degree in Biomedical Science through the Graduate School of Biomedical Science and Engineering at the University of Maine. During her graduate career, Ashley studied under the primary mentorship of Dr. Lucy Liaw at the MaineHealth Institute for Research. It is Ashley's hope to apply her education to improve human health through therapy development. Ashley is a candidate for the Doctor of Philosophy degree in Biomedical Science at The University of Maine in May 2023.